UNIVERSIDADE DE LISBOA
FACULDADE DE CIÊNCIAS

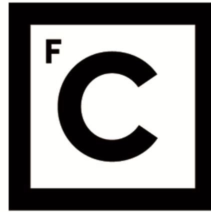

Ciências
ULisboa

Resonant Tunnelling Diode Optoelectronic Receivers and Transmitters

" Documento Definitivo"

Doutoramento em Engenharia Física

Saif Asem Yasin Alomari

Tese orientada por:
(Prof. Dr. José Maria Longras Figueiredo)

Documento especialmente elaborado para a obtenção do grau de doutor

2022

UNIVERSIDADE DE LISBOA

FACULDADE DE CIÊNCIAS

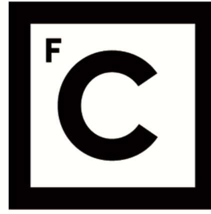

Ciências
ULisboa

Resonant Tunnelling Diode Optoelectronic Receivers and Transmitters

Doutoramento em Engenharia Física

Saif Asem Yasin Alomari

Tese orientada por:

(Prof. Dr. José Maria Longras Figueiredo)

Júri:

Presidente:

- José Manuel de Nunes Vicente e Rebordão, Investigador Coordenador e Presidente do Departamento de Física da Faculdade de Ciências da Universidade de Lisboa

Vogais:

- Doutor Henrique Manuel de Castro Faria Salgado, Professor Associado da Faculdade de Engenharia da Universidade do Porto;
- Doutor Paulo Miguel Nepomuceno Pereira Monteiro, Professor Associado do Departamento de Eletrónica, Telecomunicações e Informática da Universidade de Aveiro;
- Doutor Bruno Miguel Patarata Romeira, Staff Researcher do INL – International Iberian Nanotechnology Laboratory (Portugal);
- Doutor António Joaquim Rosa Amorim Barbosa, Professor Catedrático da Faculdade de Ciências da Universidade de Lisboa;
- Doutor José Maria Longras Figueiredo, Professor Associado da Faculdade de Ciências da Universidade de Lisboa (orientador).

Documento especialmente elaborado para a obtenção do grau de doutor

This work has been funded by the european union horizon 2020 TeraApps project (Agreement No. 765426)

2022

Resumo

__palavras-chave__: ***díodo de túnel ressonante / optoeletrônico / foto-detector / de alta velocidade / transmissores ópticos***

Esta tese descreve o trabalho de investigação em transmissores e recetores optoeletrónicos baseados em díodo de efeito de túnel ressonante (*RTD*) de pouço quântica de dupla a barreira de potencial, focando-se no projeto e na caracterização de foto-detetores de díodo de efeito de túnel ressonante (*RTD-PDs*) implementados no sistema material $In_{53}Ga_{47}As/InP$, para operação nos comprimentos de onda 1,55 µm e 1,31 µm, e avaliando numericamente os méritos da integração de um *RTD/RTD-PD* com díodos laser (*LD*) para atuar como transmissores optoelectrónico simples.

Os fotodetectores (*PD*) são parte integrante de muitas tecnologias usadas na vida cotidiana. Eles desempenham um papel vital em muitas aplicações, como por exemplo, sistemas de comunicação, imagens aplicacões, militares, defesa, direção autónoma e até detectores infravermelhos em smartphones. Com a crescente demanda por dados, os fotodetectores tornaram-se importantes no desenvolvimento de circuitos integrados fotônicos (*PICs*). Portanto, é benéfico ter fotodetectores rápidos, altamente responsivos, económicos e fáceis de fabricar.

O objetivo do trabalho foi investigar arquiteturas de transmissor e recetor simples, rápidos e de baixo custo tirando partido das propriedades dos *RTDs*, como a simplicidade estrutural, a operação a muito alta frequência (até terahertz) e o ganho elétrico de banda larga (praticamente de dc até terahertz). Também são descritos os estudos preliminares da operação à temperatura ambiente de *RTD-PDs* como detetores de "single photon", utilizando a propriedade de excitabilidade.

Neste trabalho, tentamos responder à questão de quais os fatores que afetam a largura de banda dos *RTD-PDs*. Sabendo a resposta a isto, propusemos regras e otimizações necessárias para obter *RTD-PDs* de grande largura de banda (<10 GHz). Além disso, mostramos como utilizar ganho elétrico intrínseco decorrente da curva de corrente-tensão (IV) não linear, e da presença da região de resistência diferencial negativa (*NDR*), como forma de construir foto-detetores de elevada responsividade que possam superar as tecnologias comerciais atuais, nomeadamente foto-díodos *PIN*, em novas aplicações.

Um *RTD* pode ser realizado incorporando uma estrutura de poço quântico de barreira dupla (*DBQW*) entre duas regiões; o emissor e o coletor. Desde que a largura do poço quântico seja comparável ao comprimento de onda do electrão, os efeitos de quantização de energia ocorrem dentro do poço quântico. Esses níveis atuam como canais para os electrãos no emissor fazerem um túnel quando o alinhamento apropriado com o nível de Fermi é satisfeito, levando a condições ressonantes e a um pico de corrente. Perturbar este alinhamento leva a uma diminuição de corrente (devido à diminuição da probabilidade de tunelamento) e a um vale de corrente. Isso dá origem a uma curva corrente-tensão (*IV*) muito interessante e altamente não linear

A fotodetecção usando absorção interbanda é usada para detectar luz em vários comprimentos de onda, dependendo do banda proibida do material de fotoabsorção. Semicondutores compostos, (especialmente III-V) compostos ternários e quaternários, com engenharia de *banda proibida*, permitem a detecção em diferentes comprimentos de onda. Esses detectores operam pela geração de portadores de carga devido à absorção de energia luminosa. Quando a luz tem energia mais alta que o banda proibida, os electrãos na banda de valência ganham energia suficiente para transferir para a banda de condução e criar pares electrão-lacuna. Os transportadores recém-gerados requerem um mecanismo de transporte de carga (principalmente campo elétrico) para separá-los e, eventualmente, contribuir para a corrente fotogerada. Um fotodetector de diodo de tunelamento ressonante (*RTD-PD*) é realizado quando uma ou ambas as camadas espaçadoras ao redor do *DBQW* (ou seja: o emissor e o coletor) são feitas para serem fotossensíveis. Quando a luz incide no dispositivo, ela é absorvida nessas regiões e os pares electrão-buraco são gerados devido à absorção entre bandas.

O trabalho de projeto e modelação baseou-se em simulações numéricas utilizando o formalismo de funções de Green fora de equilíbrio ("non-equilibrium Green's function formalismo", *NEGF*), que implementamos usando o Atlas Silvaco. Descrevemos de forma breve o método *NEGF* e o ATLAS Silvaco, e utilizámo-los para fazer o projeto das estruturas epitaxiais dos dispositivos que pretendemos. Os resultados são novos modelos que nos permitem prever o efeito que os parâmetros estruturais do *RTD* (concentração de dopantes e as espessuras tanto do emissor como do coletor) têm no valor da tensão de pico do *RTD*. O modelo é utilizado em conjunto com o modelo Schulman para a característica corrente-

tensão do *RTD* para implementar um programa MATLAB que prevê a curva *IV* do *RTD* para um conjunto de parâmetros (níveis de dopagem do emissor e do coletor, largura do poço e a espessura do coletor) para os *RTDs* de $In_{53}Ga_{47}As/InP$.

Estudamos experimentalmente os fatores que afetam a largura de banda através da caracterização ótica de várias estruturas epitaxiais e propomos hipóteses que ajudam a explicar as larguras de banda medidas. Mostramos que para se obterem *RTD-PDs* com tempo de resposta rápidos (sub-nano-segundo), as camadas de absorção de luz devem estar confinadas aos locais onde o campo elétrico é suficiente elevado e evitar o emprego de camadas semicondutoras para contactos elétricos com hiatos inferiores à energia dos fotões que se pretendem detetar.

Além disso, definimos um conjunto de regras para a conceção de detetores *RTD-PD* baseados em hetero-estruturas *n-i-n* e *p-i-n*, onde a extensão, localização e o nível de dopagem das regiões de absorção são os parâmetros relevantes considerados para a determinação da largura de banda e da responsividade dos dispositivos. Além disso, medimos e reportamos as medidas de responsividade dos *RTD-PDs* sob excitação ótica de *DC* e *AC*.

Mostramos que os *RTD-PDs* podem apresentar valores de responsividade muito elevados atingindo 1×10^{7} A/W, e largura de banda elétrica de cerca de 1,26 GHz (1,75 GHz ótica) que é limitada pelo tempo de vida dos portadores minoritários fotogerados (as lacunas).

A última parte da tese é dedicada ao estudo de circuitos *RTD-PD*, onde a integração entre um *RTD-PD* e um díodo laser (*LD*) é cuidadosamente examinada. O *LD* funciona como uma "carga" cuja operação é controlada pela corrente do RTD-PD. Derivamos e estudamos o circuito equivalente de tal sistema incorporando a função do Schulman para a curva IV do RTD-PD, usando a solução para estudar vários regimes de operação usando o código MATLAB desenvolvido. Estes regimes incluem *RTD-PD* polarizado na primeira região de resistência diferencial positiva (*PDR*), quando é polarizado na região *NDR*, e quando o ponto de operação é induzido para comutar entre a PDR e a *NDR*. Também mostramos como a propriedade de excitabilidade do *RTD-PD* pode ser usada para deteção de um único fotão ("single photon"), e a capacidade de *RTDs* funcionar em como osciladores controlados por tensão quando polarizados na região de *NDR*.

Abstract

Keywords: *resonant-tunneling-diode / optoelectronics / photodetectors / high-speed / optical-transmitters*

This thesis describes the research work on double barrier quantum well (*DBQW*) resonant tunneling diode (*RTD*) based optoelectronic transmitters and receivers, focused on the design and characterization of resonant tunneling diode photodetectors (*RTD-PD*) implemented in the $In_{53}Ga_{47}As$/*InP* material system for operation at 1.55 μm and 1.31 μm wavelengths, and evaluate numerically the merits of the integration of an *RTD/RTD-PD* with a laser diode (*LDs*) to act as simple optoelectronic transmitters.

The aim of the work was to investigate simple, low-cost, high-speed transmitter and receiver architectures taking advantage of *RTDs* properties such as the structural simplicity, high frequency (up to terahertz), and wide-bandwidth built-in electrical gain (roughly, from dc to terahertz). Also described are the preliminary studies of *RTD-PDs* operation as single photon detector at room temperature utilizing the excitability property.

In this work, we evaluate which factors affect the bandwidth of *RTD-PDs*. Knowing the answer to this, we propose rules and optimizations necessary to achieving high bandwidth (>10 GHz) *RTD-PDs*. Furthermore, we show how to utilize the built-in amplification, arising from the RTD non-linear current-voltage (*IV*) curve and the presence of a negative differential resistance region (*NDR*) to building high responsivity photodetectors that can outperform current commercial technologies, particularly *PIN* photodiodes, in novel applications.

The design and modeling work relied on numerical simulations utilizing the non-equilibrium Green's function formalism (*NEGF*), which we implement using Silvaco ATLAS. We briefly introduce the *NEGF* method and Silvaco ATLAS and utilize them to do the design of the epitaxial structure of novel devices. The results of which are novel models which allow us to predict the effect that the *RTD* structural parameters (doping concentration and the lengths of both the emitter and collector) have on the peak voltage of the *RTD*.

We study experimentally the factors affecting the bandwidth by optical characterization of several epitaxial layer stacks and propose hypotheses that help to explain the measured bandwidths. We show that for high-speed *RTD-PDs* (sub nanosecond), the light

absorption layers should be confined to the locations where the electric field is sufficiently high and avoiding highly doped thick contact layers with band gap energies below the energy of the photons being detected.

Additionally, we outline a set of rules for the design of *RTD-PD* detectors based on *n-i-n* and *p-i-n* heterostructures, where the length, location, and doping level of the absorption regions are the relevant parameters to be considered in determining the bandwidth and responsivity of the devices. Moreover, we measure and report on the responsivity of *RTD-PDs* under both *DC* and *AC* optical excitation.

We show that *RTD-PDs* can have very high responsivity values reaching up to 1×10^7 A/W, and electrical bandwidth of around 1.26 GHz (1.75 GHz optical) that is limited by the lifetime of the photo-generated minority carriers (the holes).

The last part of the thesis is dedicated to the study of *RTD-PD* circuits, where the integration between an *RTD-PD* and a laser diode (*LD*) is thoroughly examined. The *LD* acts as a load that is driven by the *RTD-PD* current. We derive and investigate the equivalent circuit for such a system incorporating the Schulman function for the *RTD-PD IV*, using the solution to study several operation regimes using MATLAB code. These regimes include the *RTD-PD* biased in the positive differential resistance region (*PDR*), when it is biased in the *NDR* region, and when induced to switch between the *PDR* and *NDR* regions. We also show how the excitability property of the *RTD-PD* can be used for detecting very low signal intensity levels, and the ability of *RTDs* to operate as voltage-controlled oscillators while biased in the *NDR* region.

Acknowledgment

The author would like to thank the team at the University of Glasgow, Prof. Edward Wasige, Dr. Abdullah Al-Khalidi, Dr. Qusay Al Tai, and Maira Elknse for fabricating the resonant tunneling diode photo detectors. A big thank you to Prof. Sven Höfling's team at the University of Würzburg, particularly Dr. Fauzia Jabeen, Dr. Fabian Hartmann and my colleague Begüm Yavas Aydin for the tremendous effort during the secondment time to grow RTDs on InP.

Special thanks to my colleagues at FCUL, David Alves and Bruno Couto for all the help and advice during my work. And of course, many thanks to the team at FC.ID, Helia Rodrigues and Carla Marques for all the help during the project.

Special thanks to the EU commission for generously funding this work, and to my supervisor Prof. José Figueiredo for giving me the opportunity to work on an interesting topic and for his guidance.

This project has received funding from the European Union's Horizon 2020 research and innovation program under the Marie Skłodowska-Curie grant, Agreement No. 765426 (TeraApps).

Table of Contents

CHAPTER 1 : INTRODUCTION....... 1

1.1 OUTLINE AND METHODOLOGY....... 1

1.2 MOTIVATION....... 2

1.3 BACKGROUND ON PHOTODETECTION AND *RTD-PD*....... 5

1.3.1 Photoconductors....... 5

1.3.2 Quantum-well-based photodetectors....... 7

1.3.3 Resonant tunnelling diode-based photodetectors....... 8

1.4 THESIS OUTCOMES AND CONTRIBUTIONS....... 11

CHAPTER 2 : INTRODUCTION TO RESONANT TUNNELLING DIODES....... 12

2.1 INTRODUCTION....... 12

2.2 REVIEW ON SEMICONDUCTOR PHYSICS....... 12

2.1.1 Effective mass approximation....... 12

2.1.2 Density of states....... 13

2.2.1 Semiconductor junctions....... 13

2.2.2 Quantum mechanical tunnelling....... 21

2.3 QUANTUM WELLS....... 23

2.4 INFINITE POTENTIAL WELL....... 24

2.5 FINITE POTENTIAL WELL....... 25

2.6 RESONANT TUNNELLING DIODES....... 26

2.7 RESONANT TUNNELLING DIODE TIME CONSTANTS....... 30

2.8 SUMMARY AND CONCLUSION....... 32

CHAPTER 3 : SIMULATION OF *RTD* STRUCTURAL PARAMETERS USING SILVACO ATLAS....... 33

3.1 INTRODUCTION....... 33

3.2 INTRODUCTION TO SILVACO ATLAS....... 33

3.2.1 Using NEGF with ATLAS....... 36

3.3 DESIGN AND OPTIMIZATION OF RTDS....... 38

3.3.1 Methodology....... 39

3.3.2 The effect of collector carrier concentration....... 39

3.3.3 The effect of emitter carrier concentration....... 55

3.3.4 Effect of emitter layer thickness....... 61

3.3.5 Effect of collector layer thickness....... 62

3.3.6 Effects on peak to valley current ratio, ΔV and ΔI....... 63

3.3.7 Effects of doping concentrations....... 65

3.3.8 The effect of the double barrier quantum well....... 69

3.4 SUMMARY AND CONCLUSION....... 77

CHAPTER 4 : RESONANT TUNNELLING DIODE PHOTODETECTOR DESIGN CONSIDERATIONS 78

4.1 INTRODUCTION 78

4.2 LIGHT INTERACTION WITH A SEMICONDUCTOR 78

4.3 PHOTOCONDUCTORS AND PHOTOCONDUCTIVE GAIN 83

4.3.1 Conductivity (σ) 87

4.3.2 Mobility and electric field 89

4.3.3 Carrier lifetime 89

4.3.4 Rise time (carrier transit time, speed of response (BW)) 90

4.3.5 Current responsivity 90

4.4 PN-PHOTODETECTORS. 91

4.5 PIN PHOTODIODES 92

4.6 RESONANT TUNNELLING DIODE PHOTODETECTORS 93

4.6.1 High-speed RTD-PD design considerations 95

4.6.2 n-i-n epitaxial layer design 97

4.6.3 PIN-RTD design 99

4.7 SUMMARY AND CONCLUSION 104

CHAPTER 5 : OPTICAL CHARACTERIZATION OF RESONANT TUNNELLING DIODE PHOTODETECTORS 105

5.1 INTRODUCTION 105

5.2 EPITAXIAL LAYER DESIGNS 105

5.3 DC CURRENT RESPONSIVITY 106

5.3.1 Epi-layer NC1800 108

5.3.2 Epi-layer S99 115

5.3.3 Sample S98 120

5.3.4 Sample P-A323 125

5.3.5 Sample P-A325 130

5.3.6 Wafer A73 135

5.3.7 Photoconductive wafer 136

5.3.8 Sample PIN-RTD 140

5.3.9 Discussion and notes 144

5.4 IMPULSE RESPONSE 148

5.4.1 3dB bandwidth 154

5.5 AC SIGNAL DETECTION AND AMPLIFICATION 157

5.5.1 Operation as an amplifier in the NDR 157

5.6 SUMMARY AND CONCLUSION 161

CHAPTER 6 : RESONANT TUNNELLING DIODE – LASER DIODE INTEGRATION 162

6.1 INTRODUCTION 162
6.2 MOTIVATION 162
6.3 METHODOLOGY 164
6.3.1 Modelling of RTD-PD-LD circuits 164
6.3.2 RTD-PD-LD modes of operation 175
6.4 PRACTICAL EXPERIMENTATION WITH *RTD-PD* 178
6.4.1 RTD-PDs as excitable systems 180
6.5 RESULTS 182
6.5.1 Multisim integration of LD and RTD-PD 182
6.6 MATLAB SIMULATION RESULTS OF *RTD-PD-LD* 183
6.6.1 Operation in the PDC region 183
6.6.2 Operation in the PDC region with RF input 184
6.6.3 Operation in the NDC region 186
6.6.4 Operation between PDC and NDC regions 191
6.6.5 RTD-PD operation as a VCO 192
6.7 SUMMARY AND CONCLUSION 194

CHAPTER 7 : CONCLUSION AND FUTURE WORK 196

7.1 CONCLUSION 196
7.2 FUTURE WORK 199
7.2.1 Mixing in resonant tunnelling diodes 200

Appendix: 202

References: 205

List of figures

Figure 1: Typical RTD schematic (left side) and energy band diagram (right side) showing two quantized states E_0 and E_1. 3

Figure 2: Typical RTD IV curve. 3

Figure 3: Electromagnetic spectrum and THz technologies [1]. 4

Figure 4: RTD-PD concept showing the main structure (left side) and the band diagram (right side) with two Eigenstates E_0 and E_1 with inter-band absorption. 8

Figure 5: OOK transmission using RTD-PD concept. The inset shows the output from the RTD-PD (oscillations) when a pulse is applied to it (red rectangular pulse). 10

Figure 6: RTD-PD-LD and RTD transceivers for RoF concept [50]. 10

Figure 7: Types of semiconductor junctions. 14

Figure 8: example of a p-n homojunction. 15

Figure 9: Heterojunction types and interface discontinuities. 19

Figure 10: Sample n+ - n heterojunction. 20

Figure 11: IV characteristics of a tunnel diode [63]. 21

Figure 12: Energy band diagram of a tunnel diode under various bias points [63]. a- At zero bias. b- At the peak. c- in the NDR. d- The second PDR. e- interband tunneling. 22

Figure 13: Double barrier quantum well structure. 23

Figure 14: RTD concept illustration. 27

Figure 15: Principle of operation of a resonant tunneling diode. (a- zero bias conditions, b- PDR current, c- peak current, d- valley current). 28

Figure 16: Equivalent circuit of an RTD. 31

Figure 17: SILVACO program suite outline. 34

Figure 18: Typical SILVACO workflow. 34

Figure 19: Schematic of the simulated device. 40

Figure 20: IV curves for various collector doping concentrations. 41

Figure 21: Conduction band profile for various collector doping levels with the first bound Eigenstates. 41

Figure 22: IV curves for various collector doping levels. 44

Figure 23: Electric field profiles for various collector doping levels at zero bias. 45

Figure 24: Proposed model for RTD resistance. 46

Figure 25: Conduction band diagram for the 1×10^{12} cm^{-3} case at 0.6- and 1.0-volt bias. 48

Figure 26: Electric field profile for various collector doping levels. 49

Figure 27: Electron concentration for various collector doping levels. 51

Figure 28: Conduction band energy at peak voltage for various collector doping levels. 52

Figure 29: Energy evolution of the first Eigen state for various collector doping levels vs voltage. 53

Figure 30: Rate of change of the first bound state with respect to voltage for various collector doping. 55

Figure 31: IV curves for various emitter doping levels. *55*
Figure 32: Conduction band diagram with the first Eigenstate for various emitter doping levels. *56*
Figure 33: conduction band diagram for the second case (emitter has more doping than the collector). *58*
Figure 34: Evolution of the first bound state with applied bias for various emitter doping levels. *59*
Figure 35: Portion of the applied potential drop on the first Eigenstate as function of voltage. *59*
Figure 36: Carrier concentration in the quantum well for various voltage levels for 1×10^{14} cm^{-3}. *60*
Figure 37: Peak voltage dependence on emitter length. *62*
Figure 38: Peak voltage dependence on the collector length. *63*
Figure 39: IV curves of fabricated devices by [94] *64*
Figure 41: IV curves for GaAs/AlGaAs RTD with various emitter doping levels. *65*
Figure 42: PVCR dependence on emitter doping levels for GaAs/AlGaAs structure. *66*
Figure 43: Peak and valley current dependence on emitter doping for GaAs/AlAs structure. *66*
Figure 44: ΔV dependence on emitter concentration *67*
Figure 45: IV curves for changing the collector doping for GaAs/AlAs structure. *68*
Figure 46: ΔV dependence on the collector doping level. *69*
Figure 47: IV curves for various barrier widths (reverse bias case). *70*
Figure 48: IV curves for various barrier widths (reverse bias case). *70*
Figure 49: IV curves for various barrier widths (forward bias case). *71*
Figure 50: IV curves for various barrier widths (forward bias case). *71*
Figure 51: Peak and valley currents dependence on barrier widths (forward bias case). *72*
Figure 52: Peak and valley currents dependence on barrier widths (reverse bias case). *72*
Figure 53: PVCR dependence on barrier widths. *73*
Figure 54: ΔI dependence on barrier width. *73*
Figure 55: ΔV dependence on barrier width *74*
Figure 56: optimizing ΔVΔI for various barrier widths. *75*
Figure 57: PVCR dependence on the width of the quantum well. *76*
Figure 58: ΔV dependence on the width of the quantum well. *76*
Figure 59: Peak and valley current dependence on well width. *77*
Figure 60: Light beam interaction with a semiconductor. *80*
Figure 61: Quantum efficiency of $In_{53}Ga_{47}As$ vs. wavelength [98]. *83*
Figure 62: Sketch of photo-generated carriers' movement. *84*
Figure 63: Electron mobility dependence on carrier concentration for $In_{53}Ga_{47}As$ at 77 K (a) and 300 K (b) for different compensation ratios $\theta = (N_D + N_A)/n$. 1. $\theta = 1$, 2. $\theta = 2$, 3. $\theta = 5$, 4. $\theta = 10$. [107]. *88*
Figure 64: Hole mobility dependence on carrier concentration [107]. *88*
Figure 65: Electron mobility for In(x)Ga(1-x)As as function of composition. Electron drift (dashed curves) and Hall (solid curves) mobility versus composition parameter (x) at 300 K. 1, 1'. n = 3×10^{15} cm^{-3}, 2, 2'. n = 4×10^{16} cm^{-3}, 3. n = 2.3×10^{17} cm^{-3}. For curve 3 clectron Hall and drift mobility values are practically equal. [108]. *88*
Figure 66: Drift velocity dependence on electric field $In_{53}Ga_{47}As$ [109]. *89*

Figure 67: Carrier lifetime dependence on carrier density for $In_{53}Ga_{47}As$ [110]. 90
Figure 68: PN-junction photodiode [111]. 91
Figure 69 Physical layout of a PIN diode [112]. 92
Figure 70: Saturation voltage dependance on well width and Debye length. 96
Figure 71: Simulated IV curve for n-i-n RTD-PD. 99
Figure 72: Conduction band diagram and collector's electric field at the peak (0.95 V) and valley (1.2 V). 99
Figure 73: Zero-bias energy band diagram of PIN-RTD. 100
Figure 74: IV curve of proposed PIN detector. 103
Figure 75: Energy band diagram at 1 V bias. P-doped emitter at the left, n-doped collector at the right. Contacts are not shown. 104
Figure 76: Electric field in the emitter and collector at 1 V. 103
Figure 77: DC-optical characterization setup. 106
Figure 78: Typical characterization setup. The right side shows the probes and fiber alignment over the chip. These probes (and fiber) are controlled through micro-positioners. 107
Figure 79: Left - Typical RTD-PD mask for a 10x10 μm^2 device (University of Glasgow process). Right - Sample fabricated device with RTD and ground-signal-ground lines. 108
Figure 80: IV curves in reverse bias for sample NC1800. 109
Figure 81: PVCR and ΔV evolution with illumination power for sample NC1800. 110
Figure 82: Peak voltage and peak voltage shift for sample NC-1800. 111
Figure 83: Peak current and peak-photocurrent dependence on illumination power. 112
Figure 84: Current responsivity in reverse bias for sample NC1800. 113
Figure 85: An illustration of how V_{shift} is calculated. 113
Figure 86: Voltage shift as function of applied voltage for sample NC1800. The inset is a magnification for the 30 µW illumination level from 0.6 V to 1.3 V. 114
Figure 87: Peak responsivity as function of illumination power under reverse bias for sample NC1800. 115
Figure 88: IV curves in reverse bias for sample S99 (10×10 μm^2). 116
Figure 89: PVCR and ΔV evolution with illumination power. 116
Figure 90: Peak current and peak photocurrent dependence on illumination levels. 117
Figure 91: Peak voltage and peak-voltage shift as function of applied illumination levels. 117
Figure 92: Current responsivity curves for sample S99 as function of voltage under reverse bias. 118
Figure 93: Responsivity as function of applied illumination levels for sample S99. 119
Figure 94: Low illumination responsivity of sample S99. 120
Figure 95: Sample S99 IVs under low illumination levels. 120
Figure 96: IV curves under reverse bias for sample S98 (10×10 μm^2). 122
Figure 97: IV curves for sample S98 under reverse bias for 20x20 μm^2 devices. 123
Figure 98: Peak voltage and peak-voltage shift versus illumination levels for sample S98 (20×20 μm^2). 123
Figure 99: Current responsivity as function of voltage in reverse bias for S98 (10×10 μm^2). 124

Figure 100: Current responsivity for sample S98 (20x20 µm^2) – Inset shows ΔV vs V for 30 µW illumination. Notice the similarity between the two curves as highlighted earlier. 124
Figure 101: Responsivity versus illumination power under reverse bias for sample S98 (10×10 µm^2). 125
Figure 102: Sketch and 3D render of typical devices fabricated by the University of Würzburg. 127
Figure 103: Optical microscope images of fabricated RTD-PD devices for samples P-A323/5. 127
Figure 104: IV curves under forward bias for sample P-A323 (12 µm^2 diameter). 127
Figure 105:IV curves under reverse bias for sample P-A323 (12 µm^2 diameter). 128
Figure 106: Current responsivity curves under forward bias for sample P-A323. 129
Figure 107: Responsivity versus illumination power under forward bias for sample P-A323. 129
Figure 108: Current responsivity curves under reverse bias for sample P-A323. 130
Figure 109: Responsivity versus illumination power under reverse bias for sample P-A323. 130
Figure 110: IV curves under forward bias for sample P-A325 (15 µm^2 diameter). 132
Figure 111: IV curves under reverse bias for sample P-A325 (15 µm^2 diameter). 132
Figure 112: Responsivity versus illumination power under forward bias for sample P-A325. 133
Figure 113: Current responsivity under forward voltage for sample P-A325. 133
Figure 114: Current responsivity under reverse bias for sample P-A325. 134
Figure 115: Responsivity versus illumination power under reverse bias for sample P-A325. 135
Figure 119: conduction band diagram (flat-band) of DHD (green line is the Fermi-energy). 137
Figure 120: Silvaco simulation of DHD with drift diffusion and Tunneling models. Inset shows the NDR resulting from the Gunn effect between 0.15 V and 0.35 V. 138
Figure 121: Double-heterostructure diode NDR-like behavior. 139
Figure 116: IV curves for double heterostructure diode (10×10 µm^2). 139
Figure 117: Current responsivity for double heterostructure diode (10×10 µm^2). 140
Figure 118: Responsivity as function of the applied illumination level for double heterostructure diode. 140
Figure 122: IV curves under reverse bias for sample PIN-RTD (25x25 µm^2). 141
Figure 123: Current responsivity under reverse bias for sample PIN-RTD. 142
Figure 124: Responsivity versus illumination levels under reverse bias for sample PIN-RTD. 143
Figure 125: Emission power at 1.55 µm from sample PIN-RTD in forward bias. 143
Figure 126: Responsivity versus illumination levels for all wafers in reverse bias mode. 144
Figure 127: Optical characterization setup used to measure the optical impulse response. 150
Figure 128: Lifetime as function of voltage for epi-layers grown by IQE. 150
Figure 129: Lifetime as function of voltage for epi-layers grown at the university of Würzburg. 151
Figure 130: Response progress as function of voltage of PIN-RTD (reverse bias conditions). 153
Figure 131: Impulse response for all tested samples. 153
Figure 132: Bode plots showing the 3dB bandwidth of all samples. 154
Figure 133: PIN-RTD IVs for various devices. 155
Figure 134: 3dB-Bandwidth of the device with the mildest NDR. 156
Figure 135: RTD amplification in the NDR, the inset shows the 180 ° phase shift and the amplitude increase. 157

Figure 136: RTD equivalent circuit as an amplifier (left – for high frequency, right – low frequency). 158

Figure 137: Wafer 73A - RTD-PD and PIN photodiode detected signals with original modulating light signal. 160

Figure 138: Wafer 73A - RTD-PD and PIN photodiode detected signals (DC offset removed). 160

Figure 139: RTD-PD under dark and illumination conditions (10x10 μm^2). 164

Figure 140: Large signal equivalent circuit of an RTD. 165

Figure 141: IV curves of measured RTD vs. MATLAB simulation. 167

Figure 142: AC electrical equivalent circuit of a laser diode. Without modeling spontaneous emission, self-pulsation. 170

Figure 143: Equivalent circuit of RTD-LD. 171

Figure 144: IV curve of LD. 172

Figure 145: Output optical power of LD. 172

Figure 146: IV curve of the RTD with parameters in Table 6-2. The line shows the linear approximation of the NDC region. 174

Figure 147: RTD-PD equivalent circuit at high frequency. 175

Figure 148: RTD-PD equivalent circuit with linearized NDC region. 177

Figure 149: IV curves of actual devices under dark and illumination conditions. Device size 10x10 μm^2. 180

Figure 150: optical spike generation using actual devices. 181

Figure 151: IV curve of a LD run on Multisim (on voltage approx. 1.7V). 182

Figure 152: IV curve of RTD-LD circuit run on Multisim. 182

Figure 153: LD relaxation oscillations. 183

Figure 154: Output current of the RTD-PD when biased at 0.5 V and associated LD photon density. 184

Figure 155: RTD-PD current and LD photon density when biased in the PDC (0.5 V) with 1 GHz RF signal. 184

Figure 156: S modulation depth of LD. 185

Figure 157: RTD-PD current modulation index. 186

Figure 158: RTD-PD relaxation oscillations. 186

Figure 159: RTD-PD current and LD photon density when biased in the NDC. 187

Figure 160: RTD output current spike. 187

Figure 161: RTD-PD current and LD photon flux using 2 ps lifetime. 188

Figure 162: Relaxation frequency dependence on resistance. 189

Figure 163: Relaxation frequency dependence on inductance. 189

Figure 164: Relaxation frequency dependence on capacitance. 190

Figure 165: Relaxation oscillations in the tens of GHz range while biased in the NDR (0.8 V). 190

Figure 166: RTD voltage spikes and input pulses. 191

Figure 167: RTD-PD current and LD output photon density. 191

Figure 168: relaxation oscillation frequency as function of voltage in the NDC region). 192

Figure 169: IV curve and capacitance of $In_{53}Ga_{47}As$ RTD. 194

Figure 170: RTD-PD mixer concept. 200

Figure 171: IV characteristics of an RTD-PD. 200

List of abbreviations

RTD	*Resonant tunneling diode*
RTD-PD	*Resonant tunneling diode-based photodetector*
LD	*Laser diode*
THz	*Teraherz*
RADAR	*Radio detection and ranging*
DBQW	*Double quantum well*
Epi-layers	*Epitaxial grown layers*
ORTD	*Optical resonant tunneling diode*
PDC	*Positive differential conductance*
NDC	*Negative differential conductance*
PVCR	*Peak to valley current ratio*
RTD-OW	*Resonant tunneling diode optical waveguide*
RTD-EAM	*Resonant tunneling diode electro absorption modulator*
OCES	*optical controlled electronic oscillators*
APD	*Avalanche photodiode*
PIN diode	*P-type, intrinsic, N-type photodiode*
NDR	*Negative differential resistance*
PDR	*Positive differential resistance*
DHD	*Double heterojunction diode*
NEGF	*Non-equilibrium Greens function*
TLM	*Transmission line method*
MBE	*Molecular beam epitaxy*
MOCVD	*Metal organic chemical vapor deposition*
RF	*Radio frequency*
RT	*Resonant tunneling*
RoF	*Radio over fiber*
IV	*Current – Voltage*
IR	*Infrared*
NIR	*Near infrared*
MIR	*Mid infrared*
PIC	*Photonic integrated circuit*
PVCR	*Peak to valley current ratio*
RFID	*Radio frequency identification*
EDFA	*Erbium doped fiber amplifier*

MSM	*Metal semiconductor metal*
QW	*Quantum well*
2DEG	*2-dimensional electron gas*
FB	*Forward biased*
RB	*Reverse biased*
HEMT	*High electron mobility transistor*
MQW	*Multi-quantum well*
SL	*Super lattice*
RITD	*Resonant inter-band tunneling diode*
IoT	*Internet of things*
VCO	*Voltage controlled oscillator*
LO	*Local oscillator*
IDE	*Integrated development environment*
VWF	*Virtual wafer fab*
SMU	*Source measure unit*
SRH	*Shockley-Reed-Hall*
PRBS	*Pseudo random binary sequence*
DFB	*Distributed feedback*
SNR	*Signal to noise ratio*
MOSFET	*Metal oxide semiconductor field effect transistor*
KCL	*Kirchoff's current law*

Chapter 1 : Introduction

1.1 Outline and methodology

This thesis outlines the work on resonant tunneling diodes-based photodetectors (*RTD-PD*) and *RTD*-based optoelectronic receivers and transmitters for the operation at the telecom wavelengths of 1.55 µm and 1.31 µm utilizing the $In_{53}Ga_{47}As/InP$ material system.

The approach used in this work is based on both simulations and practical device characterization. Starting with several epitaxial-layer designs featuring an *RTD-PD,* we did the first set of optical and electrical characterizations on the devices. The main limitation with these devices was the low speed of response for optical stimuli, for which the reason was unknown at the time. This low speed of response was reported by some in the literature, however there was no through study on the source of this limitation [1]–[4]. From here on, it was necessary to simulate the tested structures to get a better idea about the inner workings of the devices and to pinpoint the possible causes for such low speeds. Working towards that goal, we used the data obtained from the measured devices to calibrate a simulation package (Silvaco ATLAS) based on the employed material system. The calibration was done by optimizing the material parameters to give outputs that closely resemble the measurements. Afterward, comparisons between the simulated data with our results and others from the literature showed the reliability of the simulation package. The package can simulate the current-voltage (*IV*) curve and provide details regarding electric field, carrier concentration, and band diagrams. Silvaco has a built-in non-equilibrium Greens' function solver that can simulate *RTD*s assuming ballistic transport through the quantum well. Therefore, it detects the peak voltage location satisfactorily but with an overrated current. With that done, we used the simulator to design new epitaxial layers that overcame the shortcoming of the previous samples. The new designs were grown using molecular beam epitaxy (*MBE)*, (some designs were grown at the University of Würzburg, and others were grown by third-party commercial growers), and the devices were fabricated. The new samples were thoroughly characterized, both optically and electrically, using various setups with multiple measurements for each

device. Finally, the data obtained were analyzed using MATLAB, and accordingly, conclusions were deduced.

Chapter 1 (the current chapter) begins with the motivation behind the research and the main points of investigation involved. It commences further with a briefing on the background of photodetection techniques starting from photoconductors and reaching up to the state-of-the-art in *RTD-PD*. The chapter concludes by presenting the main achievements of the work. Chapter 2 discusses some basic semiconductor physics and the *RTD* principle of operation and finishes with an introduction to Silvaco ATLAS and the *NEGF* approach. Chapter 3 shows how to simulate *RTDs* using the simulation package Silvaco ATLAS. Silvaco is employed to conduct various theoretical studies on the effect of the structural parameters on the main features of the resonant tunneling diode. Chapter 4 commences by discussing how light interacts with semiconductors and outlines various physical parameters that affect the operation of any semiconductor photodetector. Afterward, we discuss the design considerations for high-speed and high-responsivity *RTD-PD*s and verify the designs through simulations. Chapter 5 covers the optical and electrical characterization results of various designs and discusses these results in light of the simulations and theory. The *RTD*s' amplification effect is also clearly shown in the results. Chapter 6 covers the potential use of *RTD*s in transmitter circuits and as single photon detectors. We present that with a MATLAB simulation where the *RTD* is used to drive a laser diode (*LD*). Furthermore, all *RTD* operating modes under *AC* and *DC* excitations are studied; when it is operated in the positive differential resistance region (*PDR*), when it is operated in the negative differential resistance region (*NDR*), and when it is switched between the two. We further investigate the latter case for the possible operation of the *RTD* as a single photon detector. Finally, chapter 7 presents the main conclusions of the work and what future work on the subject might be.

1.2 Motivation

Photodetectors (*PD*) are an integral part of many technologies used on daily bases. They play a vital role in numerous applications from communication systems, imaging, military and defense, autonomous driving, and even smartphones' infrared (*IR*) detectors. With the ever-increasing demand for data, photodetectors are eminent in the developing

field of photonic integrated circuits (*PICs*). Therefore, it is advantageous to have fast and highly responsive photodetectors that are cost-effective and easy to fabricate.

An *RTD* can be realized by incorporating a double barrier quantum well structure (*DBQW*) between two regions: the emitter and the collector. Figure 1 shows a sketch of a typical *RTD* structure.

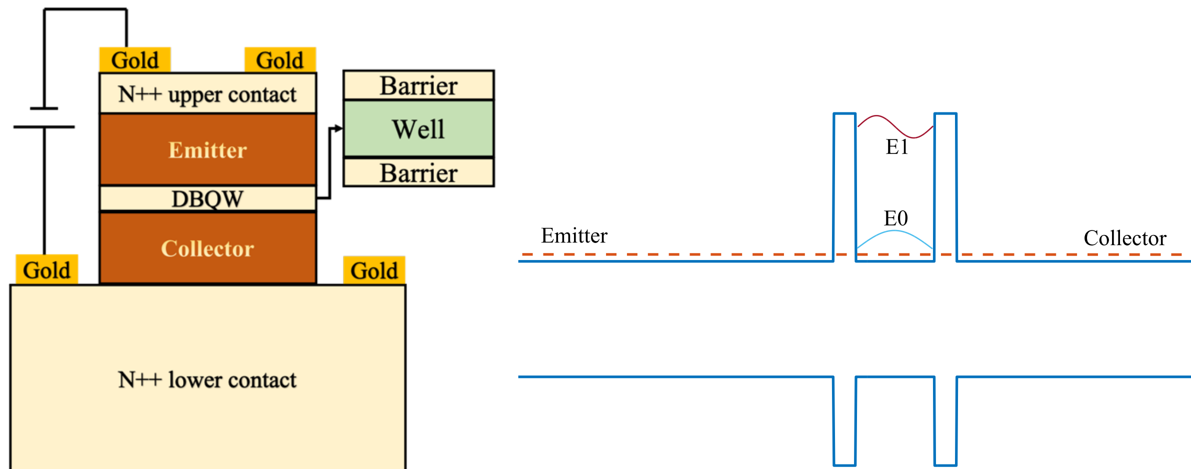

Figure 1: Typical RTD schematic (left side) and energy band diagram (right side) showing two quantized states E_0 and E_1.

As long as the width of the quantum well is comparable to the wavelength of the electron, energy quantization effects take place inside the quantum well. These levels act as channels for the electrons at the emitter to tunnel through when appropriate alignment with the Fermi level is satisfied, leading to resonant conditions and to a current peak. Disturbing this alignment leads to a current decrease (due to the decrease in the tunneling probability) and to a current valley. This gives rise to a very interesting and highly nonlinear current-voltage (*IV*) curve depicted in Figure 2.

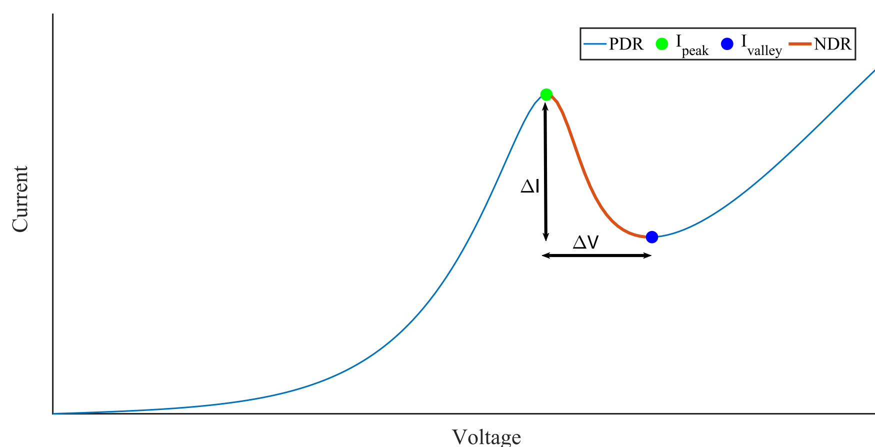

Figure 2: Typical RTD IV curve.

The main features of the *IV* are an exponential *PDR* and the presence of an *NDR*. Owing to the fast charge transport time through the quantum well, *RTD*s can operate at extremely high frequencies reaching up to 1.9 THz [5] at room temperature, making them the fastest pure electronic devices to date operating at room temperature. This also makes *RTD*s suitable as *THz* sources for next-generation technologies such as the internet of things (*IoT*) and *5G* communications, although the output power is still low (around 1 mW). Moreover, this shows the potential role that *RTDs* can play in bridging the *THz* gap as shown in Figure 3. The THz gap is the region of the electromagnetic spectrum between microwaves and infrared radiation, which is still not fully utilized. Since *RTDs* generate THz radiation, they can be part of the technology which bridges this gap.

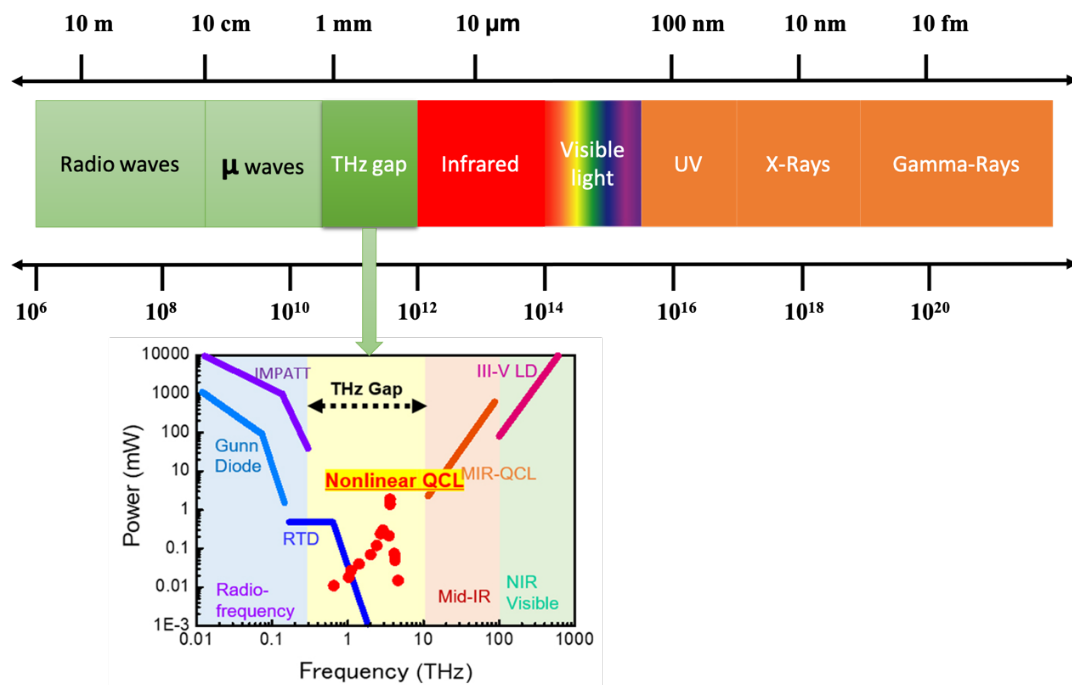

Figure 3: Electromagnetic spectrum and THz technologies [6].

With that in mind and after examining the shape of the *PDR*, *RTD*s can operate as high-frequency mixers as well as *THz* detectors in this region. Furthermore, when biased in the *NDR*, they can provide gain to an external resonant circuit, making them suitable for *THz* oscillators and amplifiers [5], [7], [8]. This built-in amplification eliminates the need for other circuitry (amplifiers) in detector circuits, reducing complexity and power consumption. Additionally, *RTD*s have shown low noise levels that are characterized by a reduced Fano Factor when biased in the *PDR* and *NDR* regions, which further supports their use as detectors [9]–[11].

The figures of merit related to the highest peak-to-valley current ratio (*PVCR*) for *$In_{53}Ga_{47}As$/AlAs RTD*s at room temperature go up to 22 using a *DBQW-RTD* [12]. This number goes up to 50 when considering *RTD* structures with an *InAs* sub-well inside the main well [13] and can even reach 144 for a resonant inter-band tunneling diode (*RITD*) [14]. One more core feature of the *RTD* IV curve is the maximum current density. The maximum reported number by Izumi et al. [5], to the author's best of knowledge, is around 3000 kA/cm^2.

Firstly, we aim to design, fabricate, and characterize photodetectors with an *RTD* structure (*RTD-PD*) that takes advantage of the merits mentioned a priori. These devices shall have higher current responsivity values than current-day technologies (mainly avalanche photodiodes (*APD*) and *PIN* photodiodes) and can operate at high speeds up to 10 GHz. The concept of the *RTD-PD* relies on making one or both regions surrounding the *RTD* (the emitter and the collector) photosensitive. With applications in telecommunications in mind, the project aims at devices that operate at the telecom windows in the near-infrared (NIR) region, specifically at 1.55 μm and 1.31 μm wavelengths. The material of choice for such wavelengths is *InGaAs/InP* and the main scheme corresponds to vertically illuminated devices.

Secondly, we will exploit the excitability property of the *RTDs* for their potential use as single photon detectors. Excitable systems are common in biological systems particularly neuroscience, where the system's response depends on the energy of the stimulus. When the stimulus is below a certain energy, the system does not produce any response, while it responds with a large signal (spike) to a stimulus that is above this minimum value [15], [16]. The dynamics of such non-linear systems are described by the non-linear dynamics theory and chaos [17].

Finally, we will theoretically model the integration between an *RTD-PD* with a laser diode (*LD*) and show that opto-electronic transmitters can be realized with this approach [18].

1.3 Background on photodetection and *RTD-PD*

1.3.1 Photoconductors

Photodetection using inter-band absorption is used to detect light at various wavelengths depending on the bandgap of the photo-absorption material. Compound semiconductors, (especially III-V) ternary and quaternary compounds, with bandgap

engineering, allow for detection at different wavelengths. These detectors operate by the generation of charge carriers due to light energy absorption. When the light has higher energy than the bandgap, electrons in the valence band gain enough energy to transfer into the conduction band and create electron-hole pairs. The newly generated carriers require a charge transport mechanism (mainly electric field) to separate them and eventually contribute to photo-generated current. Photoconductors are unipolar devices that resemble the simplest form of a semiconductor photodetector.

Photoconductors date back to the sixties when they operated as photoconductive switches (they are referred to by that name also in the literature, and sometimes as Auston switches or metal-semiconductor-metal (*MSM*) detectors although *MSM* do have a distinction in the type of contacts used) [19], [20]. High bandwidth detectors were reported early on by Chou et. al [21] when nanoscale *MSM* photodetectors were fabricated using *GaAs* technology and had response times of 0.85 ps and 1.5 ps which translate to a bandwidth in the hundreds of *GHz* range. In 1994 Krotkus et. al [22] reported on high-speed photoconductors using low-temperature grown $In_{53}Ga_{47}As$ lattice mismatched to *GaAs*. The low-temperature growth of metal-organic chemical vapor deposition (*MOCVD*) reduced the carrier lifetimes to the pico-second range. Chen et. al [23] in 1998 discussed the trapping and recombination dynamics of low-temperature grown $In_{53}Ga_{47}As/InAlAs$ systems using both bulk and quantum wells and showed how defects such as *Be* can be added to $In_{53}Ga_{47}As$ along with low temperature growth to modify the aforementioned dynamics. Fast response devices based on $In_{53}Ga_{47}As$ photoconductive switches were reported by Mangeney et. al [24], the paper discusses the methods used to reduce the carrier lifetime by *Be* doping and annealing, *ErAs* incorporation, and ion irradiation. These techniques lowered the response time to 2.2 ps but reduced the responsivity values to around 1.1 mA/W. Further studies about the dynamics of low-temperature-grown *InGaAs/GaAs* systems were presented by Jo. et. al [25] where they reduced the carrier lifetime in *InGaAs* through traps from a metamorphic layer. They also pointed to the carrier lifetime changes with the annealing temperature during processing. In 2007 an $In_{53}Ga_{47}As$ photoconductor was used as an electro-optic mixing device. The device had a low bandwidth in the range of 160 MHz that resulted from long carrier lifetimes in the nanoseconds range [26]. The application of $In_{53}Ga_{47}As$ based photoconductors as mixers is still being investigated; in 2018 Horvath et. al [27]

demonstrated an ultrafast photoconductive switch that worked as a mixer. Various other papers have been investigating ways to reduce response times. We point the interested reader to these references for further information [28]–[30].

1.3.2 Quantum-well-based photodetectors

According to the way light is absorbed, light detection in quantum well (*QW*) based systems can be divided into two categories: inter-band absorption and inter-sub-band absorption. The former refers to the movement of electrons from the valence band to the conduction band due to light absorption. The latter refers to the transfer of electrons between the quantized energy eigenstates due to quantum mechanical confinement in the same band. The inter-sub-band absorption mechanism has been utilized by many to produce detectors operating in the mid-infrared regions (*MIR*) of the optical spectrum. These detectors took advantage of the narrower energy separation between sub-bands to absorb longer wavelengths. The physics governing these devices rely on the capture and escape rate of the charge carriers located inside the quantum well. This mechanism shapes the devices' main characteristics, mainly gain and speed. Gain and bandwidth are always a compromise in the engineering of photodetectors. In this case, high values of gain result due to higher carrier confinement times in the quantum wells and accordingly lead to lower speeds [31]. The first devices reported using this technology were by Esaki et. al [32] in 1978. These devices had quantum wells (*QW*) in a superlattice structure (*SL*) that resulted in a multi-wavelength *IR-PD*. Five years later, actual devices were fabricated and tested by Smith et. al [33], these devices showed very high responsivity values, up to 200 A/W (at 77 K), but showed slow response times due to a long carrier lifetime. In 1987 the first *IR* detectors utilizing quantum wells with resonant tunneling (*RT*) in a superlattice were proposed by Levine et. al [34]. The devices were based on *GaAs* technology and showed 0.57 A/W responsivity values at an operating speed of 5.7 GHz when operated at 77 K. All these devices are multi-quantum-well structures (*MQW*). Later Bandara et. al [35] proposed the first single quantum well *IR-PD* that showed higher responsivity values than *MQW* devices but operated at low temperatures. More recent works have been able to demonstrate design rules for *QWIR* detectors in the THz range and have shown some detectors to operate up to 110 GHz [36], [37]. Others have been utilizing effects such as Avalanche gain [38] and superlattices [39] to improve the overall efficiency. This is still a vital research subject with promising applications in silicon photonics [40]–[42].

The previous history outlines the main achievements of using inter-sub-band absorption for making *IR*-PDs. However, various other attempts were made by many. We point the interested reader to references [43]–[50].

1.3.3 Resonant tunnelling diode-based photodetectors

A resonant tunnelling diode photodetector (*RTD-PD*) is realized when one or both spacer layers around the *DBQW* (i.e.: the emitter and the collector) are made to be photosensitive. When light is shined on the device, it gets absorbed in these regions and electron-hole pairs are generated due to inter-band absorption. This concept is illustrated in Figure 4.

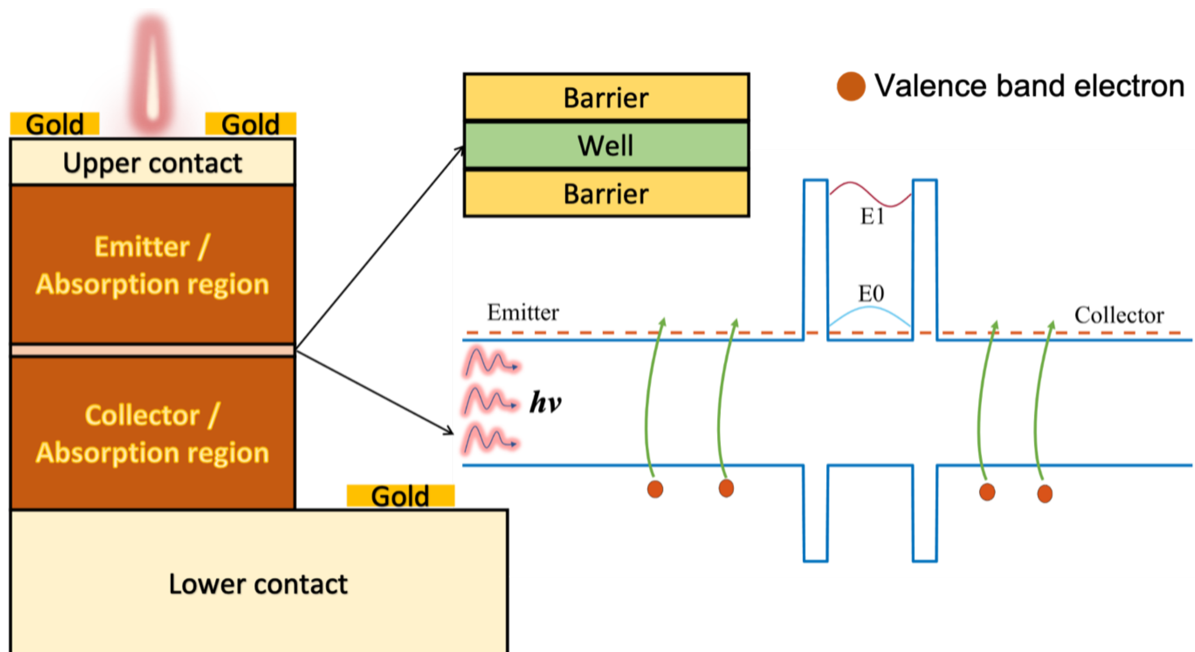

Figure 4: RTD-PD concept showing the main structure (left side) and the band diagram (right side) with two Eigenstates E_0 and E_1 with inter-band absorption.

People have explored the possibility of incorporating an *RTD* with a photoconductor to exploit the non-linear behavior of RTDs. In 1991 an *RTD-PD* based on the *GaAs/AlGaAs* material system was reported by [51], and another based on the *InGaAs/AlAs* material system by [52]. These works registered observations related to changes in the peak and valley currents due to light absorption and reported on a peak-voltage shift to a lower value associated with the absorption of light. This shift was reported as well by Park et al. [53], and it is mainly attributed to hole accumulation near the collector barrier. Moise et. al [54], [55] proposed one of the first devices that incorporate an *RTD* using $In_{53}Ga_{47}As$ technology. The

reported device had a responsivity of 15 A/W (optical to electronic gain) and operated at speeds up to 2 Gbps at room temperature. This is still the current state of the art in terms of speed. Since then, people have tried to build on the idea and produce faster and more responsive devices. Photodetectors that employ an *RTD* with a waveguide structure have been demonstrated by Figueiredo, et al. [2], [56] and Romeira, et. al [57]. The reported results were about the high gain obtained from the *RTD-PD*, but the speed of response was in the nanoseconds range. The current responsivity of *RTD-PD*s shows an inverse dependence on the illumination power. In the low-illumination power regime (pico-watt range), Dong et. al [58] have measured 1.92×10^4 A/W at room temperature which was the highest number reported until a new record was set by [59] of 3×10^4 A/W. This work utilized a double Bragg reflector to enhance the responsivity. In 2005 Blakesley, et. al [60] have demonstrated a high sensitivity single photon detector based on *RTD* structures and quantum dots. Zhao, et. al [61] have shown another photodetector capable of single photon detection with amplification using self-assembled quantum dots on the barrier layers of an *RTD* structure. The potential use of *RTD-PD*s as single photon detectors has mainly been explored in conjunction with quantum dot, since the capture of an electron in the quantum dot gives the *RTD-PD* photon counting capabilities as well [62].

When biased in the *NDR*, *RTDs* oscillate at very high frequencies up to the terahertz range (*THz*). Therefore, they pose as good candidates to operate as optoelectronic oscillators (*OEO*). Carefully design oscillators can integrate with *RTD-PD*s to produce optically excited THz oscillators. In 2011 Romeira, et al. [63] demonstrated an *RTD-PD*-OEO with low phase noise that did not need an additional erbium-doped optical amplifier (*EDFA*) or an electronic amplifier. A year later, a paper by Cantu, et. al proposed [64] the use of *RTD* based optical transceivers in pico- and femto- cell structures for 5G applications. In 2019 *RTD-PD*-OEO where demonstrated to operate at 35 GHz and showed speeds up to 80 Mbps using encoded light signals [4]. *RTD*-based oscillators up to 300 GHz and 1 mW output power have also been demonstrated by Al-Khalidi, et. al [65]. *RTD-PD*-OEO which were directly modulated using light signals encoded with data showing optical operation at 50 MBps and coupled to an oscillator at 79 GHz was shown by Zhang, et. al [3].

The attractive properties of the *RTD-PD* of high switching speeds, ease of fabrication and low cost of production make it a core player in next generation optoelectronics.

Particularly, it can find its place in opto-electronic oscillators, photo-detectors and opto-electronic mixers [26]. One might utilize the oscillatory nature of the *RTD-PD* in the *NDR* and its intrinsic high switching speed to build transmitters using on-off keying to transmit data. Figure 5 shows this concept. This has been demonstrated in the literature using electronic stimuli [66]–[68] and optical as well by [3].

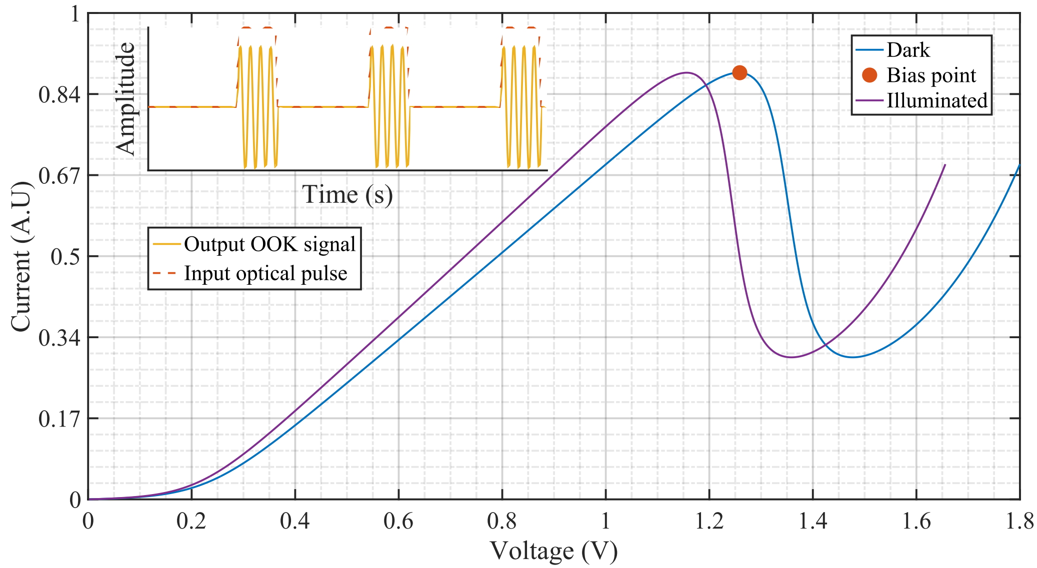

Figure 5: OOK transmission using RTD-PD concept. The inset shows the output from the RTD-PD (oscillations) when a pulse is applied to it (red rectangular pulse).

Other interesting applications of *RTD-PD*s is their integration with a laser diode (*LD*) for use as optoelectronic transceivers for radio over fiber (*RoF*). *RoF* systems deal with the transmission of data through modulation of an optical signal (by an *RF* source), and then transmitting this data through optical fibers. This has the advantage of lower noise, higher speed, and lower loss. The schematic in Figure 6 explains how such an application might work [64].

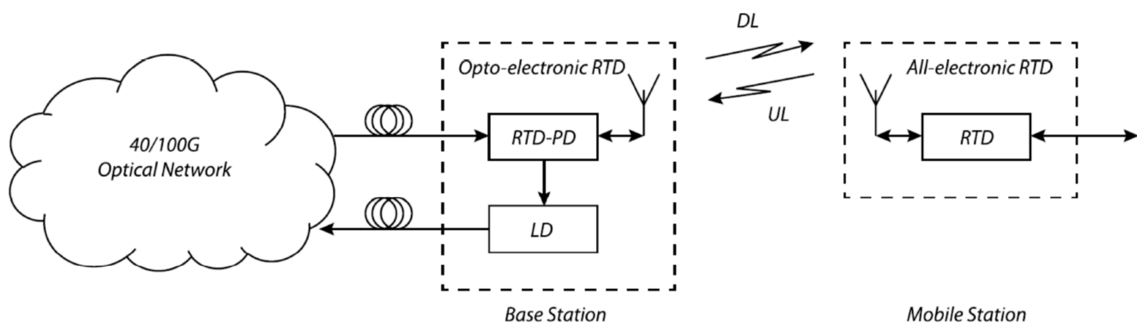

Figure 6: RTD-PD-LD and RTD transceivers for RoF concept [64].

1.4 Thesis outcomes and contributions

During this work we were able to determine the speed limitations of *RTD-PD*s at the physical level. We show that the photogeneration taking place at the highly doped and thick contact regions are a major source of lifetime limitation. The work also resulted in new *n-i-n* and *p-i-n* designs that show record speeds of up to 1.75 GHz (3dB optical bandwidth), and low illumination (pico-watt range) responsivity values reaching up to 1×10^7 A/W and milli-Watt range illumination levels responsivity of around 65 A/W for some devices. Both numbers outpace the state of the art reported in literature. We also show that the peak-voltage might shift either to higher or to lower values depending on the region where light is mostly absorbed (the emitter or the collector) and provided models and simulations to support our findings, which was not reported in the literature before.

Our results show that the *PIN-RTD* design proposed has potential to reach higher operating speeds with responsivity values greater than unity making *RTD-PD*s a real contender to *PINs* and *APDs*. Finally, we showed that the excitability characteristics of *RTD-PD*s can be used to detect low illumination levels down to 30 nano-watts. However, this is still far from single photon detection at room temperature.

The work resulted in the following publications and disseminations while being the first author:

- Simulation and Modelling of Resonant Tunneling Diode Peak Voltage Dependence on Spacer Layers. 2021 35th Symposium on Microelectronics Technology and Devices (SBMicro). 10.1109/SBMicro50945.2021.9585751
- Resonant Tunneling Diode Based Photodetectors Design Rules for Telecom Applications. 2021 IEEE International Conference on Telecommunications and Photonics (ICTP). 10.1109/ICTP53732.2021.9744181
- Resonant tunneling diode-based photodetectors. International School on Terahertz photonics and electronics. Sala Azzurra, Scuola Normale Superiore, Pisa, Italy 2022.
- A journal paper is anticipated with a title of: "Speed limitations of resonant tunneling diode-based photodetectors".

Chapter 2 : Introduction to resonant tunnelling diodes

2.1 Introduction

This chapter introduces resonant tunneling diodes (*RTDs*) by providing an overview of their development and key features. We start with a general review on some of the basic semiconductor physics related to the work presented in this thesis in particular, semiconductor junctions and the tunneling transport leading to the introduction of the *RTD*. For a detailed explanation on these subjects, many textbooks can be reviewed such as those in references [69]–[72].

2.2 Review on semiconductor physics

This section gives a general review on some of the basic semiconductor physics related to the work presented in this thesis.

2.1.1 Effective mass approximation

Since electrons moving in a crystal lattice experience different forces and go through different potentials (depending on the structure of the crystallographic plane), the mass of the electron cannot be taken as constant at every location. From here emerged the approximation of effective mass, where the mass of the electron is modified by a factor that is material dependent. For instance, the effective mass of the electron in *GaAs* is different from that of the *AlAs*. Using such an approximation saves a lot of effort as having a mass that is energy dependent is not easy to solve. However, for this approximation to be true, the area of the material we are dealing with has to be large with respect to the area covered by the electron's movement. The effective mass can be calculated using (*2-1*) to (*2-3*),

$$m^* = \hbar^2 \left(\frac{\partial^2 E}{\partial k^2}\right)^{-1} \tag{2-1}$$

$$m^*(E) = m^*(0) \times \left(1 + \alpha(E - U)\right) \tag{2-2}$$

$$\alpha = \frac{1}{E_g} \tag{2-3}$$

where m^* is the effective mass, $\hbar$ the reduced Planck's constant, E the energy, k the crystal momentum, U the potential, and Eg the bandgap energy.

2.1.2 Density of states

The density of states is a mathematical function which gives the number of energy states per unit volume per unit energy of a given solid. It physically resembles the number of energy states in a solid between energy level E and $E + dE$. By integrating such function between two energy states, the number of available (permitted) energy states can be found. The importance of the effective mass approximation also appears here, as it was found that the density of states is constant as long as the mass is energy independent [73].

The density of states in both the conduction and valence bands for bulk semiconductors are given by (*2-4*) and (*2-5*), with typical values for $In_{53}Ga_{47}As$ of 2.1×10^{17} cm^{-3} and 7.7×10^{18} cm^{-3} respectively [74]

$$N_C = 2\left(\frac{m_e^* kT}{2\pi\hbar^2}\right)^{3/2} \tag{2-4}$$

$$N_V = 2\left(\frac{m_h^* kT}{2\pi\hbar^2}\right)^{3/2} \tag{2-5}$$

where Nc, Nv are the effective density of states in the conduction and valence bands respectively, k the Boltzmann constant, and T the temperature in kelvin.

2.2.1 Semiconductor junctions

When two semiconducting materials come into contact there will be an exchange of charge between the two regions until an equilibrium state is reached. This sort of charge exchange is due to the concentration difference of the charge carriers at both materials, which is a diffusion driven process. Such an interaction results in a junction area, where the charge distribution in it is quite different from the rest of the original material. It is these junctions that form the exciting physics of electronic devices and determine the functions they perform. Therefore, it is of essence for any semiconductor device engineer to know how to handle such junctions and to engineer them in a way that supports the functionality of an electronic device. A semiconductor junction can have two types according to the materials that form it, a homojunction arises when two pieces of the same semiconductor material

come into contact, where as a heterojunction forms when two dissimilar semiconductor materials are brought together. Junctions can also be classified according to the doping type of the semiconductor materials that form it; these include isotype junctions and bipolar junctions. An isotype junction is formed between two materials with similar doping type (*n-n*) or (*p-p*), where a bipolar junction is formed between $p - n$ materials. Figure 7 shows a summary of these types.

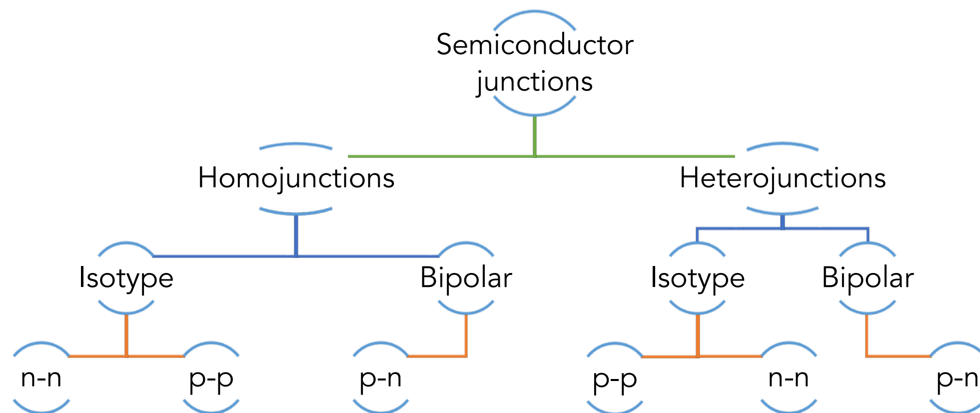

Figure 7: Types of semiconductor junctions.

2.1.2.1 Homojunctions

In this section we will analyze the two types of homojunctions: iso-types and bipolar. In each case we will demonstrate how the junction works and derive an expression for calculating the width of the depletion region, the electric field across that region and the built-in potential associated.

Starting with the bipolar (*p-n*) type junction, when a p-type and an n-type material are brought into contact and due to the concentration difference of electrons between the two, electrons will start to diffuse from the n-type material to the p-type material. Each electron that leaves the n-type material will leave behind it a hole in the form of immobile ionized impurity atoms from the dopant, which effectively depletes the n-type material from the electrons at the junction. This is also known as uncovered charge. The electrons which diffuse into the p-type material will also form a region where the majority carrier (the hole) is depleted. This is mainly due to the recombination process which uncovers the charge of the immobile impurity atoms of the p-type dopant. This sort of charge redistribution forms a depletion region at both sides of the junction and results in a potential difference between these two charge distributions.

This potential difference is called the built-in potential. Such a potential difference gives rise to an electric field, known as the built-in electric field, which serves to stop this diffusion process and brings the junction into equilibrium. This charge redistribution results in band-bending of the conduction and valence bands of the two materials, such that the Fermi-potentials at both regions stays constant at thermal equilibrium. An example *p-n* junction made between p-type and n-type $In_{53}Ga_{47}As$ is shown in Figure 8. The current-voltage relationship for such a junction is the well-known pn-junction diode equation given in (*2-6*), where I_0 is the reverse saturation current, η the ideality factor, and V_T the thermal voltage.

$$\mathrm{I} = I_0(e^{\frac{V}{\eta V_T}} - 1) \tag{2-6}$$

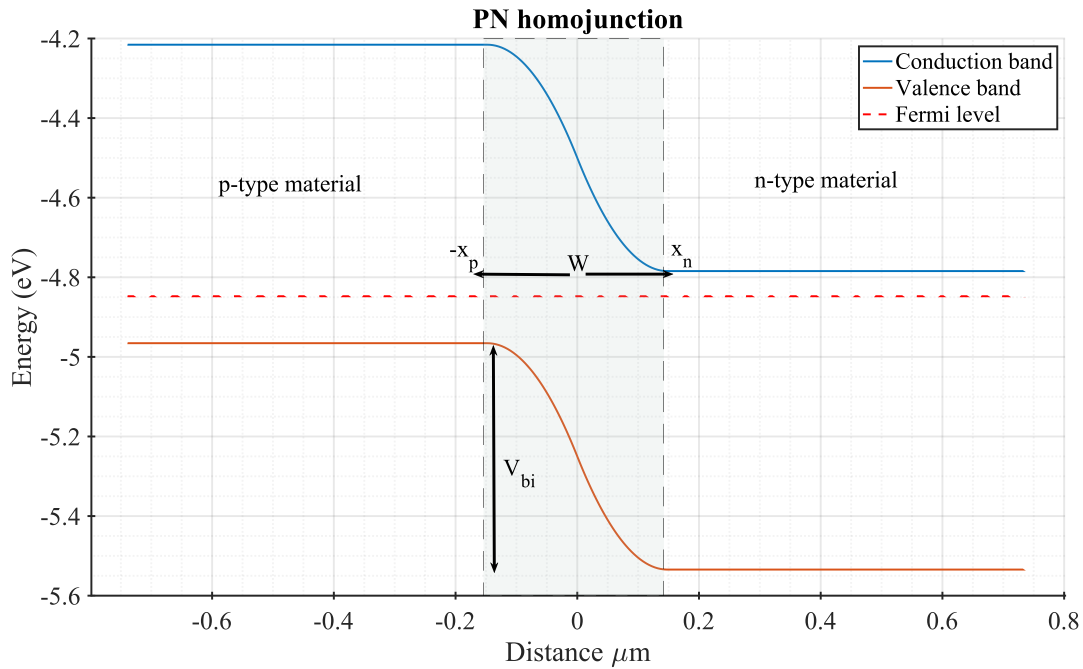

Figure 8: example of a p-n homojunction.

Assuming that the n-type material has a doping N_D and the p-type material has a doping of N_A, the Poisson equation (*2-7*) can be used to derive the value of the potential and electric field as function of position (*2-12*) and (*2-13*), where ϵ is the dielectric permittivity, and ρ_v the carrier density. This will allow us to determine the width of the depletion region (W) from each side of the junction (x_n from the n-type side, and x_p from the p-type side).

$$\frac{\partial^2 V}{\partial x^2} = -\frac{e\rho_v}{\epsilon} \tag{2-7}$$

$$E_p(x) = \int_{-x_p}^{x} \left(\frac{e\rho_v}{\epsilon}\right).dx \tag{2-8}$$

$$E_n(x) = \int_{x}^{x_n} \left(\frac{-e\rho_v}{\epsilon}\right).dx \tag{2-9}$$

$$V_p(x) = \int_{-x_p}^{x} E_p.dx \tag{2-10}$$

$$V_n(x) = \int_{x}^{x_n} E_n.dx \tag{2-11}$$

$$V_p(x) = \frac{eN_A x^2}{2\epsilon} + \frac{eN_A x_p x}{\epsilon} \tag{2-12}$$

$$V_n(x) = \frac{-eN_D x^2}{2\epsilon} + \frac{eN_D x_n x}{\epsilon} \tag{2-13}$$

From the above we can deduce a formula for the built-in potential given by (*2-14*) and (*2-15*)

$$V_{bi} = V_n(x_n) - V_p(-x_p) \tag{2-14}$$

$$V_{bi} = \frac{eN_D x_p^2}{2\epsilon} + \frac{eN_A x_n^2}{2\epsilon} \tag{2-15}$$

The depletion width (W) is given by the distance between x_p and x_n and is therefore, given by (*2-16*) and (*2-17*)

$$x_p = \sqrt{\frac{2\epsilon N_D V_{bi}}{eN_A(N_D + N_A)}} \tag{2-16}$$

$$x_n = \sqrt{\frac{2\epsilon N_A V_{bi}}{eN_D(N_D + N_A)}} \tag{2-17}$$

As stated earlier the Fermi levels at both areas should be the same when equilibrium is reached. This means that the built-in potential can be given by the separation between the Fermi levels before the junction is formed. For an n-type material the separation between the Fermi-potential and the conduction band edge under the Boltzmann approximation is given by (*2-18*) and by (*2-19*) for the separation between the valence band and the Fermi energy for a p-type material, where N_C, N_V, n, *and* p are the effective density of states in the conduction and valence bands, the electron concentration and hole concentration respectively.

$$E_c - E_F = kTln\left(\frac{n}{N_C}\right) \tag{2-18}$$

$$E_F - E_v = kTln\left(\frac{p}{N_V}\right) \quad (2\text{-}19)$$

Since the Fermi levels at equilibrium are the same, we can add the above two equations which gives an expression for the built-in potential as in (*2-22*).

$$E_c - E_v = kTln\left(\frac{n}{N_c}.\frac{p}{N_V}\right) \quad (2\text{-}20)$$

$$np = n_i^2 = N_c N_V e^{-\frac{E_g}{kT}} \quad (2\text{-}21)$$

$$V_{bi} = \frac{kT}{e}ln\left(\frac{np}{n_i^2}\right) \quad (2\text{-}22)$$

Where n_i is the intrinsic carrier concentration, n and p are the doping levels, E_c, E_v, and E_f are the conduction band edge, valence band edge and Fermi potentials respectively.

We now move to isotype junctions, starting with the *n-n* junction. These types of junctions are very common in devices between highly doped areas of a material and lower-doped areas of the same material such as between contacts and grading layers. They will mostly be encountered as n^+ - *n* junctions, where the n^+ denotes the higher doped region and *n* the lower doped one.

The rationale behind these junctions is the same as with the *p-n* case. Electrons will diffuse from the region with the higher concentration to that of the lower concentration, leaving positive charge behind in the form of immobile impurity atoms. However, in this case the recombination at the lightly doped n-type material results in a net negative charge that is free to move. Therefore, the built-in electric field and potential for this sort of junction are much lower than those for a *p-n* type junction.

The same logic as the one used before can be applied to derive the built-in electric field by calculating the difference between the Fermi-levels before contact. The result is shown in (*2-23*).

$$V_{bi\,(n^+-n)} = \frac{kT}{e}ln\left(\frac{n^+}{n}\right) \quad (2\text{-}23)$$

The depletion width from each side of the junction is derived using the Poisson equation, from which the total depletion width (W) can be deduced as shown below:

$$x_{n^+} = \sqrt{\frac{2\epsilon N_D V_{bi}}{eN_D^+(N_D + N_D^+)}} \quad (2\text{-}24)$$

$$x_n = \sqrt{\frac{2\epsilon N_D^+ V_{bi}}{eN_D(N_D + N_D^+)}} \tag{2-25}$$

$$W = x_{n^+} + x_n \tag{2-26}$$

p^+ - p junctions are exactly the same as n^+ - n junctions. The equations governing these junctions are simply stated below (*2-27*) to (*2-29*).

$$V_{bi\,(p^+-p)} = \frac{kT}{e} ln\left(\frac{p^+}{p}\right) \tag{2-27}$$

$$x_{p^+} = \sqrt{\frac{2\epsilon N_A V_{bi}}{eN_A^+(N_A + N_A^+)}} \tag{2-28}$$

$$x_p = \sqrt{\frac{2\epsilon N_A^+ V_{bi}}{eN_A(N_A + N_A^+)}} \tag{2-29}$$

We would like to emphasize that the above derivations take into account the Boltzmann approximation and assume the junction to be fully depleted.

2.1.2.2 Heterojunctions

Heterojunctions are semiconductor junctions that are formed between two dissimilar semiconductor materials. This means that the material properties of each semiconductor are different, and we have different bandgaps, electric permittivity, effect mass, and effective density of states in both valence and conduction bands. This leads to special physical effects arising from these junctions, particularly with the way the band energies of the two materials line up when they are brought into contact.

Heterointerfaces can be classified according to their line-ups to three types known as type I (straddling gap), II (staggered gap) and III (broken gap). A straddling gap is formed when the band diagram of the lower bandgap material is completely encapsulated by that of the higher bandgap material, while a staggered gap has the conduction band bottom of the lower bandgap material within the band gap of the higher bandgap material while the valence band edge of the low bandgap material below that of the higher bandgap material. Finally, a broken gap is formed when the entire band diagram of the lower bandgap material does not coincide with the one of the higher bandgap material. These types are shown in Figure 9.

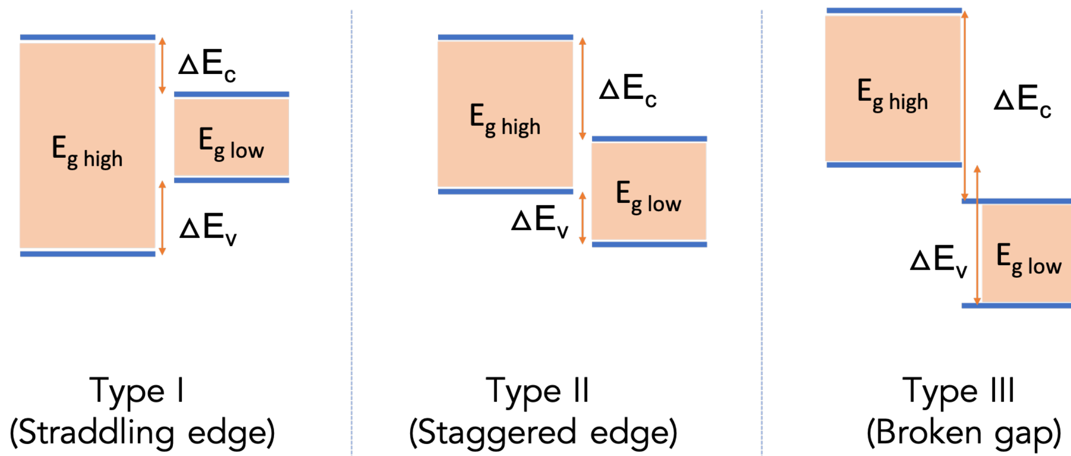

Figure 9: Heterojunction types and interface discontinuities.

One important aspect of heterojunctions is the bandgap discontinuity imposed by the variation in bandgaps between the two materials. One way to calculate these discontinuities is by Anderson's rule for a given type of heterointerface between the two materials. We will concentrate of straddling edge interfaces as these are the ones present in the material systems we will use in this work. The conduction band discontinuity is given by the difference between the electron affinities of both materials (χ_1 and χ_2). The electron affinity is the distance between the vacuum level and the conduction band edge.

$$\Delta E_c = \chi_2 - \chi_1 \tag{2-30}$$

The reminder of the discontinuity goes to the valence band, and can be calculated using

$$\Delta E_v = \Delta E_g - \Delta E_c \tag{2-31}$$

However, it is important to note that Anderson's rule does not always give correct results. Usually, these bandgap discontinuities are measured practically using photoluminescence measurements. Nonetheless, this rule still gives a first impression on how the heterointerface would look like.

We now move to calculate the built-in potential and depletion widths of such interfaces. Again, we have two cases one for isotype junctions and the other for bipolar ones. We will discuss the isotype n^+ - n heterojunctions only as the exact same analysis applies to the rest of the junction types.

Since the materials are now different, when they are brought into contact the electrons will start to flow from the material with a lower work function to the material with the higher work function. This process will continue until the Fermi levels of the two materials

are the same, at which an equilibrium state will be reached. Given this information, we see that the built-in potential is given by the difference between work functions (ϕ) as in (*2-32*).

$$\mathrm{V_{bi}} = \phi_2 - \phi_1 \tag{2-32}$$

The material which losses electrons becomes depleted near the junction with a positive charge, while the material that gets the electrons will form an accumulation region near the junction and become negative. These accumulated electrons are free to move in the transverse directions, however they are confined in the longitudinal dimension due to the energy barrier formed between the discontinuity and the conduction band edge. This is shown in Figure 10.

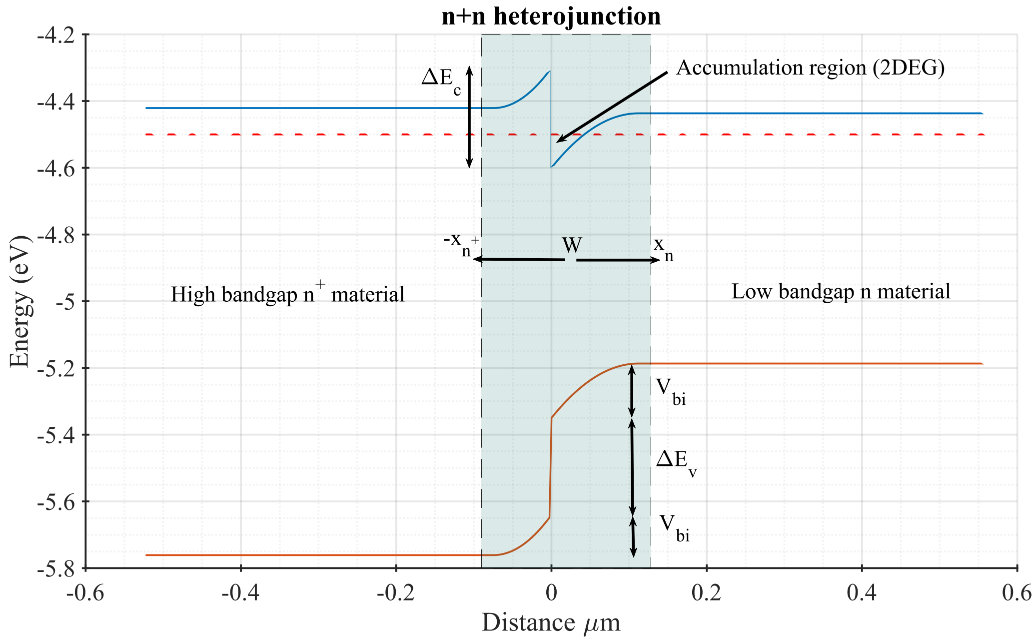

Figure 10: Sample n+ - n heterojunction.

This sort of accumulation leads to a formation of a two-dimensional electron gas (*2DEG*) which plays an important role in high-speed electronic devices such high electron mobility transistors (*HEMT*), and in resonant tunneling diodes (*RTDs*) as will see in this work.

The depletion length and electric fields are calculated in the same fashion as before, with the main difference being the variation in dielectric permittivity in the two materials. Equations (*2-33*) to (*2-36*) show the potential at each side of the junction, and the depletion length at each side [69].

$$V_{n^+}(x) = \frac{eN_D^+ x_{n^+}^2}{2\epsilon^+} - \frac{eN_D^+ x_n^+ x}{\epsilon^+} \tag{2-33}$$

$$V_n(x) = \frac{-eN_D x_n^2}{2\epsilon} + \frac{eN_D x_n x}{\epsilon} \tag{2-34}$$

$$x_{n^+} = \sqrt{\frac{2\epsilon^+ \epsilon_n N_D V_{bi}}{eN_D^+(\epsilon_n N_D + \epsilon^+ N_D^+)}} \tag{2-35}$$

$$x_n = \sqrt{\frac{2\epsilon^+ \epsilon_n N_D^+ V_{bi}}{eN_D(\epsilon_n N_D + \epsilon^+ N_D^+)}} \tag{2-36}$$

2.2.2 Quantum mechanical tunnelling

Quantum mechanical tunnelling is a carrier transport mechanism that allows a microscopic object (like the electron) to penetrate (tunnel) through potential barriers having greater potential than the electron itself, given the barrier is thin enough.

The tunnelling effect can be explained using the wave particle duality principle, in light of the de Broglie relationship of the wave nature of particles. Since electrons act as waves, and as waves do not terminate abruptly at boundaries, there is a finite probability that a wave will be found at the opposite side of a potential barrier. This can be seen by solving the Schrödinger equation for that quantum system.

The tunnelling probability through a barrier is governed by the transmission probability given by (*2-37*), where w is the width of the barrier and $< k >$ is the average value of the momentum [75].

$$e^{-2<k>w} \tag{2-37}$$

One of the first devices to utilize quantum mechanical tunneling was the tunneling diode. Tunnelling diodes are built using a *PN* junction in a degenerate semiconductor. The semiconductor has very high doping concentration in such a way that for an n-type material, the Fermi-level (E_f) lays above the conduction band's energy level E_c, and below it in a p-type material. The IV characteristics of tunnelling diodes is shown in Figure 11.

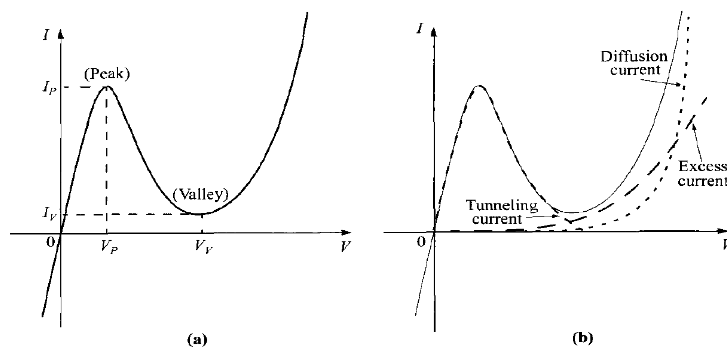

Figure 11: IV characteristics of a tunnel diode [75].

It can be seen that the device shows a different IV curve than an ordinary PN junction diode. The most interesting part is the region where an increase in voltage results in a decrease in current. This area represents a negative differential resistance (*NDR*), since $\frac{\Delta V}{\Delta I}$ is negative. *NDR* rises because of the non-monotonic nature of the device's voltage (bias) dependence. On a physical level, the tunnelling current can be explained by examining Figure 12 which shows the energy diagram of the heterojunction under study.

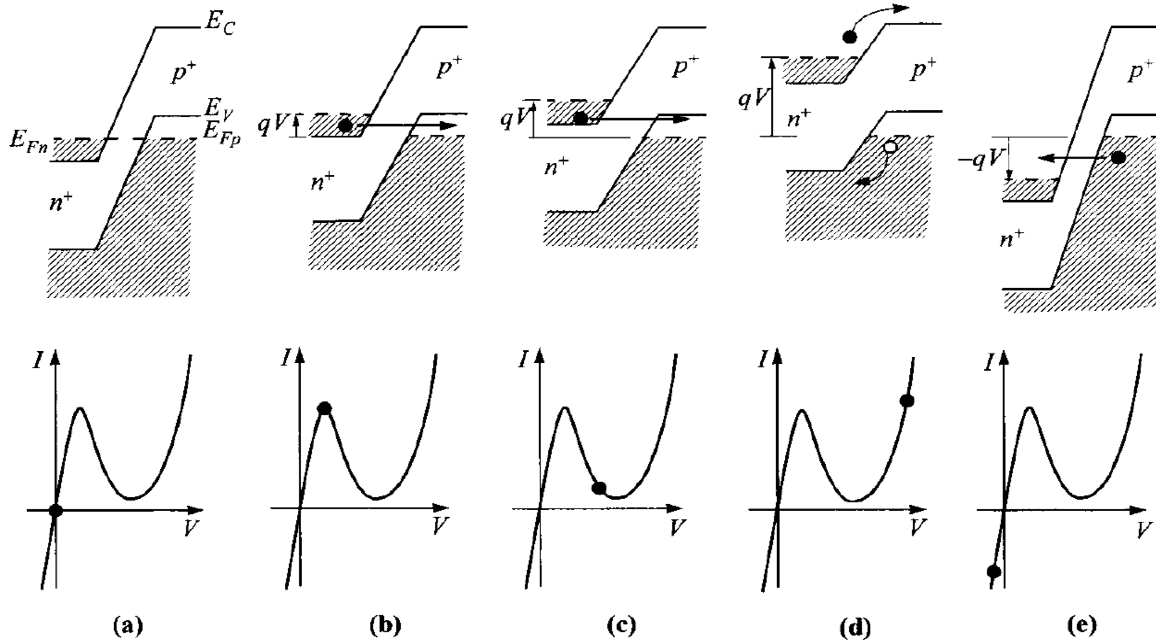

Figure 12: Energy band diagram of a tunnel diode under various bias points [75]. a- At zero bias. b- At the peak. c- in the NDR. d- The second PDR. e- interband tunneling.

In order for electrons to tunnel through a barrier, the energy levels from the n^+ $region$ (where electrons are present) have to be aligned with energy levels from the $p^+region$ (where holes are present). When forward voltage is applied, bending of the energy bands occurs while the width of the depletion region shrinks and electrons tunnel through the junction. This gives rise to the increasing current in the first region.

The device will reach peak tunnelling current when the forward bias voltage causes a total overlap between the whole energy bands of the $n^+$and p^+ regions. Increasing the voltage further, will decrease the overlap resulting in tunnelling current decay giving rise to the *NDR* region. Further increase in voltage eventually puts the junction at forward bias conditions and normal diode current flows. In a PN junction diode, the current is due to drift and diffusion of charge carriers. However, in a tunnelling diode the current has an additional

component due to quantum mechanical tunnelling. Current densities due to tunnelling varies by material type, ranging from 1.5 mA/μm^2 in $SiGe$, and reaches up to 4.5 mA/μm^2 in InP.

Tunnelling diodes are usually built using III-IV semiconductors, as their direct band gap structure gives higher tunnelling probability. For a direct bandgap material, the bottom of the conduction band and the maximum of the valence band exist at the same momentum (k), while an indirect bandgap material requires momentum change. This change must be accompanied by production of phonons to satisfy conservation of momentum. It is therefore more likely for a direct bandgap material to have tunnelling than indirect bandgap material [75].

2.3 Quantum wells

A quantum well is a structure by which an area of low potential energy is sandwiched between two higher potential barriers forming a well. The quantum well and the two barriers are referred to as a double-barrier quantum-well (*DBQW*). An illustration of such a structure is given in Figure 13.

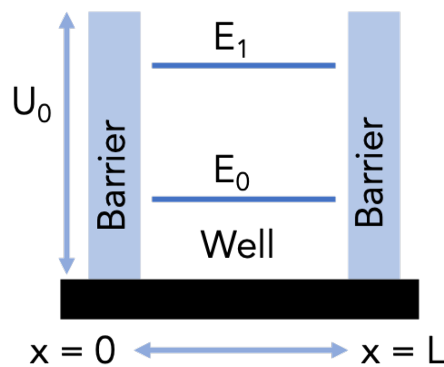

Figure 13: Double barrier quantum well structure.

The difference in energy bandgaps and the discontinuities at heterointerfaces of different material (especially III-V) semiconductors can be used to form such structures. Commonly used material for making quantum wells include $AlAs/In_{(x)}Ga_{(1-x)}As/AlAs$, $Al_{(x)}Ga_{(1-x)}As/GaAs/Al_{(x)}Ga_{(1-x)}As$, where (x) denotes the concentration of the respective material in the compound semiconductor, *AlAs/GaAs/AlAs, GaN/InGaN/GaN* and many others.

This structure gives rise to quantum mechanical confinement in the quantum well region, when the width of the quantum well is of the order of the electron's wavelength. When an electron is trapped inside a potential well, the energy states at which it could exist

are quantized (in the direction of confinement) and are no longer continuous. This system is usually referred to as a particle in a box, and the quantized energy states can be obtained by solving the Schrödinger equation for the quantum well system. There are two approaches to the solution, the first is to assume that the barriers an infinitely high (particle in an infinite potential well), and the second when the height of the barriers is taken into consideration (particle in a finite potential well) [73]. Both of these cases will be analyzed next.

2.4 Infinite potential well

Considering a quantum well with a width (*L*), where the potential energy inside is zero and infinite everywhere else (Figure 13 – neglecting the height (U_0)), with a free particle inside confined in the x direction. According to the theory of quantum mechanics any particle confined in a box must exist within specified (quantized) energy states E_n.

Given that the well is infinitely large, a solution of the Schrödinger equation can be described by an energy Eigen function $\phi_E(x)$ as in (*2-38*), where α and β are complex numbers.

$$\phi_E(x) = \alpha\cos(kx) + \beta\sin(kx) \tag{2-38}$$

Since the well is infinitely large, at the boundaries of $x = 0\ and\ L$, $\phi_E(x)$ is equal to zero. Applying these boundary conditions to $\phi_E(x)$ yields $\alpha = 0$, and $kx = n\pi\ , where\ n = 1,2,3,4,5\ ....$

$$k = \frac{n\pi}{x} \tag{2-39}$$

k is the wave number of the particle and is given by

$$k = \frac{\sqrt{2m^*E}}{\hbar} \tag{2-40}$$

where $\hbar$ is the reduced Plank's constant, m^* is the effective mass of the particle, and E is its energy. Therefore,

$$k^2 = \frac{n^2\pi^2}{x^2} \tag{2-41}$$

from which the quantized energy levels inside the box can be given by

$$E_n = \frac{\pi^2\hbar^2n^2}{2m^*L^2} \tag{2-42}$$

From this result it can be seen that the energy inside the well is quantized and not continuous. With the energy at each level inversely proportional to the width of the well and its effective mass [76].

The quantum well structure discussed here is one dimensional, which means that the electron is bound in that dimension only and is free to move in the other two. This also means that in those other directions can be thought to be continuous (they are quantized but with a very large number of energy eigenstates effectively making a continuous band). These are called energy sub-bands and are responsible for making the *2D* electron gas [73].

2.5 Finite potential well

Practically, some quantum systems cannot be treated as being infinite wells. In that case the potential inside the well can be considered zero (free particle), but the assumption that the particle is bound inside is no longer valid. In such case, the Schrödinger equation has to be solved in all three regions (emitter, well and collector). For the well region, the solution still holds as long as the particle is free (no external influence), and the wavefunction ψ is given by (*2-43*)

$$\psi(x) = A\, sin(kx) + B\, cos(kx) \tag{2-43}$$

In the other two regions the Schrödinger equations becomes

$$E\psi(x) = U(x)\psi(x) - \frac{\hbar^2}{2m^*}\frac{\partial^2\psi(x)}{\partial x^2} \tag{2-44}$$

Given that the potential in these two regions is finite $U(x) = U_o(x)$ the equation becomes:

$$E\psi(x) = U_o(x)\psi(x) - \frac{\hbar^2}{2m^*}\frac{\partial^2\psi(x)}{\partial x^2} \tag{2-45}$$

A solution to this equation can be written in the form of

$$\psi(x) = Ce^{\alpha x} + De^{-\alpha x} \tag{2-46}$$

This result suggests that the wave function of the electron inside the quantum well is a sinusoid, with rising and dying exponentials at the boundaries of the emitter and collector respectively. This implies a finite probability of finding the electron outside the well and in the barrier region. The above equations can be solved to find the values of *A*,*B*,*C* and *D* using the boundary conditions of the continuity of the wave function, and the fact that it is normalizable [9].

Practically, solving such a system requires a computer, as a graphical method is usually employed to the solve for the wavefunction and get the energy Eigenvalues as outlined in [92]. The method is built on solving the Schrödinger equation in all locations (emitter, well, and collector), while during the solving process constants are introduced that lump a number of physical quantities in order to get a closed form solution. This is a typical method employed in books. The interested reader can refer to [77] for more details. Here we wrote a MATLAB program that solves this problem graphically and gives the energy Eigen states. Table 2-1 shows the calculated Eignestates inside a number of $In_{53}Ga_{47}As$ quantum well widths between *AlAs* barriers. These values can be compared with the ones we show for similar structures using the ATLAS simulator later on. The results are in good agreement.

Table 2-1: Stationary energy Eigenstates using graphical method.

Well width (nm)	Eigenenergy (meV)
4.5	E_0 = 222
	E_1 = 800
5.7	E_0 = 158
	E_1 = 600
7.5	E_0 = 104
	E_1 = 406
	E_2 = 860
9.5	E_0 = 71
	E_1 = 280
	E_2 = 613
	E_3 = 1012

2.6 Resonant tunnelling diodes

In this section we introduce another device that utilizes both quantum mechanical confinement and tunneling to produce a highly non-linear current-voltage characteristic with an *NDR* region. These devices are called resonant tunneling diodes (*RTD*). An *RTD* is formed by incorporating and *DBQW* structure between two highly-doped regions called the emitter and the collector as shown in Figure 14. The emitter is the electrode from which electrons are emitted (i.e.: where the negative supply terminal is connected), and the collector is the electrode which collects these electrons (i.e.: where the positive supply terminal is connected). This configuration forms an open quantum system with quasi-bound states that are responsible for the resonance phenomena as will be seen [78].

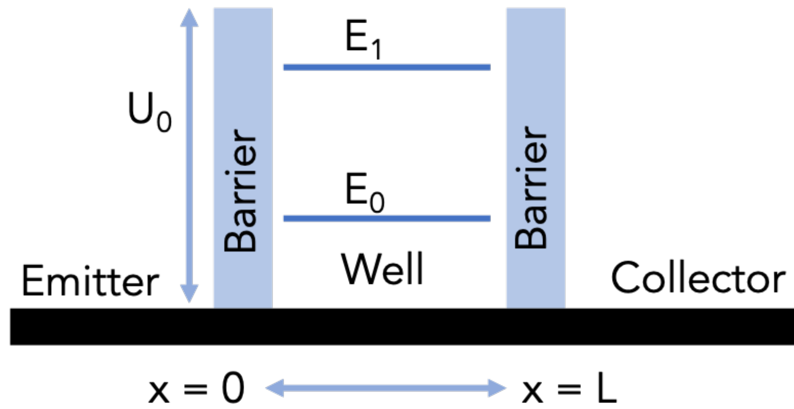

Figure 14: RTD concept illustration.

Ever since the discovery of quantum mechanical tunnelling and resonant tunnelling by Leo Esaki in 1958 [79] and 1973 [32], people have been studying electronic devices utilizing such phenomena. *RTDs* have shown great potential in high frequency electronic and optoelectronic circuits [3], [57], [63], [65].

One way of looking at the operation of the device is by examining Figure 15, which shows the electron distribution probability (Fermi-Dirac) superimposed over the *RTD* structure. The allowed energy levels inside the well are also shown. As we have explained earlier, the *DBQW* structure gives rise to quantized Eigenstates, this gives it a unique transmission probability function with sharp resonances at these energies, and nearly zero elsewhere as depicted by Figure 15.

When voltage is applied to the device, the energy bands are bent in a way proportional to that voltage leading to the injection of electrons from the emitter's side. These electrons will start to accumulate at the boundary of the first barrier (the emitter's barrier) and start to form a *2DEG*, with a small percentage of them tunneling through the first energy Eigenstate (E_0) and get collected at the collector. The current that results from this transport is small at the beginning and starts to build up as voltage is increased and so does the accumulated electrons which eventually turn into a *2DEG* with quantized states. This resembles the current in the positive differential resistance region (*PDR*), highlighted in red in Figure 15. Further increasing the bias, electrons at the emitter will have energies equal to those of the resonant states and a resonance condition is formed giving rise to a very sharp peak in the tunnelling probability. These transmission peaks result in current maxima in the IV curve (green area in the IV of Figure 15 -a).

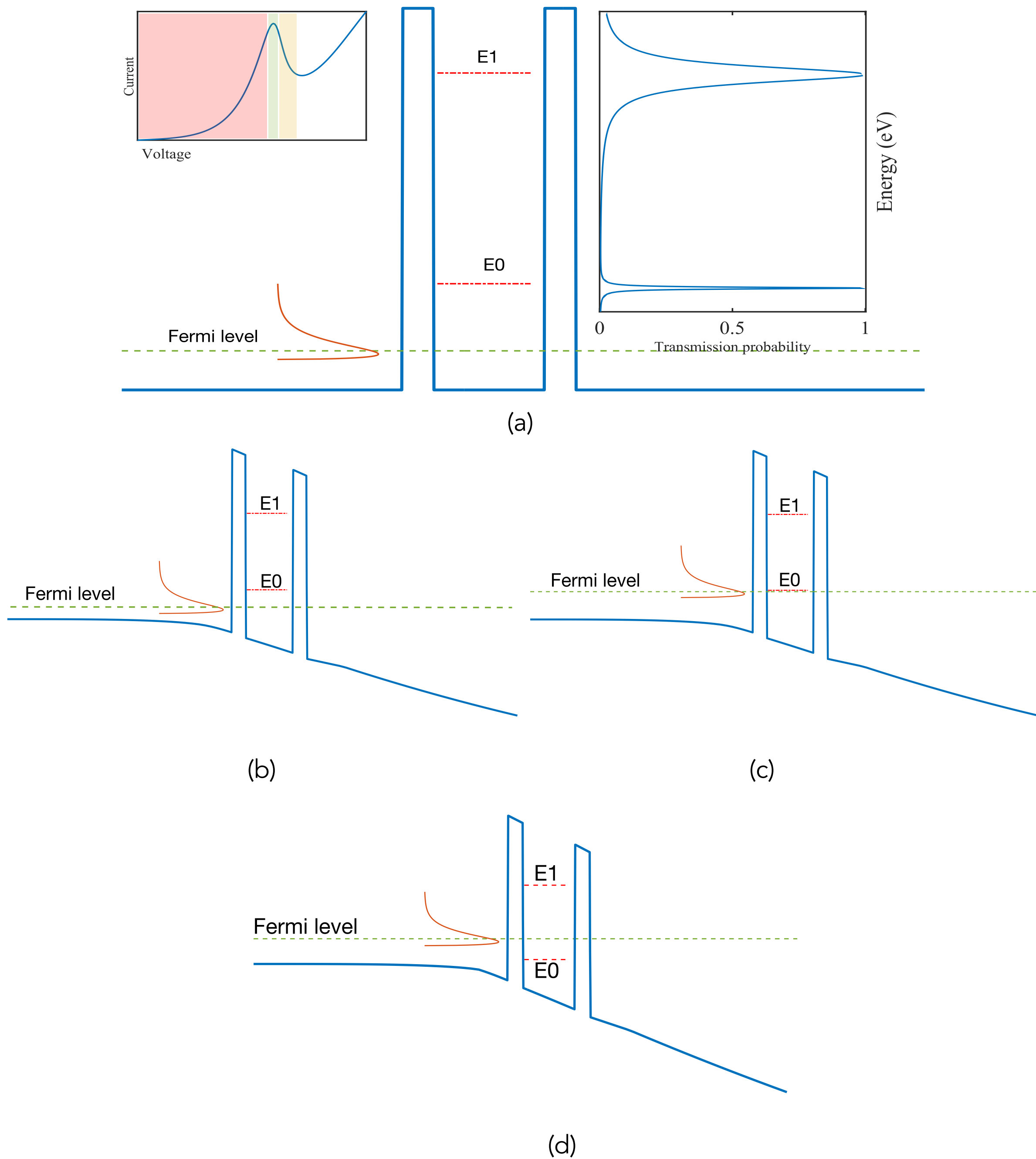

Figure 15: Principle of operation of a resonant tunneling diode. (a- zero bias conditions, b- PDR current, c- peak current, d- valley current).

When more voltage is applied, the electrons in the emitter are taken off resonance and the tunneling probability decreases, so the current decreases as well. At the extreme point when electrons are not aligned with any energy state in the well, a valley occurs. This behavior repeats for every quasi-bound state inside the well. Given this probability of transmission vs energy, the *IV* characteristics of such device will eventually show multiple *NDR* regions each corresponding to resonance at a given energy level E_n [71], [80].

An analogous physical system that operates in a similar fashion is an optical Fabry-Perot Etalon. The Etalon is a device made out of two parallel transparent plates separated by a certain distance. The insides of the plates are coated with a reflective coating. When light is transmitted from one side, it goes through the first plate until it reaches the reflective coating. At that point it either reflects back or gets transmitted. The light that does get transmitted reaches the other reflective coating which then either gets reflected or transmitted. The distance between the two plates can be made such that certain wave lengths reflect back and interfere constructively inside the device, effectively making a state of resonance while the other wavelengths interfere destructively [81], [82].

By analogy, in an *RTD* a particle at the emitter having the same energy as that of one of the quantized quasi-bound energy states will have a probability of transmission equal to 1 (i.e.: resonance), and a current peak is achieved.

For a particle to go through the well (from emitter to collector) it has to tunnel through the emitter-well and well-collector barriers. The probability of tunnelling is given by (*2-47*)

$$\mathbb{P}_{tunneling} = \mathbb{P}_e \mathbb{P}_c \tag{2-47}$$

where $\mathbb{P}_e \, and \, \mathbb{P}_c$ are the probabilities of tunneling through the emitter and collector respectively. At resonance the transmission probability is given by (*2-48*), which is 1 if the barriers is symmetric [75].

$$\mathbb{P}_{resonance} = \frac{4\mathbb{P}_c \mathbb{P}_e}{(\mathbb{P}_e + \mathbb{P}_c)^2} \tag{2-48}$$

The current density resulting in this case can be calculated using the density of states function with the Fermi-Dirac probability density function. By multiplying the density of states function with the probability distribution we get the concentration of charge carriers (also known as the density of occupied states). This concentration multiplied by the charge of the electron gives the current as in (*2-49*).

$$J = \frac{q}{2\pi h} \int \rho(E).\mathcal{F}(\mathrm{E}).T(E).dE, \tag{2-49}$$

where *ρ(E)* is the density of states function, *ℱ(E)* is the Fermi-Dirac distribution, and *T(E)* is the transmission probability function.

The Fermi-Dirac distribution is a probability distribution function which gives the probability of finding an electron at a given energy state, as shown in (*2-50*),where E_f is the Fermi level.

$$\mathcal{F}(E) = \frac{1}{1 + e^{\frac{E - E_F}{kT}}} \tag{2-50}$$

The Fermi level is defined as the level at which the probability equals 0.5. The integration of the Fermi-Dirac distribution gives rise to an improper integral, which needs to be calculated numerically. The solutions are tabulated and are known as the Fermi half functions [72], [83].

It is important to highlight the differences between resonant tunnelling diodes and the tunnelling diode. With *RTDs* there are a number of energy states at which the transmission probability will be one (i.e.: resonant states). This means that multiple peaks with multiple *NDR* regions can be achieved as compared to only one in the tunnelling diode. Furthermore, the peak to valley ratio of *RTDs* is much higher than that of normal tunnelling diodes. The same is true for current density [75].

2.7 Resonant tunnelling diode time constants

Mainly there are two time-constants affecting the speed of *RTD* circuits, the first is the time it takes an electron to cross through the well structure known as the tunnelling time, and the second is the *RC* time constant of the entire circuit including contact resistance and the overall capacitance (that of the quantum well and any additional ones in the circuit).
An expression for the tunnelling time can be deduced by examining the width of the peaks at resonance. The time it takes an electron to tunnel through the well structure is proportional to the width of the resonance peaks. Using the Heisenberg uncertainty relationship gives an expression for the tunnelling time (dwell time), where ΔE is the uncertainty in energy.

$$\tau = \frac{h}{\Delta E} \tag{2-51}$$

Therefore, it can be argued that the time for the electron to tunnel through one barrier is twice that (i.e., corresponds to the half-width of the resonant state's energy). Tunnelling time can be affected by surface roughness, scattering and phonon assisted tunnelling [8], [84].

The speed of the *RTD* can also be influenced by the RC time constant. To better demonstrate this, consider the *RTD* equivalent circuit shown in Figure 16.

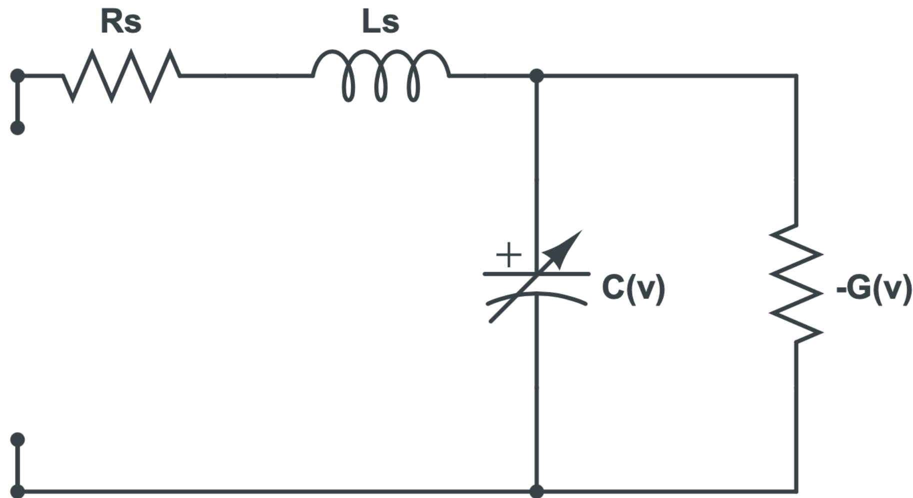

Figure 16: Equivalent circuit of an RTD.

The circuit has the basic elements which characterize the *RTDs* operation. The series resistance and inductance R_s *and* L represents the Ohmic contacts resistance and the inductance of the wires respectively. The parallel branch has a voltage dependent capacitor $C(V)$ representing the overall capacitance of the *RTD* (that of the quantum well and the geometric capacitance), and the negative conductance $G(V)$ modeling the *NDR* region, which is also voltage dependent.

At this point, it is important to highlight the sources contributing to the capacitance of the *RTD* which include, capacitance due to the depletion regions formed at the interface of the highly doped emitter layer, the capacitance in the quantum well itself due to electron accumulation, and the parallel plate capacitor formed between the two Ohmic contacts.

To model an *RTD*, the values of such elements must be determined. The series resistance R_s can be measured using the transmission line method (*TLM)*, while the value of the negative conductance can be determined from the slope of the *NDR* region at a given voltage. Another way would be to apply a *DC* bias to the circuit, at which the inductor and capacitor in the equivalent model will be treated as short and open circuit respectively. The current measured at that bias voltage can be used to determine the resistance of the circuit which is no more than the sum R_s *and* R_{NDR} (inverse of *G(v)*). The *NDR* resistance is calculated from the slope at that voltage bias which gives the value of the series resistance. Having determined the series resistance and the *NDR* conductance values, an *RF* signal (AC test) can

be made to measure the equivalent impedance of the system Z_{eq}. This value is the parallel combination of the negative conductance with the capacitance plus the series combination of the inductance and series resistance as shown in (*2-52*).

$$Z_{eq} = (j\omega L_s + R_s) + \left(\frac{\frac{R_{NDR}}{j\omega C}}{R_{NDR} + \frac{1}{j\omega C}}\right) \tag{2-52}$$

$$\mathrm{Z_{eq}} = \mathrm{R_s} + \frac{\mathrm{R}_{NDR}}{1 + (\omega \mathrm{R_{NDR}} \mathrm{C})^2} + \mathrm{j}\left(\omega \mathrm{L_s} - \frac{\omega \mathrm{R_{NDR}^2} \mathrm{C}}{1 + (\omega \mathrm{R_{NDR}} \mathrm{C})^2}\right) \tag{2-53}$$

For practical purposes, the inductance is usually very small (mainly due to the measuring wires) and therefore its contribution to the total impedance can be neglected. In which case the capacitance can be calculated from the total equivalent impedance [85]. By setting the real part of Z_{eq} to zero, It can be shown [86] that the resistive cut-off frequency of the *RTD* is given by (*2-54*)

$$f_{cutOff} = \frac{1}{2\pi C}\sqrt{-\frac{G}{R_s} - G^2} \tag{2-54}$$

If we equate the imaginary part of Z_{eq} to zero, we get the resonant frequency given by:

$$f_{resonant} = \frac{1}{2\pi C}\sqrt{\frac{C}{L} - \frac{1}{R_{NDR}^2}} \tag{2-55}$$

From (*2-54*), it is clear that the smaller the series resistance (i.e.: the better the Ohmic contacts and the device's semiconductor layers resistance are), the higher the frequency at which the *RTD* can operate.

2.8 Summary and conclusion

In this chapter we covered the basics of semiconductor physics necessary for the understanding of resonant tunnelling diodes (*RTD*). We introduced the types of semiconductor junctions, particularly heterojunctions, and how these junctions can be used to build a quantum well and eventually an *RTD*. We showed that an *RTD* can be made by sandwiching a double-barrier-quantum-well (*DBQW*) between an emitter and a collector and explained the principle of operation of the *RTD*, and how it's interesting *IV* curve comes about.

Chapter 3 : Simulation of *RTD* structural parameters using Silvaco ATLAS

3.1 Introduction

In this chapter we discuss the physics and operation of *RTDs* and the factors that influence their design, mainly the effects of changing the doping concentration and the lengths of the emitter and collector regions, in addition to the various aspects of designing the double barrier quantum well system itself. This work will allow us to gain a deeper understanding of the physical operations of the *RTD* particularly, related to the distribution of the electric field around the device. High electric field values are key for fast carrier transport in electronic devices, which will be vital for high-speed design of *RTD* based photodetectors. The results of this chapter will be built-on in the next chapter, where we discuss the design of high speed *RTD-PD*. Furthermore, by studying the behavior of the *RTD* under various doping conditions for both the emitter and the collector, we can gain a deeper understanding of the peak voltage shift we observe when light is shined on an *RTD-PD*. We will develop novel semi-analytical models that describe the peak voltage dependence on the *RTD* structural parameters for the $In_{53}Ga_{47}As$ material system. We back our arguments up using simulations run on Silvaco ATLAS employing a non-equilibrium Greens' functions (*NEGF*) approach to solving the charge transport problem in *RTDs* which we introduce next.

3.2 Introduction to Silvaco ATLAS

Silvaco is a set of simulation tools which were originally developed by Stanford University. Together these tools form a virtual wafer fab (*VWF*) that allows the simulation of electronic devices from fabrication to characterization and SPICE modeling. Each of these programs has a set of physical models programmed into specific packages, with the appropriate numerical solvers.

Generally, all the programs within the Silvaco package can be categorized in one of the following areas: process simulation, structure definition, physical simulation, and result interpretation and parameter extraction. These programs are SSupre4, Athena, DevEdit,

ATLAS, Utmost, and TonyPlot. All these programs are linked together through a common integrated development environment (*IDE*) known as DeckBuild. As shown in Figure 17.

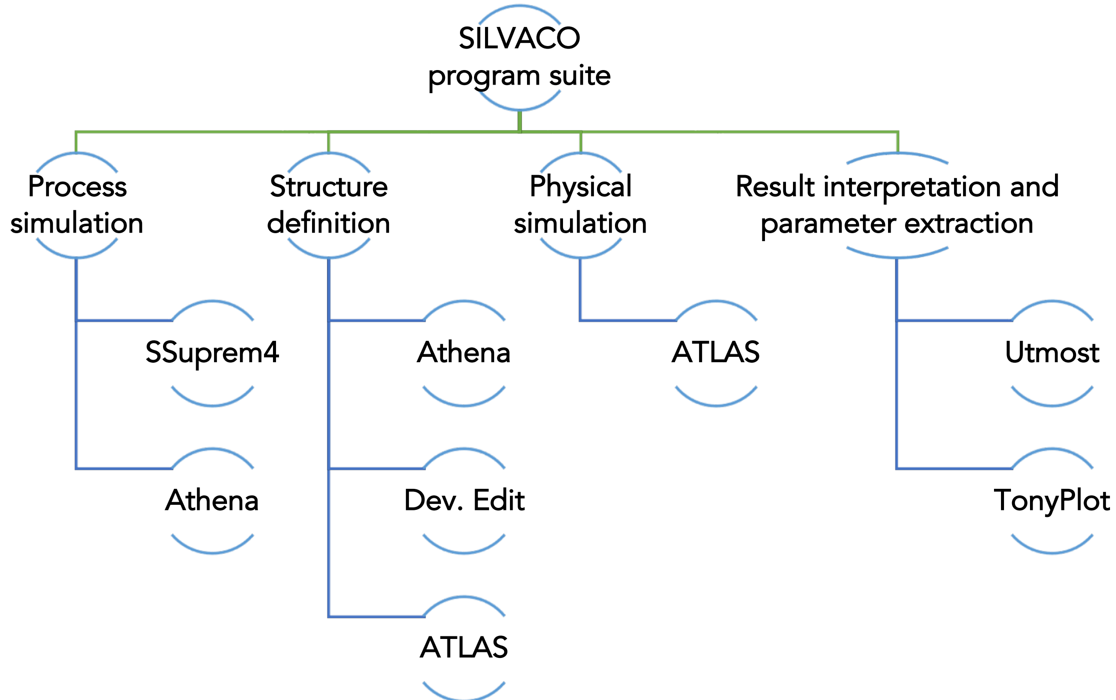

Figure 17: SILVACO program suite outline.

A general workflow that utilizes all the SILVACO software suite is depicted in Figure 18.

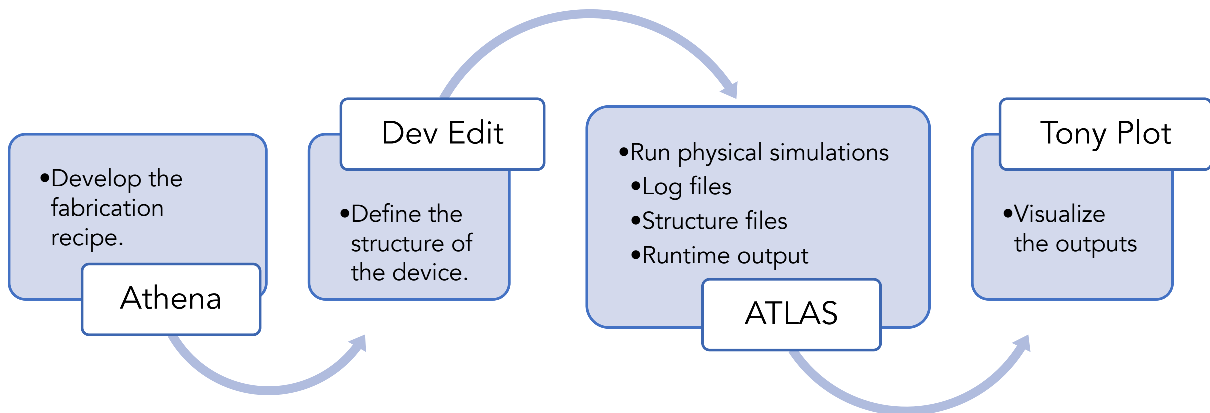

Figure 18: Typical SILVACO workflow.

In this work we will only be using ATLAS from the above set of tools. This will allow us to define the electronic structure of the devices, do a physical simulation to calculate the current – voltage relationships and many other physical quantities like the electric field, carrier distribution, energy bands, etc. The results of the simulations will be shown on TonyPlot and the actual code will be written on DeckBuild.

ATLAS is a physical design and simulation software that solves *2D* and *3D* problems. It uses meshing to break up the problem into regions, on which it solves select physical models numerically. ATLAS has 16 packages built into it, and each one deals with a specific physical problem. Some of these packages include Pisces, which is a *2D* simulator for silicon devices only. Blaze, which is a *2D* simulator for compound semiconductor devices, Quantum, that simulates quantum mechanical effects, and Luminous for optoelectronic processes. The remaining packages with their descriptions can be found in the ATLAS manual. The work done in this thesis will utilize two packages from ATLAS, which are Blaze and Quantum.

For quantum phenomena, Silvaco offers seven different simulation techniques that can -independently- simulate various effects. These methods broadly solve quantum confinement and quantum transport problems. We are interested in using it to simulate *RTDs* based on the non-equilibrium Green's function formalism (*NEGF*) [87]. The *NEGF* implementation in ATLAS is currently limited to ballistic transport without considering scattering effects resulting in higher peak currents and inaccurate valley currents. Unlike analytical simulation tools, physical simulators are tricky to calibrate, and the results highly depend on the material parameters and meshing. Unfortunately, there are no set rules that determine a functioning mesh. Generally, meshes should include enough points to ensure accuracy but not too many that hinder speed. ATLAS uses triangular meshes, so it is not advisable to have obtuse triangles, nor triangles that are too long and thin. Finally, the mesh should be denser around areas of expected change like: under the gate of a *MOSFET*, around a heterojunction, or at the barriers and the quantum well regions. The first technique is the Self-consistent coupled Shrödinger-Poisson model that simulates quantum confinement only and hence, should not be used to solve transport-related problems. The second is the Density gradient (quantum moments model). This model describes the quantum transport phenomena but does not include a description of confinement-related parameters such as the bound energy states or the wave functions of electrons. The third technique is the Bohm quantum potential model, which is a modified version of the second method, offering better convergence and precision. Next comes the Quantum correction models. These models are based on papers and are phenomenological in nature; meaning that they address the specific problem of quantum confinement in the inversion layer under the gate of a MOSFET. Next is the parabolic quantum-well model, used mainly with quantum well-based light emitting

diodes (*LEDs)*. The model predicts the gain and the recombination rates efficiently in such devices.

The *NEGF* method in Silvaco has two models: planar and mode-space, with the planar model being the advised one for simulating *RTDs*. Another way to simulate quantum transport is to use the transfer matrix method using coherent or sequential tunneling. Finally comes the drift-diffusion mode- space method. This method is not a fully quantum simulator; instead, it offers a semi-classical approach by incorporating some correction potentials to the original drift-diffusion model to simulate quantum effects. Given the above, the best method to simulate *RTDs* is the planar *NEGF* approach, which we will use throughout this work [87].

To simulate a device on ATLAS, we start with defining the structure of the device. We first need to define a mesh, which will cover the entire area of the device. Then we need to define the regions of the device each with its own material, followed by specifying the location of the electrodes, and finally, specify the required doping levels and dopant types. These steps must be adhered to in sequence, otherwise the simulations will not run properly. The actual ATLAS syntax for defining the above steps can be found in the ATLAS manual, and a sample code for one of the simulations of this work can be found at the appendix.

3.2.1 Using NEGF with ATLAS

In this section we will briefly discuss the non-equilibrium Greens functions formalism and highlight how to implement it on ATLAS.

NEGF is a mathematical tool used to solve partial differential equations, it does so by introducing new functions in the partial differential equation called Green's functions, after the mathematician George Green, which can be easier to solve. Greens functions have many applications in physics including electricity and magnetism and quantum mechanics [88]. This method has been employed in physics to solve the Schrödinger equation, making it possible to get a fully-quantum solution to the charge transport problem. The derivation of the *NEGF* equations requires through knowledge of the many-body perturbation theory, which was pioneered by Keldysh [89], and the inclusion of dissipative (heat) process going on in the device as well. This discussion is quite involved and is outside the scope of this work. We will however, derive the *NEGF* equations without considering the dissipative processes following the approach highlighted in [90], [91]. This will be sufficient to understand what the simulator is doing and how the results are generated.

If we consider the time independent Schrödinger equation

$$E\psi = H\psi \tag{3-1}$$

where H is the Hamiltonian of a free electron given by (*3-2*), with P being the momentum, m the effective mass and $U(x)$ is the potential energy

$$H = \frac{P^2}{2m} + U(x). \tag{3-2}$$

The *NEGF* formalism introduces two new terms to the Schrödinger equation, a supply term that acts as the source of electrons (S), and a sink term ($\Sigma_{out}\psi$) that acts as a collector.

$$E\psi = H\psi + \Sigma_{out}\psi + S \tag{3-3}$$

Rearranging the terms gives

$$S = (EI - H - \Sigma_{out})\psi \tag{3-4}$$

From which we define G^R as the retarded Green function given by:

$$G^R = (EI - H - \Sigma_{out})^{-1} \tag{3-5}$$

Therefore, ψ can be given by

$$\psi = G^R S \tag{3-6}$$

In the context of *NEGF*, the product of $\psi^t\psi$ gives the total number of electrons (N), where ψ^t is the conjugate transpose of the wavefunction ψ.

From (*3-6*) we find that

$$\psi^t = S^t (G^R)^t \tag{3-7}$$

We now define the advanced Green function G^A as the transpose conjugate of the retarded Green function G^R given by:

$$G^A = {G^R}^t \tag{3-8}$$

From the above, the number of electrons is given by

$$N = \psi^t\psi \tag{3-9}$$

Another way to get the total number of electrons is to calculate the matrix G^n, given by $\psi\psi^t$

$$G^n = G^R S S^t G^A \tag{3-10}$$

In this case the number of electrons is given by the trace of G^n. Equations (*3-5*) and (*3-10*) are the commonly used form of the *NEGF* equations.

The ATLAS implementation of *NEGF* uses the above equations to calculate the number of electrons at each bias point. It then feeds this number of electrons into the Poisson equation to find a new value for the potential. The Schrödinger equation and the Poisson equation are solved self-consistently for all bias points.

In order to implement the planar *NEGF* solver in ATLAS, the emitter and collector regions should be treated at quasi-equilibrium regions, while the *DBQW* structure is treated as a non-equilibrium region. To ensure better convergence, all regions other than the *DBQW* should be denoted as quasi-equilibrium regions. This is done by invoking the EQUIL.NEGF command in the material statement when the structure is defined.

The main statement to implement *NEGF* in ATLAS is the N.NEGF_PL1D and P.NEGF_PL1D which is to be written as part of the models statement. The first statement solves for electrons and the other for holes.

The solver needs to know as well, the maximum number of Eigenstates it should solve for, this needs to be input in the output statement by specifying the EIGENS parameters.

Finally, to save the eigenvalues to the log and output files, NEGF.EIG should be written for each solve command, and NEGF.LOG NEGF.EIG need to be added to the save command.

3.3 Design and optimization of RTDs

The output characteristics (peak voltage, peak current, peak-to-valley current ratio *PVCR*, and peak-to-valley voltage span ΔV) of *RTDs* play a vital role in many applications, such as *RTD* based electronic oscillators where the maximum output power and oscillation frequency depends on the values of *PVCR*, ΔV and ΔI [92], in using *RTDs* to build analog to digital converters [93] and photodetectors [94]. Many authors have reported on the effects various physical parameters have on the beforementioned characteristics [95]–[98]. However, due to the cost and time implications of fabricating and testing actual devices and the variations in growth, doping profiles and fabrication recipes, the results obtained could be influenced by a lot of variables like temperature, growth rates, clean room conditions, etching rates, and optical lithography doses to name a few. Also, the number of samples produced by each publication are limited [99]. Therefore, it would be beneficial to study the effects of changing multiple structural parameters in a controlled way using simulations based on non-

equilibrium Greens' functions formalism (*NEGF*). Banasree et. al [96] have reported on simulations that change only the width of the well and barriers with little detail on mathematical modeling. Charmi and Yousefi have reported on *NEGF* simulations of *RTDs*, but the study did not include the effect of any built-in potentials (the electric potential rising from the diffusion of carriers between areas of variable doping levels) due to doping profiles and did not provide any sort of mathematical modeling for the results. Additionally only a single bias direction was taken into consideration [100]. Recently a study by Ipsita et al. showed an attempt to optimize the *PVCR* for a given *RTD* structure [101]. The authors used the transfer matrix method to simulate the *RTDs* and mainly focused on *PVCR* and did not give insights into what happens to the peak voltage and why. The results of the study can then be compared and contrasted with practical devices reported in literature [113].

3.3.1 Methodology

Simulations are made using Silvaco ATLAS which uses a 1-dimensional non-equilibrium Greens' functions formalism to self-consistently solve the Schrödinger-Poisson equations numerically. The *RTD* uses the $In_{53}Ga_{47}As/AlAs$ material system with the parameters listed in Table 3-1at 300 K. All simulated devices have an area of 1 μm^2.

Table 3-1: RTD material parameters for simulation [74].

Property	Material	
	$In_{53}Ga_{47}As$	$AlAs$
Bandgap (eV)	0.75	2.9 (Γ point)
Relative dielectric constant	13.9	10.9
Effective electron mass	0.043	0.06 [102]
Effective hole mass (light hole)	0.056	0.15
Conduction band density of states (cm^{-3})	2.1x10^{17}	1.5x10^{19}
Valence band density of states (cm^{-3})	7.7x10^{18}	1.7x10^{19}
Intrinsic carrier concentration (cm^{-3})	6.3x10^{11}	9.5

The band diagrams in these simulations assume the Fermi level at zero energy and the separation between the quasi-Fermi levels to equal the applied potential. The carrier concentrations are according to the Fermi-half functions without using any simplifications.

3.3.2 The effect of collector carrier concentration

Simulations take place of a *RTD* structure made from 100 nm $In_{53}Ga_{47}As$ emitter and collector regions. Two *AlAs* barriers each 2.5 nm wide and a 4.5 nm wide $In_{53}Ga_{47}As$ quantum

well. These are values for test structures to study the trends observed when changing the beforementioned structural parameters. Choosing any other values for the barriers or quantum well will not have any effect on the resulting trends or conclusions. The thick barriers have shown to give better convergence at coarser meshes, which translates into less computation time. Nonetheless, structures with 1.7 nm barriers were also simulated and the results are satisfactory. The emitter region is doped with a fixed uniform n-type concentration of $1x10^{15}$ cm^{-3}. The carrier concentration at the collector is changed systematically from intrinsic to $1x10^{17}$ cm^{-3} n-type in the following steps ($1x10^{12}$, $5x10^{12}$, $1x10^{13}$, $5x10^{13}$, $1x10^{14}$, $5x10^{14}$, $1x10^{15}$, $5x10^{15}$, $5x10^{16}$, $1x10^{17}$ cm^{-3}). This range takes into account all possible cases when the collector has less, equal and more carriers compared with the emitter. Table 3-2 shows the epi-layer which was simulated.

Table 3-2: Epilayer design of simulated RTD.

Layer	Type	Material	Thickness (nm)	Doping level (cm^{-3})
1	N	$In_{53}Ga_{47}As$	100	Variable
2	I	AlAs	2.5	I
3	I	$In_{53}Ga_{47}As$	4.5	I
4	I	AlAs	2.5	I
6	N	$In_{53}Ga_{47}As$	100	Variable

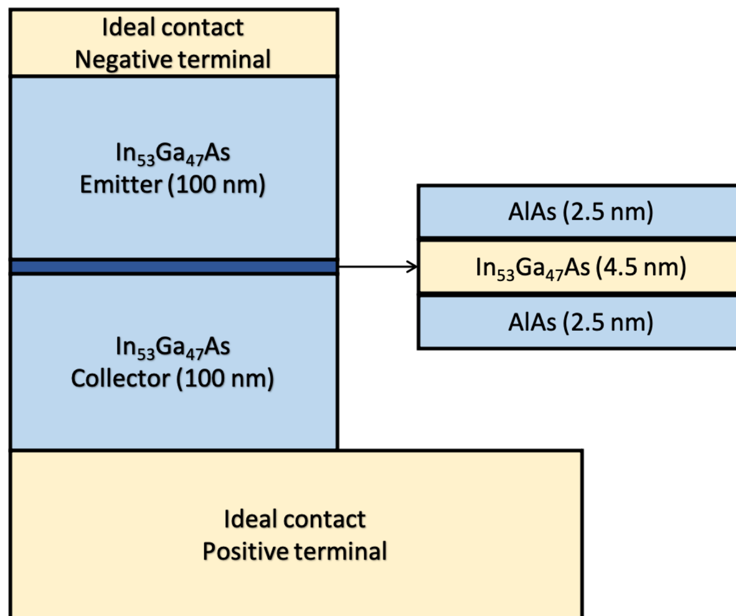

Figure 19: Schematic of the simulated device.

Starting with the first case, when the collector has less carriers than the emitter. The voltage is ramped up from zero to 2.5 V in increments of 10 mV, with the collector connected to the positive terminal and the emitter to the negative terminal. The resulting *IV* curves are shown in Figure 20.

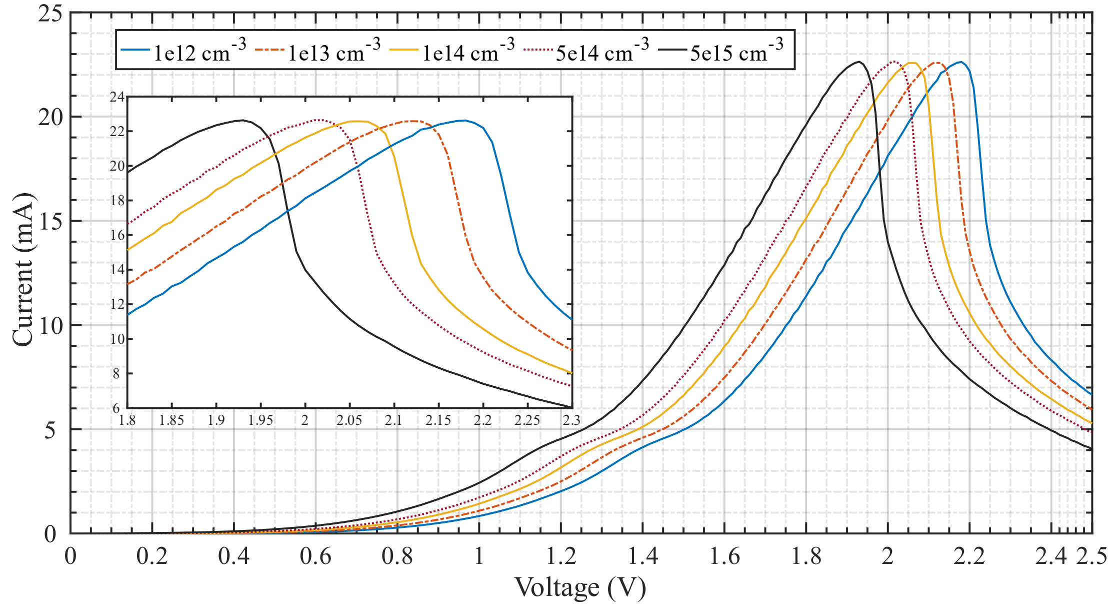

Figure 20: IV curves for various collector doping concentrations.

Notice how the peak voltage shifts to a lower value while the peak current remains constant. Figure 21 shows the equilibrium energy band diagrams for all the doping concentrations corresponding to this case with the first quantized Eigenstate superimposed.

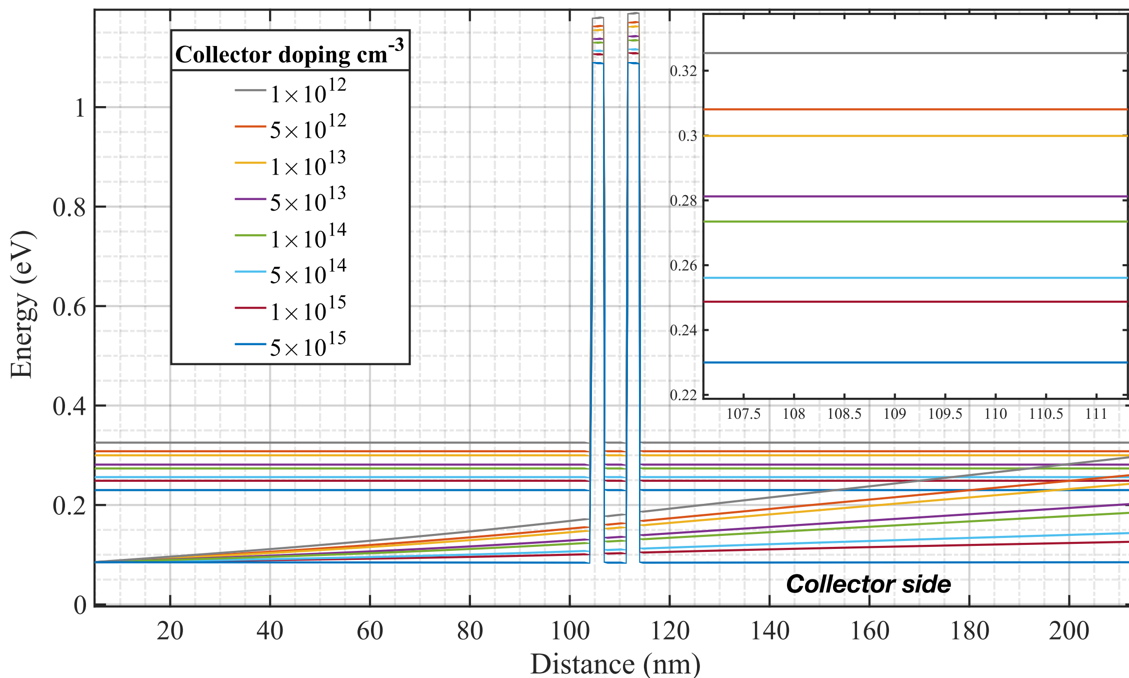

Figure 21: Conduction band profile for various collector doping levels with the first bound Eigenstates.

Table 3-3: Quantized energy Eigenstates in the quantum well.

Doping level (cm^{-3})	En (meV)
$1x10^{12}$	325
$5x10^{12}$	308
$1x10^{13}$	300
$5x10^{13}$	281
$1x10^{14}$	273
$5x10^{14}$	256
$1x10^{15}$	249
$5x10^{15}$	230

The figure shows a clear built-in potential pointing from the emitter to the collector due to the concentration gradient. This potential, for an isotype junction, is calculated (assuming the Boltzmann approximation) using (*3-11*)

$$V_{bi} = \frac{kT}{e} \ln \frac{N_{d^+}}{N_d} \qquad (3\text{-}11)$$

where N_d^+ is the doping of the higher-doped region, N_d is the doping in the lighter-doped region, *k* the Boltzmann constant, *T* the temperature in kelvin, and *e* the electron charge. This built-in potential causes an initial voltage-drop on the *DBQW* and hence changes the energy Eigenstates as depicted by Figure 21 (also in Table 3-3). The built-in potential is taken to be between the emitter and collector regions. The heterojunctions between the emitter and the barrier and the barrier and the collector do not play a role here. This is because the accumulated charges at the emitter will cause an accumulation of holes in the collector. A junction is made between two areas where charge distribution gets changed, the barriers mainly act as insulators (particularly the high bandgap *AlAs*).

Note how, due to the polarity of the built-in potential, the first energy Eigenstate is moving downwards as the built-in potential decreases towards the equilibrium state (i.e.: the state where the emitter and collector are equally doped). From a first glance at these values and by examining Figure 20 and Figure 21, it is plausible that the shift in peak voltage is related to the change in built-in potential. As increasing the carrier concentration at the collector in this instance reduces the built-in potential. It can be argued that under higher carrier concentrations less energy is required to align the conduction band edge with the energy Eigenstates.

The voltage shift between two different carrier concentrations can be calculated using (3-11). Suppose that N_{D1} and N_{D2} are two collector carrier concentrations. The built-in potential for each case having a fixed emitter charge N_{DE} is given by:

$$V_{bi1} = \frac{kT}{e} \ln \frac{N_{D1}}{N_{DE}} \tag{3-12}$$

And the built-in potential for the second case is:

$$V_{bi2} = \frac{kT}{e} \ln \frac{N_{D2}}{N_{DE}} \tag{3-13}$$

The difference between the two gives the voltage shift observed:

$$V_{shift} = \frac{kT}{e} \ln \frac{N_{D1}}{N_{D2}} \tag{3-14}$$

Table 3-4 shows the peak voltage as function of the carrier concentration.

Table 3-4: Simulated peak voltage for various collector doping levels.

Collector doping (cm^{-3})	Peak voltage (V)	Measured shift from equilibrium state (mV)	Calculated shift from equation (3-14) (mV)
$1x10^{12}$	2.18	250	221
$5x10^{12}$	2.13	200	180
$1x10^{13}$	2.12	190	162
$5x10^{13}$	2.08	150	120
$1x10^{14}$	2.06	130	102
$5x10^{14}$	2.015	85	59.9
$1x10^{15}$	1.995	65	42.8
$5x10^{15}$	1.930	0	0.00

Notice that (3-14) assumes the Boltzmann approximation which is reasonable for non-degenerate conditions. Looking closely at the numbers there is a slight mismatch. First the error from using the Boltzmann approximation will eventually propagate to the calculations. Second the peak current density in the Fermi-Dirac distribution lies between a couple of *kTs* around the Fermi-energy level. This means that the peak will occur about one *kT* above the energy Eigenstate. If (3-12) and (3-13) are modified by adding a value equal to the thermal voltage (26 mV at 300K) the results will be in close agreement. Notice that (3-14) still holds true as is, since the thermal voltage term will simply cancel out when taking the difference between any two levels.

To further clear the point, one can look at this shift in another way utilizing the perturbation theory first order approximation to solve the problem of a particle in a slanted box [103]. Starting with a reference Hamiltonian, which in this case corresponds to a collector

having a doping of 5x10^{15} cm^{-3}, to which the solution for a particle in a box is readily achieved [104]. The change in the collector's doping concentration induces a built-in potential which acts as a small perturbation to the quantum system resulting in a slanted box. The first order approximation shows that the energy Eigenstates in the quantum well will have to be modified (in this case lowered) by a value equal to half the applied perturbation.

$$\mathrm{E}_{\mathrm{n_{slanted}}} = E_{n0} + \frac{E_{bi}}{2} \tag{3-15}$$

E_{n0} is the energy state at equilibrium. This can be verified by looking at Figure 21, which shows the first energy Eigenstates for various concentrations. By comparing the values of the built-in potential with the separation of Eigenstates, it can be seen that indeed the energy separation between the Eigenstates from equilibrium falls down by half the built-in potential.

The conduction band edge at the emitter's side is also lowered by increasing the collector's concentration (decreasing the built-in potential). This lowering is also approximately equal to the lowering taking place at the Eigenstates resulting in a total shift equal to that of the built-in potential.

At this point, the evidence suggests that the built-in potential is indeed a good measure of the observed voltage shift in this case. Nonetheless, this is not the full story, if we examine the second case when the collector has more carriers than the emitter, it is seen that the shift in Figure 22 is much more drastic. Calculating the shift as in (*3-14*) does not give accurate results in this case, so clearly there is more going on.

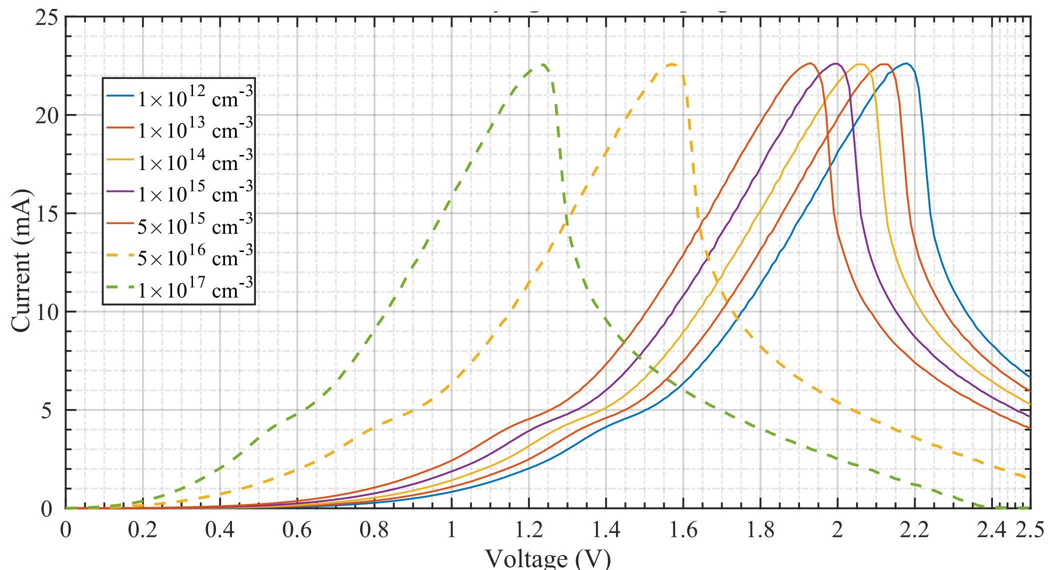

Figure 22: IV curves for various collector doping levels.

In order to understand what is happening, it is important to understand the state of the junction bias with different carrier concentrations at the collector. Figure 23 shows the electric field profiles at zero bias.

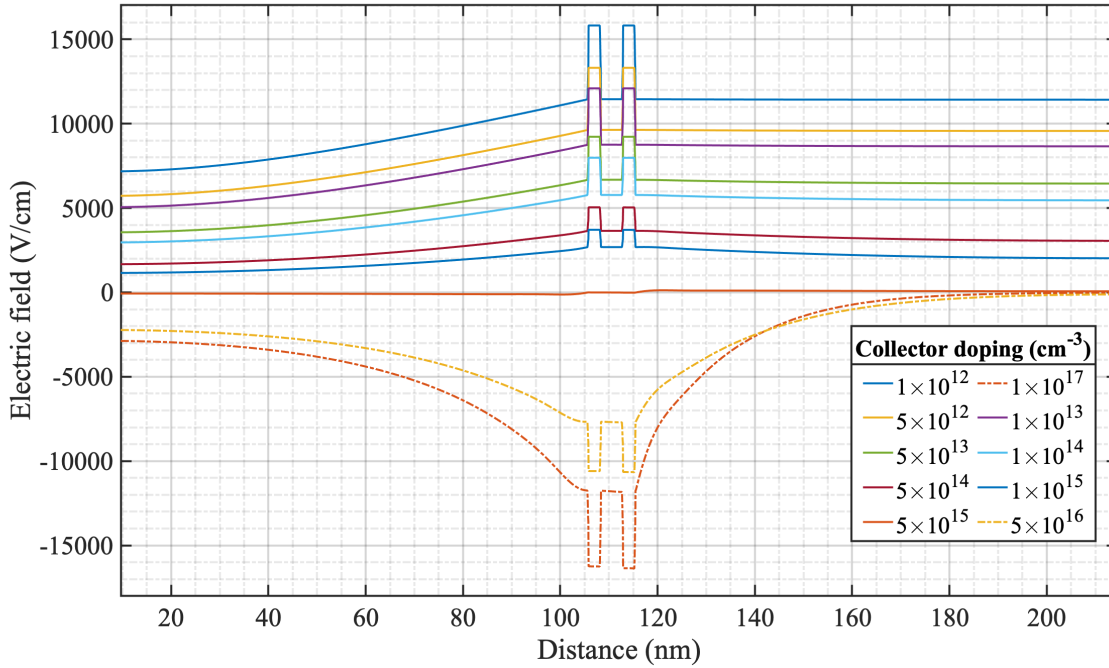

Figure 23: Electric field profiles for various collector doping levels at zero bias.

Consider the first case where the emitter has more carriers than the collector. The electric field points in the positive Y direction (from the emitter to the collector). This means that the built-in potential has a positive polarity at the emitter and a negative one at the collector. When proper bias is applied (i.e., the positive terminal is connected to the collector and the negative terminal to the emitter), the applied electric field will have an opposite polarity to the built-in field. This corresponds to the junction being forward biased. The opposite case is also true, that is, in the second case, when the collector is more doped than the emitter, the built-in potential will have a polarity from the collector to the emitter, and applying the same bias results in a junction that is being reverse biased. A forward bias will work to weaken the built-in field so as to allow further diffusion of carriers. A reverse biased junction will strengthen it. Going back to the original point, in the second case, the additional voltage shift observed will be the result of resistance change imposed by the change in the depletion width in the collector region.

To quantify this shift, a model for the device at peak voltage under *DC* conditions is proposed. It is built around the idea of treating the device, when biased at the peak, as

consisting of regions each with its own resistance. Consider the resistance of the emitter and collector regions given by (*3-16*)

$$\mathrm{R} = \frac{L}{\sigma A} \tag{3-16}$$

where *L* is the length of the emitter/collector region, σ the conductivity of that region and *A* the cross-sectional area of the device. While the resistance of the double barrier structure is considered as a ballistic resistor (Landauer resistor) with a resistance (at peak voltage) given by(*3-17*). In a Landaur resistor the electron transport is considered not to go through any scattering. The ballistic resistance approximation here is valid since we are dealing with a small number of states (quantized states), and small dimensions in the tunneling direction. The transverse direction does not influence this approximation with regard to device operation [90].

$$\mathrm{R_{Landaur}} = \frac{h}{2e^2} \tag{3-17}$$

h is Planck's constant and *e* the electron charge. However, at peak voltage there is an additional quantum well just before the emitter barrier. This quantum well is a result of the two-dimensional electron gas (*2DEG*) resulting form charge accumulation. For simplicity, it will be regarded as another Landauer resistor. Hence the proposed device model will be as shown in Figure 24.

Figure 24: Proposed model for RTD resistance.

It is important at this point to explain why this additional *2DEG* formulates and when it does so? Since we have a potential barrier at the emitter's side, electrons coming from the emitter contact will not all pass from the barrier leading to charge accumulation. The accumulation rate at the emitter's side can be given by (*3-18*). The accumulated charge density is high, up to degeneracy conditions, and can reach as high as 1×10^{19} cm^{-3}, depending on the structure and applied bias.

$$\mathrm{R_{acc}} = (R_{injection} - R_{transmission}) \tag{3-18}$$

where $R_{injection}$ is the rate of electron injection (number of incident waves per unit time), and $R_{transmission}$ is the number of transmitted waves per unit time. The former is simply the

emitter current divided by the electron charge and the latter is related to the transmission rate of the single barrier structure given by [77] (*3-19*):

$$\mathrm{T(E)} = 16\frac{E}{V_o}e^{-2l_b\sqrt{\left(2m\frac{V_o-E}{\hbar^2}\right)}} \tag{3-19}$$

where E is the energy, V_0 is the height of the barrier, l_b the width of the barrier and m the mass under the effective mass approximation. This accumulation lowers and bends the conduction band edge at that point, forming a quantum well with at least one quantized Eigenstate, which is the source of the *2DEG*.

But how much charge would have to accumulate until such a region forms? The answer to this question can be found in the following scenario. Consider a device operating at cryogenic temperatures, this assures that no electrons exist above the Fermi-energy level. Electrons will start to accumulate at the boundary of the emitter barrier when the Fermi-level eventually reaches the edge of the conduction band (i.e., when that region of the conduction band becomes degenerate) plus a small offset corresponding to the quantized Eigenstate in that well. Accumulation then starts and lasts for a couple of kT above the first quantized state until a state of dynamic equilibrium is reached. Applying the same reasoning to devices operating at room temperature one can use (*3-20*)

$$\mathrm{E_F} - \mathrm{E_c} = \mathrm{kT}\ln\left(\frac{n}{N_c}\right) \tag{3-20}$$

to show that this region begins to formulate at a concentration given by (*3-21*) assuming we go lkT above the first Eigenstate, where 2 < l < 3.

$$\mathrm{n_{acc}} = N_c e^{l} \tag{3-21}$$

To show this point using the simulator, Figure 25 depicts the conduction band profile with the electron concentration superimposed. The electron concentration at the emitter's barrier at a bias voltage of 0.6 V is not enough to formulate a quantum well, while a potential well starts to form at a bias of 1 V. The electron concentration also shows that using (*3-21*) gives a very good approximation of the carrier density at that point, since N_c for $In_{53}Ga_{47}As$ is about 2.1×10^{17} cm^{-3}, which gives a carrier density of 1.55×10^{18} cm^{-3} using (*3-21*) compared to around 5×10^{17} cm^{-3} resulting from the *NEGF* simulations. The limitations of (*3-20*) and (*3-21*) arise from the Boltzmann approximation which is known to give errors near degeneracy, however, the use of a more complicated model such as the Joyce-Dixon

approximation (which will be introduced in chapter 4) will give better results on the expense of a more complicated solution. That is, (*3-21*) will need to be solved graphically using a software like MATLAB. Nonetheless, as we demonstrated, (*3-21*) gives satisfactory results.

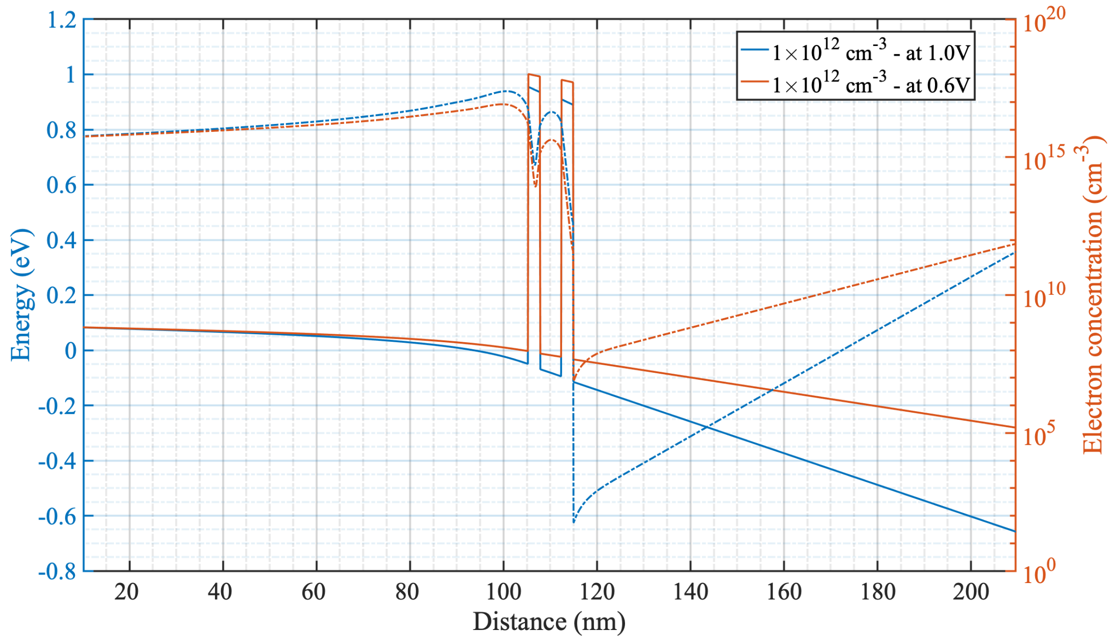

Figure 25: Conduction band diagram for the 1×10^{12} cm^{-3} case at 0.6- and 1.0-volt bias.

At this point it is important to account for the consequences of this new *2DEG*. The carrier concentration at this region tends to be quite high. It is high enough to screen most of the emitter region's electric field. Electric field screening is a physical phenomenon by which the electric field of a charge is hidden (screened) by the presence of other charges around it. For our case, this can be quantified by calculating the Thomas-Fermi screening length of a *2DEG* given by (*3-22*)

$$L_{TF} = \frac{2\pi\epsilon\hbar^2}{e^2 m^*} \tag{3-22}$$

Plugging in the numbers for $In_{53}Ga_{47}As$ it is readily seen that the screening length is around 10 nm. After three screening lengths the electric field decays to 5% of its peak value (assuming exponential decay), which would suggest that the electric field will be screened substantially after 30 nm. This can be confirmed by looking at the electric field profile shown in Figure 26.

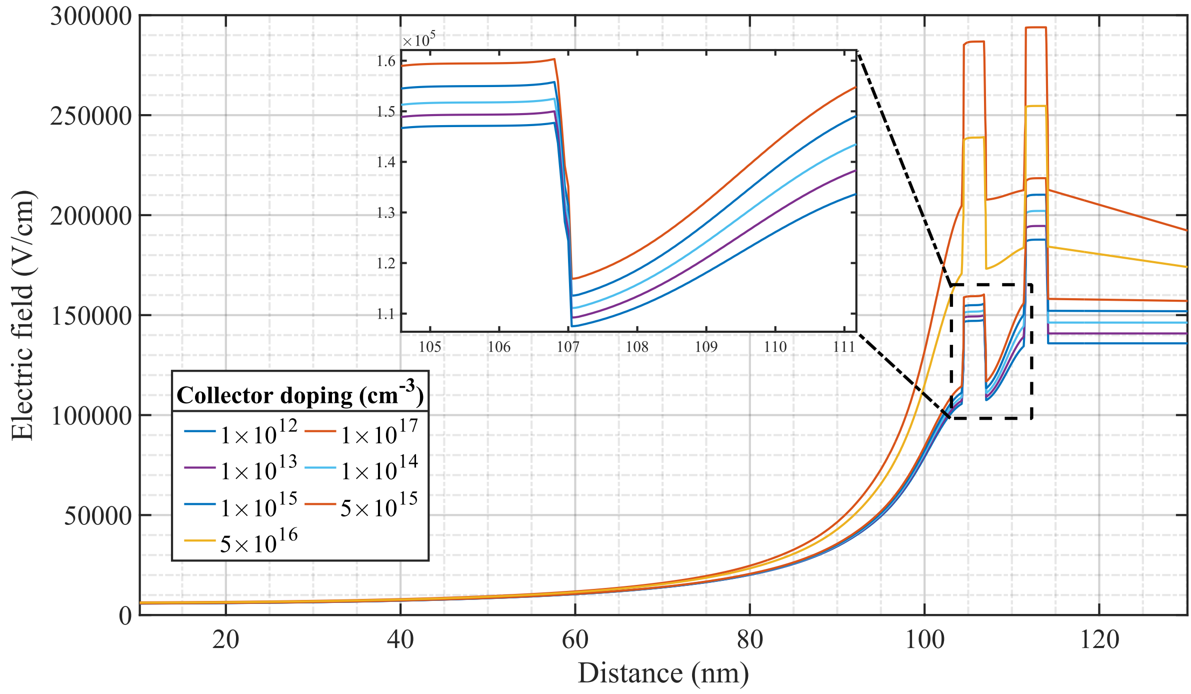

Figure 26: Electric field profile for various collector doping levels.

The vital thing to note here, is that after 30 nm the emitter will not be getting any additional voltage drop (the voltage drop across that region will be approximately zero) when bias voltage is increased.

The other consequence to consider is the formation of a space charge region at the collector's side due to charge accumulation at the emitter. This space charge creates a depletion region which has a substantially higher resistance value than the reminder of the collector. The width of the depletion region decreases as the carrier concentration at the collector's side increases. The width of the depletion region from the collector's side can be calculated using the expression given in (*3-23*) [69]

$$X_{coll} = \sqrt{\left(2\epsilon \frac{\mathrm{N_{acc}} V_{bi}}{eN_{coll}(N_{acc} + N_{coll})}\right)} \tag{3-23}$$

where N_{acc} is the concentration of charges accumulated at the emitter's side, V_{bi} is the built-in potential between the accumulated charges at both ends of the *DBQW*, e the electron charge and N_{coll} is the concentration of positive charge at the collector's side. Equation (*3-23*) however, assumes an abrupt junction. A more appropriate measure for practical devices is to use the Debye length to characterize the depletion given by (*3-24*)

$$L_{Debye} = \sqrt{\frac{\epsilon kT}{e^2 N_{total}}} \tag{3-24}$$

where N_{total} is the net charge in the region that is to be screened. Notice that the Debye length imposes a restriction on the length of the collector. For instance, if the collector was doped to $1\text{x}10^{15}$ cm^{-3} the Debye length will be approximately 145 nm. Depending on the value of the electric field at the junction and the actual value required to transport the charges, the collector's length will be a multiple of L_{Debye}. Three Debye lengths will reduce the initial electric field to 5% of its peak value, while (as a rule of thumb) after 7 to 9 Debye lengths the depletion region will be over [105]. If the collector was sized to be much longer than this value, electric field dead zones will arise.

A short note on the collector length and its relation to the Debye length. At peak voltage the accumulation region at the emitter and the depletion region at the collector would have formed. We have shown that the carrier concentration at the accumulation regions can reach up to around 1×10^{18} cm^{-3}, with an n-accumulation region at the emitter side, and a p-accumulation region at the collector's side. If we calculate the built-in potential between these two charge distributions using(*3-25*), we get about 750 meV for $In_{53}Ga_{47}As$ at room temperature.

$$V_{bi} = \frac{kT}{e} \ln\left(\frac{N_a N_d}{n_i^2}\right) \tag{3-25}$$

If we now equate the width of the depletion region in (*3-23*) to a multiple of the Debye length in (*3-24*) we get (*3-26*), where P is the multiple of Debye lengths we need.

$$P\sqrt{\frac{\epsilon kT}{e^2 N_{total}}} = \sqrt{\left(2\epsilon \frac{N_{acc} V_{bi}}{e N_{coll}(N_{acc} + N_{coll})}\right)} \tag{3-26}$$

Solving (*3-26*) yields

$$P = \sqrt{\frac{2V_{bi}}{V_T}} \tag{3-27}$$

Considering accumulation carrier concentrations ranges from 5×10^{17} cm^{-3} up to 1×10^{19} cm^{-3}, the value for P would be between 7 and 9, with an average value of 8.

Building on these facts most of the potential will drop across the depleted region of the collector. The collector itself, at peak voltage, will have a conductivity value that is much

less than that calculated from the simple Drude formula given by (*3-28*), assuming a constant charge distribution.

$$\sigma = e(n\mu_n + p\mu_p) \tag{3-28}$$

This is because of the carrier concentration gradient at that region as depicted by Figure 27. Notice that the depletion width decreases at a given voltage with an increase in carrier concentration as suggested by the Debye length formula.

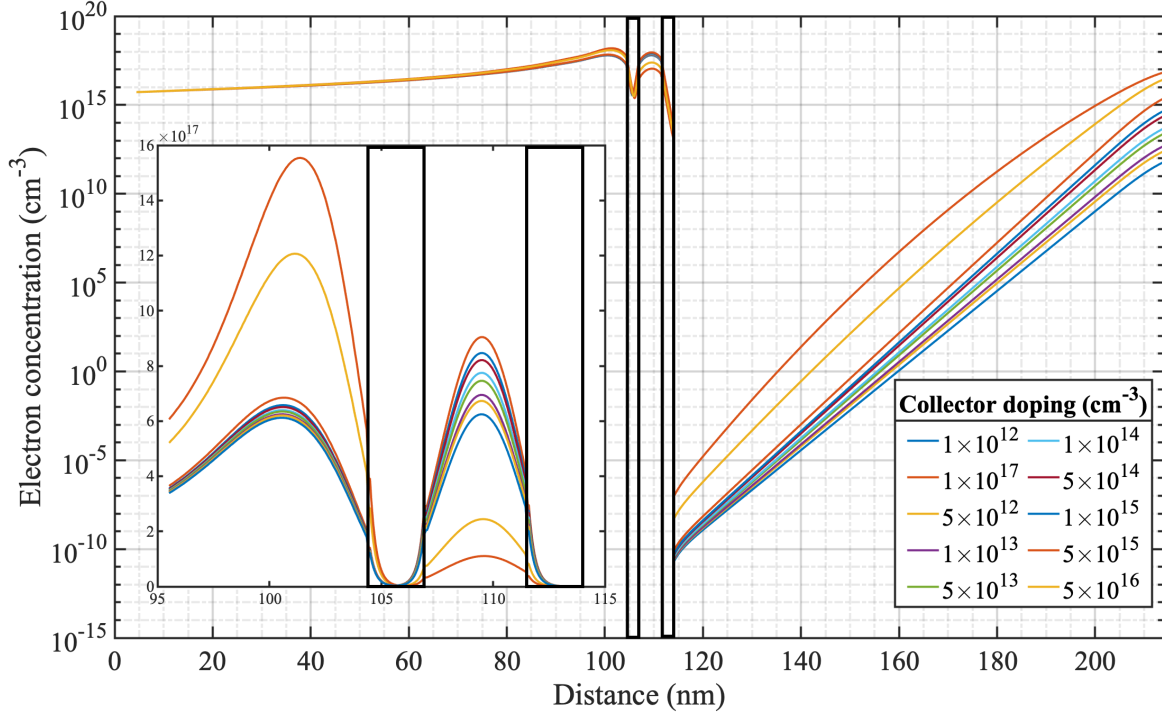

Figure 27: Electron concentration for various collector doping levels.

Given the above, at the peak voltage, we have an emitter region that is mostly screened, two quantum wells which are treated as ballistic resistors, and a collector that is partially depleted and hence highly resistive.

Given the above, it is now time to build the model for the shift in the second case. Going back to the same scenario where there are two carrier concentrations N_{D1} and N_{D2} the voltage drop across the collector at peak voltage will be

$$V_{C1} = \frac{V_{p1}R_{C1}}{Req_1} \tag{3-29}$$

and for the second case (N_{D2})

$$V_{C2} = \frac{V_{p2}R_{C2}}{Req_2} \tag{3-30}$$

The potential drop across the quantum well is:

$$V_{DBQW} = V_s \frac{R_{DBQW}}{R_{eq}} \tag{3-31}$$

Where R_{DBQW} is the lumped resistance of the double barrier structure, and R_{eq} is the equivalent series resistance given by:

$$R_{eq} = R_e + R_c + R_{DBQW} + R_{2DEG} \tag{3-32}$$

Notice that in order to calculate the shift given by (V_{c2}-V_{c1}), V_{p2} is needed which is unknown. The equation can be deduced by applying an approximate condition that, at peak voltage, regardless of the carrier concentration, the voltage drop across the *DBQW* is the same. This is evident in Figure 28 which shows the voltage drop across the device at peak voltages for each of the simulated cases.

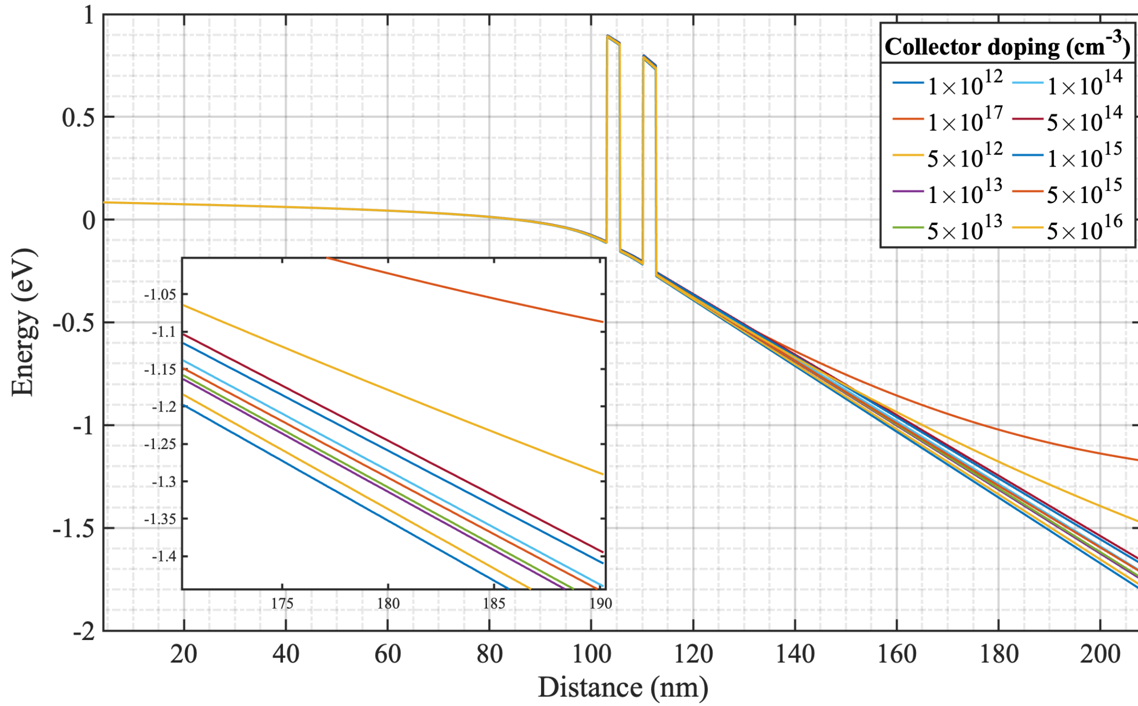

Figure 28: Conduction band energy at peak voltage for various collector doping levels.

Applying this condition to the above equation and since the resistance of the *DBQW* is the same we get:

$$V_{DBQW1} = V_{p1} \frac{R_{DBQW}}{R_{eq1}} \tag{3-33}$$

$$V_{DBQW2} = V_{p2} \frac{R_{DBQW}}{R_{eq2}} \tag{3-34}$$

which gives an equation for the second peak voltage given the first peak voltage:

$$V_{p2} = V_{p1} \frac{R_{eq2}}{R_{eq1}} \tag{3-35}$$

The equivalent resistance can be readily calculated from (*3-32*) above as the only variable here is the collector's resistance. The model can be tested by plugging in the values of the resistances for each region. The collector depletion region can be taken as three Debye lengths with an intrinsic doping concentration (approx. $1x10^{12}$ cm^{-3}). The results of the calculations for the cases of $5x10^{16}$ and $1x10^{17}$ cm^{-3} have equivalent resistances of 401 kΩ and 290 kΩ respectively, the equivalent resistance at a doping of 1×10^{12} cm^{-3} is 651 kΩ. Plugging these numbers gives a predicted peak at 1.35 V and 1.04 V respectively, which agrees quite well with the simulated results of 1.5 V and 1.2 V respectively.

Before moving forward, it is important to highlight how the energy eigenstates inside the quantum well evolve as function of the applied potential. Here only the effects of carrier concentration in the collector region will be discussed. The evolution of Eigenstates also depends on the length of the collector region as will be shown later. Figure 29 shows how the energy Eigenstates inside the quantum well change as function of voltage for all doping concentrations.

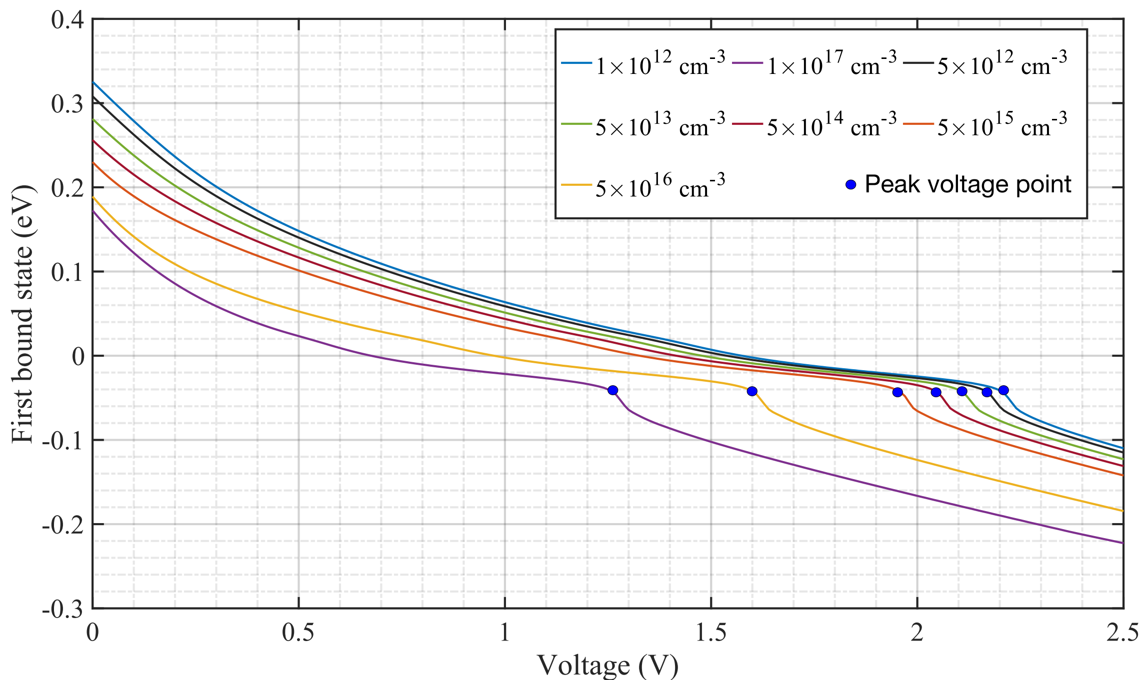

Figure 29: Energy evolution of the first Eigen state for various collector doping levels vs voltage.

The first thing to note is the reduction in the zero-bias Eigenstates as the doping concentration is increased (i.e., lower built-in potential). Under bias the potential across the quantum well starts to drop sharply until a certain bias point is reached, then there is a sort of saturation (reduction of the rate of decrease) observed. There are mainly two mechanisms

that tend to saturate the rate of decay; first is the formation of the *2DEG*, and second is charge accumulation inside the quantum well. Recall that once the *2DEG* is formed the voltage will start to drop on the collector and not so much on the emitter's side. This means that the potential drop across the two barriers is no longer symmetric (i.e., the collector barrier will be lowered more that the emitter barrier). This leads to a reduction in the pace by which the Eigenstates inside the quantum well are lowered leading to the saturation observed. Furthermore, while increasing the applied potential, charges accumulate more in the quantum well making it more conductive, hence lowering the amount of voltage dropping across it. Note that the *2DEG* inside the quantum well has a limit to the number of charges at equilibrium, after this maximum has been reached the tunneling rate out of the quantum well will exceed the injection rate leading to a net loss of charge. This is what is happening in the *NDR*, charges are escaping from the quantum well leading to a further increase in its resistance. This is portrayed in the previous figure as there is a noticeable sharp dip in the Eigenstate energy at the peak value.

In order to gain a figure of merit on how much potential drops across the quantum well after the formation of the *2DEG* and as charge accumulates in the well, the derivative of energy with respect to voltage is calculated. Notice that the derivative will give the portion of the applied voltage which ends up affecting the quantum well. At low bias voltages, the portion of the potential dropping at the *DBQW* to lower the Eigenstates is nearly half. This is expected and agrees well with the first order approximation for a particle in a slanted box discussed earlier. However, after a certain potential the potential drop across the well seems to saturate and only 10-15% of it now works on lowering the Eigenstates as in Figure 30.

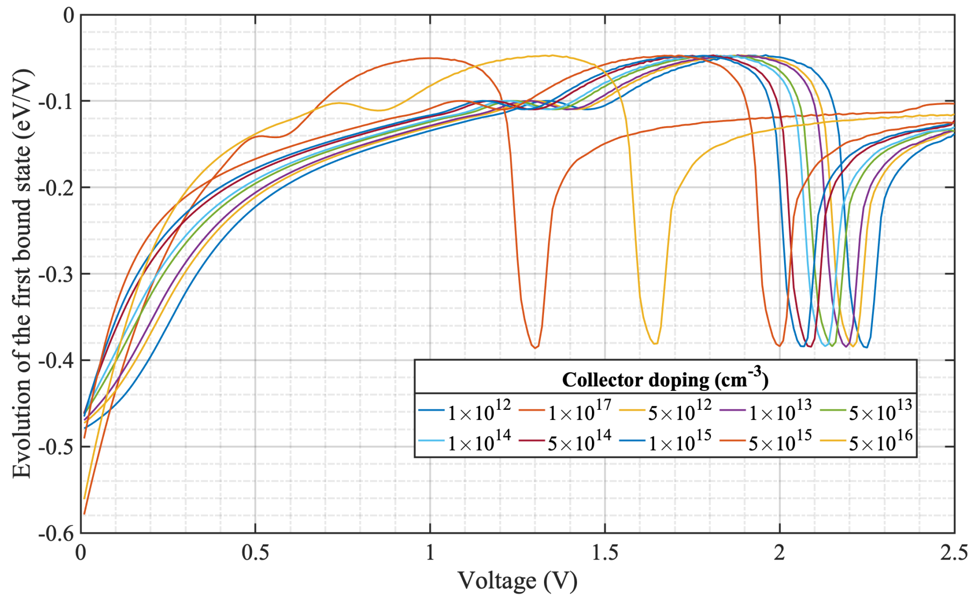

Figure 30: Rate of change of the first bound state with respect to voltage for various collector doping.

3.3.3 The effect of emitter carrier concentration

In these simulations, the doping at the emitter is changed in a similar way and the collector is held fixed at a concentration of $5x10^{15}$ cm^{-3}. The *IV* curves resulting from the simulations are shown in Figure 31. The peak voltage shifts to a higher value and the peak current is increasing. It is also notable that the width of the resonance (in the *IV* curves) is increasing, and the amount of shift is less than that observed from the collector's case. Again, the carrier concentrations are chosen such that the emitter has more, equal, and fewer carriers than the collector.

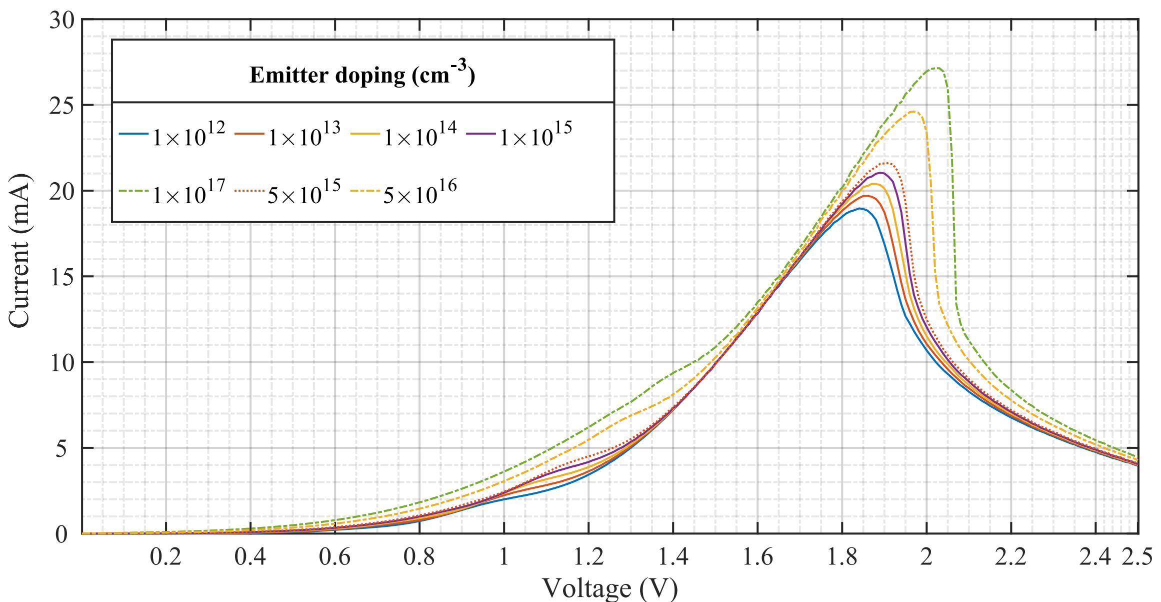

Figure 31: IV curves for various emitter doping levels.

Considering the case when the emitter has fewer carriers and examining the potential profiles at equilibrium (Figure 32), the effect of the built-in potential is apparent, specifically how it affects the conduction band edge at the emitter's side. The higher the carrier concentration, the lower the conduction band edge is. This means that more energy is required to align the conduction band with the energy Eigenstates. The difference between the conduction band edge and the Fermi-energy is given by (*3-36*)

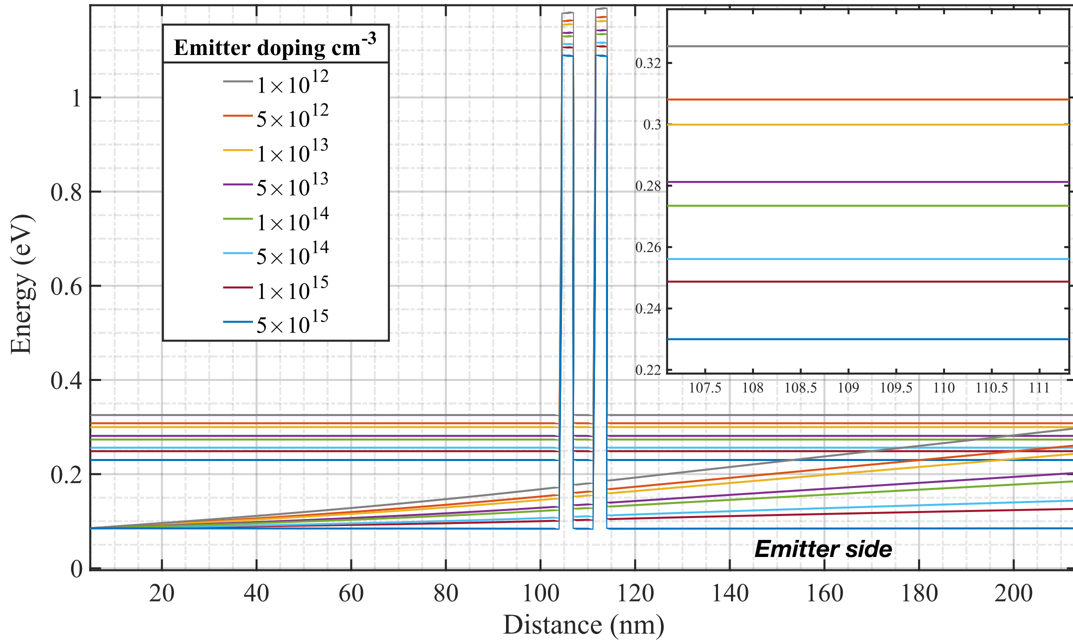

Figure 32: Conduction band diagram with the first Eigenstate for various emitter doping levels.

$$E_f - E_c = kT \ln\left(\frac{N}{N_c}\right) \tag{3-36}$$

where *n* is the carrier concentration at the emitter's side, N_c is the effective density of states in the conduction band. From (*3-36*), and given two different doping levels, the difference between the conduction band edge can be found using (*3-37*):

$$\Delta E_c = kT\ln\left(\frac{N_1}{N_2}\right) \tag{3-37}$$

where N_1 and N_2 are the carrier concentrations of the two doping levels under investigation. This is the same equation of the built-in potential used earlier. However, a few things must be investigated first before reaching any conclusions. First let us consider the effect of carrier concentration in the emitter's side. When more carriers are present, the conduction band edge will decrease (or the Fermi-level will increase). The point is that the difference between the Fermi-energy and the conduction band edge will increase with the rise of the carrier

concentration at the emitter. At equilibrium if the collector has a fixed number of carriers and the concentration at the emitter increases, then the built-in potential will decrease leading to a lower drop across the *DBQW*. This has the effect of lowering the energy Eigenstates in the quantum well as depicted in Figure 32.

Therefore, it is probable that the voltage shift observed is the difference between the two shifts, that of the conduction band edge and that of the Eigenstates. It is as if you would have to apply more energy to align the new conduction band edge while simultaneously lowering the energy Eigenstates in the well. Using the same reasoning as before, relaying on the first order perturbation theory approximation, the energy Eigenstates of the quantum well will go down by half of the applied voltage. With this into consideration the total shift observed is given by (*3-38*)

$$\Delta V = \frac{V_T}{2} \ln \frac{\mathrm{N}_1}{\mathrm{N}_2} \tag{3-38}$$

Table 3-5 shows the calculated values using (*3-38*) and the measured values of the shift from the simulated data. The model shows good agreement.

Table 3-5: Calculate peak shift values from (3-38) vs peak shift from the simulated IV curves.

Carrier concentration (cm^{-3})	Simulated shift between two doping levels (mV)	Calculated shift from equation (*3-38*) (mV)
1×10^{12} - 5×10^{12}	20	21
1×10^{13} - 5×10^{13}	20	21
1×10^{14} - 5×10^{14}	20	21
1×10^{15} - 5×10^{15}	20	21

Moving on to the second case, where the emitter has more carriers than the collector. The same argument for the state of the junction discussed previously applies here as well. Notice that in the first case both the applied and built-in potentials were in the same direction. In the second case, the built-in potential is opposite to that of the applied potential. Figure 33 shows the conduction band diagram for this case.

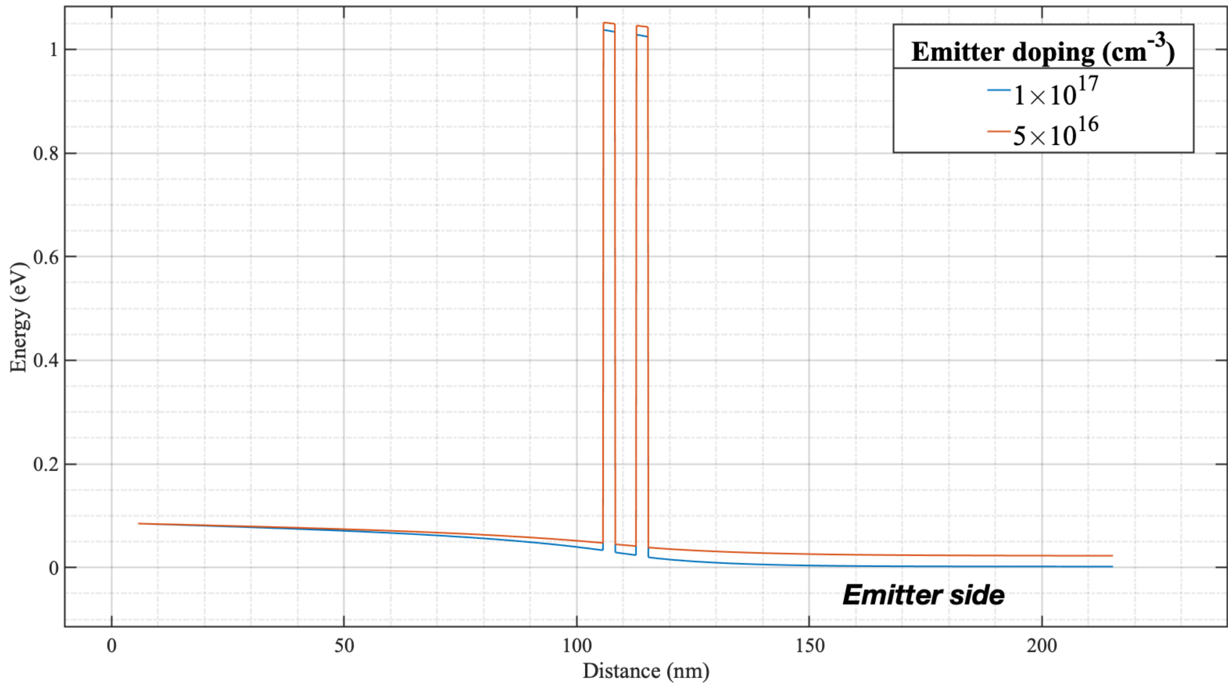

Figure 33: conduction band diagram for the second case (emitter has more doping than the collector).

There are two mechanisms here that control the overall shift; the lowering of the Eigenstates inside the well and the additional potential required to overcome the built-in potential (notice that the built-in potential is now opposing the applied potential, so a minimum of twice the built-in potential value is required to overcome it). Assuming that the built-in potential is not too large such that the *2DEG* does not form before it is overcome, then at least twice the amount of the built-in potential is required and since the Eigenstate is lowered by half of the applied potential the overall effect is given by (*3-39*)

$$\Delta V = \frac{3V_T}{2} \ln \frac{\mathrm{N}_1}{\mathrm{N}_2} \tag{3-39}$$

Applying (*3-39*) to the concentrations given for the second case, the predicted shift between a doping concentration of 1x10^{17} and 5x10^{16} cm^{-3} is around 27 mV, while the simulated value is about 30 mV.

One thing to pay attention to is that when the emitter has more carriers, the *2DEG* will form at an earlier applied potential. When that happens, any further applied voltage will drop across the depleted collector region. This has the effect of lowering the energy Eigenstates in the well at a much lower pace. This can be observed by looking at the evolution of the first Eigenstate inside the quantum well as function of the applied voltage (Figure 34).

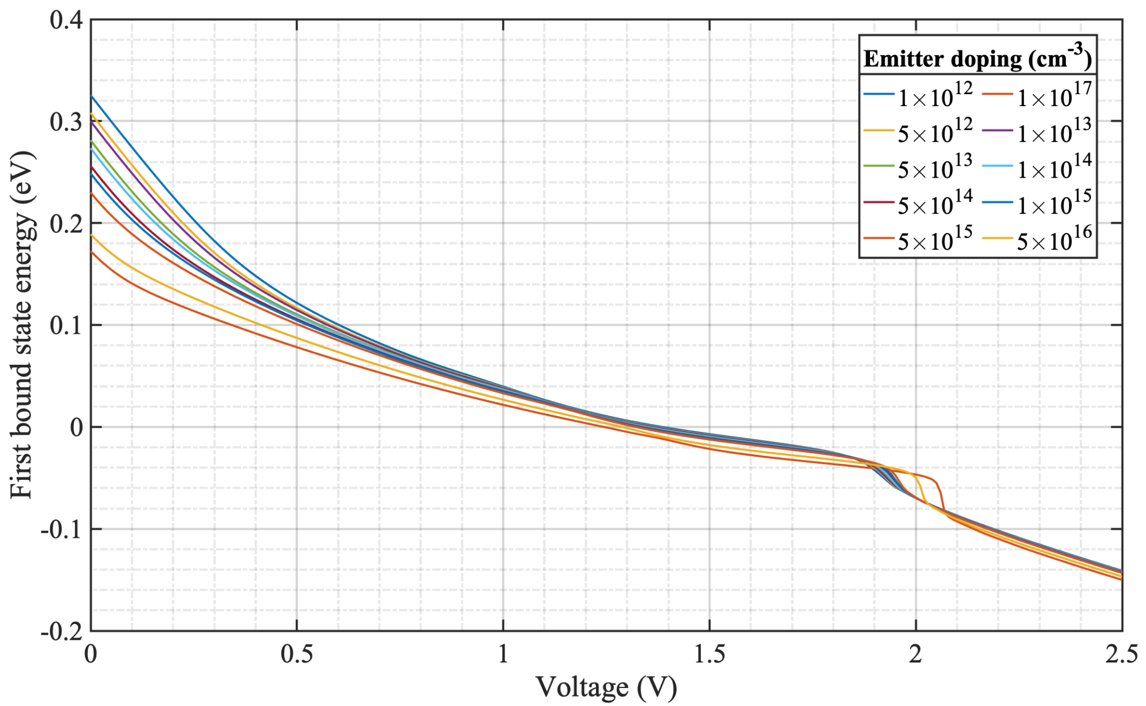

Figure 34: Evolution of the first bound state with applied bias for various emitter doping levels.

To make things clearer the first derivative of the Eigenstates as function of applied voltage is shown in Figure 35. The first derivative designates the portion of the applied potential which affects the energy Eigenstates. Notice as the doping increases, the portion of the potential drop across the *DBQW* starts to go more rapidly towards saturation (decrease of the pace).

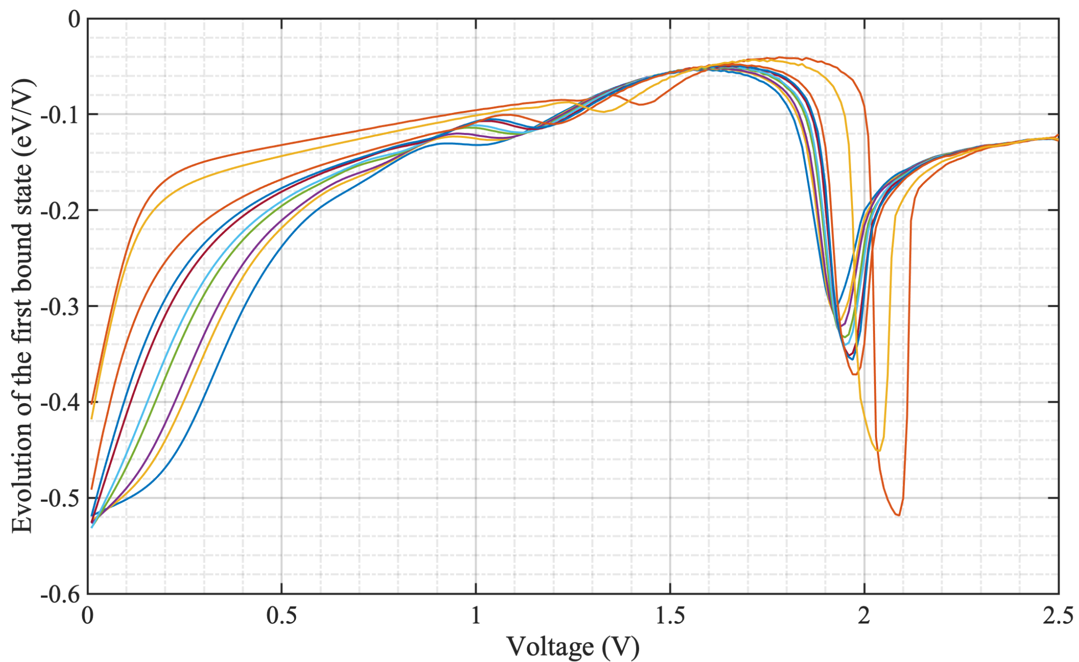

Figure 35: Portion of the applied potential drop on the first Eigenstate as function of voltage.

Now the alignment between the conduction band edge and the quantized Eigenstates will last longer (increasing the resonance width) before they become misaligned. This has the effect of increasing the non-resonant tunneling component of the tunneling current. Since the conduction band edge is now closer to the Eigenstate, the tunneling probability increases and so does the current.

Examining the IV curves, it is noticed that the resonant state broadens as the emitter doping increases, and also the shift is much more profound for higher doping concentrations. The reasoning behind this could be regarded to charge accumulation inside the quantum well. As the carrier concentration in the emitter is increased, so does the total charge-accumulated in the quantum well. The quantum well itself will be able to hold a maximum charge that is dependent of the total density of states in the well. For a *DBQW* of this height (1.2 eV) and well width (4.5 nm), there are only two resonant states. The point here is that the higher the emitter concentration, the faster (at a lower applied potential) the quantum well will be filled. Filling the states of the quantum well means that the conductance of the well will be highest and hence the potential drop across its will be less. This mechanism also contributes to the saturation behavior observed in the resonant state shown in Figure 34.

To show this, the charge density inside the quantum well was simulated for a doping concentration of $1\text{x}10^{17}$ cm^{-3} for various applied bias voltages. Charge builds up inside the quantum well until it is saturated at around 2 V. Afterwards it is seen that charge starts to go down, this could be due to the lower injection current from the emitter, or it could be signaling a higher escape rate from the quantum well.

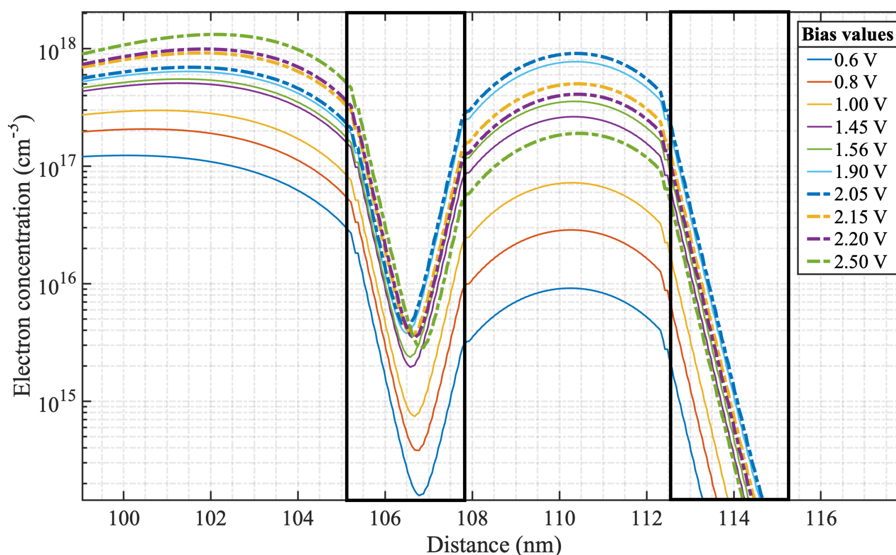

Figure 36: Carrier concentration in the quantum well for various voltage levels for 1×10^{14} cm^{-3}.

One final thing to note is what happens at some extreme cases. Consider a scenario where the emitter has a carrier concentration of 1x10^{19} cm^{-3} and the collector is doped to 5x10^{15} cm^{-3}. The built-in potential in this case would be around 200 mV which is comparable to the location of the first Eigenstate in the well. In this case the first Eigenstate will not show any resonant tunneling (only non-resonant tunneling), and the first resonant peak will be shown when the second Eigenstate is aligned. In this case it would seem like the peak shifts drastically to higher voltages.

3.3.4 Effect of emitter layer thickness

Now we move on to discussing the effect of changing the emitter spacer layer thickness. The simulations use the same quantum well structure, however, the collector has a fixed 5 nm spacer layer, and the emitter is changed from 5 nm up to 640 nm. The idea is to use a very short collector (5 nm in this case) such that the effect of the emitter alone is observed, and to reduce computation time. Although any other value would be sufficient as well. Both collector and emitter doping concentrations are fixed at 5x10^{15} cm^{-3} n-type with uniform doping profiles. The profiles were chosen such that there is no built-in potential to start with. The step sizes in the simulation are (5, 10, 20, 30, 40, 80, 160, 320 and 640 nm). Figure 37 shows the resulting peak voltage points. Looking at the figure it is apparent that the peak voltage shifts to a higher value as the length of the emitter increases up to a certain limit. It then stops and becomes not much dependent on the length. Figure 37 presents a plot of peak voltage as function of doping concentration, which shows this behavior more clearly.

The results actually emphasize the idea of the potential screening of the emitter discussed earlier. The shift observed at lengths less than 30 nm can be attributed to the potential drop across the emitter region. The longer the length of the spacer layer, the more the potential drop across it and hence less on the *DBQW*. This leads to the peak shifting to higher voltage as more potential is required to have the same drop across the quantum well and have proper alignment.

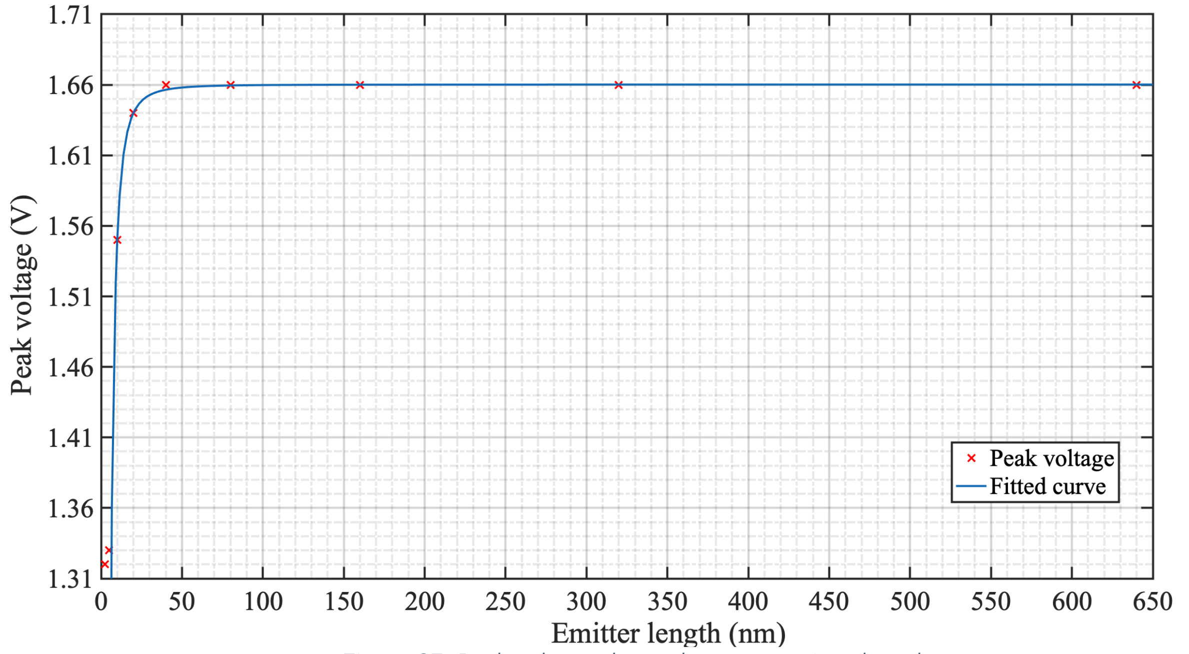

Figure 37: Peak voltage dependence on emitter length.

After 30 nm V_p does not change. This can be modeled using an exponential function of the form given in (*3-40*)

$$V_p(L_{emitter}) = V_s - Ye^{-\frac{L_{emitter}}{L_{TF}}} \tag{3-40}$$

where $L_{emitter}$ is the emitter's length, L_{TF} the Thomas-Fermi screening length for a *2DEG*, V_s the peak saturation voltage and *Y* is the potential difference between the saturation voltage and the equilibrium voltage (twice the separation between the Fermi-level and the bound energy state in the well) given by (*3-41*) and (*3-42*)

$$Y = V_s - V_{eq} \tag{3-41}$$

$$V_{eq} = 2(E_n - E_F) \tag{3-42}$$

with E_n being the nth quantized Eigenstate in the quantum well and E_f the Fermi-level. The model has an R^2 value of 95.5% and an adjusted R^2 value of 95%.

3.3.5 Effect of collector layer thickness

The same rational can be applied to increasing the collector's length but the effect here is much more profound. As stated before, the depletion length in the collector's side is approximated to be 7-9 Debye lengths. Since the depletion width in the collector is due to charges in the bulk (space charge) and not a *2DEG* the screening length is expected to be much longer. For instance, at the given doping concentration (5x10^{15} cm^{-3}), the Debye length

will be around 64 nm giving rise to a depletion width of about 500 nm. Figure 38 shows the peak voltage values as function of collector length.

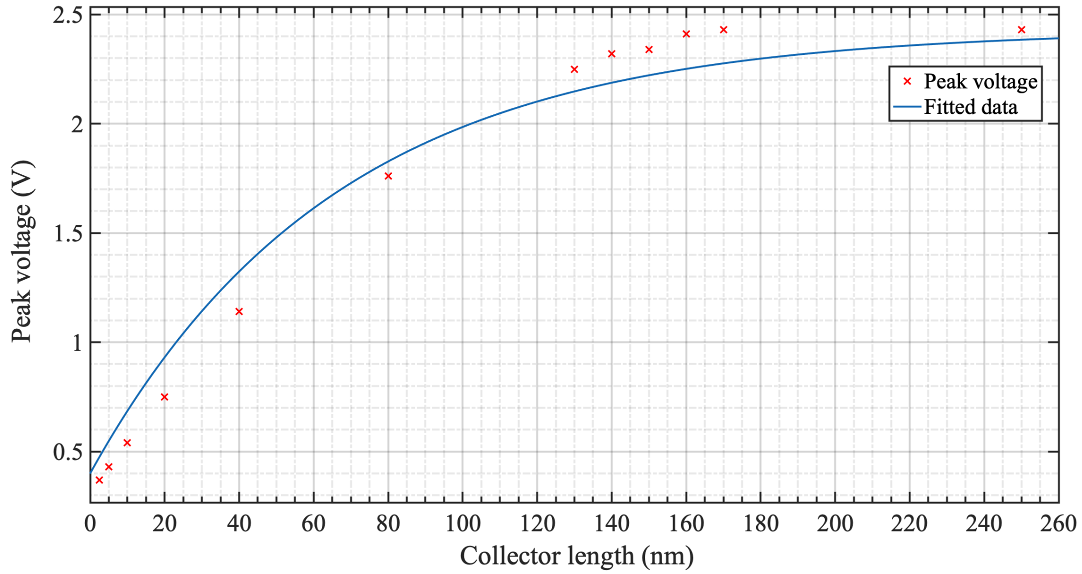

Figure 38: Peak voltage dependence on the collector length.

This effect can also be modeled in the same way as that of the emitter with the decay constant in the exponential term changed to represent the Debye screening length.

$$V_p(L_{collector}) = V_s - Ye^{-\frac{L_{collector}}{L_{Debye}}} \tag{3-43}$$

All the variables have the same meaning as previously mentioned.

The voltage span of the positive differential conductance region (from zero volts to the peak) is getting wider as the collector depletion region gets longer. This is a consequence of less potential being dropped across the quantum well and hence adjusting the transmission probability function to increase slower to the peak value. More on this point will be addressed later.

3.3.6 Effects on peak to valley current ratio, ΔV and ΔI

It is quite known that the energy Eigenstates are inversely proportional to the square of the width of the quantum well, and directly proportional to the height of the barriers. These dependencies are given by solving the Schrödinger equation for a particle in a finite potential well problem [104]. In this section a study of the resonant tunneling structure parameters (i.e.: well width, barrier height, emitter and collector layer doping and thickness) effects on the peak to valley current ratio, ΔV and ΔI will be presented. To do this a new structure based on the material system *GaAs/AlAs* is simulated. The choice of such structure has multiple

advantages: first it gives an opportunity to test a different material system using the ATLAS simulator, this should show the capability of the simulator to handle multiple material systems and gives more confidence into the results. Second, it resembles devices which have already been fabricated and tested, which gives a great opportunity to compare the simulated data with actual devices. The structure is based on the *RTD* design reported by [106]. As a calibration step, the *RTD* is first simulated and the *IV* is compared to that reported by the authors. Examining Figure 39, it can be seen that the results are satisfactorily accurate. Table 3-7 shows the simulated *PVCR*, ΔV and ΔI and those measured from the reported *IV* curves in the original paper.

Table 3-6: Epitaxial layer design of GaAs sample (data after [106]).

Layer	Type	Material	Thickness (nm)	Doping level (cm^{-3})
Collector	N++	GaAs	500	7×10^{18}
Spacer	I	GaAs	15	Undoped
Barrier	I	AlAs	1.7	Undoped
QW	I	GaAs	6.5	Undoped
Barrier	I	AlAs	1.7	Undoped
Spacer	I	GaAs	35	Undoped
Emitter	N++	GaAs	800	3×10^{18}
Buffer	I	GaAs	132	Undoped
Substrate	SI	GaAs	-	-

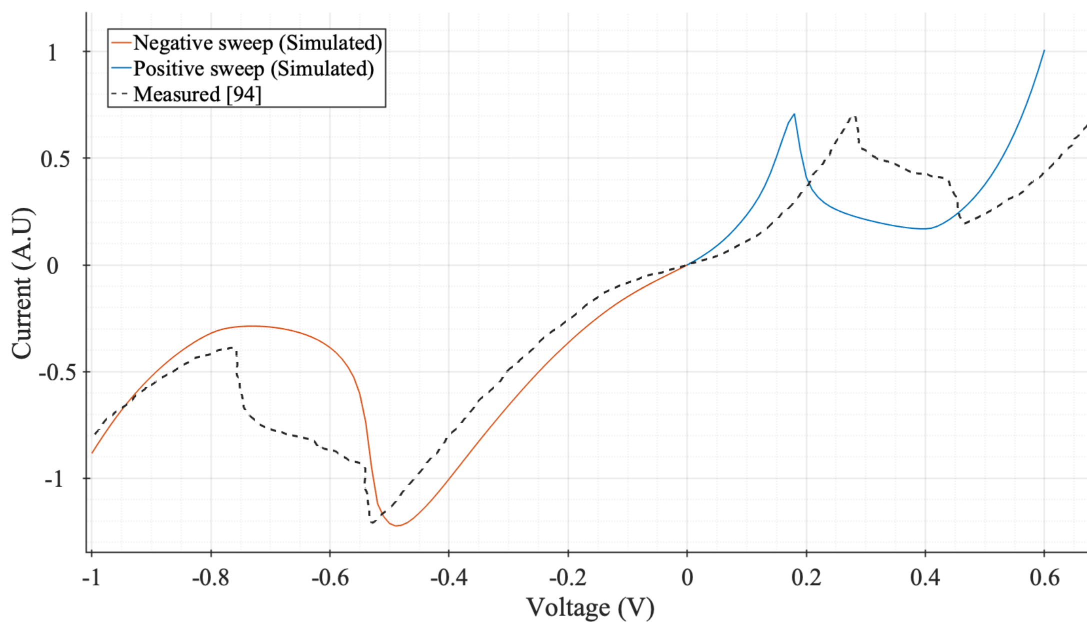

Figure 39: IV curves of fabricated devices by [106].

Table 3-7: Measured vs. simulated metrics of the GaAs/AlAs RTD in [106].

Quantity	Measured from Figure 39		Simulated	
	Positive bias	Negative bias	Positive bias	Negative bias
PVCR	4.00	3.01	4.17	4.25
ΔV (mV)	180	260	200	240
ΔI (mA) *Device area 25 μm² for both cases*	3	4	13	22.5

It is expected that the *PVCR* from the simulator to be higher as SILVACO does not take into account scattering effects which increase the valley current leading to a reduction in the *PVCR* from the ideal case. The currents from the simulation do not resemble real devices as the effect of contacts and their material was not taken into account in the simulation.

3.3.7 Effects of doping concentrations

Figure 40 shows the *IV* curves resulting from simulating structures with emitter doping ranging from 1x10^{12} cm^{-3} up to 1x10^{19} cm^{-3} under reverse bias conditions.

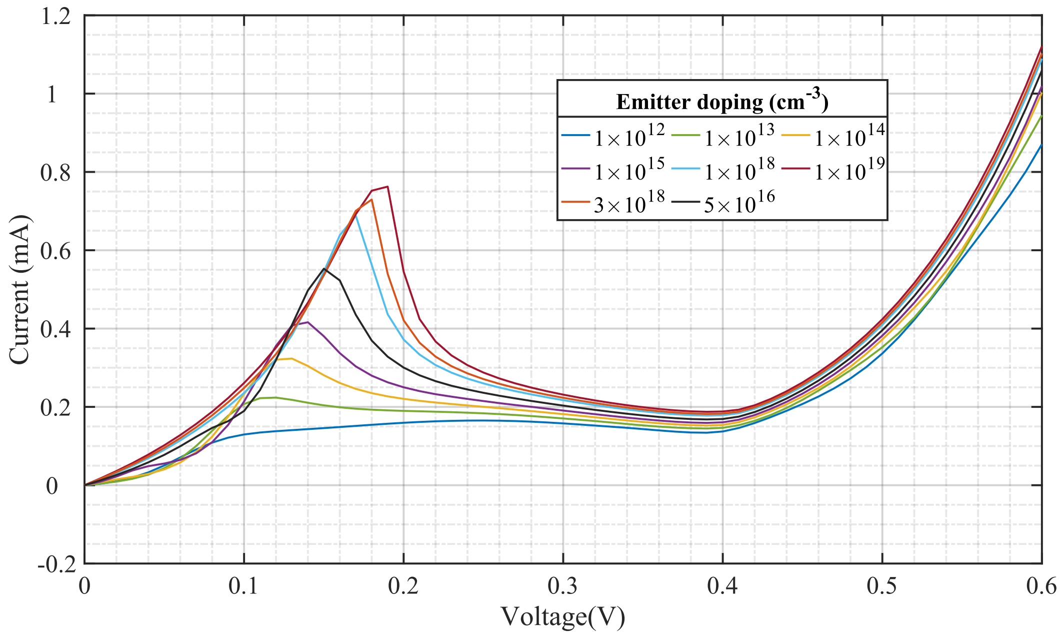

Figure 40: IV curves for GaAs/AlGaAs RTD with various emitter doping levels.

Due to the doping gradient between the collector and emitter, the junction will have a built-in electric field pointing from the collector to emitter. Therefore, for the positive bias values, the junction is actually being reverse biased while for negative voltages the junction

will be pulled towards forward bias. This is apparent from the shifting behavior of the peak voltages as discussed in the previous sections. The *PVCR* is seen to increase while increasing the emitter doping as shown in Figure 41, where the fitted data has an R^2 value of 99.2%.

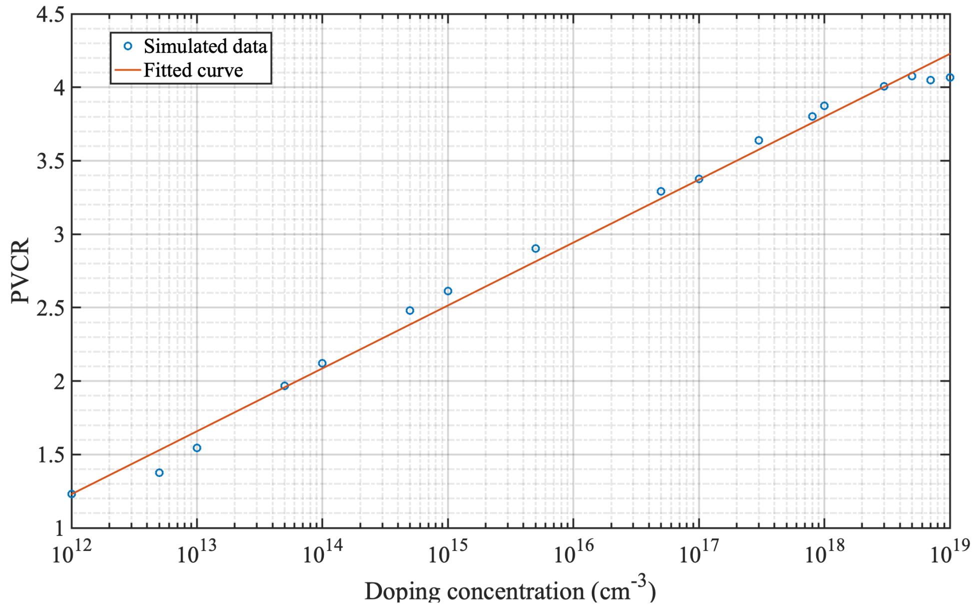

Figure 41: PVCR dependence on emitter doping levels for GaAs/AlGaAs structure.

Notice from the *IV* curves that as the doping increases the peak current grows more rapidly than the valley current does. The reason for such behavior is the same as that discussed in the previous section. Mainly the faster the formation of the *2DEG* and the more charge going into the quantum well increasing its conductivity and hence decreasing the potential drop across it, which tend to keep the energy Eigenstates aligned for longer. It is therefore expected that ΔI increases.

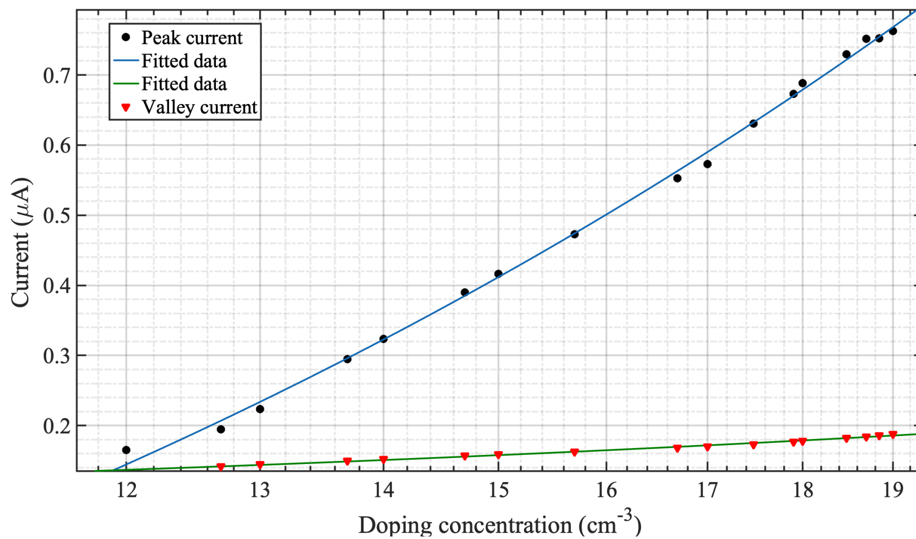

Figure 42: Peak and valley current dependence on emitter doping for GaAs/AlAs structure.

From the above plots (Figure 42), both the peak and valley current dependencies on the carrier concentration can be mathematically modeled using the below equations:

$$I_v(g) = Ag + B \tag{3-44}$$

$$g = \log(n) \tag{3-45}$$

$$I_p(g) = Ag + B \tag{3-46}$$

where I_v and I_p are the valley and peak current respectively, and n is the doping concentration at the emitter in cm^{-3}. The fitting parameters for the above equations are given in the table below. The confidence interval is 95%.

Table 3-8: Fitting parameters for peak and valley current dependence on emitter doping.

	A	B	R^2 (%)	Adjusted R^2
I_p	8.91e-08 (8.689e-08, 9.125e-08)	-9.243e-07 (-9.596e-07, -8.889e-07)	99.8	0.9979
I_v	6.98x10-9 (6.64e-09, 7.324e-09)	5.31x10-8 (4.752e-08, 5.862e-08)	99.2	0.9916

ΔV on the other hand seems to decrease, the reason behind that is attributed to the shift in the peak voltage to higher values. Notice that the decrease in *ΔV* is the same as the shift observed in the peak. The *IVs* also show that the valley voltage does not change in this case. The results are plotted in Figure 43, with the fitted data having an R^2 and adjusted R^2 values of 96.6% and 96.35% respectively.

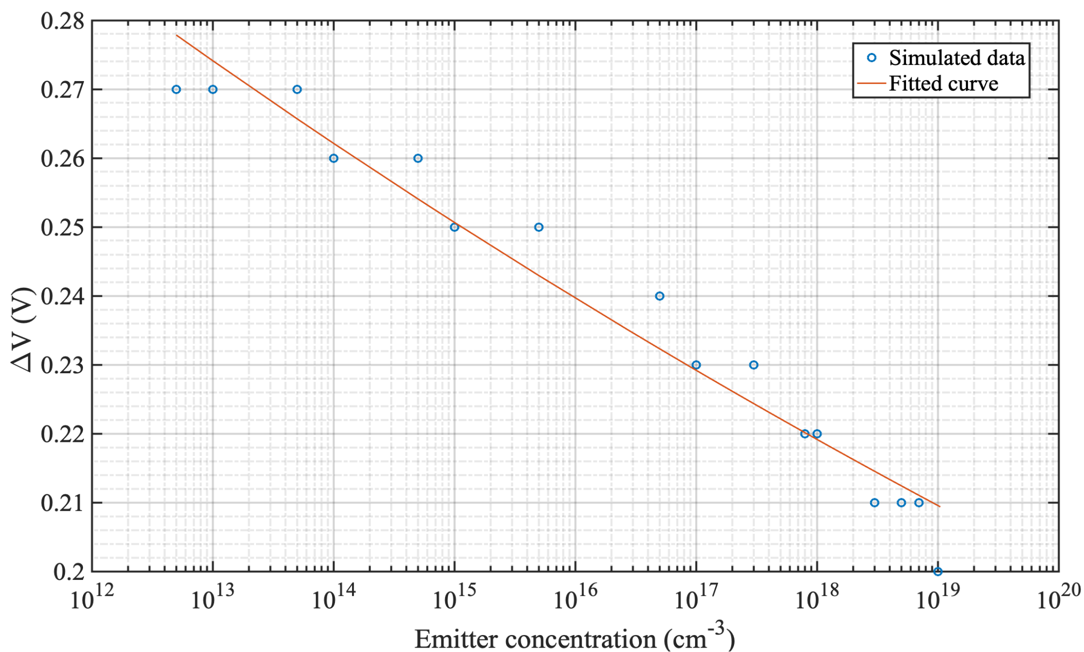

Figure 43: ΔV dependence on emitter concentration.

Figure 44 shows the *IV* curves resulting from changing the doping in the collector side.

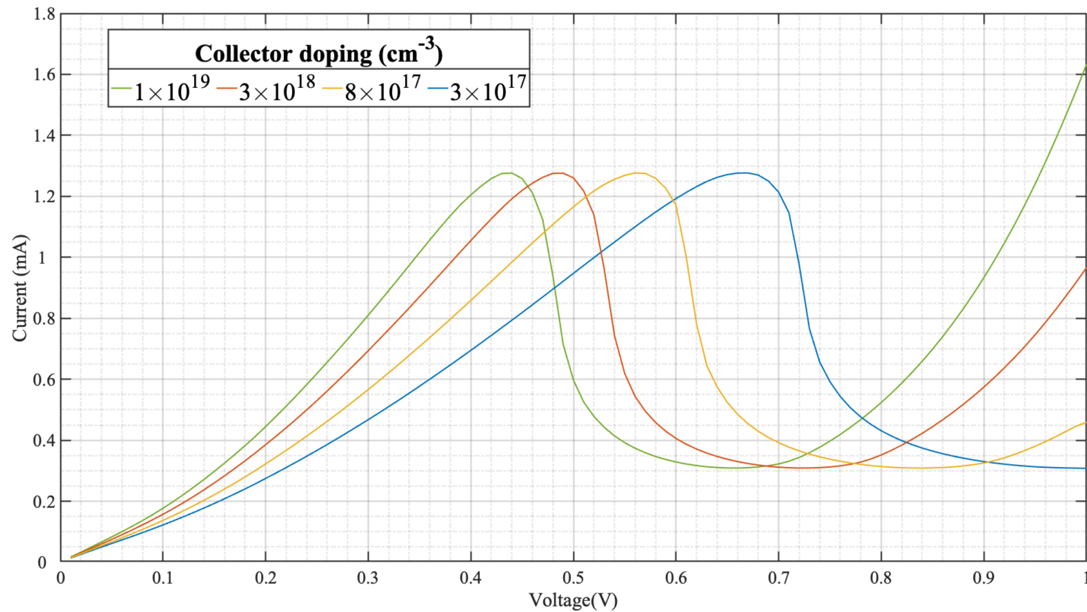

Figure 44: IV curves for changing the collector doping for GaAs/AlAs structure.

This case resembles the change in concentration in the collector region. Notice, as before, the peak is shifting to lower voltages and the width of the resonance seems to increase at lower concentrations. This increase in width can be looked at from different perspectives. Energy Eigenstates that are further away from the edge of the conduction band tend to have broader resonances. This is because of the lower confinement effect as you go up in energy. This is particularly true for barriers which are not too long. As highlighted previously, the built-in potential due to the concentration gradient between the emitter and collector will lower the energy Eigenstates inside the quantum well, hence making them more confined and sharper. From the *IVs* it is noticed that the peak occurs at a potential that is superior to the *2DEG* potential. This means that the less the doping concentration the higher the resonance width due to the saturation of the *2DEG*. To make this point clearer examine the shape of the first positive differential conductance (*PDR*) in each case. Notice that as the built-in potential increases, the rise in the *PDR* becomes sharper and follows a more linear fashion than an exponential one. This is a signature of the fact that the first Eigenstate (at higher doping levels) is now closer to the Fermi-energy. This translates to a transmission probability function that goes faster to the peak. This sharp rise to the peak is also a signature of better conductivity.

Since the resonance width is inversely proportional to the tunneling time [107], it is expected that the speed of operation of the device is enhanced, when the collector is not highly doped.

Since there is no change in both the peak and valley currents, the peak to valley current ratio remains unchanged and so does ΔI. As for ΔV, the main components that affect it are the shift in the peak voltage to lower values and the accompanying shift of the valley voltage also to lower values. Figure 45 shows a plot of ΔV as function of doping concentration for the collector. Notice that ΔV seems to decrease. This points to the fact that the valley voltage decreases more than the peak. This effect can be explained by the discharge happening in the quantum well at the peak. Recall that the quantum well starts to release charge at the *NDR* making it less conductive. This enhances the potential drop across the *DBQW* and eventually only affects the location of the valley voltage.

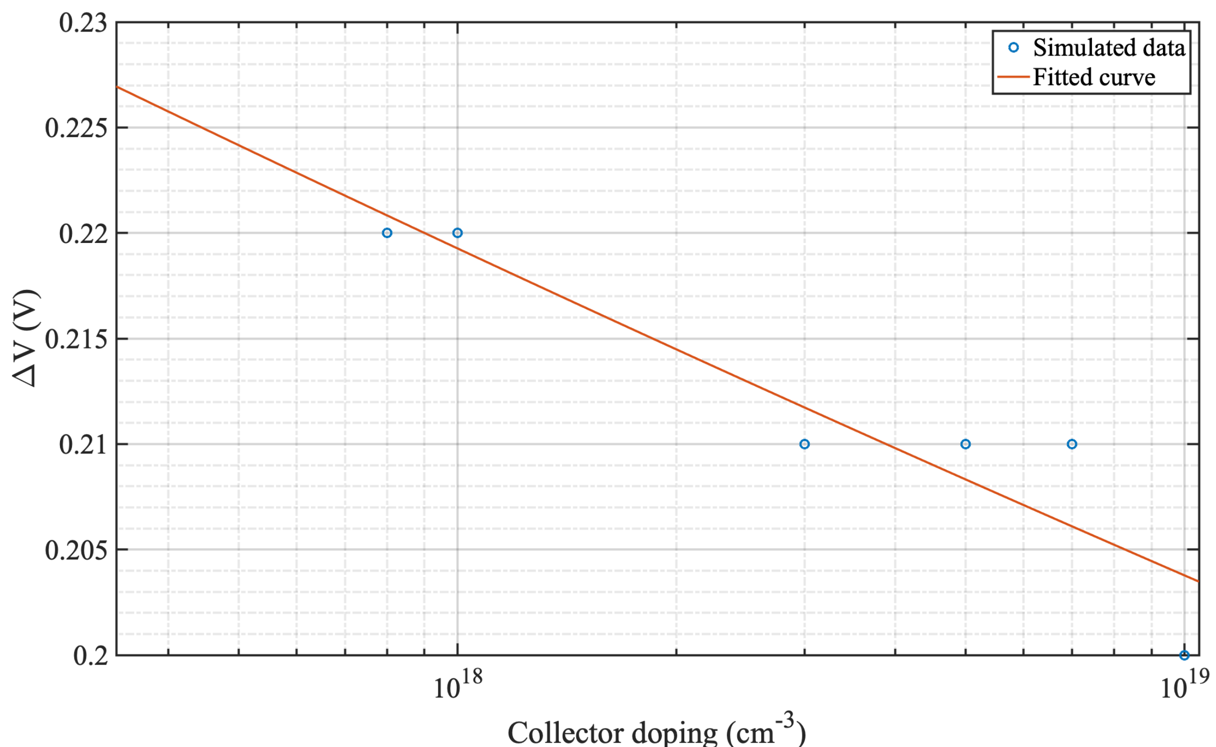

Figure 45: ΔV dependence on the collector doping level.

3.3.8 The effect of the double barrier quantum well

Figures (Figure 46 to Figure 49) show the output results of simulations for symmetrical barriers ranging from 0.7 nm up to 5 nm for reverse and forward bias cases. Due to the scale difference in the current each bias simulation result was split into two: from 0.7 nm to 2 nm

and from 3.5 nm to 5 nm. The reverse bias cases are shown in Figure 46 and Figure 47. The forward bias cases are portrayed in Figure 48 and Figure 49.

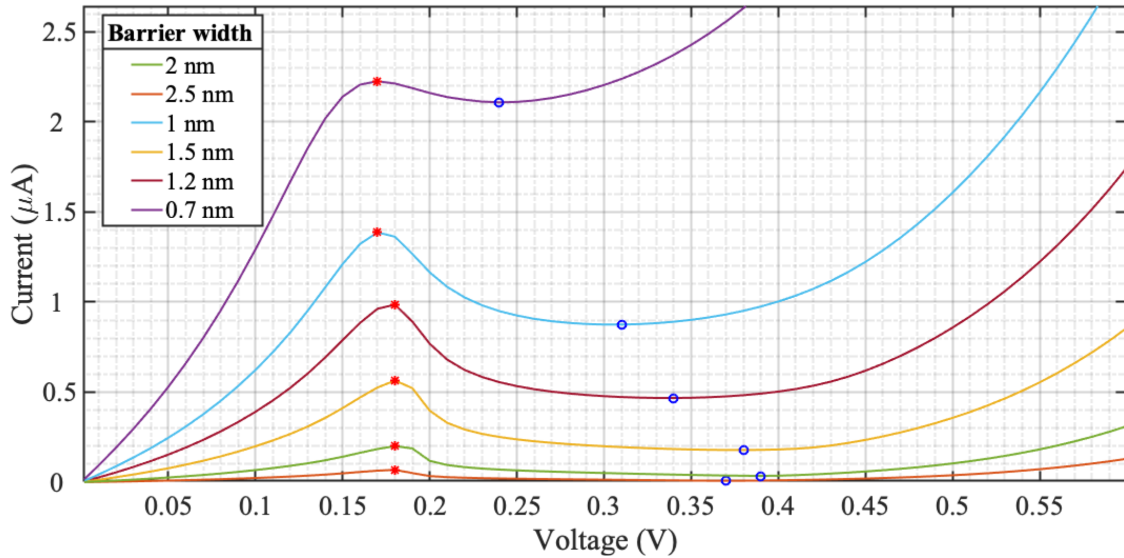

Figure 46: IV curves for various barrier widths (reverse bias case).

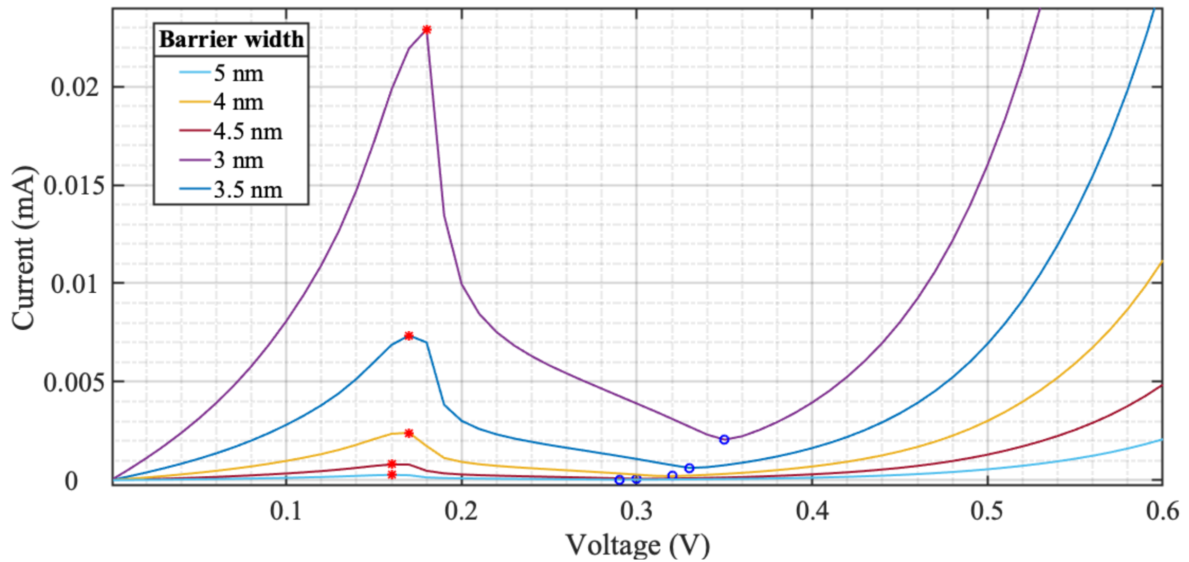

Figure 47: IV curves for various barrier widths (reverse bias case).

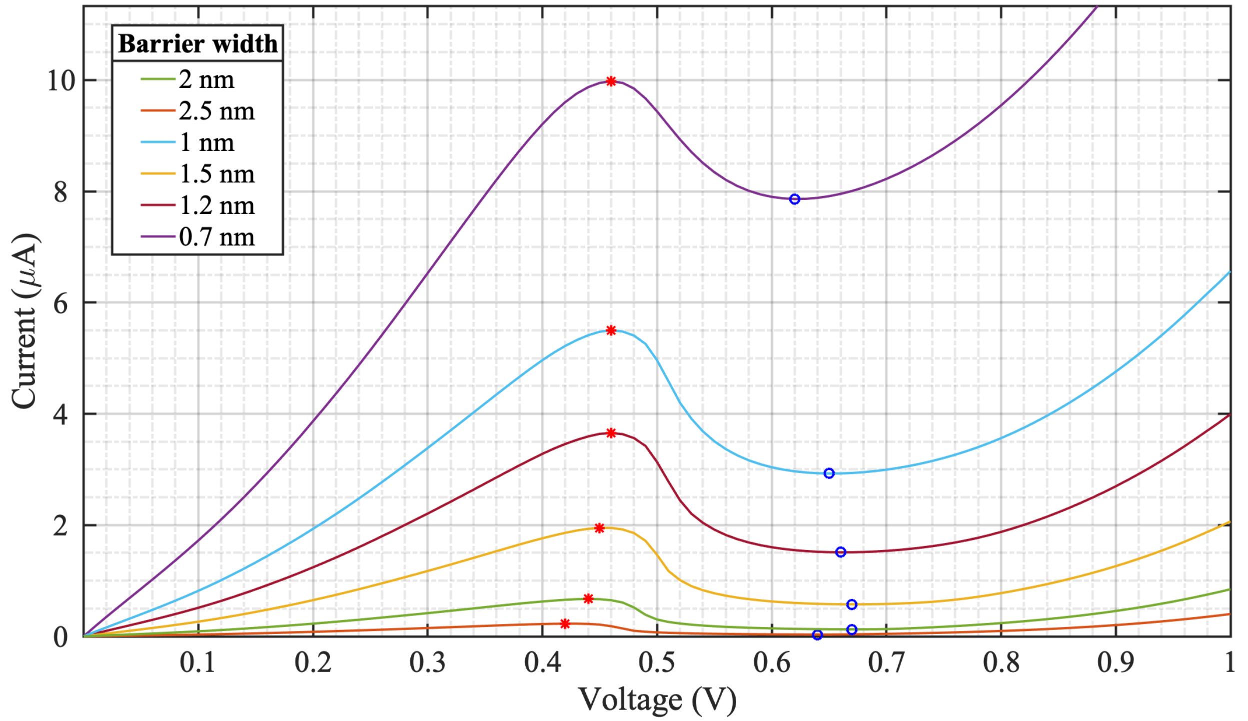

Figure 48: IV curves for various barrier widths (forward bias case).

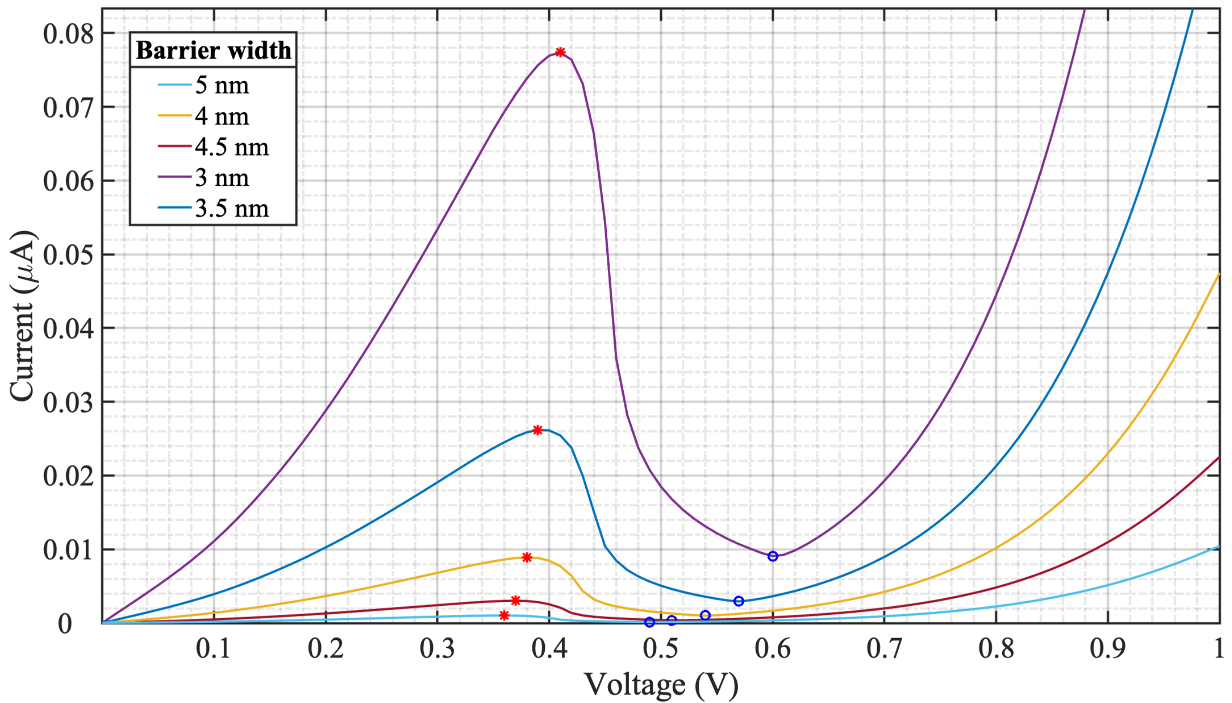

Figure 49: IV curves for various barrier widths (forward bias case).

It can be seen that increasing the width of the barriers reduces the overall peak and valley currents in both bias directions. This is expected as the tunneling probability decays exponentially with the barrier width. However, the decrease in valley current is greater than that of the peak current which produces a lower ΔI and a higher *PVCR*. It is interesting to see

that the peak and valley currents tend to reach the maximum at a value which is around 3.5 nm in this case (recall the studies are about symmetric barriers). These results are illustrated in figures (Figure 50 to Figure 52). (*FB* then *RB*)

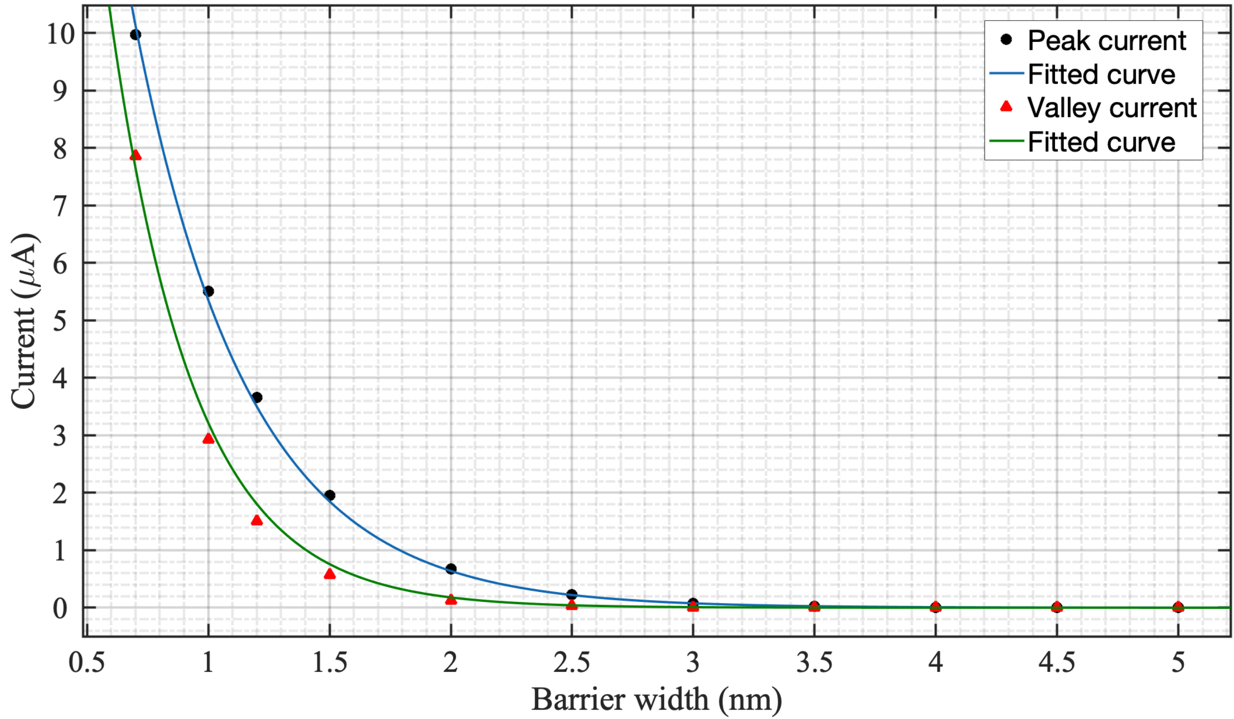

Figure 50: Peak and valley currents dependence on barrier widths (forward bias case).

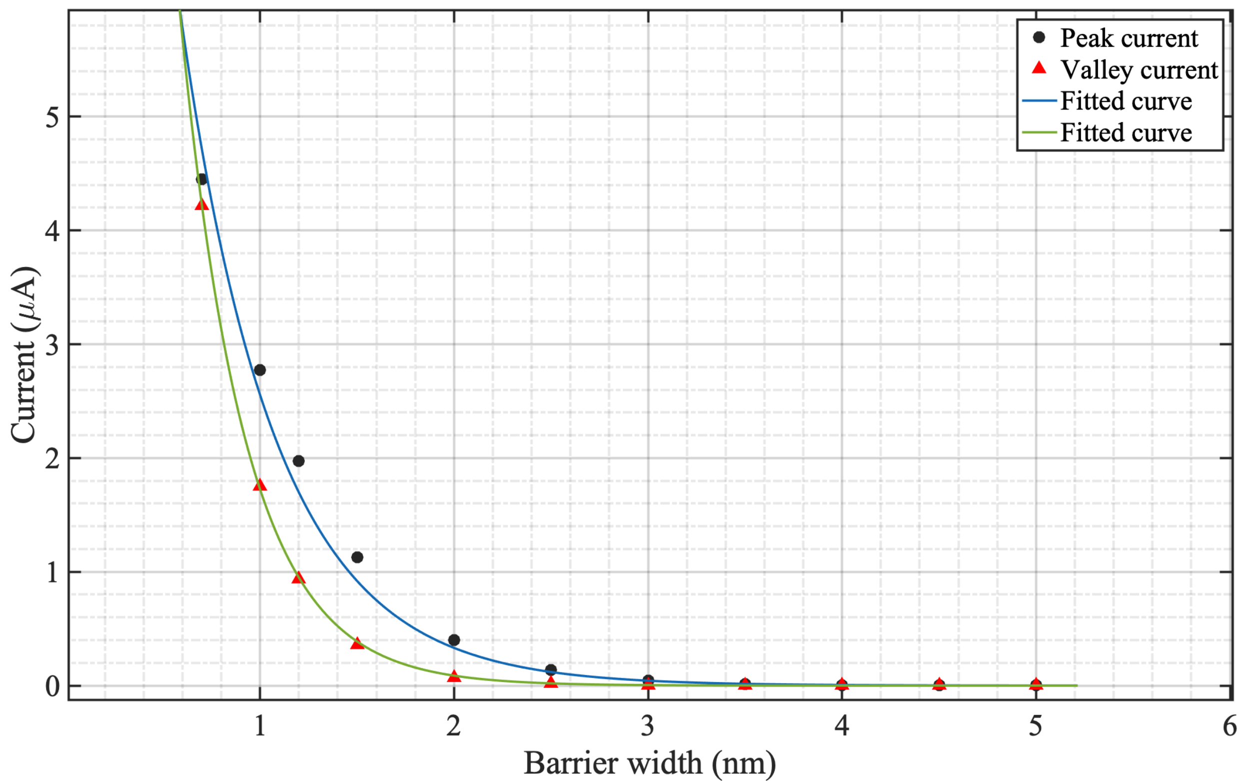

Figure 51: Peak and valley currents dependence on barrier widths (reverse bias case).

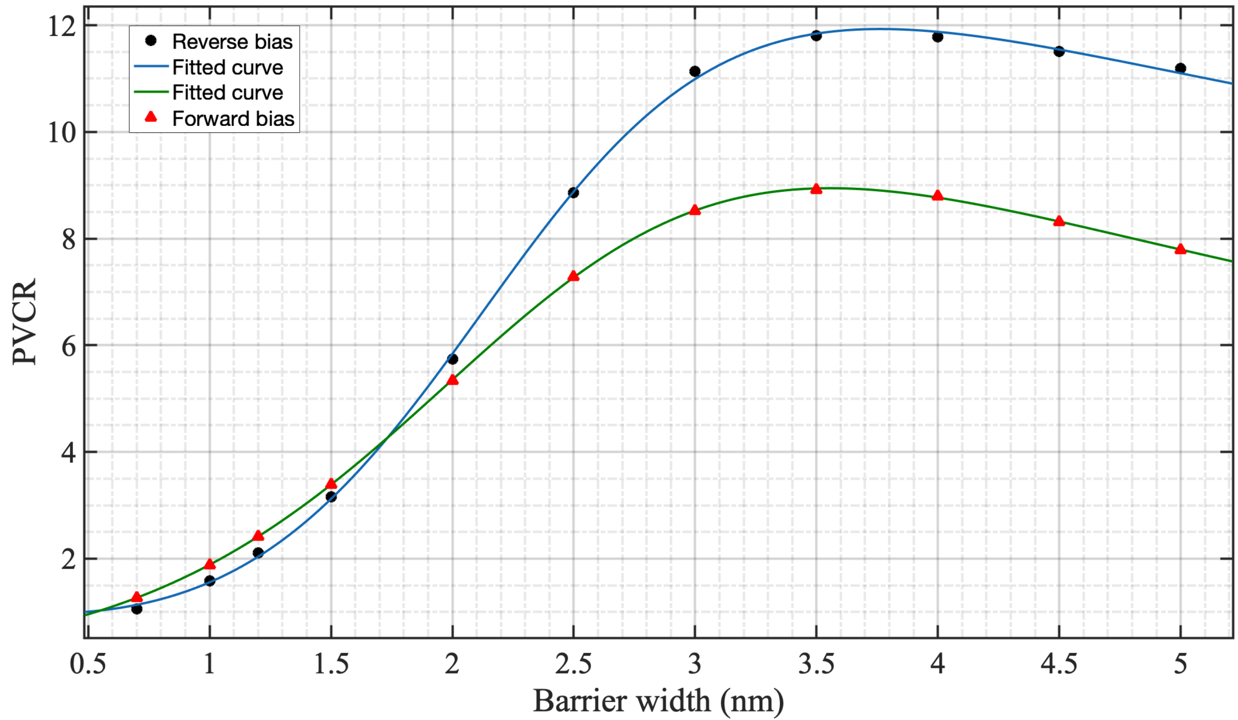

Figure 52: PVCR dependence on barrier widths.

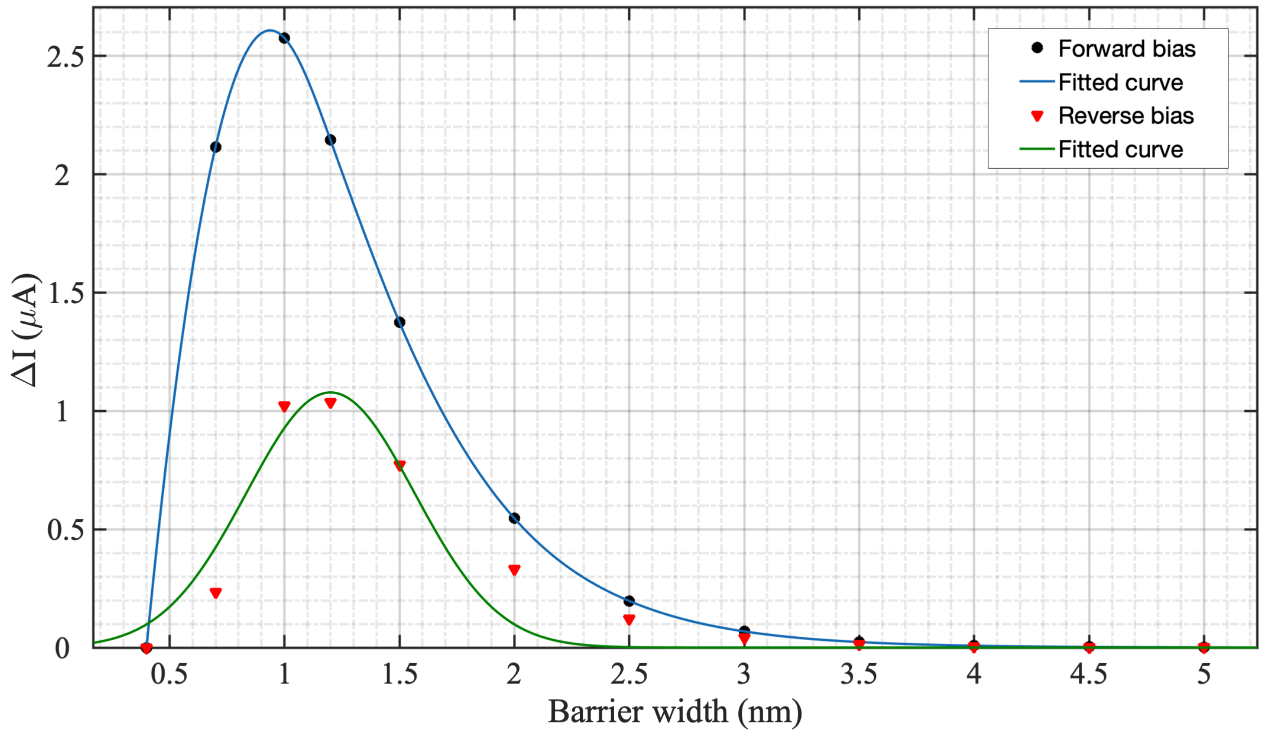

Figure 53: ΔI dependence on barrier width.

The total voltage span (ΔV) is seen to increase with an increasing barrier thickness up to a certain level after which ΔV exhibits a decreasing behavior. Remark that for low barrier widths the tunneling rate from the double barrier structure is greater, giving rise to higher

current. A high tunneling rate means that a lower number of charges is being stored in the quantum well thereby increasing the potential drop across the quantum well. Doing so will shift the peak and valley voltage points to lower values. Increasing the barrier width will have the effect of accumulating more charges inside the quantum well enhancing its conductivity and increasing, thereby, ΔV. After a certain width the carriers inside the quantum well will reach their maximum concentration (which is governed by the density of states in the quantum well). At that point increasing the barrier width further tends to increase the escape rate of the carriers out of the quantum well making the valley voltage shift to a lower value and hence decreasing ΔV.

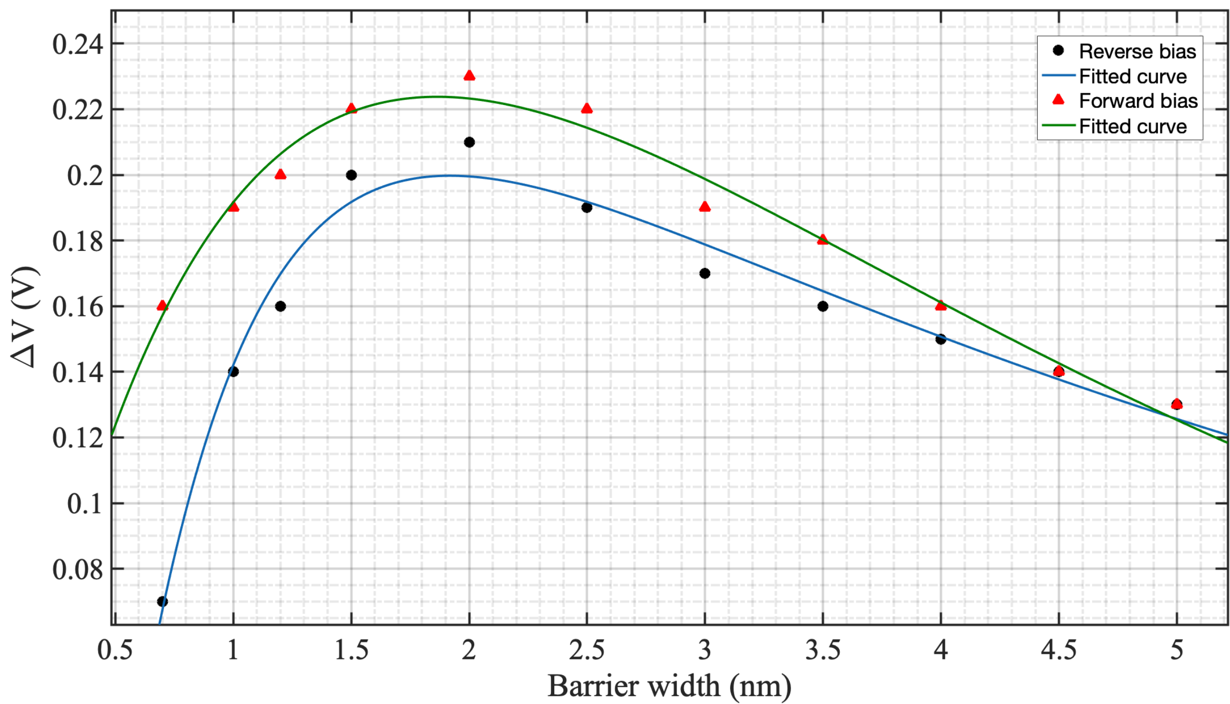

Figure 54: ΔV dependence on barrier width.

From Figure 54 the maximum output *RF* power from the *RTD* can be maximized when $\Delta V \Delta I$ is maximum, which happens at a barrier width of around 1.3 nm. Figure 55 shows a plot of $\Delta V \Delta I$.

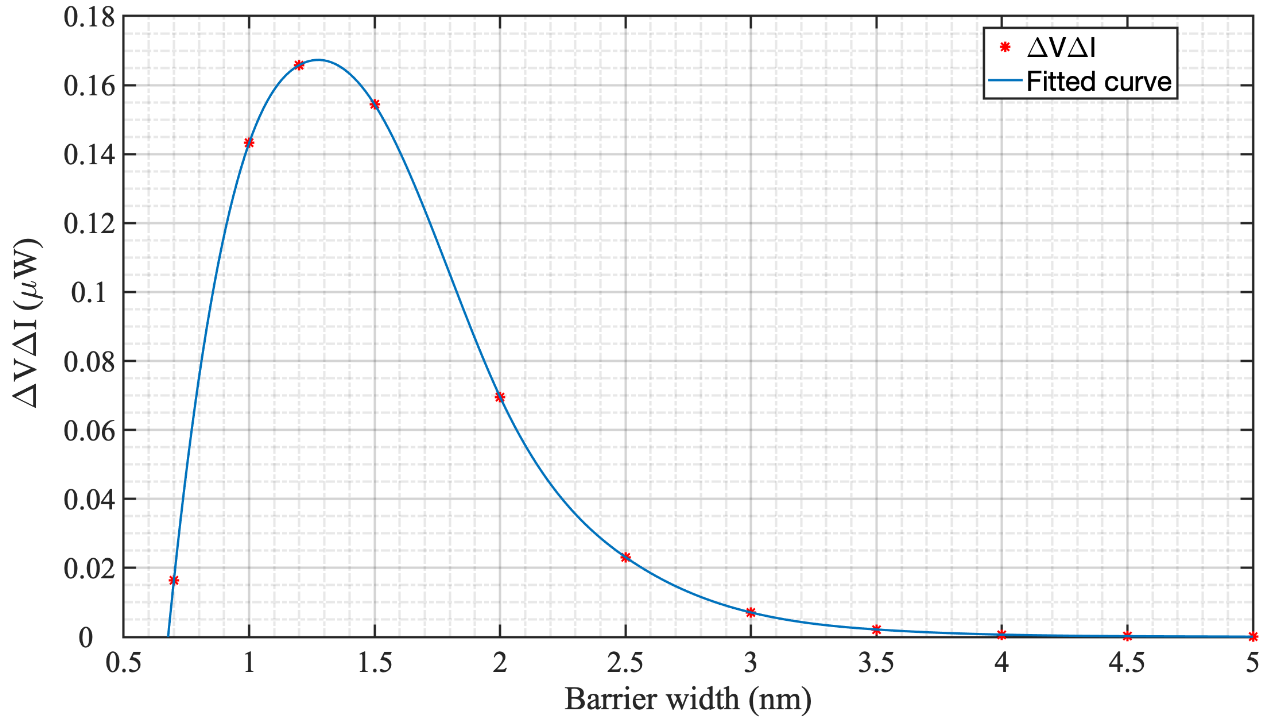

Figure 55: optimizing ΔVΔI for various barrier widths.

Finally, the increase in the width of the well tends to lower all three metrics at the same time (*PVCR*, ΔV and ΔI). As stated, a wider well produces lower Eigenstates, this has the effect of reducing the peak current for the first Eigenstate. It also means that the first Eigenstate will be showing at a lower potential. This leads to less charge accumulation at the emitter's side and hence higher potential drop across the quantum well leading to the lowering of the Eigenstate below the conduction band edge faster and thereby decreasing ΔV. The results suggest that the best *PVCR* occurs at a well-width of around 6 nm and its dependence on the well width has a Gaussian shape to it. The relationship can be modeled in accordance with (*3-47*), to which the peak occurs at 5.7 nm. The results are clearly observable in Figure 56 to Figure 58.

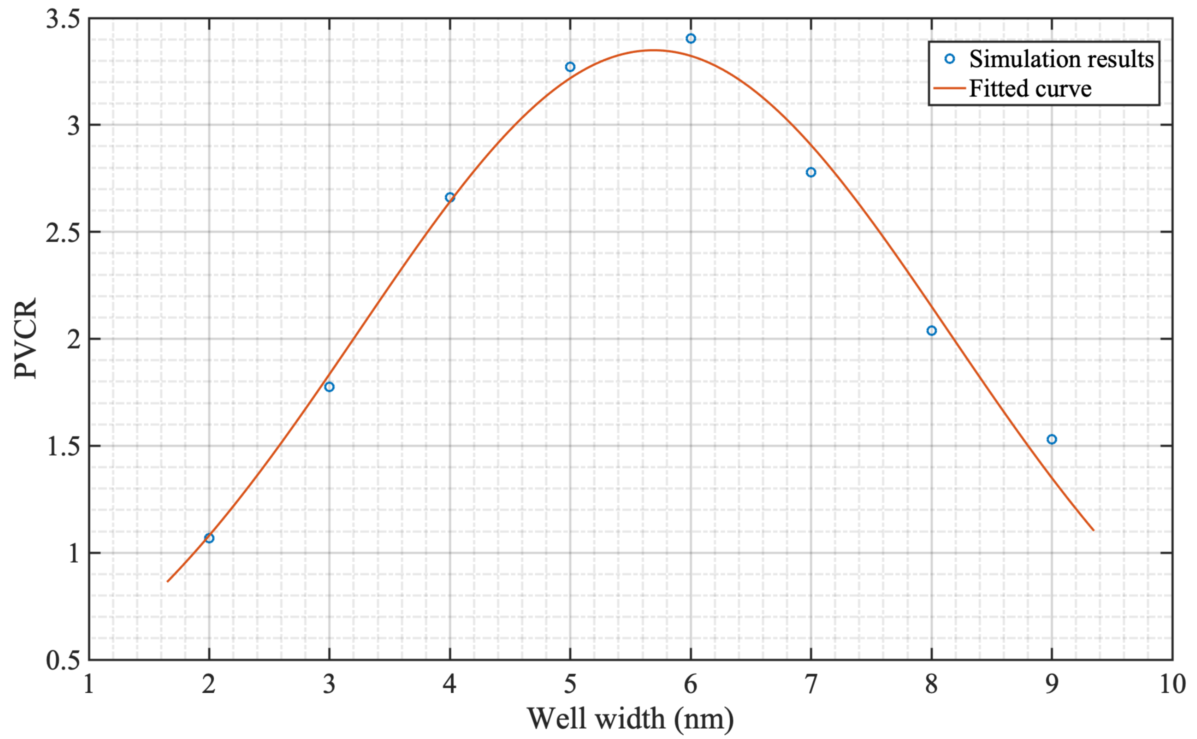

Figure 56: PVCR dependence on the width of the quantum well.

$$PVCR\ (\mathrm{w}) = 3.35\mathrm{e}^{-\left(\frac{\mathrm{w}-5.7}{3.47}\right)} \tag{3-47}$$

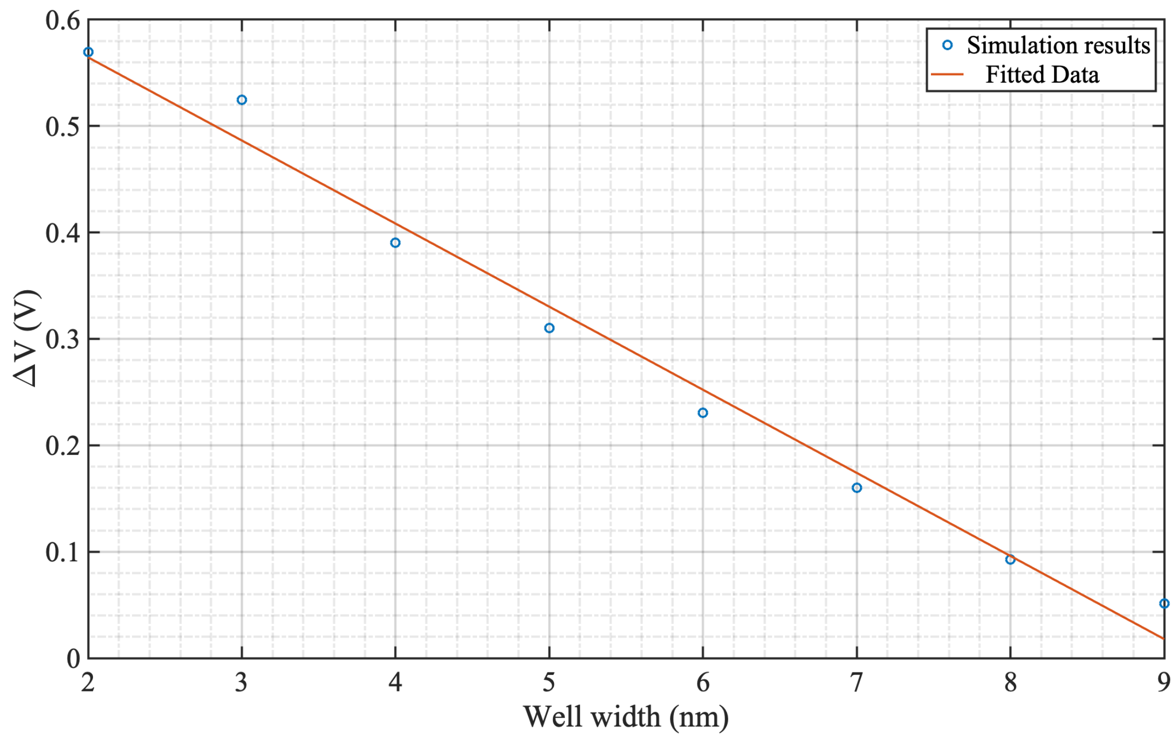

Figure 57: ΔV dependence on the width of the quantum well.

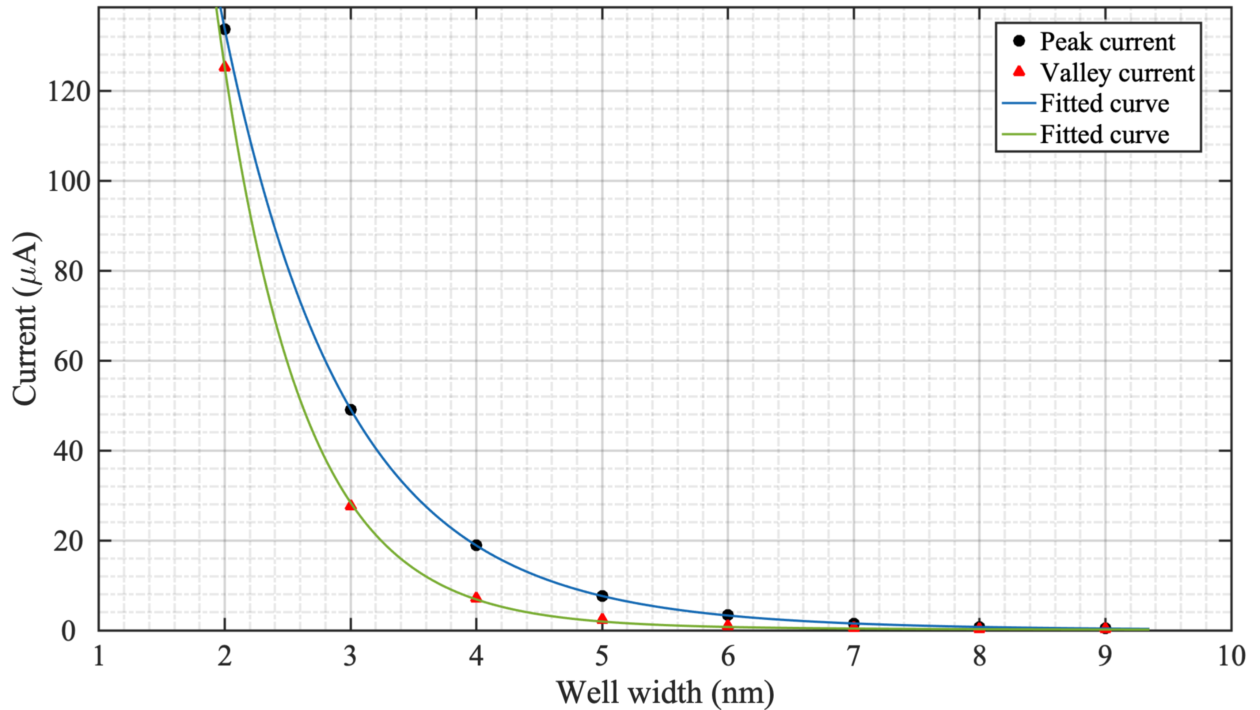

Figure 58: Peak and valley current dependence on well width.

3.4 Summary and conclusion

In this chapter we have introduced the simulation package Silvaco ATLAS and how it can be used to simulate resonant tunnelling diodes (*RTD*) using the non-equilibrium Greens functions formalism. The simulator was used to conduct a series of single factorial studies that showed the dependence of the *RTD* output parameters (peak voltage, peak-to-valley current ratio (*PVCR*), ΔV, and ΔI) on its structural parameters, namely the doping levels in the emitter and collector, their lengths, and the design of the quantum well itself. It was found that due to charge accumulation at the emitter side it gets screened with a screening length that is proportional to the Thomas-Fermi screening length resulting from the 2-dimensional electron gas (*2DEG*). The collector shows a depletion region that is proportional to the Debye length and is much longer than that of the emitter. The results of these studies were modelled mathematically based on these physical interpretations. Two main material systems were simulated, one using *InGaAs/InP* and another using *GaAs* with the aim of testing the fidelity of the simulator under various material systems and to compare the simulations with results from the literature.

Chapter 4 : Resonant tunnelling diode photodetector design considerations

4.1 Introduction

This chapter discusses the physical design rules of *RTD*-based photodetectors (*RTD-PD*). We approach this by highlighting the best design criteria for a given application of the *RTD-PD*, specifically: high-speed and high responsivity applications. We start by introducing the background required for light interaction with matter, then study the physics behind the operation of photoconductors and *PIN*-photodiodes. This will be essential to the understanding of the operation of *RTD-PD*s. Afterward, we go through the various topologies available for *RTD-PD*s, and how to calculate the proper doping concentrations and absorption lengths to optimize the *RTD-PD* for speed or responsivity. The chapter concludes by demonstrating the two main schemes for an *RTD-PD*: either *n-i-n* or *p-i-n*.

4.2 Light interaction with a semiconductor

It is important here to know what happens to a light beam that is incident on a piece of semiconductor in terms of reflections and penetration depth in order to get a feel on the basic physics involved in the operation of a photodetector. The details here will not be thorough, the interested reader is pointed to [81] [108] for more information. In this work we will only be addressing absorption resulting from the direct transition of electrons from the valence band to the conduction band.

When a photon with sufficient energy, (higher than that of the semiconductor's bandgap), is incident on a semiconductor, the semiconductor absorbs the photons' energy and generates electron/hole pairs. Therefore, for a semiconductor to absorb light energy, there has to be an electron in the valence band and an empty state in the conduction band such that the photon energy equals (at least) the energy between these two energy states. The reverse is also required for the material to emit a photon; that is, there must be an empty state in the valence band with an electron in the conduction band. The states available for

such transitions are mathematically modeled using the optical joint density of states function as in (4-1) [81]

$$\rho_{\text{optical}}(\nu) = \frac{(2\mathrm{m_r})^{\frac{3}{2}}.(h\nu - Eg)^{0.5}}{\pi\hbar^2} \tag{4-1}$$

where m_r is given by the sum of the effective masses of the electrons (m_e) and the holes (m_h) as in (*4-2*). h and $\hbar$ are Plank's constant and the reduced Plank's constant respectively, ν the frequency, and E_g the bandgap.

$$\frac{1}{m_r} = \frac{1}{m_e} + \frac{1}{m_h} \tag{4-2}$$

The probability of absorption and emission can be modeled as well using (4-3) and (4-4)

$$\mathrm{P_a} = \mathcal{F}_\mathrm{v}(1 - \mathcal{F}_\mathrm{c}) \tag{4-3}$$

$$\mathrm{P_e} = \mathcal{F}_\mathrm{c}(1 - \mathcal{F}_\mathrm{v}) \tag{4-4}$$

where P_a and P_e are the probabilities of absorption and emission respectively, $\mathcal{F}$v and $\mathcal{F}$c are the probability of finding an electron in the valence band and conduction band respectively given by (*4-5*) and (*4-6*) where E_f is the Fermi-energy, *k* the Boltzmann constant and *T* the temperature in kelvin.

$$\mathcal{F}_\mathrm{c}(\mathrm{E}) = \frac{1}{1 + \mathrm{e}^{\frac{\mathrm{E}-\mathrm{E_f}}{kT}}} \tag{4-5}$$

$$\mathcal{F}_\mathrm{v}(\mathrm{E}) = \frac{1}{1 + \mathrm{e}^{\frac{\mathrm{E_f}-\mathrm{E}}{kT}}} \tag{4-6}$$

At thermal equilibrium conditions, the probability of emission is very small (nearly zero), but the probability of absorption is high. This can be shown using (*4-4*) and assuming the Boltzmann approximation and thermal equilibrium conditions (i.e., there is one Fermi level) then the probability of emission would be:

$$\mathrm{P_e} \approx \mathrm{e}^{\frac{-\mathrm{h\nu}}{\mathrm{kT}}}. \tag{4-7}$$

If we plugin typical numbers of $In_{53}Ga_{47}As$, we see that it is indeed a small number (of the order of 10^{-14}). This situation can be reversed in quasi-equilibrium when the semiconductor becomes biased (we now have two quasi-Fermi levels one for the conduction band and another for the valence band), as this has the effect of introducing a second term to (*4-7*) that resembles the applied bias.

$$\mathrm{P_e} \approx \mathrm{e}^{\frac{-\mathrm{h\nu}}{\mathrm{kT}}} \times \mathrm{e}^{\frac{\mathrm{E_{fc}}-E_{fv}}{kT}} \tag{4-8}$$

The condition that must be satisfied for a semiconductor to emit light can be deduced from (4-9),

$$P_e > \mathrm{P_a} \tag{4-9}$$

which results in the condition stated in (4-10)

$$\mathrm{E_{fc}} - \mathrm{E_{fv}} > \mathrm{E_g} \tag{4-10}$$

This means that for a semiconductor to emit light, the difference between the quasi-fermi potentials (E_{fv} and E_{fc}) has to be greater than the bandgap. This condition is analogous to the population inversion condition required in atomic systems. As long as (4-10) is not satisfied, then the material will be absorbing light.

Our aim now is to derive an expression for the intensity of the propagating beam inside the semiconductor such that we can determine the depth of absorption (i.e., the depth after which the beam intensity is small and no electron/hole carriers can be generated).

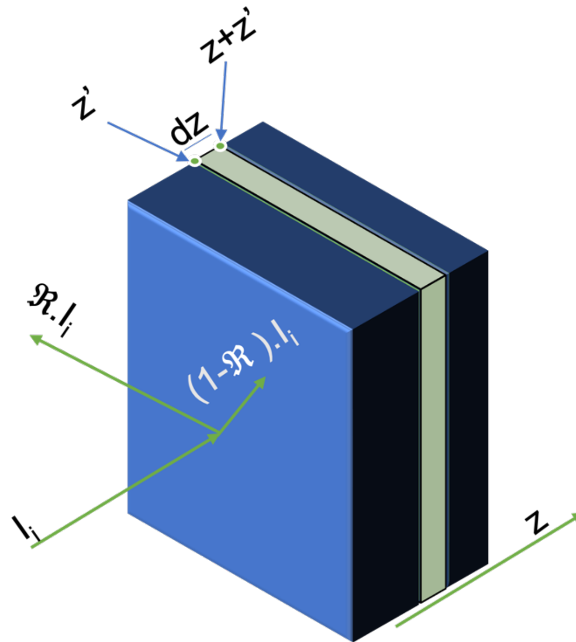

Figure 59: Light beam interaction with a semiconductor.

If we consider a beam of light with intensity I_i that is incident on a piece of semiconductor (Figure 59), then the reflected beam is described by the reflectivity times the incident beam:

$$I_{ref} = I_i \Re \tag{4-11}$$

where $\Re$ is the reflectivity. The remaining beam is transmitted through to the semiconductor.

$$I_{tran} = I_i(1 - \Re). \tag{4-12}$$

When a semiconductor is absorbing or emitting light, it does so at particular rates known as the rates of absorption (η_{ab}) and rates of emission. The latter could be due to spontaneous or stimulated emissions (η_{sp} and η_{st} respectively). As for absorption, η_{ab} is directly proportional to both $\rho_{optical}$, P_a, and to the power density of the incident beam (U), with the proportionality constant B given by (4-13).

$$\eta_{ab} = B\rho(\nu)P_a(\nu)U \tag{4-13}$$

B can be calculated using the relationship in (4-14) with A being related to the radiative recombination lifetime ($\tau_{radiative}$). Both A and B are known as the Einstein coefficients.

$$\frac{A}{B} = \frac{8\pi h\nu^3}{\left(\frac{c}{n}\right)^3} \tag{4-14}$$

$$A = \frac{1}{\tau_{radiative}} \tag{4-15}$$

Similarly, the rates of spontaneous and stimulated emissions are given by (4-16) and (4-17)

$$\eta_{st} = B\rho_{optical}(\nu)P_e(\nu)U \tag{4-16}$$

$$\eta_{sp} = A\rho_{optical}(\nu)P_e(\nu) \tag{4-17}$$

The energy per unit time gained by the semiconductor from the incident beam (i.e., the energy lost by the beam) is then given by (4-18)

$$E_G = h\nu(\eta_{st} - \eta_{ab}).Area.dz \tag{4-18}$$

where dz, is the infinitesimal unit width as shown in the figure above. This energy is equal to the intensity of the beam at point (z'+dz) minus the intensity at the point (z').

$$E_G = Area.(I_{tran}(z' + dz) - I_{tran}(z')) \tag{4-19}$$

The energy density of the incident beam (U) is given by (4-20)

$$U = \frac{I(z)}{volume} \tag{4-20}$$

By equating equations (*4-18*) and (*4-19*) and substituting the values for U, η_{st} and η_{ab} we get an expression for the intensity of the beam as function of penetration depth,

$$I(z) = I_{trans}e^{\gamma d} \tag{4-21}$$

where γ is called the gain coefficient and is given by (*4-22*)

$$\gamma = \frac{\left(\frac{c}{n}\right)^2 (m_r^{\frac{3}{2}} \left(h\nu - E_g\right) P_g(\nu))}{8\pi^2 \nu^2 \tau_{radiative}} \tag{4-22}$$

$P_g(\nu)$ is the difference between the probability of absorption and emission and known as the Fermi-inversion factor.

$$P_g(\nu) = P_e(\nu) - P_a(\nu) \tag{4-23}$$

m_r is the effective mass of the carriers which is given by (*4-24*), with m_e and m_h are the effective masses of electrons and holes respectively. And τ is the minority carrier lifetime.

$$\frac{1}{m_r} = \frac{1}{m_e} + \frac{1}{m_h} \tag{4-24}$$

When P_g is negative, the probability of absorption will be greater than that of emission. At this point, γ is called the absorption coefficient and is denoted by α. Therefore, whatever light is absorbed by the material is given by:

$$\mathrm{I(d)} = I_{trans} e^{-\alpha d} \tag{4-25}$$

The penetration depth is defined as the depth after which the beam decays to 1/e of its original value. This happens at a depth (*d*) equal to α^{-1}. It is important to know the absorption coefficient of the material used in order to know the penetration depth, and hence determine the length of the detector accordingly. Sizing the detector to have a length below the absorption depth will lead to loss in quantum efficiency because not all photons (which could generate carriers) will be absorbed by the material. The following shows why this is indeed the case.

The quantum efficiency is given by equation (*4-26*)

$$\eta = \zeta(1 - \Re)(1 - e^{-\alpha d}) \tag{4-26}$$

The term (1- $\Re$) resembles the portion of light that is not reflected, and the term ($1-e^{-\alpha d}$) resembles the portion of the beam which is not lost in the material. ζ is the internal quantum efficiency for a given material. The above equation can be intuitively understood by reasoning that the quantum efficiency is just the internal quantum efficiency multiplied by the transmittance. To maximize the quantum efficiency the product (αd) must be maximized [109].

Quantum efficiency is a measure of the number of electron-hole pairs generated from the absorption of photons. There are two ways in which quantum efficiency is referred to in

literature; either through the internal quantum efficiency (ζ) or the external quantum efficiency (η). Internal quantum efficiency gives the number of generated electron-hole pairs due to the absorption of a single photon; it, therefore, does not take into account photons that get reflected nor does it take absorbance into account. Internal quantum efficiency is a material property that changes according to the semiconductor in question, and relays on the radiative and non-radiative carrier lifetimes as given by (*4-27*).

$$\zeta = \frac{\tau_{\mathrm{non-radiative}}}{\tau_{non-radiateive} + \tau_{\mathrm{radiative}}} \qquad (4\text{-}27)$$

External quantum efficiency takes the above into account and is defined as the number of generated electron-hole pairs per incident photon. From now on, the word quantum efficiency is taken to mean the external quantum efficiency (η) and is given by (*4-26*). It is here where a distinction between the responsivity and quantum efficiency of a photodetector is vital. Quantum efficiency is a physical property of the material however, responsivity does depend on the electric field (bias), device geometry, and carrier lifetime.

Figure 60 shows the dependence of the internal quantum efficiency on wavelength for $In_{53}Ga_{47}As$. At 1.55 μm the quantum efficiency is around 0.7, and at 1.31 μm it is about 0.9 [110].

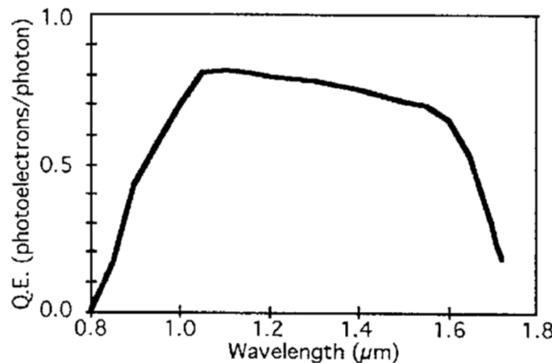

Figure 60: Quantum efficiency of $In_{53}Ga_{47}As$ *vs. wavelength [110].*

4.3 Photoconductors and photoconductive gain

A photoconductor is the simplest form of photodetectors, being a simple slab of semiconducting material between two highly doped contact regions. A graph showing a photoconductor is shown in Figure 61.

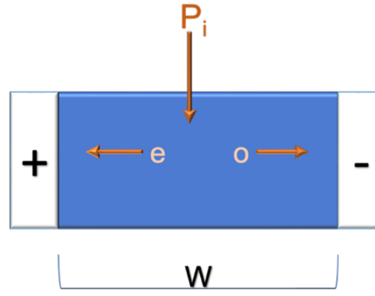

Figure 61: Sketch of photo-generated carriers' movement.

In a photoconductor, the current responsivity (in A/W) depends on the quantum efficiency and on the type of the light beam (continuous wave or modulated signal with various pulse shapes). For now, we would be interested in continuous-wave and sinusoidal-modulated light beams.

For a continuous wave source, the photo current is given by (4-28)

$$J_{photonic} = e.n_{photonic}.v_{drift} \tag{4-28}$$

where $n_{photonic}$ is the excess carrier concentration resulting from the absorption of the light beam and is given by (4-29)

$$\mathrm{n_{photonic}} = P_{light}.\frac{\tau.\eta}{V.h.\nu} \tag{4-29}$$

with (V) being the volume of the absorption region and P_{light} is the power of the incident light beam. The quantity $\frac{P_{light}}{h\nu}$ is known as the photon flux ϕ_{photon}. By substituting (4-29) in (4-28) we get the responsivity given by equation (13) [111]

$$\mathrm{R} = \frac{\eta\lambda}{1.24}\frac{\tau}{t_r} \tag{4-30}$$

where τ is the carrier lifetime (minority carrier lifetime), t_r is the charge carrier transit time, λ is the wavelength in micro-meters and η is the quantum efficiency. The term $\frac{\tau}{t_r}$ is known as the amplification factor or gain. This gain factor is explained using a combination of Ramo-Shockley theorem and the principle of charge neutrality [112], [113].

When an electron/hole pair is generated in a semiconductor - assuming this to happen in the middle of the semiconductor - and there is a sufficient electric field, the electrons will travel at a higher drift velocity than the holes. Meaning that the electrons will reach the collector terminal before the holes do. Once the electron is collected it no longer is part of the semiconductor. Charge neutrality mandates that the number of electrons and holes in a semiconductor remains the same (electrons and holes generate and annihilate in pairs).

Therefore, the power supply will introduce a new electron into the semiconductor, and the process continues until the hole reaches the negative terminal. Accordingly, one incident photon generates multiple electrons, which is why we get the amplification effect. Hence, the responsivity of a photoconductor depends on the device's geometry as well. If we design a photoconductor such that the electrons are generated closer to the collector than the holes are to the emitter, we can increase the amplification and get high responsivity values. However, this comes at the cost of the operating speed (bandwidth), as the bandwidth depends on the transit time of the slowest charge carrier (the hole). The transit time under drift is given by (*4-31*).

$$t_r = \frac{D_{travelled}}{v_{drift}} \tag{4-31}$$

where $D_{travelled}$ is the distance a charge carrier travels, and V_{drift} the drift velocity given by (*4-32*), where $\mu_{carrier}$ being the mobility of the carrier

$$v_{drift} = \mu_{carrier}.E \tag{4-32}$$

Hence for devices that are meant to give very high responsivity values, they should be designed in a way such that the point of charge carrier generation is closer to the collector. The contact material used and its shape do influence the number of electrons emitted and hence this can also be optimized to get better responsivity values [114] [115] [116].

The expression derived for responsivity above has to be taken with caution, as will be apparent in the results presented in chapter 5 since it has some hidden assumptions which are not always present such as the diode being long enough (more than one diffusion length) for recombination to take place, and that the drift time is comparable to the diffusion time in these detectors. Although this is the derivation currently present in literature, it does have some flaws. First, it only accounts for the drift component of the photonic current and does not consider any diffusion-related transport. Furthermore, it uses the carrier lifetime to calculate the excess carrier density while assuming the existence of a sufficient electric field for drift-type transport. This is only true if the device is sufficiently long, such that the drift time is greater than the carrier lifetime, which is not always the case. Adjustments should be made to this derivation for *PIN* photodiodes and *RTD-PD*s to accommodate the effects found in practical devices.

As a final note on the subject, we point the attention to the work of Dan et. al [117] where the authors have argued that the theory of the photoconductive gain does not justify some of the results reported in the literature. To start with, we believe the title of the publication does not give the full story, as it suggests that a photoconductor does not have any gain which is proven to be the case by the authors themselves in their conclusion. Although they state that by "no-gain" they mean "no-high gain" in their abstract, a more careful title should have been used. Furthermore, the conclusion of the authors' is that the gain of a photoconductor is proportional to the ratio of the electron and hole mobilities in a given material. Although this conclusion is true for the work presented, it does not resemble the general case, which is explained by the Shockley-Ramo theorem. In essence, the theory states that the source of gain is due to the difference in the collection time between the hole and the electron. Under the same electric field, the transit time of the charge carriers (electrons and holes) is only influenced by the mobility (*4-32*). This means that the authors' have implicitly assumed that the distance travelled by each carrier is the same. If this assumption is not true, then a more accurate resemblance of the gain would be the ratio of transit times not just the mobility which is in tally with the main theory. Furthermore, the authors' have also made an argument which is not sound when it comes to the continuity equation (equation 5 in the same paper). For the sake of argument, we show this equation in (*4-33*). D_n is the electron diffusion constant, E the electric field, g_n the optical generation rate, μ_e the electron mobility and Δn the number of photo-generated carriers.

$$D_n \frac{\partial^2 \Delta n}{\partial x^2} + \mu_e E \frac{\partial \Delta n}{\partial x} + \mu_e \Delta n \frac{\partial E}{\partial x} - \frac{\Delta n}{\tau_n} + g_n = 0 \qquad (4\text{-}33)$$

The authors argue that, under a uniform electric field the third term vanishes and for the first and second terms to vanish Δn must be uniform as well. In this case (*4-33*) is satisfied, and the typical results of the generation rate equaling the recombination rate occurs as in (*4-34*).

$$g_n = \frac{\Delta n}{\tau_n} \qquad (4\text{-}34)$$

The problem is with the second argument; that the equation is satisfied if and only if Δn is uniform. Equation (*4-33*) is also satisfied if the sum of the first two terms is zero also. If we apply this condition, we will have a second order differential equation which can be solved assuming an exponential solution for Δn.

$$D_n \frac{\partial^2 \Delta n}{\partial x^2} = -\mu_e E \frac{\partial \Delta n}{\partial x} \qquad (4\text{-}35)$$

Assuming Δn to have an exponential solution of the form given by (*4-36*), with α being the absorption coefficient, we find that the condition in (*4-37*) satisfies the continuity equation and yields the same results.

$$\Delta n(x) = n_0 e^{-\alpha x} \qquad (4\text{-}36)$$

$$\frac{D_n}{\mu_n} = \frac{E}{\alpha} \qquad (4\text{-}37)$$

The final conclusions and results by the authors are indeed true for the assumptions and special cases they studied, but we do not see them to disagree with the original theory as the authors have stated. More on this issue will come at later sections.

4.3.1 Conductivity (σ)

The conductivity of a semiconductor is given by (*4-38*) and the change in conductivity (*Δσ*) by (*4-39*)

$$\sigma = ne\mu \qquad (4\text{-}38)$$

$$\Delta\sigma = \Delta n.e.\mu + \Delta\mu.n.e \qquad (4\text{-}39)$$

where n is the number of charge carriers, μ is the charge carrier mobility, and e being the electron charge. The charge carrier's mobility changes with carrier concentration, due to the dependence on both the effective mass (m^*) and the carrier relaxation time as seen by (*4-40*). Since the effective mass only changes for very high carrier concentrations, we will consider it to be constant. The only physical variable that changes in mobility is the relaxation time ($\tau_{relaxation}$), which goes down as more carriers are present. It is therefore expected that the mobility will decrease with an increase in carrier concentration.

$$\mu = \frac{e\tau_{relaxation}}{m^*} \qquad (4\text{-}40)$$

The intrinsic carrier concentration for $In_{53}Ga_{47}As$ is $6.3 \times 10^{11} cm^{-3}$ [118] [74], Figure 62 shows the dependence of electron mobility on carrier concentration at 300K, and Figure 63 shows the hole mobility as function of carrier concentration also at 300K.

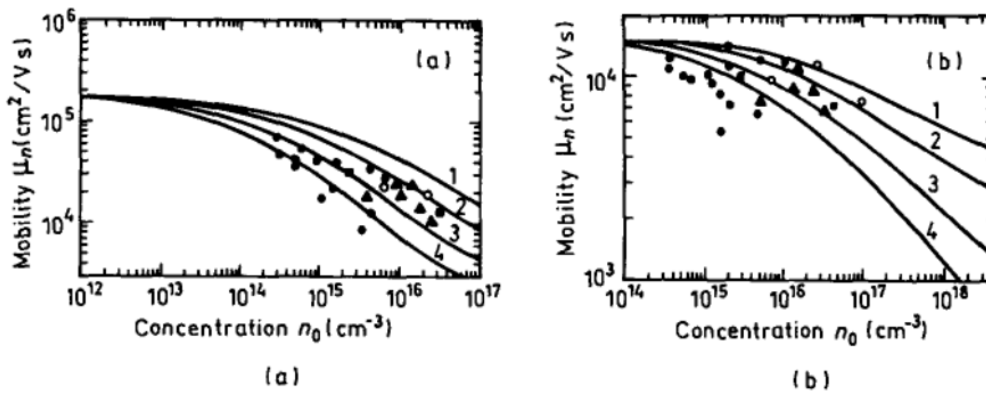

Figure 62: Electron mobility dependence on carrier concentration for $In_{53}Ga_{47}As$ at 77 K (a) and 300 K (b) for different compensation ratios $\theta = (N_D + N_A)/n$. 1. $\theta = 1$, 2. $\theta = 2$, 3. $\theta = 5$, 4. $\theta = 10$. *[119].*

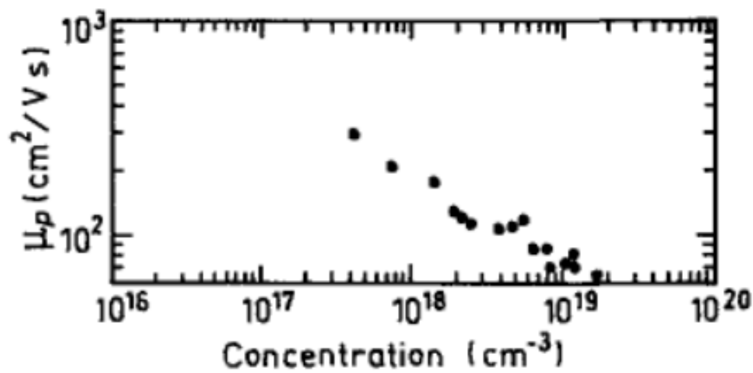

Figure 63: Hole mobility dependence on carrier concentration [119].

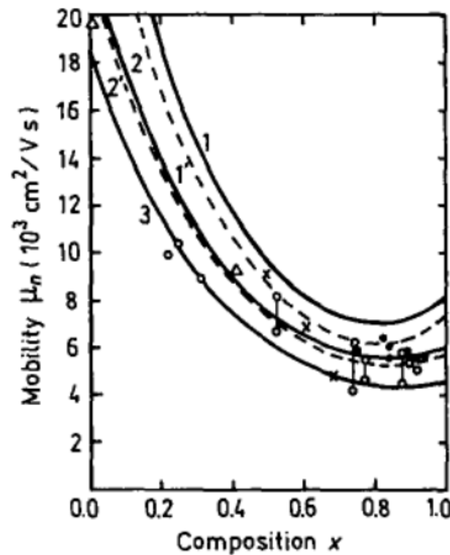

Figure 64: Electron mobility for In(x)Ga(1-x)As as function of composition. Electron drift (dashed curves) and Hall (solid curves) mobility versus composition parameter (x) at 300 K. 1, 1'. $n = 3\times10^{15}$ cm^{-3}, 2, 2'. $n = 4\times10^{16}$ cm^{-3}, 3. $n = 2.3\times10^{17}$ cm^{-3}. For curve 3 clectron Hall and drift mobility values are practically equal. [120].

According to (*4-39*), the change in conductivity is due to both the change in carrier concentration and change in mobility. Since the conductivity of the semiconductor is expected to increase with increasing carrier concentration, this means that the decrease in mobility does not affect the value of conductivity as much as the increase in carrier concentration. It is intuitive to assume that the mobility increases when the "mean free path" of the charge carrier is higher (i.e.: there are less collisions, less scattering events, and hence carriers can move ballistically for longer distances). From a theoretical point of view, and considering only a piece of bulk photoconductor, the generation of new charge carries from light is supposed to increase the carrier concentration thereby it should increase the conductivity. Indeed, that is the case with a regular photoconductor; the increase in conductivity due to excess carriers outweighs the decrease in mobility giving rise to a net increase in conductivity.

4.3.2 Mobility and electric field

In case the mobility was optimized, then the transit time of the charge carriers can be optimized by assuring that the electric field inside the drift region is around the threshold value of 2.5×10^5 V/m, which gives the highest drift velocity value of 2.7×10^7 cm/s, as can be seen in Figure 65.

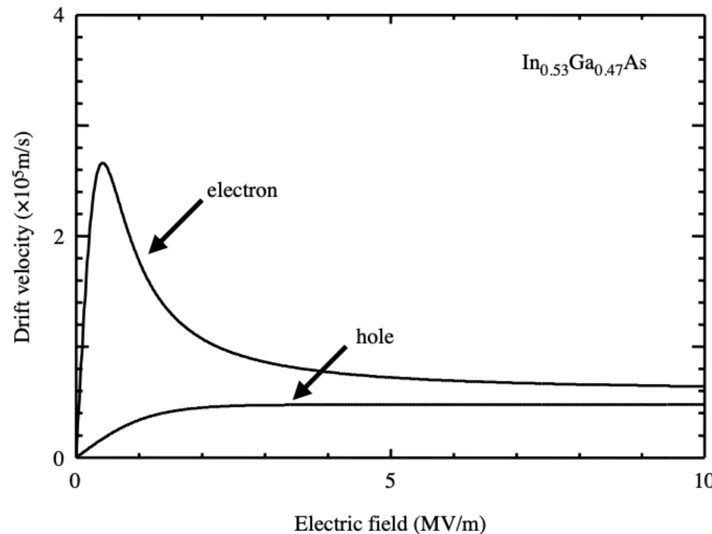

Figure 65: Drift velocity dependence on electric field $In_{53}Ga_{47}As$ *[121].*

4.3.3 Carrier lifetime

The carrier lifetime is extremely important in photoconductors as it controls the photo-current amplification effect normally seen in photoconductors. It is appropriate here to

highlight the dependence of the carrier lifetime on both the temperature and the carrier concentration. If we look at Figure 66, we see that the carrier lifetime decreases with an increase in carrier concentration. It is important here to note that we are interested in the lifetime for minority carriers, so the term carrier lifetime from here forwards implies that of minority carriers.

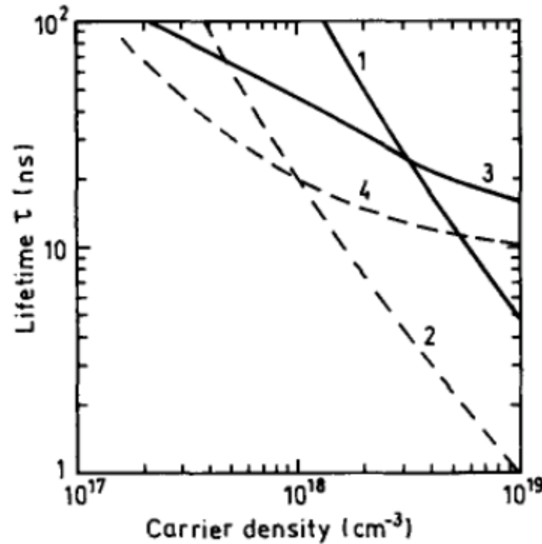

Figure 66: Carrier lifetime dependence on carrier density for $In_{53}Ga_{47}As$ *[122].*

4.3.4 Rise time (carrier transit time, speed of response (BW))

Rise time is basically the impulse response of a photodetector. Meaning the photo current resulting of a very narrow pulse of light. The rise time of a photoconductor is one of the determining factors in the speed of response and hence might be the determining factor for the bandwidth. It is mainly governed by the speed of the slower charge carrier (holes) and of course the geometry of the device. Since some devices can be designed to have the holes travel less distance than the electrons which reduces their transit time. It is important here to emphasize that the speed of a detector is determined by more than one factor, and it will be limited by the one that has the most delay time. These factors are transit time, carrier lifetime, dielectric relaxation time and overall circuit *RC* time constant.

4.3.5 Current responsivity

Photodetectors, in general, give rise to a photocurrent when exposed to light with suitable energy. The amount of photocurrent generated per unit of incident power is known as the current responsivity ($\mathcal{R}$) measured in A/W, referred to from here forward as simply responsivity, and is a metric used to compare various photodetectors. Responsivity is the

amount of charge carriers generated that contribute to the flow of a photo-generated current. This means that any charge carriers that do not produce current (those that recombine) although generated due to light, do not contribute to the responsivity value of the device. Empirically (*4-41*) can be used to determine the current responsivity,

$$\mathcal{R} = \frac{I_{illuminated} - I_{dark}}{P_{optical}} \tag{4-41}$$

Notice that the illuminated current includes the dark current as well, so (*4-41*) can be thought of as the photonic current per unit optical power.

Since carrier generation is the result of light absorption; it is important to study the various semiconductor parameters that depend on the change of charge carrier concentration Δn. The main parameters that get affected by the carrier concentration are: the conductivity σ, the mobility μ, the effective mass m^*, the absorption coefficient (α), the minority carrier lifetime (τ) and the bandgap (E_g) [74]. The effective bandgap could change in the case of a degenerate semiconductor as per Burstein-Moose effect and introduce bandgap narrowing.

4.4 PN-Photodetectors.

A PN junction photodetector is a simple diode in reverse bias conditions as shown in Figure 67

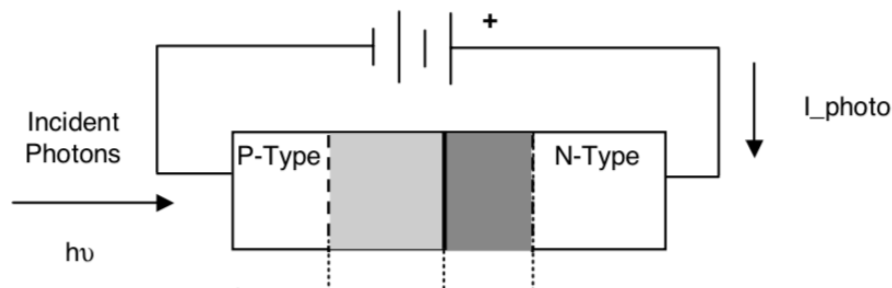

Figure 67: PN-junction photodiode [123].

When a photon is incident on the junction it gets absorbed and electrons move down from the p-region to the n-region. Likewise, holes travel up from the n-region to the p-region, resulting in current flow. The response time for these detectors is usually slow, in the orders of micro-seconds and the responsivity is low. These unwanted characteristics can be explained by photons getting absorbed in the n and p regions and not at the junction. Electrons and holes in these regions move (diffuse) very slowly since the electrical forces there

are weak. This results in a very slow rise time, and low responsivity since the current resulting from these photons is very small [14].

4.5 PIN photodiodes

PIN photodiodes are photodetectors that employ an intrinsic region sandwiched between two heavily doped n and p regions as depicted by Figure 68.

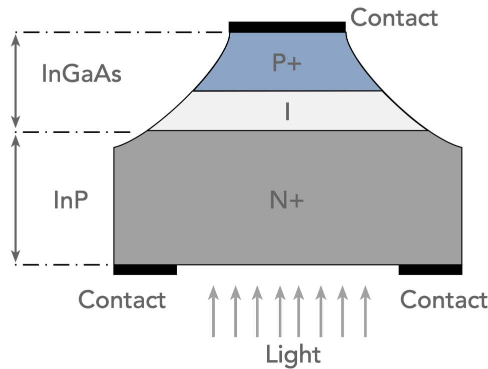

Figure 68 Physical layout of a PIN diode [124].

By introducing an intrinsic layer, the probability of a photon getting absorbed in the p or n regions gets smaller. When reverse biased any electron in the intrinsic region will move to the n region when it absorbs energy. And since the electric field in the intrinsic region is strong, electrons and holes will move faster due to the large electrical forces.

PIN photodiodes are known for their high speed of operation and their constant responsivity values as function of voltage. Based on (*4-30*), the gain in such detectors should be near unity. However, if one takes typical values for $In_{53}Ga_{47}As$ detectors for both lifetime and transit times for devices of 1µm long, it can easily be seen that the gain is much higher than 1 which is not the case practically. The problem here is what has been stated earlier in the derivation of the responsivity formula, that is the assumption that carriers are bound to recombine before being collected which is not the case for *PIN* diodes with electric field values that drive carriers with saturation velocities. Equation (*4-30*) can be adjusted based on the physical interpretation of the gain mechanism; that is gain is present because of the difference in transit speeds between electrons and holes. Since all generated carriers are swept by the field, and their transit times are much less than the typical lifetime for $In_{53}Ga_{47}As$, the actual gain should be given by the ratio of the transit time of the hole to that of the electron.

$$G_{PIN} = \frac{t_{driftHole}}{t_{driftElectron}} \quad (4\text{-}42)$$

This can be interpreted as multiplying the photon flux (ϕ) by the hole drift time instead of the lifetime, as the drift time is the actual time the hole takes to be collected. Since carriers are moving with saturation velocities, electrons, and holes both move with similar velocities as can be seen in Figure 65, thereby explaining the unity gain of *PIN* detectors.

4.6 Resonant tunnelling diode photodetectors

In this section we propose physical rules for designing resonant tunneling diode-based photodetectors. These rules are employed to design two devices based on the $In_{53}Ga_{47}As$ material system, which can theoretically reach speeds of 10 GHz. The designs are then verified using simulations on Silvaco ATLAS. Starting with (*4-26*), the quantum efficiency for a given design length (L_{design}) is given by (*4-43*)

$$\eta = \zeta(1 - \Re)(1 - e^{-\alpha L_{design}}) \quad (4\text{-}43)$$

We see that it is important to determine the maximum design length (L_{design}) required to maximize the quantum efficiency. For a given semiconductor with an absorption coefficient (α), there is an absorption length ($L_{absorption}$) given by (*4-44*), after which the intensity of the incident light beam decays to 36.7% of its initial value [111].

$$L_{absorption} = \alpha^{-1} \quad (4\text{-}44)$$

Hence, for 95% absorption, L_{design} should be around three times the absorption length ($e^{-3} \approx 0.05$) which gives:

$$L_{design} = \frac{3}{\alpha} \quad (4\text{-}45)$$

The location of the absorption region also plays a role in *RTD-PD*s. The three main topologies which an *RTD-PD* can follow are: emitter-based absorption region, collector-based absorption region, and a hybrid absorption topology where both the emitter and collector are light absorption regions. To decide on the best topology for a given application, the main aspects in the physics of *RTDs* should be considered, namely the formation of a two-dimensional electron gas (*2DEG*) at the emitter, and the depletion region at the collector. Due to charge accumulation at the emitter's barrier, the carrier concentration increases substantially there to the point of screening the electric field for most of the emitter's length.

This leaves only a small portion with a considerable electric field, which is characterized by the Thomas-Fermi screening length (L_{TF}) of a *2DEG* given by *(4-46),* and is roughly $3L_{TF}$.

$$L_{TF} = \frac{2\pi\epsilon\hbar^2}{e^2 m^*} \tag{4-46}$$

where ϵ is the dielectric constant of the material, $\hbar$ the reduced Plank's constant, e the electron charge, and m^* the effective mass. For most materials, this length is in the tens of nanometers. Therefore, for high-speed applications placing the absorber at the emitter is detrimental to speed since it is mostly screened and generated carriers will either diffuse out (if there is a concentration gradient), drift slowly under a weak electric field, or recombine. All these processes are slow and affect the speed. Stemming from this point, the highly doped contacts regions are areas where light absorption should be avoided. The contacts should be made from higher bandgap material (higher than the absorption regions) so as to eliminate any charge generation there since the electric field is nearly zero. Conversely, if responsivity is the goal, charge generation in such areas can be beneficial by providing photoconductive gain due to the difference in electron and hole transit times as per the Shockley-Ramo theorem [112].

We now move to the second topology, where the absorption is at the collector. The collector's depletion region is much longer than the one at the emitter and is related to the Debye length (L_{Debye}) given by (*4-47*) as we have shown previously [125],

$$L_{Debye} = \sqrt{\frac{\epsilon kT}{e^2 N_{total}}} \tag{4-47}$$

where k is the Boltzmann constant, T is the temperature in kelvin and, N_{total} is the total doping concentration at the collector. The Debye length can be designed to be longer through doping, thereby attaining a higher electric field for longer absorption lengths. Hence, this topology is optimized for speed.

The last topology is a hybrid approach between the previous two cases. So, when an emitter is longer than $3L_{TF}$ it starts to get screened and provides gain at the expense of speed. If this topology is to be used for high-speed applications, the emitter should be modestly sized to have acceptable diffusion times.

4.6.1 High-speed RTD-PD design considerations

Ideally, we need (at least) a depletion length equal to L_{design} to guarantee fast charge transport. The depletion length is dependent on the collector's doping concentration and is approximately $8L_{Debye}$ [105]. The Debye length can then be linked to the absorption coefficient as in (*4-48*), from which we can calculate the doping in the collector as in (*4-49*).

$$L_{Debye} = \frac{0.375}{\alpha} \tag{4-48}$$

$$N = \epsilon \frac{kT}{e^2 L_{Debye}^2} \tag{4-49}$$

For $In_{53}Ga_{47}As$ the absorption coefficient is around 8500 cm^{-1} [126], [127] resulting in L_{Debye} of 441 nm. Using (*4-49*) we can estimate the required doping level at the collector to be around 1.1×10^{14} cm^{-3}, which is slightly above intrinsic. This yields a value for L_{Design} of 3.5 µm. Practically, this low doping is not readily achievable since there is background doping present in growth chambers. Practically, one can grow $In_{53}Ga_{47}As$ with doping as low as $5\text{x}10^{15}$ cm^{-3} which is an order of magnitude higher than the calculated value. Assuming this doping level ($5\text{x}10^{15}$ cm^{-3}), L_{Debye} goes down to 64 nm shrinking the collector's depletion region, and accordingly L_{Design} as well, by 85% to 500 nm. Therefore, a collector longer than 500 nm will have electric field dead zones, that force diffusion or recombination.

Now we determine the operating electric field required at the operating voltage point, which is usually taken near the peak voltage value (V_p). The peak voltage arises when the Fermi level in the emitter aligns with one of the quantized Eigenstates in the quantum well. Therefore, it is important to determine the location of the quantized Eigenstates, where the particle in a finite potential well problem can be used to calculate the Eigenstates [77]. Recall from the previous chapter that the thicknesses of the emitter (L_e) and collector (L_c) also influence the peak voltage point. Since the effective depleted length of the emitter is usually in the tens of nanometers, its influence is minor. However, the collector's length will have a substantial impact on the peak voltage point. This dependence is described using (*4-50*) and (*4-51*) which we derived based on fitted data from single factorial studies presented in chapter 3 [125]

$$V_p(L_c) = V_s - Ce^{-\frac{L_c}{L_{CD}}} \tag{4-50}$$

$$C = V_s + V_{bi} - \frac{2(E_n - E_f)}{e} \tag{4-51}$$

where V_s is defined as the saturation voltage, V_{bi} is the built-in potential resulting from unequal doping between the emitter and collector, E_n is the energy Eigenstate of interest, L_{CD} is the depleted length of the collector, and E_f the Fermi potential. V_s is defined as the maximum peak voltage point achieved for a collector that is at least $8L_{Debye}$ long. If the collector is longer than that, no additional potential drops across the non-depleted region which leads to saturation in the peak voltage point.

To quantify this saturation voltage, we made a multifactorial study that changed the width of the quantum well (w) and L_{Debye} simultaneously. To do this we put a couple of assumptions. The emitter is assumed to be degenerately doped and the collector to be doped above 1×10^{16} cm^{-3} with barriers between 1-2 nm in thickness. A surface can be fitted to the data using (*4-52*) and is shown in Figure 69.

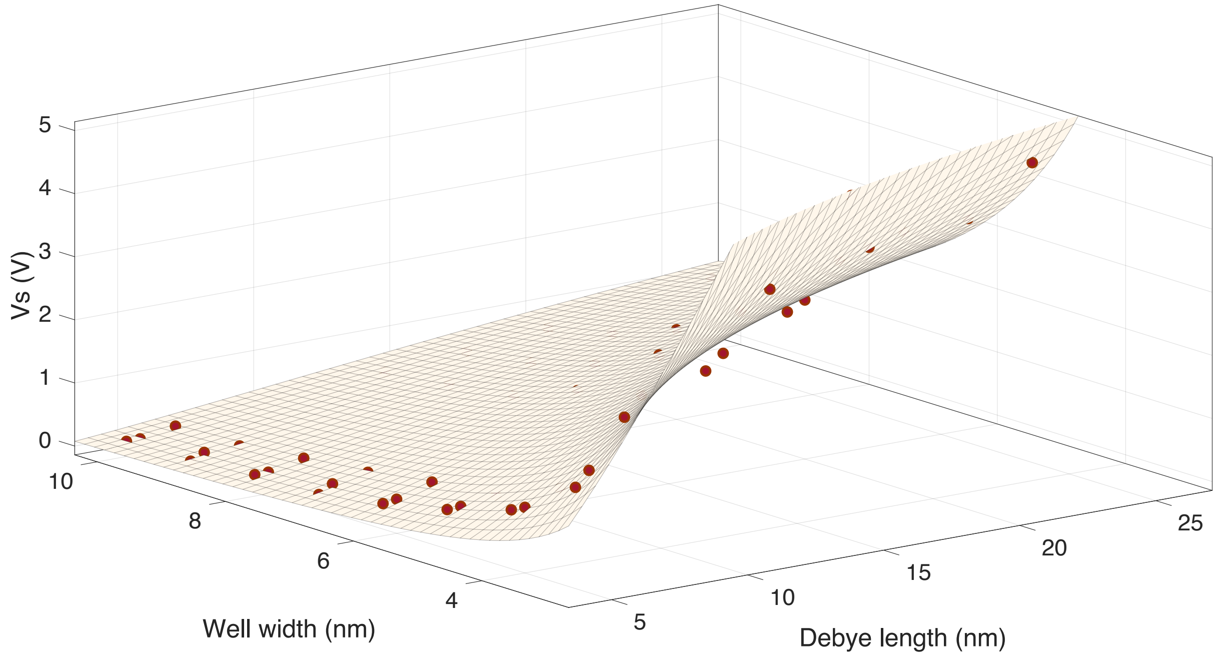

Figure 69: Saturation voltage dependance on well width and Debye length.

The fit has an adjusted R^2 value of 98.25% and both A and B are fitting parameters having values of 1.559 (1.343, 1.774) V and 0.4408 (0.4086, 0.4731) nm$^{-0.5}$ respectively with 95% confidence bounds. All lengths are in nanometers.

$$V_s(L_{Debye}, w) = A\frac{L_{Debye}^2\, e^{-B\sqrt{L_{Debye}}}}{w^2} \tag{4-52}$$

Since the collector (main absorption region) is the longest in the structure, it is fair to assume that the majority of the potential will drop across it. Using (*4-53*) an approximate

value for the collector's electric field can be deduced. Noting that this assumes a uniform electric field and was found to give fair results for the peak field value only.

$$E_{collector} = \frac{V_p}{L_{CD}} \tag{4-53}$$

Finally, we need to check for the breakdown field values for the barriers and absorption materials. The electric field between these materials will differ according to the electric permittivity (ϵ) as given by (*4-54*).

$$\epsilon_{barrier} E_{barrier} = \epsilon_{absorber} E_{absorber} \tag{4-54}$$

4.6.2 n-i-n epitaxial layer design

The layer stack we propose is based on $In_{53}Ga_{47}As$ addressing telecom wavelengths. Since we plan to fabricate and test this design, we will restrict on the collector's doping concentration to 1×10^{17} cm^{-3} since this is the minimum doping level we can verify and measure at our labs. This restricts L_{Debye} to 14 nm and reduces the depleted length to about 112 nm. This is rather short, so we make a compromise by elongating the absorption region to 250 nm at the collector and adding a 100 nm absorber at the emitter side as well. This creates areas where carriers move by diffusion, as is an application of the third (hybrid) topology we introduced earlier.

Since the Thomas-Fermi screening length is around 10 nm for $In_{53}Ga_{47}As$, we anticipate a diffusion zone of 70 nm and 138 nm in the emitter and collector regions respectively. The 138 nm in the collector are the difference between the chosen 250 nm legth and the depleted length (112 nm), the same logic applies to the emitter also. Diffusion is slower than drift, and hence the device's frequency response will be mainly limited by the diffusion of the slowest charge carriers (holes). Holes have a diffusion coefficient of around 7.5×10^{-4} m^2/s [74], which gives a diffusion time of roughly 55 ps and bandwidth between 9-10 GHz. To the author's best of knowledge, the maximum speed reported for devices with similar structures were those of Moise. et al. [55] going up to 2 Gbps data rates. For fast operating devices, we must ensure that carriers move with near saturation velocities in the depleted areas. This requires the electric field to be higher than 1×10^6 V/m [74]. For this reason, we set the target electric field to 10×10^6 V/m, and use (*4-53*) to calculate V_p, yielding a value of 1.12 V. The next step is to calculate the width of the quantum well which would result in a peak voltage (operating point) around this value. So, we use (*4-52*) and solve for

(*w*) we get a well width of roughly 7.2 nm, and we choose the *AlAs* barriers to be 1.5 nm. The final step is to make sure that we are not exceeding any breakdown field values. The electric field in *AlAs* will be 1.3×10^7 V/m as per (*4-54*). The field values are still below the breakdown limits of 20×10^6 V/m and 60×10^6 V/m for $In_{53}Ga_{47}As$ and *AlAs*, respectively [74]. The proposed epitaxial layer stack is shown in Table 4-1.

Table 4-1: The proposed n-i-n RTD-PD layer stack.

Layer	Type	Material	Thickness (nm)	Doping level (cm^{-3})
Contact	N++	InP	50	8×10^{18}
Contact	N+	InP	100	1×10^{18}
Emitter	N	$In_{53}Ga_{47}As$	100	8×10^{17}
Spacer	N	$In_{53}Ga_{47}As$	5	Undoped
Barrier	I	AlAs	1.5	Undoped
Well	I	$In_{53}Ga_{47}As$	7.2	Undoped
Barrier	I	AlAs	1.5	Undoped
Spacer	N	$In_{53}Ga_{47}As$	5	Undoped
Collector	N	$In_{53}Ga_{47}As$	250	1×10^{17}
Contact	N+	InP	100	1×10^{18}
Contact	N++	InP	100	8×10^{18}
Subst.	SI-InP			

To get some performance metrics, the quantum efficiency (η) is calculated using (*4-26*). Assuming typical values for $In_{53}Ga_{47}As$, where the absorption coefficient is about 8500 cm^{-1} and a reflectivity of 0.3 and given the absorption length to be 350 nm the expected quantum efficiency is about 14.4%. This low value is due to the drastic reduction in the absorption length, of the above design, and is typical for such *RTD-PD* designs. Also, current responsivity ($\mathcal{R}$) will be affected since the dark current is high (i.e., the current of the RTD-PD without any illumination). In the next section, we propose a *PIN* based *RTD-PD* that solves these problems.

To verify the design, the structure is simulated using Silvaco ATLAS. Figure 70 and Figure 71 show the outputs of the simulation, namely the *IV* curve and the electric field profile. We see that the simulations agree well with the proposed design calculations as the simulated peak voltage is around 0.95 V as compared to the calculated value of 1.12 V. Also, the peak electric field value is predicted well by (*4-53*).

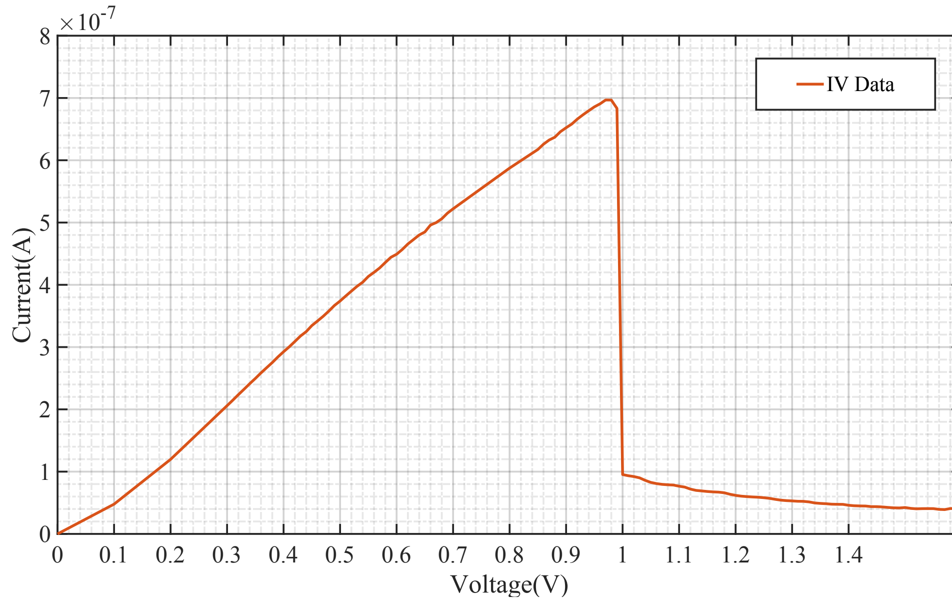

Figure 70: Simulated IV curve for n-i-n RTD-PD.

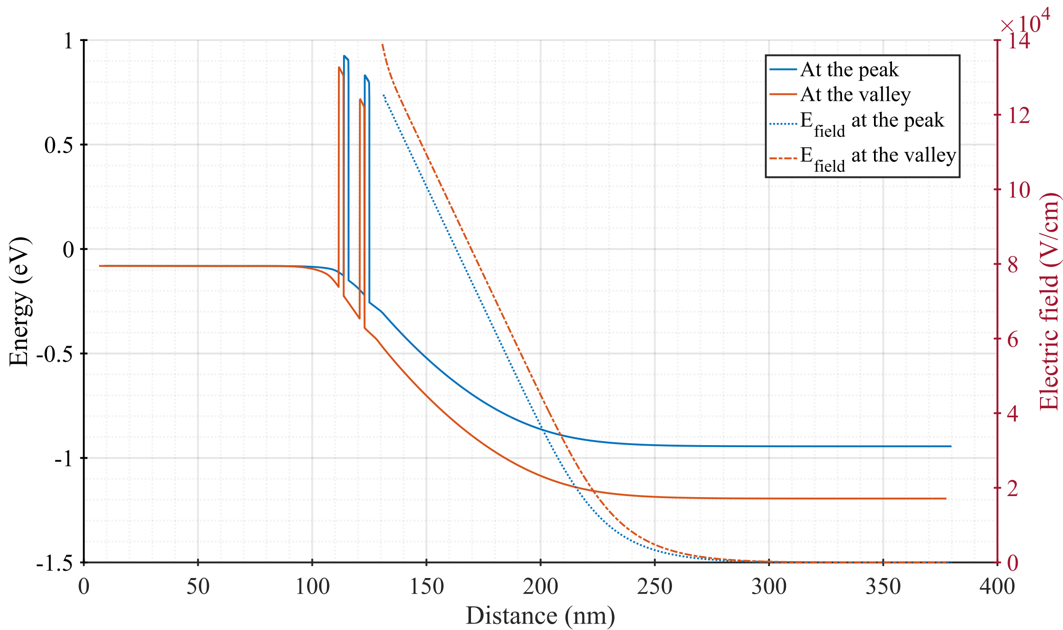

Figure 71: Conduction band diagram and collector's electric field at the peak (0.95 V) and valley (1.2 V).

4.6.3 PIN-RTD design

Previous work that integrated an *RTD* structure in a *PIN* configuration was reported by [128] using *GaAs/AlAs* material system. The devices were used to measure emission spectra and light response, however, not much emphasis was made on speed. We propose a *PIN-RTD* structure based on $In_{53}Ga_{47}As/AlAs$ and study it as a high-speed optical detector. The structure is made of lightly doped emitter and collector regions with the *DBQW* in between, and highly doped contact regions, (p^+ in the emitter and n^+ in the collector), for the formation of ohmic contacts.

Recall that the main issues with the previous *RTD-PD* design were the small absorption length in the emitter due to the screening effect, the lower overall quantum efficiency, and the non-uniform electric field. The *PIN-RTD* design addresses these issues by depleting the emitter of electrons (p-doping), thereby requiring higher bias voltages to start the electron accumulation process when applying a reverse bias polarity. We refer to this voltage point (i.e., the required voltage to form the 2DEG) as the critical voltage ($V_{critical}$). As long as the voltage is below this value, both the emitter and collector regions experience a build-up in the electric field which is necessary for fast charge transport, making it possible to extend the length of the emitter to value higher than in the *n-i-n* case. Another advantage is the low dark current which is mainly due to the tunneling of thermally generated minority carriers from each side of the well. Finally, the built-in potential given by (*4-55*) between the emitter and the collector (due to the *p* and *n* doping profiles) increases the overall electric field by adding to the applied potential, where N_A, N_D, and n_i are the acceptor, donor, and intrinsic concentrations respectively.

$$V_{bi} = \frac{kT}{e} ln\left(\frac{N_A N_D}{n_i^2}\right) \tag{4-55}$$

Figure 72 shows the energy band diagram for this design at zero-bias. The effect of the built-in potential is clear from the bending of the bands.

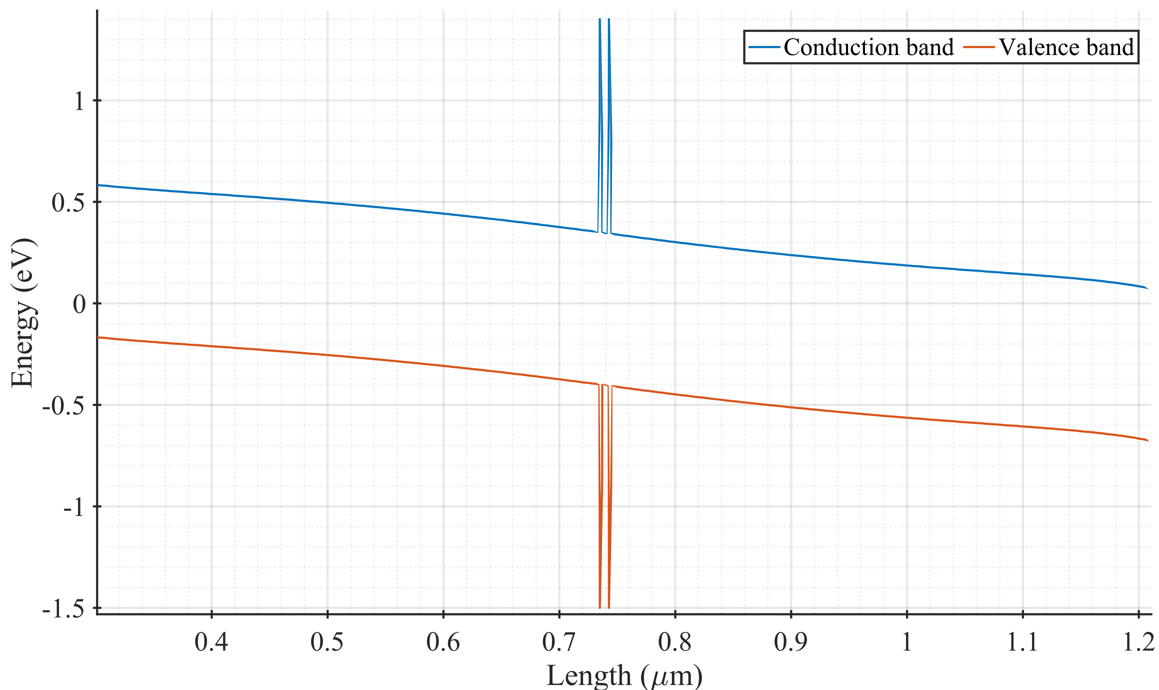

Figure 72: Zero-bias energy band diagram of PIN-RTD.

The operating point in this detector should be $V_{critical}$, which we can calculate by reasoning that, for an electron to be found in the conduction band, the Fermi energy should lay within a few *kT* near it. As a rule of thumb, 2 to 3 *kT* above the conduction band edge (degenerate conditions) will signal the presence of a considerable number of electrons. The difference between the Fermi energy and the conduction band edge for degenerate conditions is adequately calculated using the Joyce-Dixon approximation given by (*4-56*)

$$E_f - E_c = kTln\left(\frac{n}{N_c}\right) + \frac{1}{\sqrt{8}} \times \frac{n}{N_c} \tag{4-56}$$

where *n* is the doping concentration and N_c is the effective density of states in the conduction band. For $In_{53}Ga_{47}As$, N_c is around 2.1 x 10^{17} cm^{-3}, so 3 *kT* above the conduction band edge gives an electron density of around 9x10^{17} cm^{-3}. At this point, the accumulation region in the emitter will form a sort of an inversion layer by becoming electron dominated. This points that there will effectively be a *PIN* structure at the emitter, and another one at the collector due to the formation of the depletion region there. Since the emitter is p-doped, the separation between the Fermi-energy and the conduction band at zero bias can be found by (*4-57*), where N_V is the effective density of states in the valence band and *p* the doping level. The second term in (*4-57*) is the separation between the valence band and the Fermi-level at zero bias under the Boltzmann approximation, and the last term is due to the built-in potential.

$$\mathrm{E_c} - E_f = E_g - kTln\left(\frac{N_V}{p}\right) - \frac{eV_{bi}}{2} \tag{4-57}$$

$V_{critical}$ can then be approximated by adding 3kT to (*4-57*) as shown in (*4-58*).

$$V_{critial} = \frac{3kT}{e} + \frac{E_g}{e} - \frac{kT}{e}ln\left(\frac{N_V}{p}\right) - \frac{V_{bi}}{2} \tag{4-58}$$

For this structure, a doping concentration of 1×10^{15} cm^{-3} with a certain tolerance during growth which could go up to 5×10^{15} cm^{-3} can be achieved. This was confirmed by the grower (Vigo systems). Hence, both the emitter and the collector absorbers are chosen to be 500 nm long, with p-type and n-type doping, respectively. This makes the absorption region around 1 μm long and sets the minimum operating voltage to 1 V. With that in mind, the *DBQW* structure should be designed such that the first energy Eigenstate aligns with the Fermi energy at around 1 V. Since the entire structure is depleted, the potential will drop across it linearly and uniformly until the *2DEG* is formed. A very good approximation is to

assume that twice the energy difference between the Fermi energy and the first Eigenstate has to be applied to align them. So, to have a peak at 1 V, the separation between the Fermi level and the first Eigenstate should be around 500 meV. If we choose a quantum well that is 5.7 nm wide, then the first Eigenstate being around 150 meV above the conduction band. We must now include the value of the built-in potential, plugging in the numbers for the doping concentrations in the emitter and the collector we get a value of about 0.38 V of built-in potential. Using (*4-58*) the critical voltage will be around 0.4 V, which results in a separation between the first Eigenstate and the conduction band of 550 meV at zero bias. Therefore, the anticipated peak is around 1.1 V. Table 4-2 lists the proposed epitaxial layer design.

Table 4-2: Proposed epitaxial layer design for PIN-RTD.

Layer	Type	Material	Thickness (nm)	Doping level (cm^{-3})
Contact	P++	InP	50	8×10^{18}
Contact	P+	InP	100	1×10^{18}
Grading	P	$InGa_{0.12}As_{0.25}P$	15	1×10^{18}
Grading	P	$InGa_{0.19}As_{0.4}P$	30	1×10^{18}
Emitter	P-	$In_{53}Ga_{47}As$	500	1×10^{15}
Spacer	I	$In_{53}Ga_{47}As$	10	Undoped
Barrier	I	AlAs	1.5	Undoped
Well	I	$In_{53}Ga_{47}As$	5.7	Undoped
Barrier	I	AlAs	1.5	Undoped
Spacer	I	$In_{53}Ga_{47}As$	10	Undoped
Collector	N-	$In_{53}Ga_{47}As$	500	1×10^{15}
Grading	N	$InGa_{0.19}As_{0.4}P$	30	1×10^{18}
Grading	N	$InGa_{0.12}As_{0.25}P$	15	1×10^{18}
Contact	N+	InP	200	1×10^{18}
Contact	N++	InP	50	8×10^{18}
Substr.	SI - InP			

As with the previous design, we need to check for the breakdown electric field values. Using (*4-53*) the anticipated electric field will be around 1.48×10^{6} V/m, including the contribution from the built-in potential. Figure 73 shows the simulation results, which show a peak at around 1 V, agreeing well with the calculations. Figure 74 shows the electric field profile which is more uniform than in the *n-i-n* case. Its value agrees satisfactorily with the calculations.

Regarding the speed of the device, the generated carriers are expected to drift under the electric field with near-saturation velocities. At this electric field, the holes are expected

to travel at roughly 4×10^4 m/s, resulting in a transit time of around 25 ps, which gives an anticipated frequency response of 20 *GHz*. Figure 75 shows the energy band diagram with the carrier concentrations superimposed, clearly portraying the formation of the beforementioned *PIN* structures.

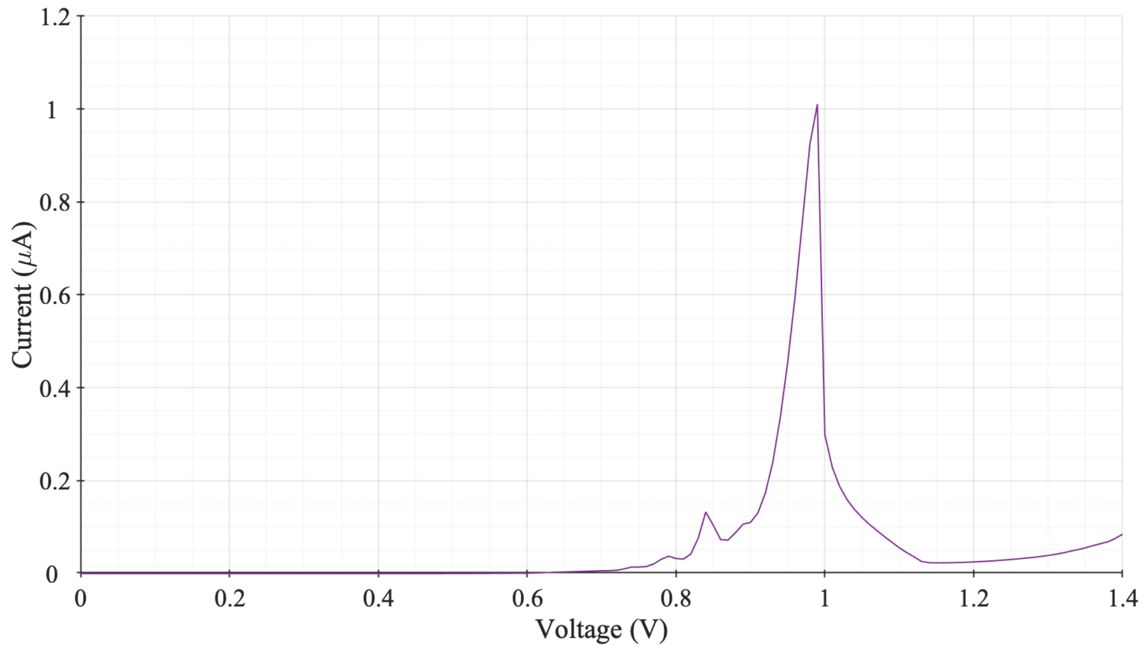

Figure 73: IV curve of proposed PIN detector.

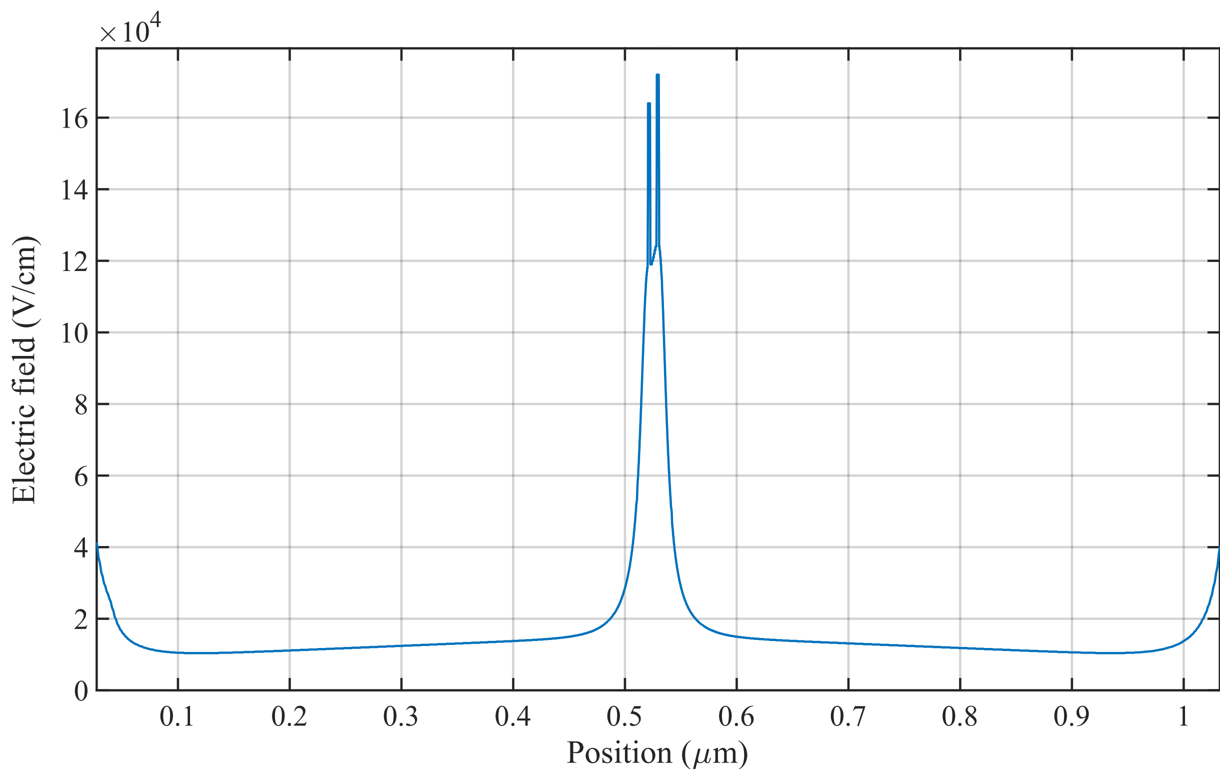

Figure 74: Electric field in the emitter and collector at 1 V.

*PIN-RTD*s are expected to give better responsivity than normal *PIN* detectors. The presence of the *RTD* results in charge accumulation at the emitter which gives rise to current amplification. Of course, the gain is expected to be at the expense of speed, since now a new constraint on the frequency response will be the charge trapping time in the accumulation region of the emitter. Hence, we anticipate the devices to operate at lower speeds. The results section in chapter 5 will discuss the outcomes of the measurements.

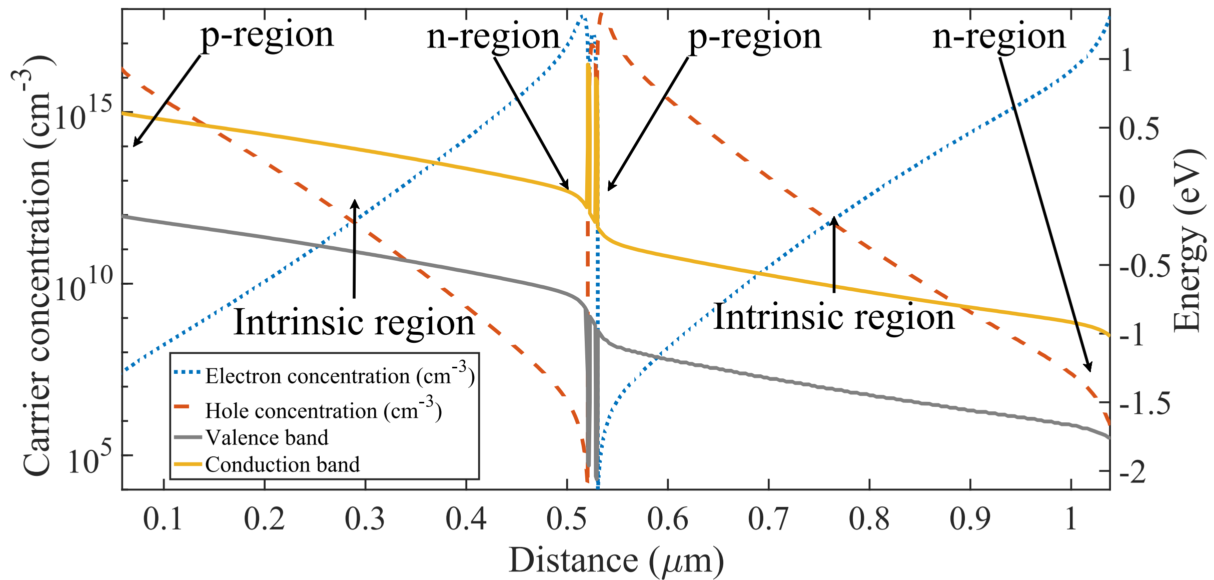

Figure 75: Energy band diagram at 1 V bias. P-doped emitter at the left, n-doped collector at the right. Contacts are not shown.

4.7 Summary and conclusion

In this chapter we showed how resonant tunnelling diode-based photodetectors (*RTD-PD*) can be designed based on a set of rules. We started by introducing the interaction between light and semiconductors with a brief introduction to various photodetectors. We clearly describe the various topologies that an *RTD-PD* can have and highlighted the use cases for each. Building on these topologies, we proposed two high speed *RTD-PD* designs using the design rules we highlighted at the beginning that can theoretically reach 10 GHz speeds. These designs were based on an *n-i-n* and a *PIN* scheme and were verified using simulations from Silvaco ATLAS.

Chapter 5 : Optical characterization of resonant tunnelling diode photodetectors

5.1 Introduction

In this chapter, we go through the optical characterization of all the resonant tunnelling diode-based photodetector epitaxial layer designs under *AC* and *DC* optical excitation. The results show the potential feasibility of using resonant tunnelling diode-based photodetectors in high-speed and high-responsivity applications. We begin with the epitaxial layer designs that include different lengths of the emitter and the collector, different doping concentrations, different contact materials, and different quantum well designs. We then go through the *DC* optical characterization steps and discuss the results of current responsivity. We then utilize the frequency response to modulated light to determine the speed limitations of the devices and to test the hypothesis portrayed in chapter 4 regarding the high-speed design considerations. Finally, we show the advantage of using resonant tunnelling diode-based detectors in terms of their built-in amplification capabilities.

5.2 Epitaxial layer designs

We characterized eight epi-layer designs referred to by the following names: 73A, NC1800, S99, S98, P-A323, P-A325, *PIN-RTD*, and photoconductive wafer. The actual epitaxial layer structure for each wafer is discussed in the characterization section for the respective wafer. Samples 73A, S99, S98, photoconductor, and NC1800 were all grown by an industrial firm (IQE) using molecular beam epitaxy (*MBE*), while the *PIN-RTD* wafer was grown by another industrial firm (Vigo systems) using metal-organic chemical vapor deposition (*MOCVD*). The last two samples (P-323 and P-A325) were grown during a secondment time at the University of Würzburg using a gas-source *MBE* system. These samples were grown through a collaboration with a college (Begüm Yavas Aydin), under the

supervision of Dr. Fauzia Jabeen. The Fabrication for these samples was done by the cleanroom technician (Monika Emmerling).

All wafers except for the *PIN-RTD* have thick $In_{53}Ga_{47}As$-based contacts, particularly at the bottom layer. One of the main ideas behind the *PIN-RTD* design was to eliminate any charge generation in the highly doped contact regions where the electric field is nearly zero, which would impose a lifetime limit on the speed.

5.3 DC current responsivity

Figure 76 depicts the *DC* characterization setup. We couple light vertically into the *RTD-PD*s' optical window through a bare-fiber cable. The fiber is aligned over the optical window until the photocurrent is maximized, after which we shine a continuous-wave (*CW*) light at a wavelength of 1.55 µm and record the *IV* using a source-measure unit (*SMU*), which has a resolution down to the pA range. Since the bare fiber is aligned such that, it directly touches the optical window, we assume that the beam is coupled completely. As a convention in this work, a forward-biased device refers to a device that has its top (uppermost) layer connected to the positive supply terminal, while the ground terminal is connected to the bottom layer. The opposite applies to a reverse-biased device. This is illustrated in Figure 77.

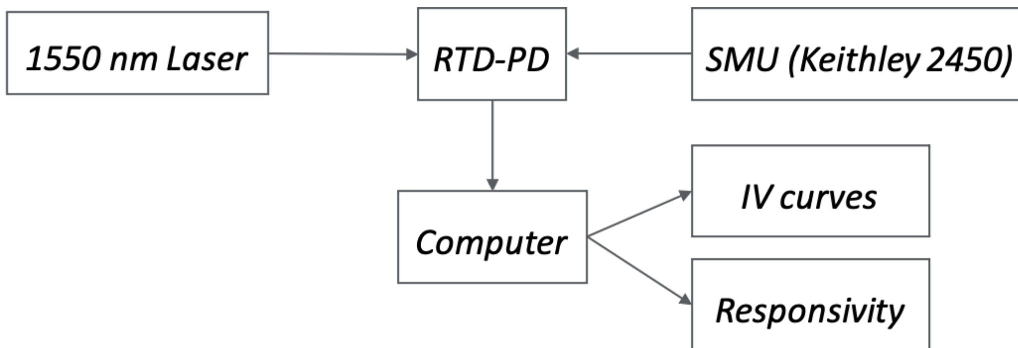

Figure 76: DC-optical characterization setup.

Figure 77 shows a typical characterization setup. We load the sample on a stage (micro-station) with a bare-fiber cable perpendicular to it. The fiber itself is fixed to another micro-station (Semiprobe MA-8000) with XYZ control which we use to align the fiber over the optical window through the microscope. The fiber cables used were mainly single-mode fibers from Thor Labs with a numerical aperture of 0.12-0.14. Some measurements were taken

as well with lensed fibers having a beam diameter of around 2.5 μm at a distance of 14 μm. The micro-positioning station used for the fiber has a resolution of around 300 μm per revolution and can get down to 5 μm resolution, so the beam should be coupled almost completely into an optical window of a 10×10 μm² device. There are two high-frequency probes from Picoprobe with a bandwidth from DC up to 26 GHz in a ground-signal-ground configuration.

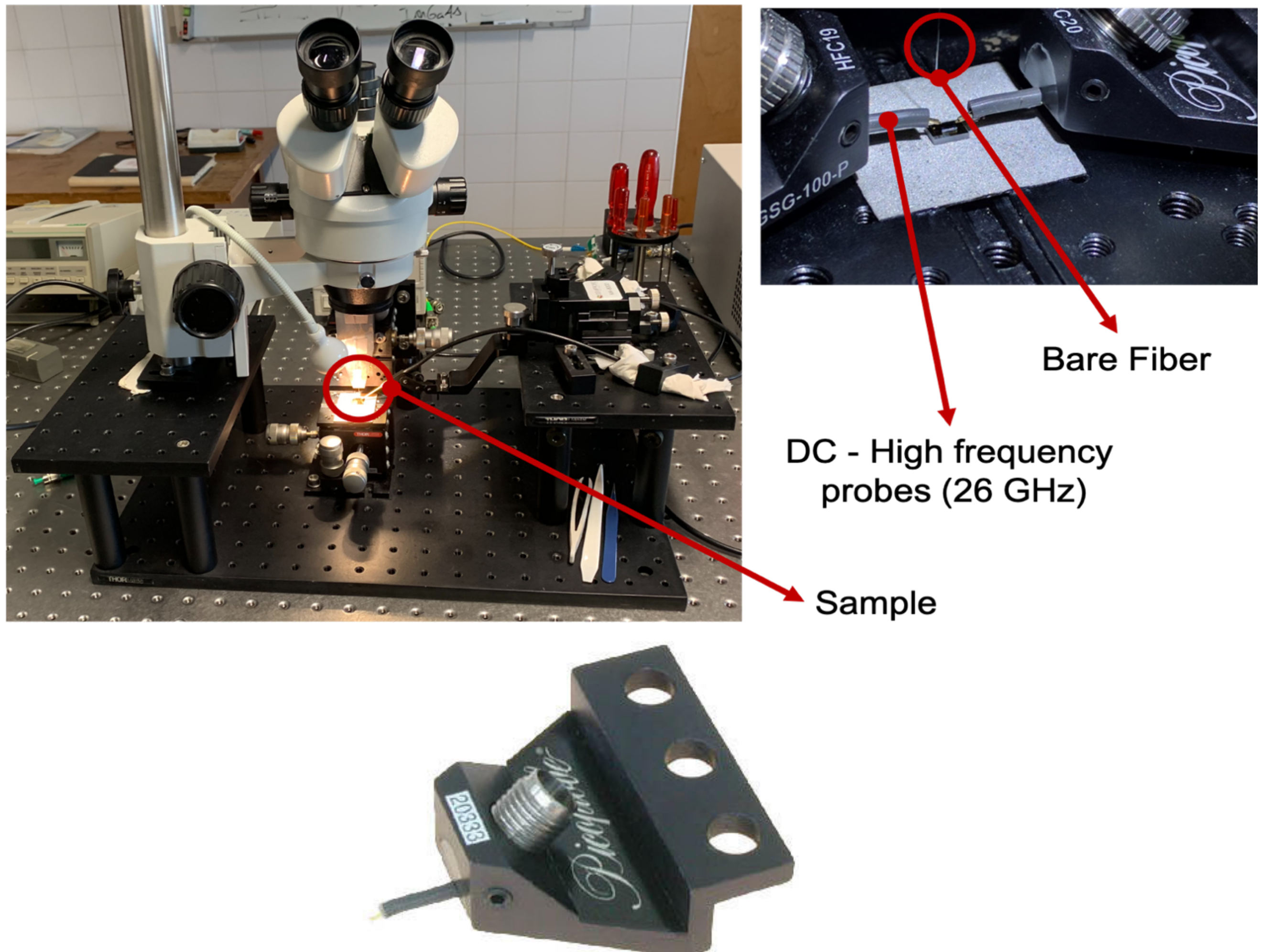

Figure 77: Typical characterization setup. The right side shows the probes and fiber alignment over the chip. These probes (and fiber) are controlled through micro-positioners.

The measurements were taken multiple times on multiple devices for each sample. Furthermore, we used different laser sources and measurement equipment. Doing so ensures the repeatability of the results under different setups, as the same phenomena shows regardless of the measurement setup. The laser source we used is a *DFB* laser from Thor Labs (S3FC1550), which is temperature-controlled and can produce output power up to 2 mW. The *SMU* is a Keithley 2450. We acquire the *IV* curves directly from the *SMU* through a

MATLAB program and calculate the current responsivity curve as a function of the applied voltage using the empirical formula an in (*5-1*)

$$\mathcal{R} = \frac{I_{illuminated} - I_{dark}}{P_{incident}} \tag{5-1}$$

Most of the *RTD-PD*s we have were fabricated by the University of Glasgow, using optical lithography. The people in charge of the fabrication were Prof. Edward Wasige's group, namely Dr. Abdullah Al Khalidi, Dr. Qusay Al-tai, and Dr. Maira Elksne. A typical device mask for this process and a microscope image of one are shown in Figure 78. These devices are pillar shaped, with ground-signal-ground lines forming a co-planar waveguide. This waveguide structure is deposited on the semi-insulating substrate and passivated.

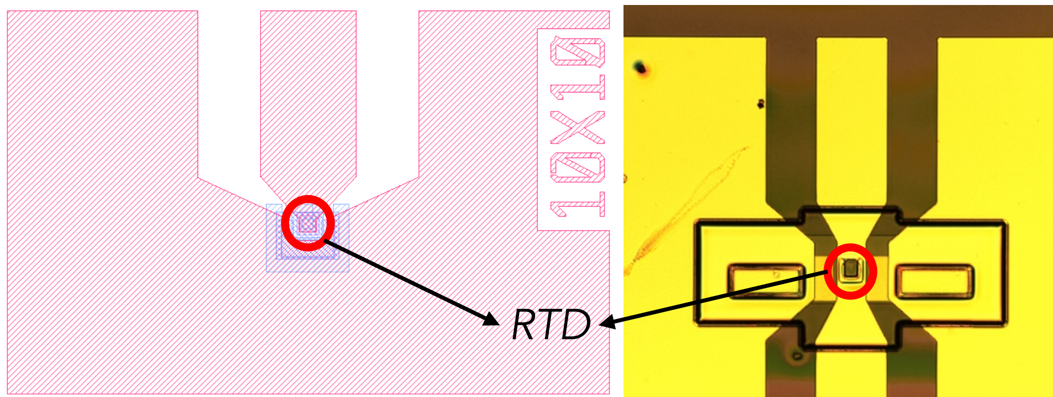

Figure 78: Left - Typical RTD-PD mask for a 10x10 μm² device (University of Glasgow process). Right - Sample fabricated device with RTD and ground-signal-ground lines.

5.3.1 *Epi-layer NC1800*

The epi-design of the first sample is shown in Table 5-1.

Table 5-1: Epitaxial layer design of wafer NC1800.

Layer	Type	Material	Thickness (nm)	Doping level (cm^{-3})
1	N++	$In_{53}Ga_{47}As$	45	3×10^{19}:Si
2	N+	$In_{53}Ga_{47}As$	80	3×10^{18}:Si
3	N-	$In_{53}Ga_{47}As$	500	5×10^{16}:Si
4	I	$In_{53}Ga_{47}As$	2	Undoped
5	I	AlAs	1.7	Undoped
6	I	$In_{53}Ga_{47}As$	4.7	Undoped
7	I	AlAs	1.7	Undoped
8	I	$In_{53}Ga_{47}As$	2	Undoped
9	N-	$In_{53}Ga_{47}As$	20	2×10^{16}:Si
10	N+	$In_{53}Ga_{47}As$	80	3×10^{18}:Si
11	N++	$In_{53}Ga_{47}As$	400	3×10^{19}:Si
12	SI	*InP*	200	-

This sample has a 500 nm absorption region at one end and a 20 nm region at the other end. The doping profile is not symmetric; the longer absorber has a doping level of 5×10^{16} cm^{-3} while the shorter one has a doping level of 2×10^{16} cm^{-3}. Regarding the quantum-well design, this sample has a 4.7 nm quantum well between two 1.7 nm *AlAs* barriers. We emphasize the presence of a thick (400 nm) and highly-doped $In_{53}Ga_{47}As$-based bottom contact. Additionally, this design consists entirely of $In_{53}Ga_{47}As$ (except for the barriers), which means that absorption takes place at all layers. The *IV* curves for this sample are shown in Figure 79.

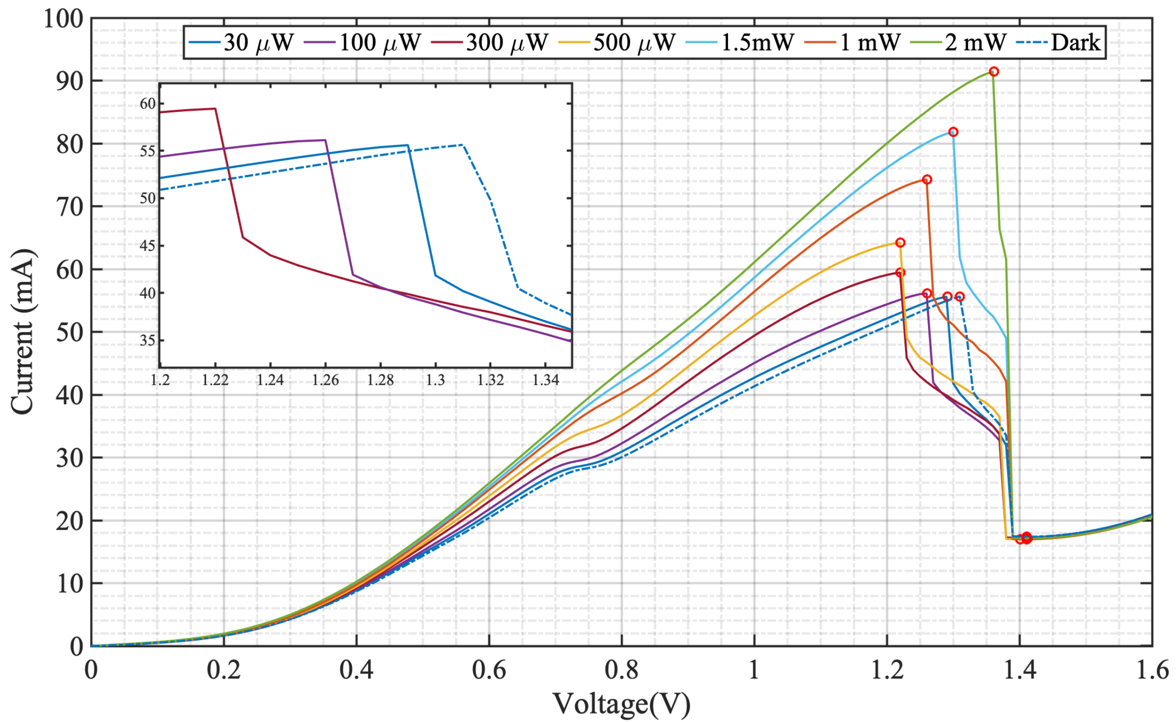

Figure 79: IV curves in reverse bias for sample NC1800.

This sample shows an *NDR* in reverse-bias mode only. This is when the 500 nm layer acts as the emitter and the 20 nm layer as the collector. We anticipate this behavior since, in forward-bias mode, the peak voltage would drastically shift to higher values. Recall that in chapters 3 and 4, we have shown that the length of the depleted collector region is proportional to the Debye length, which is doping dependent. We also showed the collector's role in determining the peak voltage. Given the doping level of 5×10^{16} cm^{-3}, the Debye length will be roughly 20 nm, and the depleted region of the collector will be 160 nm. For a 4.7 nm quantum-well, the first Eigenstate is located roughly at 210 meV. This means that the peak in forward bias will show up at a voltage near 3.7 V. Bearing in mind that, when

doing these calculations, one has to consider the tolerances in doping and growth, particularly the width of the quantum well. Unfortunately, devices burned at such voltages and only operated in reverse bias mode. We believe this to be a fabrication-related issue not an intrinsic problem with the epi-layer.

The previous results show that the device shifts to a lower voltage at low illumination levels before starting the shift to higher values. Furthermore, there are changes in the main *RTD* output characteristics; mainly the *PVCR*, ΔV, and ΔI. The dark *PVCR* is about 3.2, while it increases to 5.3 for the highest illumination level, as shown in Figure 80. This is apparent from the increase in the peak current without a similar increase in the valley current. This is particularly important in oscillators as injecting light could modulate the output *RF* power of the oscillator (*P*) as per (5-2) [92].

$$P = \frac{3}{16}\Delta V \Delta I \quad (5\text{-}2)$$

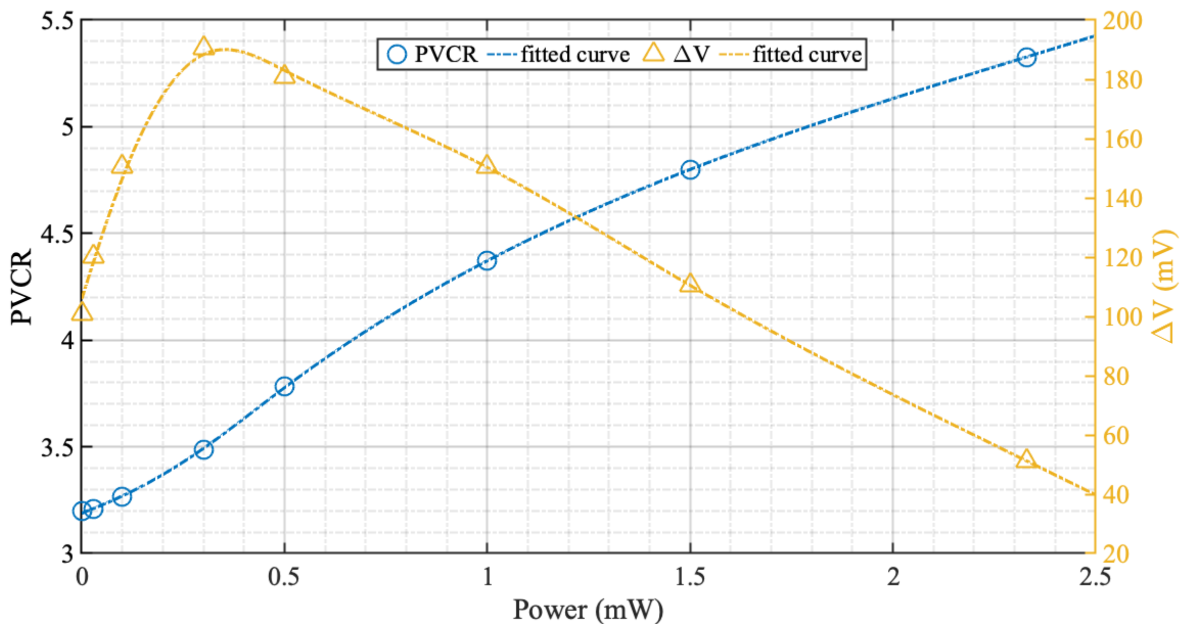

Figure 80: PVCR and ΔV evolution with illumination power for sample NC1800.

Furthermore, the peak shift to lower values at low illumination levels is unaccompanied by any increase in the current. This tallies well with the simulation results we obtained earlier from Silvaco when the carrier concentration increases in the collector. Figure 80 shows something interesting; at low illumination levels (less than 300 μW), Δ*V* shows a rapid improvement. This enhancement is because the induced shift at the peak voltage is not present at the valley voltage, while the increase in the *PVCR* is not significant at these

illumination levels. This result is logical as the *PVCR* is more affected by the current increase (the increase in the charge generation at the emitter) and not much by the charge generation at the collector. The valley voltage in an *RTD* appears when the resonant energy Eigenstate goes below the edge of the conduction band. Therefore, we can identify two main quantities that control it: the location of the Fermi-energy relative to the edge of the conduction band and the overall conductance of the collector. The latter can be estimated as highlighted in chapter 4 using (*5-3*) and (*5-4*). Where δn and δp are the excess light-generated carriers, *G* the generation rate and τ the minority carrier lifetime.

$$\Delta\sigma = \mathrm{e}(\mu_e \delta n + \mu_p \delta p) \tag{5-3}$$

$$\Delta\sigma = \mathrm{e}(\mu_e + \mu_p) G \tau_{minority} \tag{5-4}$$

As highlighted in the previous chapters, the amount of voltage that drops across the *DBQW* - lowering the Eigenstates - is determined by the structural parameters and by the formation of the *2DEG* in the emitter. Since we do not see an increase in the current for these illumination levels, we believe that the separation between the Fermi-level and conduction band edge has not changed. Furthermore, such low generation levels will not enhance the conductance of the collector, and hence the valley point does not change. This makes us more inclined towards charge accumulation as the main driver for such a shift.

Further increasing the illumination power shifts the peak voltage to the right and increases the photocurrent. The peak voltage spans between 1.22 V up to 1.36 V, which corresponds to a peak-voltage shift span between -90 mV to 50 mV. This is depicted in Figure 81.

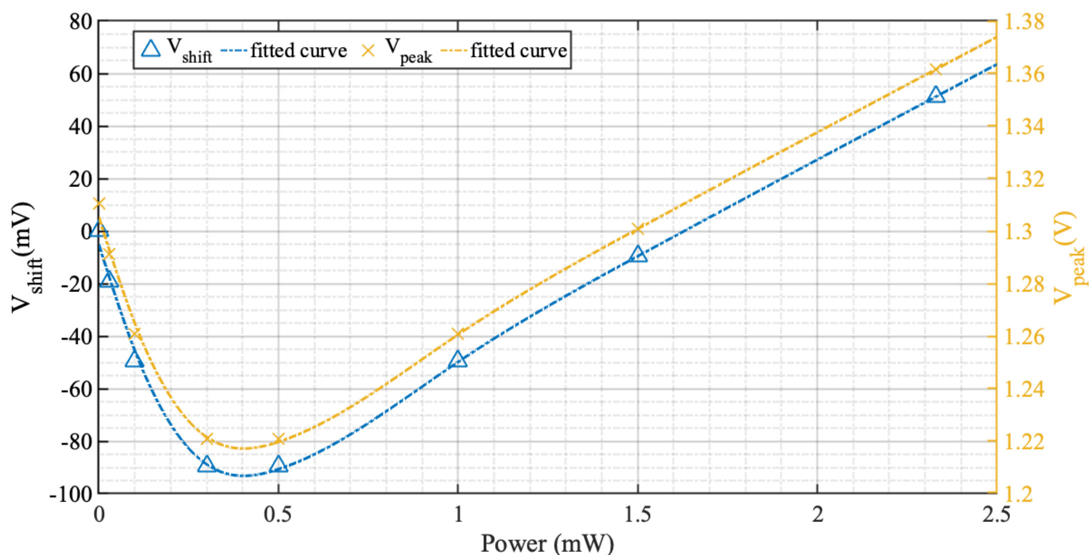

Figure 81: Peak voltage and peak voltage shift for sample NC-1800.

This is expected, since the absorption is taking place mainly at the emitter's side in this wafer. There is also evidence of a Fermi-level increase from the *IV* curves, as the shoulder observed starts to smear at higher illumination levels (which tallies well with the model where the generation takes place at the emitter). This is evident in Figure 79 at about 0.7 V. The *IVs* also show evidence of conductivity enhancement; by observing the enhancement in the slope of the *PDC* region, and the stabilization effect taking place in the *NDC* region. For the highest illumination level, the device looks more stable, which hints at the possibility of using light for bias stabilization of *RTDs*. Figure 82 shows how the photocurrent and peak currents are affected by illumination power.

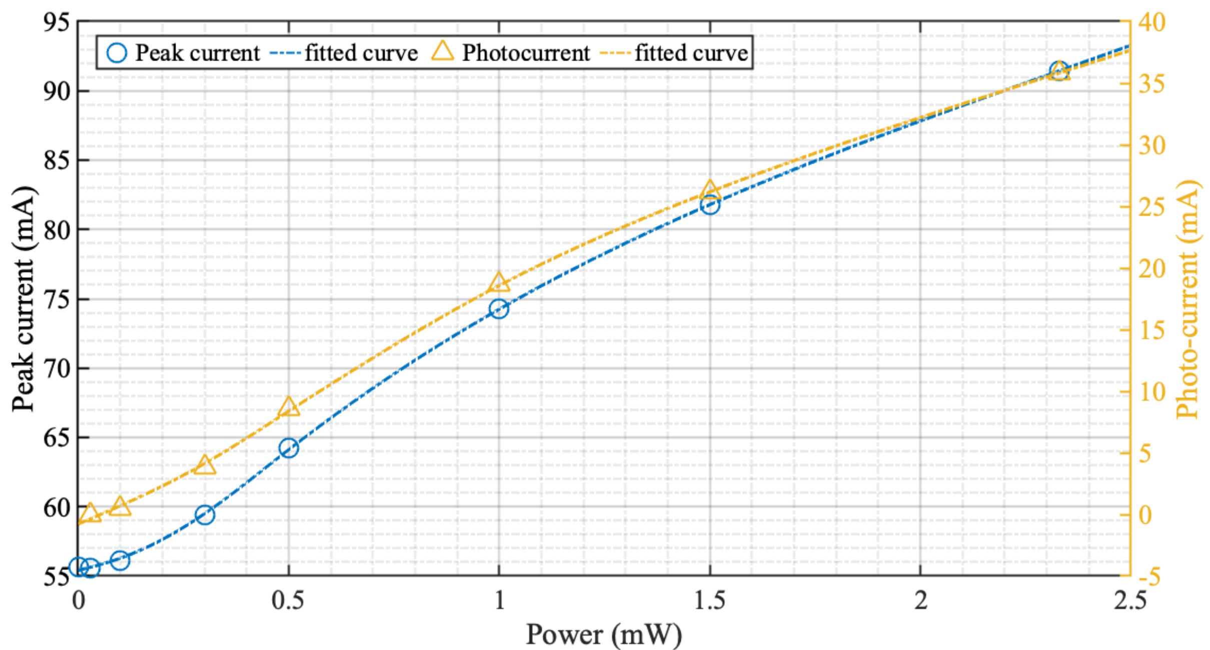

Figure 82: Peak current and peak-photocurrent dependence on illumination power.

Current responsivity curves, (calculated according to ((*5-1*)), for all illumination levels, are shown in Figure 83. This was done by measuring the dark current and the illuminated current through the SMU. These curves represent the responsivity in the *PDC* region until the peak. The areas where the *NDC* would have occurred are not plotted since devices in the *NDC* tend to oscillate and the current values obtained will not be correct. These values are higher than those obtained for typical *PIN*-photodetectors, which tend to max at a theoretical maximum near 1 as discussed in the earlier chapter. However, unlike *PIN*-photodiodes, the responsivity is a highly non-linear function of voltage pointing to a non-linear electric field profile.

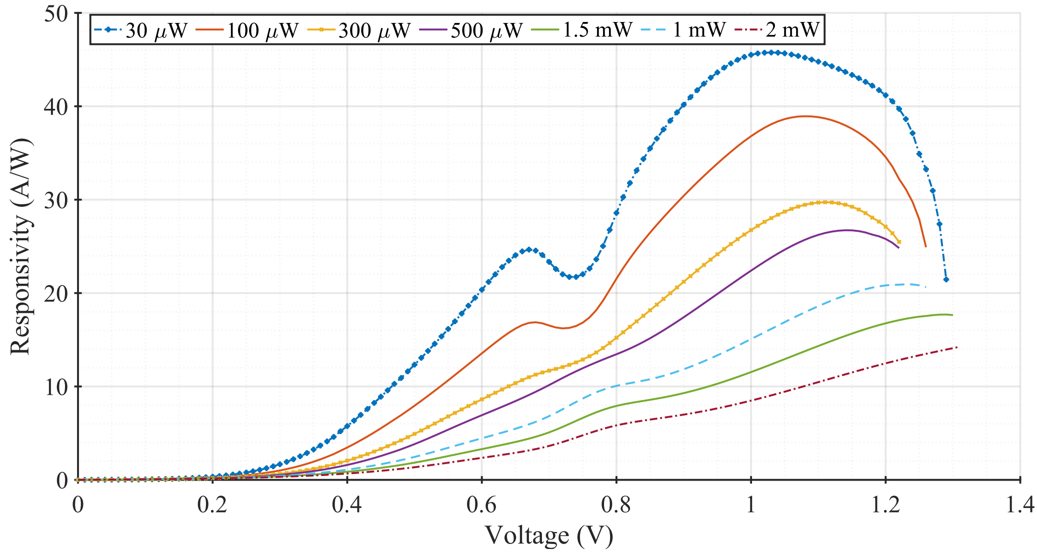

Figure 83: Current responsivity in reverse bias for sample NC1800.

The non-linear nature of the responsivity curves stems from the fact that they are the difference between two *RTD-IV* curves ($I_{illuminated} - I_{dark}$), which are non-linear in nature. Notice that the maximum responsivity occurs at voltages which are below the peak voltage point, for the devices that tend to shift to lower values, while it starts to move towards the location of the peak value as the peak-voltage start to shift to higher values. For the former case, since there is no increase in the current (i.e.: photocurrent is nearly zero), the responsivity we get is from the shifting behavior. In that case the responsivity should follow the rhythm of the voltage shift (V_{shift}) as a function of voltage which is shown in Figure 85. The voltage shift is the difference between the voltages of the dark and the illuminated *IVs* at a given current as in Figure 84. Back to the responsivity curves, for instance the two peaks in the current responsivity curve correspond to the peaks observed in the voltage shift as well.

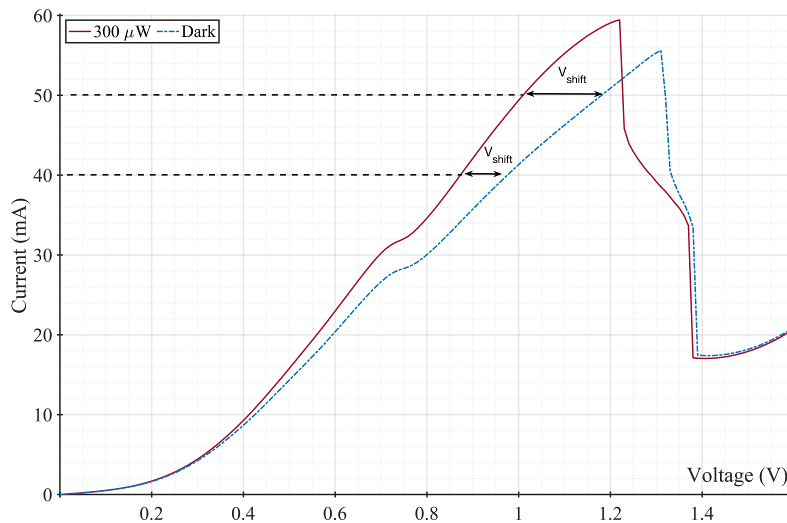

Figure 84: An illustration of how V_{shift} is calculated.

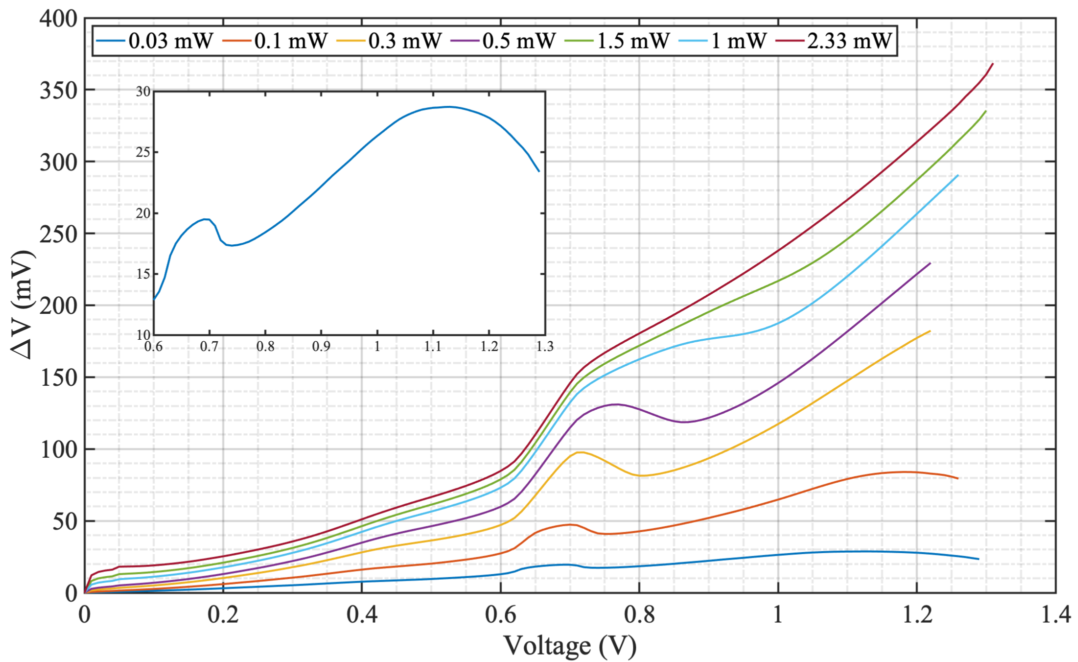

Figure 85: Voltage shift as function of applied voltage for sample NC1800. The inset is a magnification for the 30 μW illumination level from 0.6 V to 1.3 V.

In terms of the current responsivity dependence on illumination levels, we note that the responsivity decays exponentially with illumination power, as shown in Figure 86. The reason for such a behavior is the saturation effects at high illumination levels. Since high carrier concentrations promote non-linear effects such as band-filling and mobility saturation (as highlighted in chapter 4) [119], high injection levels will eventually saturate the induced photocurrent. Although the saturation is not directly observed in Figure 86, we believe that using higher illumination levels will introduce the above non-linearities, particularly, the band-filling effect where, due to high generation, the effective bandgap of the semiconductor increases and a sort of self-induced transparency is introduced. Hence, increasing the illumination power will decrease the responsivity as the increase in photocurrent is not on the same level as the power increase.

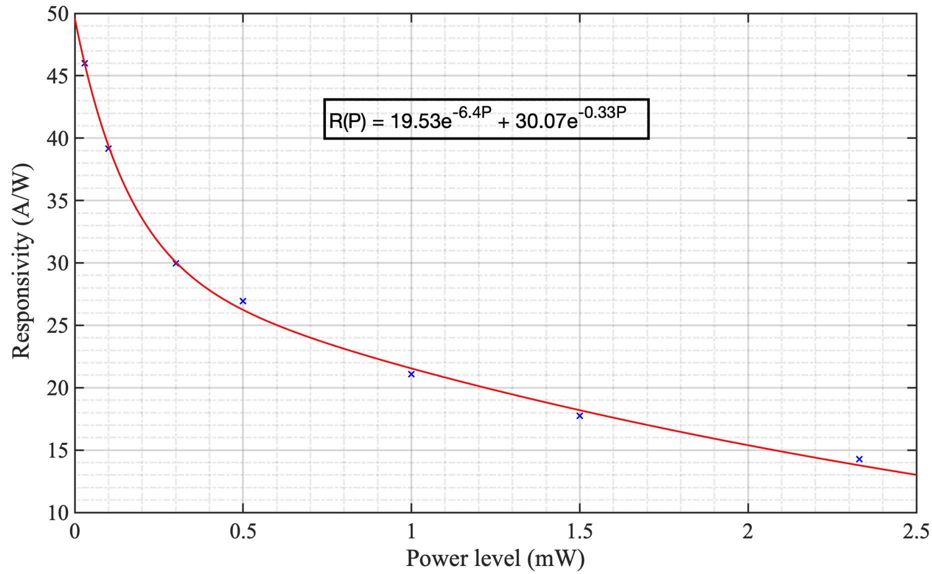

Figure 86: Peak responsivity as function of illumination power under reverse bias for sample NC1800.

5.3.2 Epi-layer S99

The epitaxial layer design for this sample is shown in Table 5-2. This epi-layer has a 250 nm absorption region at one end, and a 20 nm region at the other. The doping profile is symmetrical with both doping levels being 2×10^{16} cm^{-3}. Regarding the quantum-well design, this sample has a 5.7 nm quantum well between two 1.7 nm *AlAs* barriers. We take the opportunity again to highlight the presence of a thick (500 nm) bottom contact that is highly doped. Another thing to note is the presence of $In_{52}Al_{48}As$ layers at both ends. This layer has a higher bandgap than $In_{53}Ga_{47}As$ (around 1.47 eV) which makes it transparent to light energy coming from 1.55 µm or 1.31 µm light sources.

Table 5-2: Epitaxial layer design of sample S99.

Layer	Type	Material	Thickness (nm)	Doping level (cm^{-3})
1	N++	$In_{53}Ga_{47}As$	100	2×10^{19}:Si
2	N+	$In_{52}Al_{48}As$	100	2×10^{18}:Si
3	N-	$In_{53}Ga_{47}As$	250	2×10^{16}:Si
4	I	$In_{53}Ga_{47}As$	2	Undoped
5	I	*AlAs*	1.7	Undoped
6	I	$In_{53}Ga_{47}As$	5.7	Undoped
7	I	*AlAs*	1.7	Undoped
8	I	$In_{53}Ga_{47}As$	2	Undoped
9	N-	$In_{53}Ga_{47}As$	20	2×10^{16}:Si
10	N+	$In_{52}Al_{48}As$	100	2×10^{18}:Si
11	N++	$In_{53}Ga_{47}As$	500	2×10^{19}:Si
12	I	$In_{52}Al_{48}As$	100	Undoped
13	SI	*InP*	20	-

Again, this wafer only worked at reverse bias conditions. The anticipated peak using the calculation method is around 1 V in reverse bias mode and goes up to 3 V in forward bias mode. The same problem with the devices shorting at higher voltages persists here as well, which is believed to be related to the fabrication of the devices and not a limitation of the design itself. The results in terms of *PVCR*, ΔV, responsivity, peak voltage shift and photocurrent are in-line with the observations of the previous wafer.

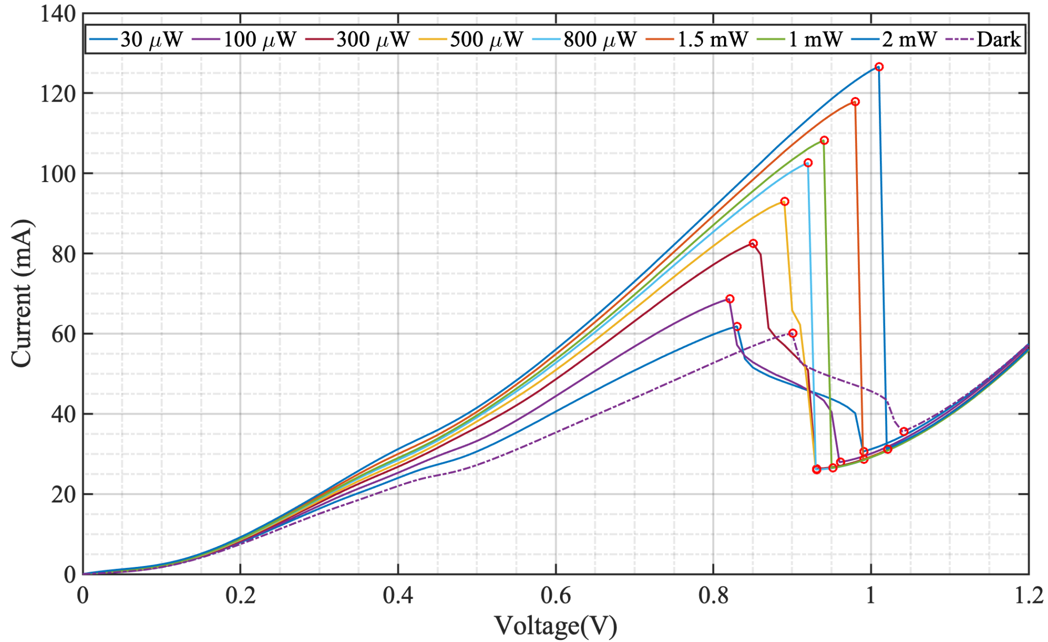

Figure 87: IV curves in reverse bias for sample S99 (10×10 μm²).

The figures below portray the relationships between the various *RTD* parameters and illumination levels. The results are in tally with the observations from the previous wafer.

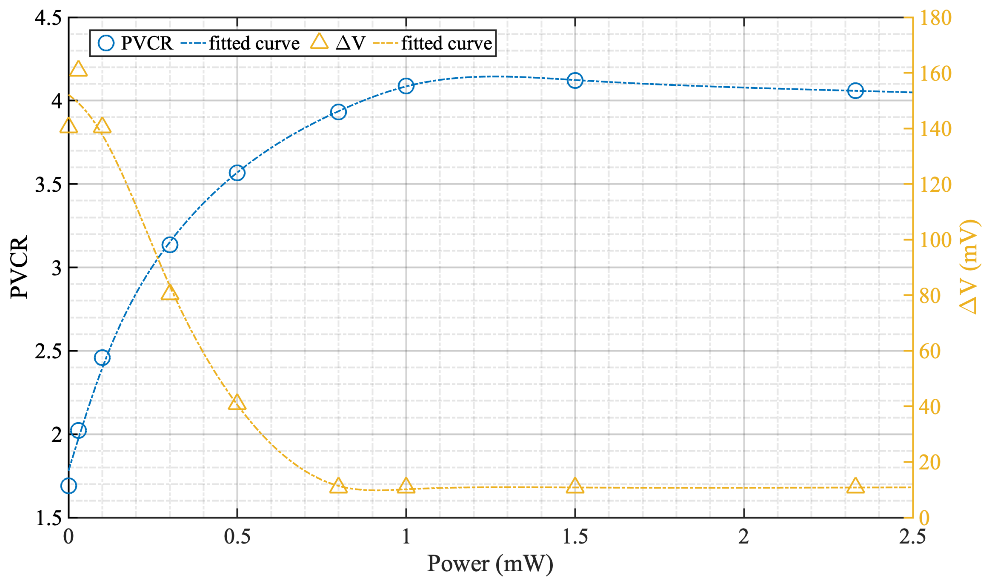

Figure 88: PVCR and **Δ**V evolution with illumination power.

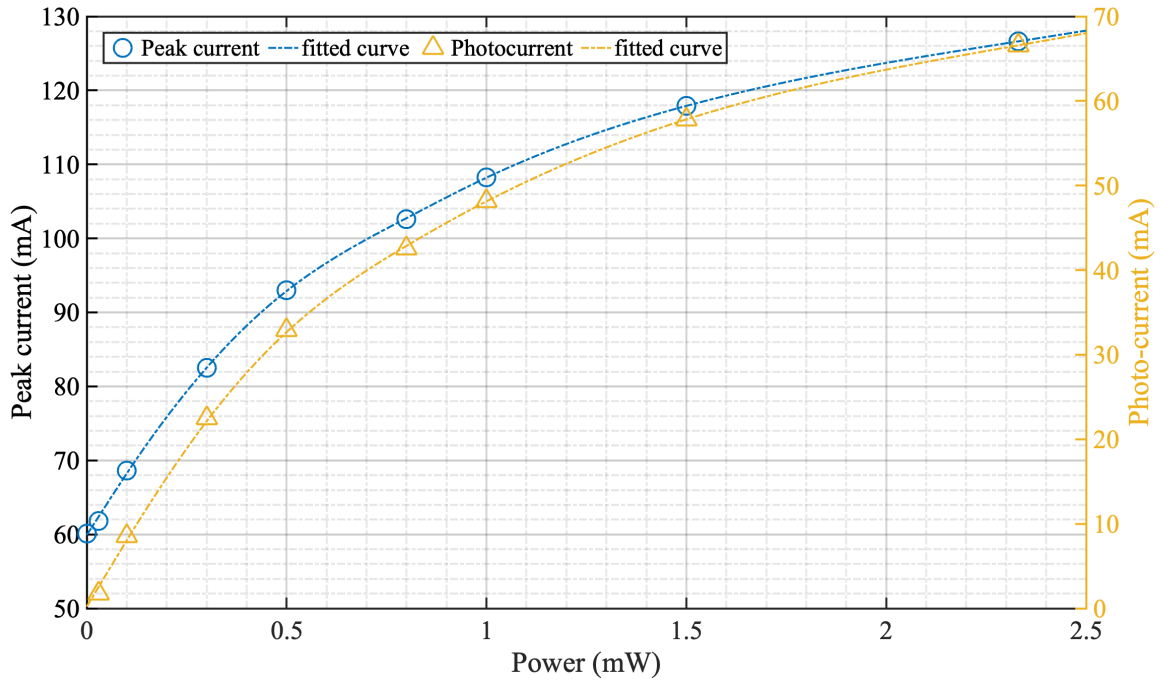

Figure 89: Peak current and peak photocurrent dependence on illumination levels.

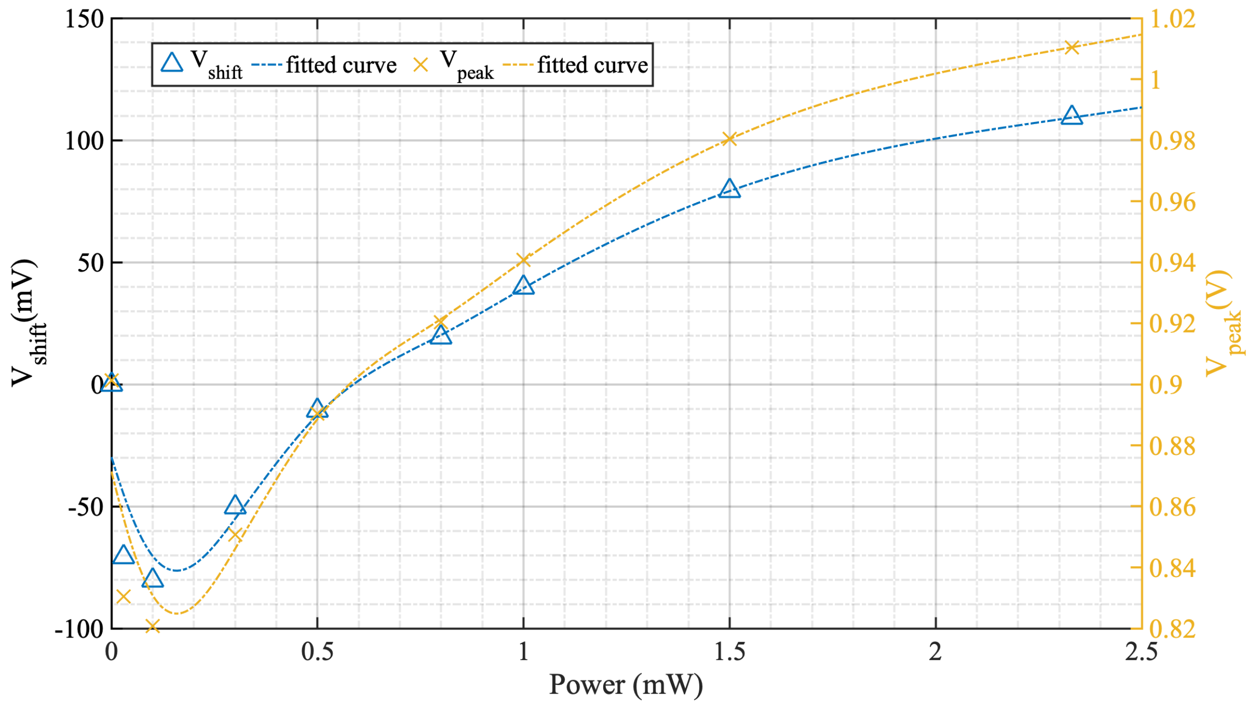

Figure 90: Peak voltage and peak-voltage shift as function of applied illumination levels.

The peak voltage spans between 0.82 V up to 1 V, which corresponds to a peak-voltage shift span between -75 mV to 110 mV.

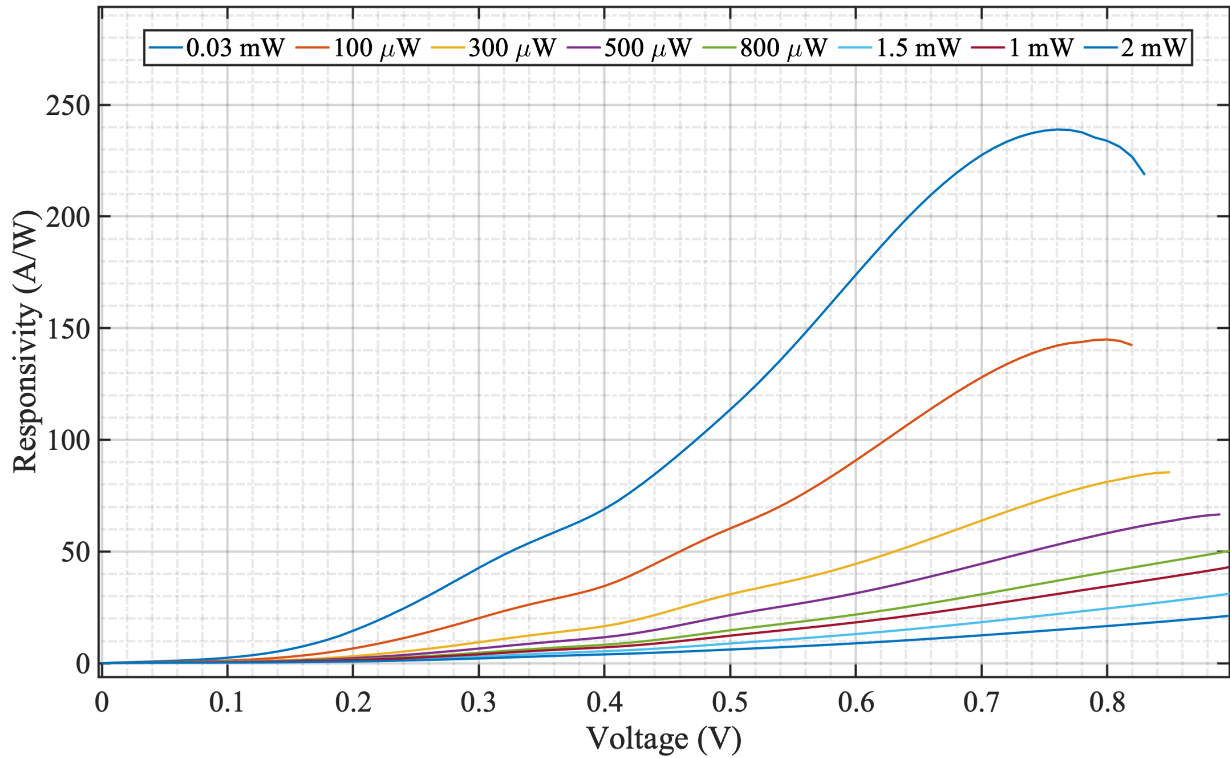

Figure 91: Current responsivity curves for sample S99 as function of voltage under reverse bias.

The *IVs* show the *PVCR* enhancement observed in wafer NC1800 with the dark *PVCR* being 1.7 and going up to 4.1 under illumination. This enhancement is accompanied by a reduction in ΔV; as the device stabilizes with increasing light illumination. The same arguments for the conductivity enhancement made for wafer NC1800 are valid here as well. Furthermore, the *IVs* and the responsivity graphs show no net current (absorption) taking place in the second *PDR*. This is interesting as this contributes to better *PVCR* by not increasing the valley current.

Examining the responsivity figures, the same observations for sample NC1800 show for this sample also. Both the non-linear behavior and the fact that the current responsivity is inversely proportional to the illumination power. Figure 92 shows this dependance.

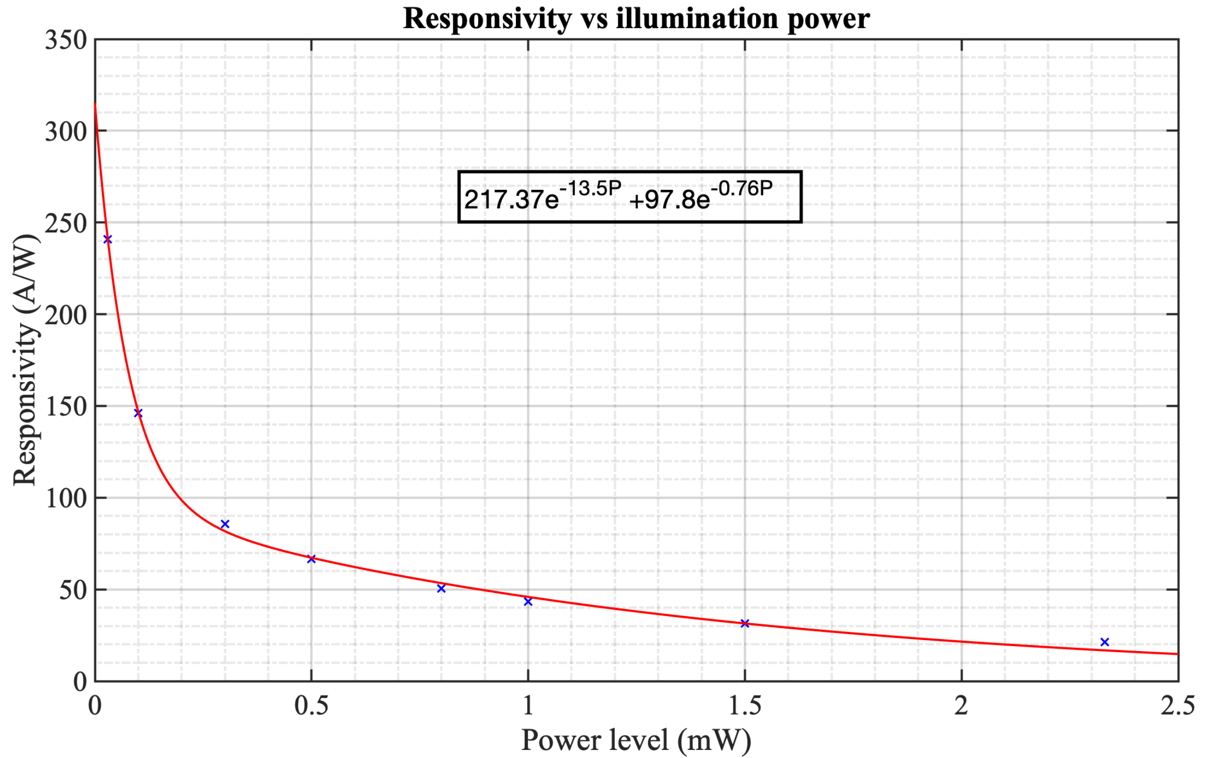

Figure 92: Responsivity as function of applied illumination levels for sample S99.

The responsivity results for this sample are impressive, so we decided to check how these devices performed under lower illumination levels. The aim is to check the possibility of operating these devices as single photon detectors at room temperature. The optical power was reduced using a variable attenuator (VOA50 from Thorlabs). The lowest power level we could verify using our optical detector (Anritsu ML9001A) was 31 pW. The selected powers were 400 pW, 100 pW, and 31 pW. Figure 93 shows the results. The inverse relationship between the illumination power and the responsivity persists, with a maximum responsivity of approximately 1.4×10^{7} A/W. This is the highest number reported for such illumination levels to date. Figure 94 shows the *IVs* with the induced peak-voltage shift.

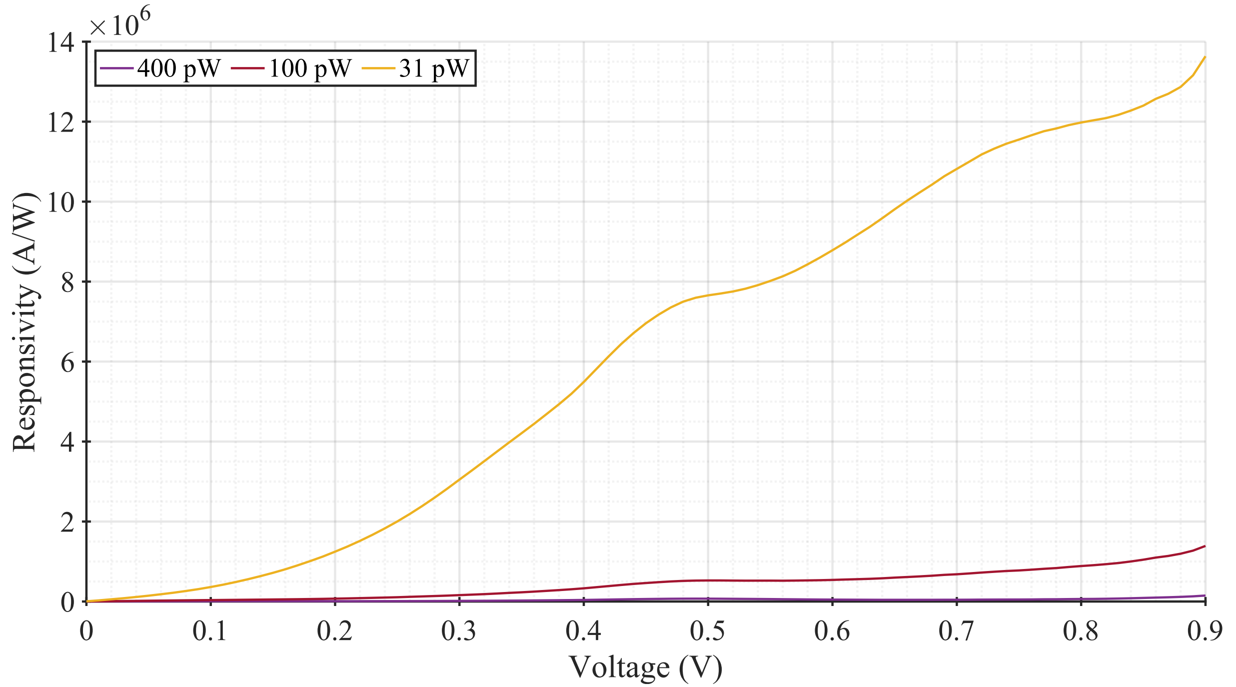

Figure 93: Low illumination responsivity of sample S99.

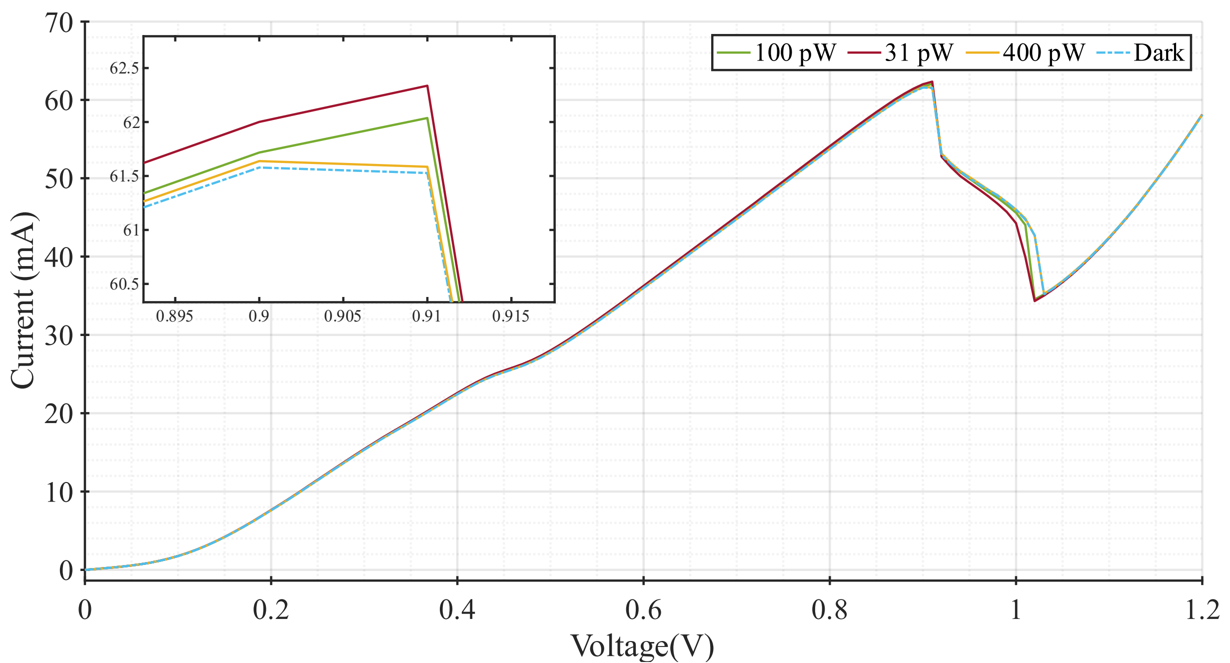

Figure 94: Sample S99 IVs under low illumination levels.

5.3.3 Sample S98

The epitaxial layer design for this sample is shown in Table 5-3. This epi-layer has a 100 nm absorption region at one end, and a 20 nm region at the other end. The doping profile is symmetrical with both doping levels being 2×10^{16} cm^{-3}. Regarding the quantum-well design, this sample has a 5.7 nm quantum well between two 1.7 nm *AlAs* barriers. We

take the opportunity again to highlight the presence of a thick (500 nm) bottom contact that is highly doped. Another thing to note about this design is the presence of $In_{52}Al_{48}As$ layers at both ends. This layer has a higher bandgap than $In_{53}Ga_{47}As$ (around 1.47 eV) which makes it transparent to light energy coming from 1.55 μm or 1.31 μm light sources.

Table 5-3: Epi-layer design of sample S98.

Layer	Type	Material	Thickness (nm)	Doping level (cm^{-3})
1	N++	$In_{53}Ga_{47}As$	100	2×10^{19}:Si
2	N+	$In_{52}Al_{48}As$	100	2×10^{18}:Si
3	N-	$In_{53}Ga_{47}As$	100	2×10^{16}:Si
4	I	$In_{53}Ga_{47}As$	2	Undoped
5	I	AlAs	1.7	Undoped
6	I	$In_{53}Ga_{47}As$	5.7	Undoped
7	I	AlAs	1.7	Undoped
8	I	$In_{53}Ga_{47}As$	2	Undoped
9	N-	$In_{53}Ga_{47}As$	20	2×10^{16}:Si
10	N+	$In_{52}Al_{48}As$	100	2×10^{18}:Si
11	N++	$In_{53}Ga_{47}As$	500	2×10^{19}:Si
12	I	$In_{52}Al_{48}As$	100	-
13	SI	InP	20	-

As with sample S99, this wafer only showed an *NDR* at reverse bias conditions. The anticipated peak using the calculation method of chapter 3 is around 1 V in reverse bias mode and goes up to 2.7 V in forward bias mode. The same problem with the devices shorting at higher voltages persists here as well, which is believed to be related to the fabrication of the devices and not a limitation of the design itself.

In terms of the peak shifting behavior, this design shows only a shift to higher voltages and does not seem to shift to lower ones even at lower illumination levels. Otherwise, the results in terms of *PVCR*, ΔV, responsivity, and photocurrent are in-line with the observations of the previous wafers.

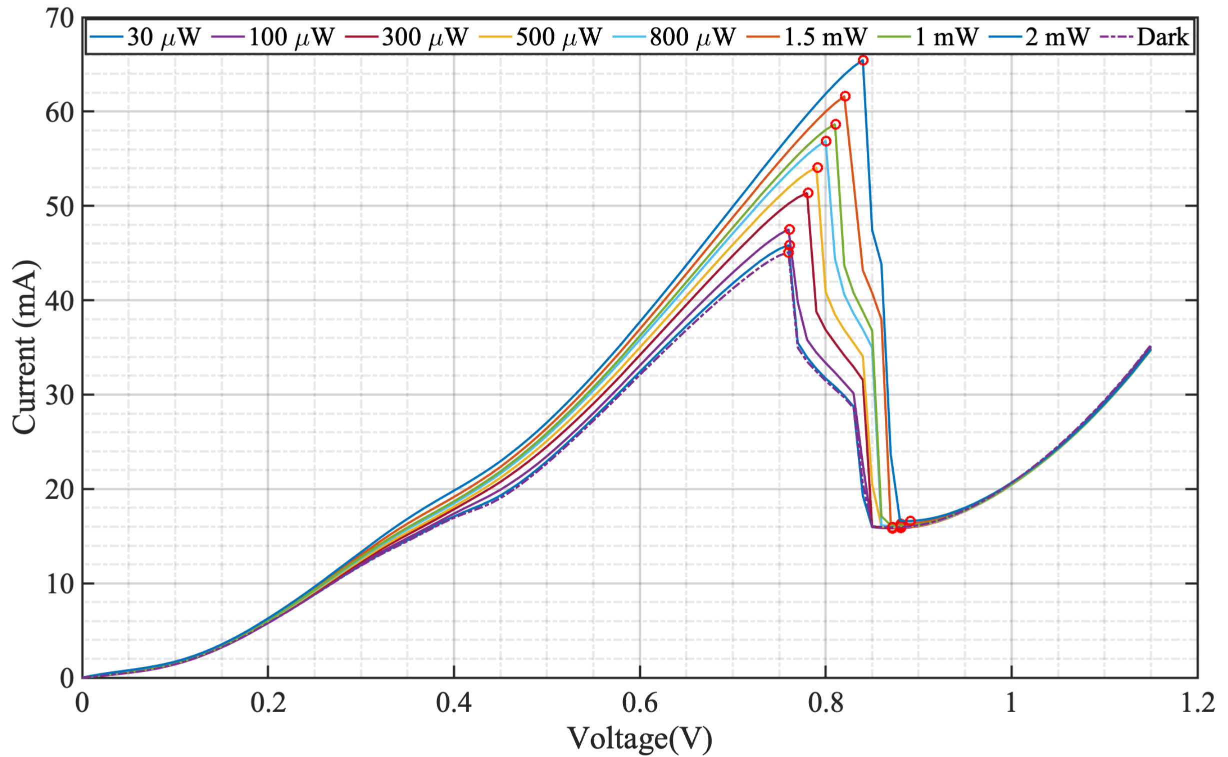

Figure 95: IV curves under reverse bias for sample S98 (10×10 μm²).

This phenomenon can be explained as follows: stemming from the idea that the observed shift is dependent on the concentration gradient between the emitter and the collector, we see that sample S99 has a longer absorption (250 nm) region at the emitter while sharing the same collector length with this sample. With that in mind, the carrier concentration of the photo-generated carriers in this epi-layer should be greater than S99 as the number of generated carriers is the same for a given illumination power. To test this hypothesis, we characterized larger-area devices from this wafer (20x20 μm²). The results seem to support the hypothesis as the *IVs* now show the same trend of shifting to lower voltages.

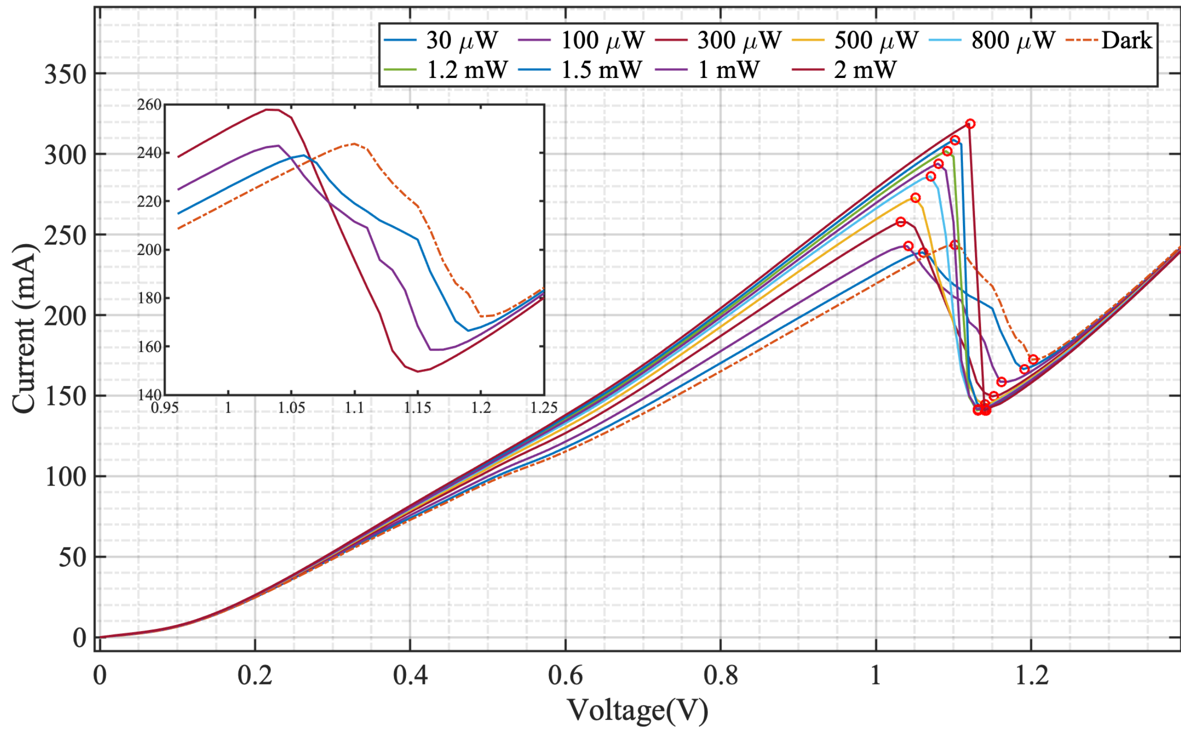

Figure 96: IV curves for sample S98 under reverse bias for 20x20 μm² devices.

Figure 97 shows how the peak voltage shift as a function of voltage for this device size changes with illumination levels. The results agree with the ones shown previously.

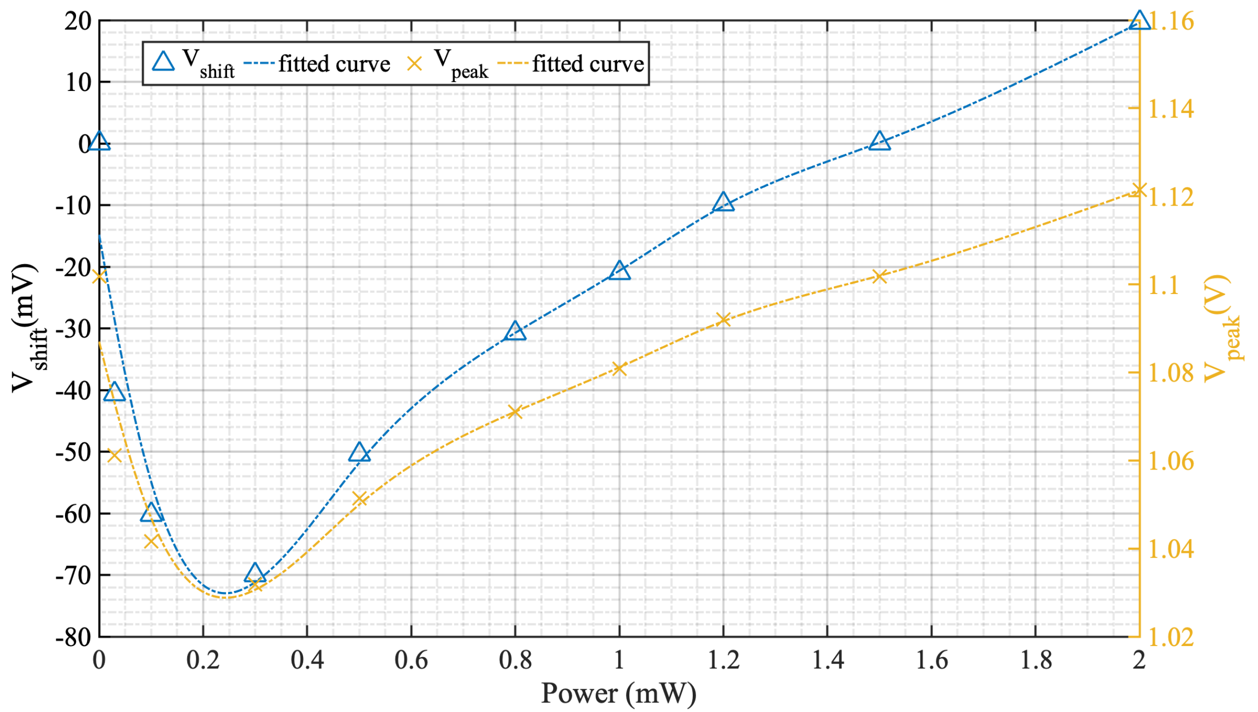

Figure 97: Peak voltage and peak-voltage shift versus illumination levels for sample S98 (20×20 μm²).

The peak voltage spans between 1.03 V up to 1.12 V, which corresponds to a peak-voltage shift span between -70 mV to 20 mV.

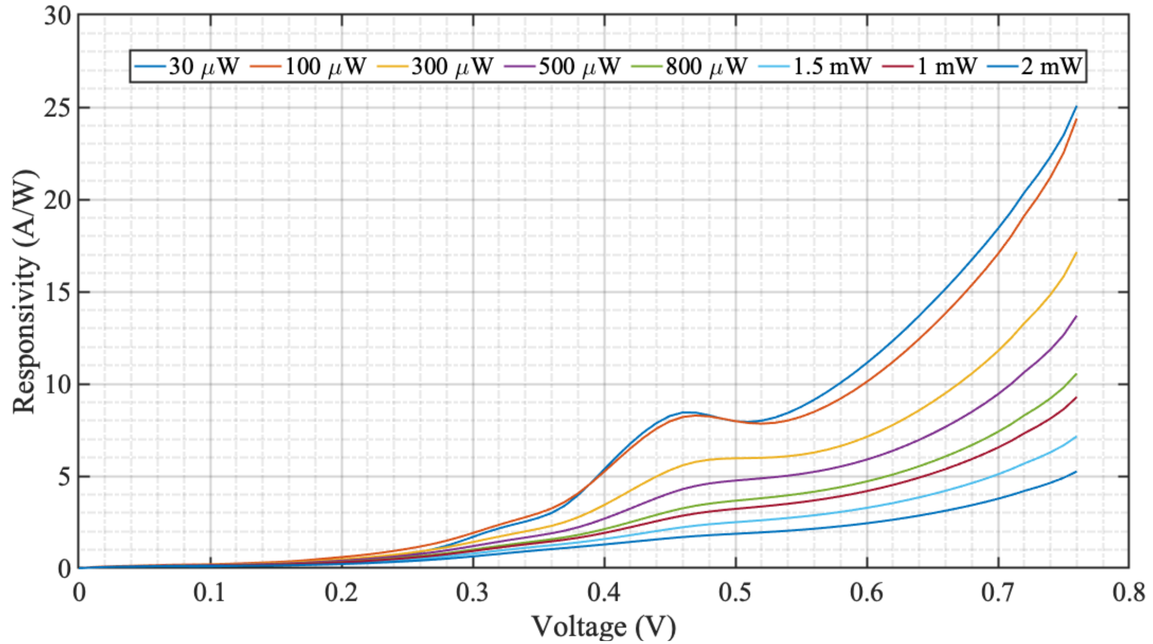

Figure 98: Current responsivity as function of voltage in reverse bias for S98 (10×10 μm²).

The current responsivity curves for the 10x10 μm² devices show that the peak responsivity happens at the peak voltage point, while the responsivity curves, (Figure 99) for the larger-area devices, show the occurrence of the peak before that point, which agrees well with the explanation provided earlier.

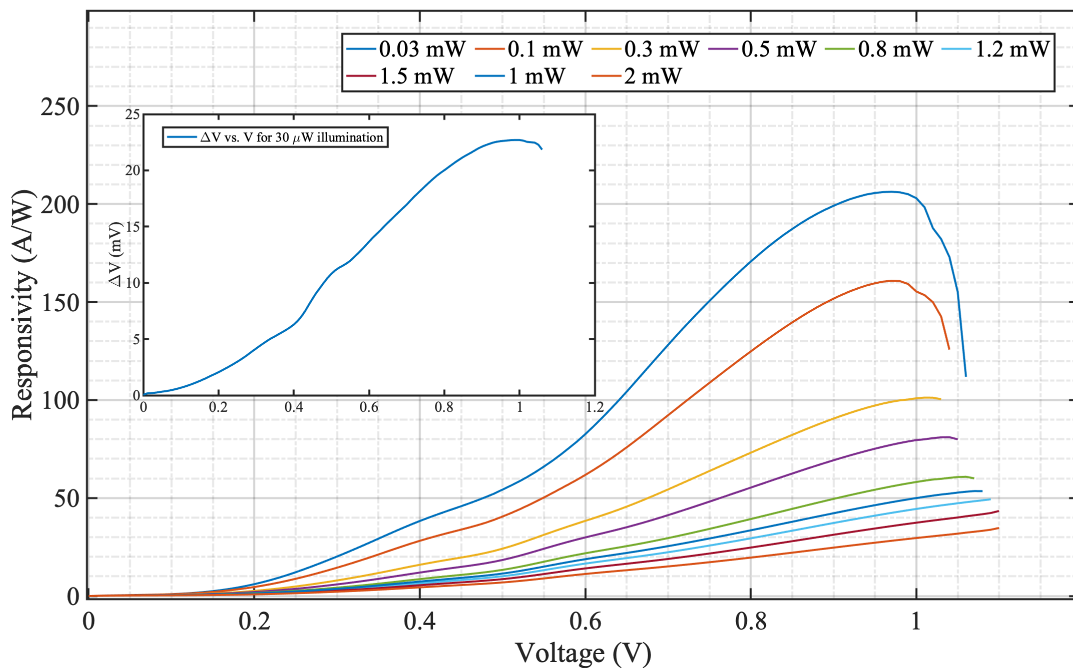

Figure 99: Current responsivity for sample S98 (20x20 μm²) – Inset shows ΔV vs V for 30 μW illumination. Notice the similarity between the two curves as highlighted earlier.

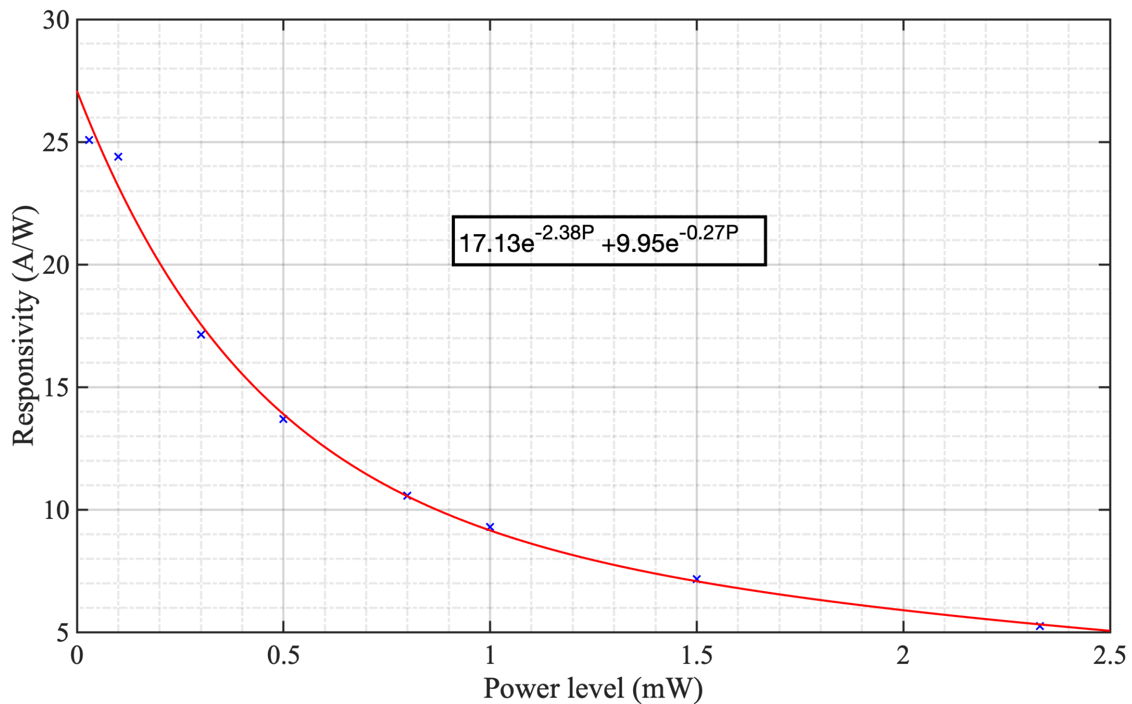

Figure 100: Responsivity versus illumination power under reverse bias for sample S98 (10×10 μm²).

The same procedure was done for this sample also, to measure the low-illumination responsivity. The maximum value obtained from this sample is around 9×10^{6} A/W at 31 pW of illumination power.

5.3.4 Sample P-A323

The epi-design of this sample is shown in Table 5-4. This epi-layer has a 200 nm absorption region at one end, and a 25 nm region at the other. The doping profile is asymmetric with the longer absorber being intrinsic (unintentionally doped), and the shorter one doped to the level of $1\text{x}10^{17}$ cm^{-3}. Regarding the quantum-well design, this sample has a wide 7.5 nm quantum well between two 1.5 nm *AlAs* barriers. We take the opportunity again to highlight the presence of a thick (200 nm) bottom contact that is highly doped. Another thing to note about this design is that it is made entirely of $In_{53}Ga_{47}As$ (excluding the barriers), which means that absorption takes place at all locations. The rationale behind designing wider wells is to produce an *NDR* in both bias directions at reasonable voltages while maintaining an intrinsic layer at the collector.

Table 5-4: Epi-layer design for sample P-A323.

Layer	Type	Material	Thickness (nm)	Doping level (cm^{-3})
1	N++	$In_{53}Ga_{47}As$	50	3×10^{19}:Si
2	N+	$In_{53}Ga_{47}As$	50	3×10^{18}:Si
3	N-	$In_{53}Ga_{47}As$	200	Undoped
4	I	$In_{53}Ga_{47}As$	5	Undoped
5	I	AlAs	1.5	Undoped
6	I	$In_{53}Ga_{47}As$	7.5	Undoped
7	I	AlAs	1.5	Undoped
8	I	$In_{53}Ga_{47}As$	5	Undoped
9	N-	$In_{53}Ga_{47}As$	25	1×10^{17}:Si
10	N+	$In_{53}Ga_{47}As$	200	3×10^{18}:Si
11	N++	$In_{53}Ga_{47}As$	200	3×10^{19}:Si
12	SI	InP	-	

This epi-layer was grown at the University of Würzburg using gas-source *MBE*. The design of the wafer was such that the absorption region remains undoped with only the background doping levels in the chamber. A Van-der-Pau measurement on a sample from the chamber shows a background doping of around 2×10^{15} cm^{-2}. Noting that this value is measured for the surface carrier distribution as the sample was not thick enough to measure the bulk. The advantage of an intrinsic layer is that the Debye length in the collector will be enhanced (around 100 nm in this case). This means the collector will be fully depleted, without any electric field dead zones, which was the case for the previous wafers. This not only allows us to study the effect of a high electric field on the overall responsivity of the device but, most importantly, on the speed of operation also as will be discussed in the sections related to the impulse response and *3dB* bandwidth. To achieve an *NDR* at reasonable voltages using such layers the quantum well is widened to lower the energy Eigenstates, thereby showing an *NDR* in both bias directions. The calculations were made with an anticipated peak voltage at 2.16 V in the forward bias case, and around 0.53 V in reverse bias. These devices are circular in shape with various diameters for the mesa of the *RTDs*. The mask used to produce these devices utilizes the back of the wafer as the ground plan. This is where the bottom metallization is deposited. Figure 101 shows a sketch and a *3D* render of typical devices using this mask. Figure 102 shows a picture of the fabricated devices. The *IV* curves for the tested devices are shown in Figure 103.

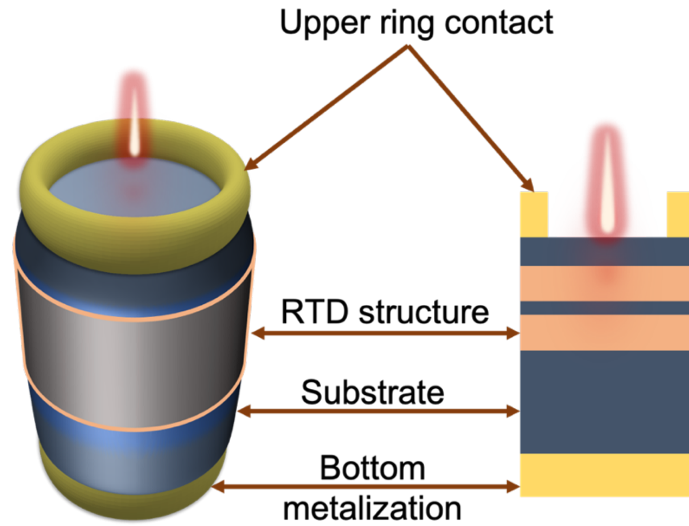

Figure 101: Sketch and 3D render of typical devices fabricated by the University of Würzburg.

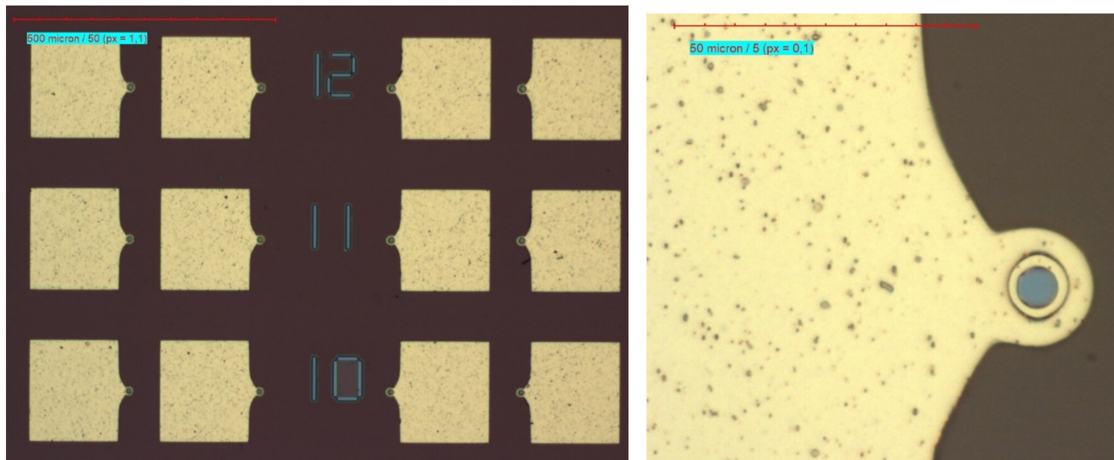

Figure 102: Optical microscope images of fabricated RTD-PD devices for samples P-A323/5.

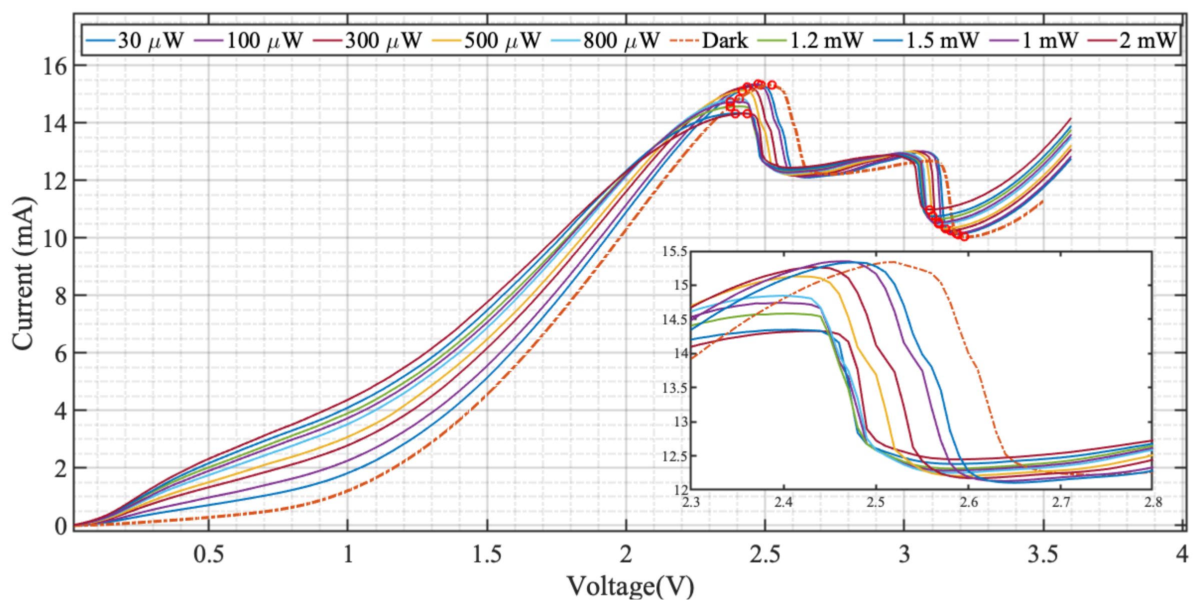

Figure 103: IV curves under forward bias for sample P-A323 (12 μm² diameter).

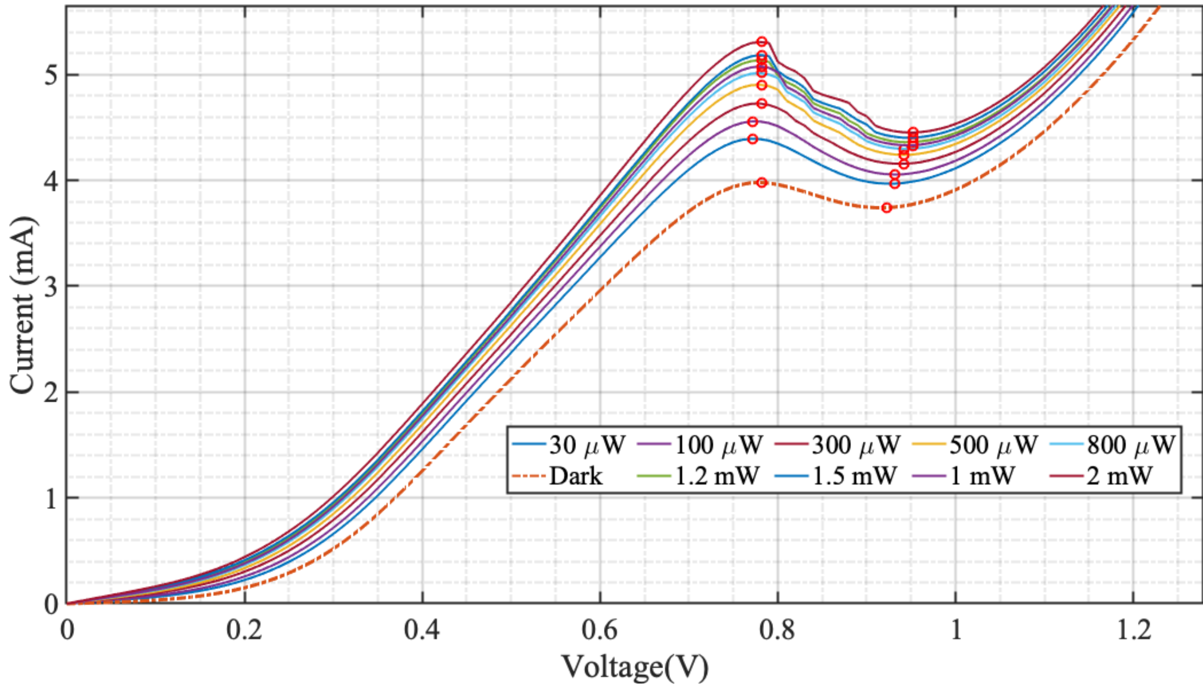

Figure 104:IV curves under reverse bias for sample P-A323 (12 μm² diameter).

The *IV* curves show an *NDR* in both forward and reverse bias modes. The peak shifting behavior in this wafer is interesting. In the forward bias mode, all illumination levels seem to shift the peak to lower values. At a certain illumination level, the peak shifts back the other way and the current decreases.

Since these wafers have an intrinsic absorption layer at the collector, which is rather long, two things will take place. Firstly, the number of generated carriers at the collector will be much greater than those at the emitter. This has to do with the increased absorption length and the enhanced absorption coefficient for an intrinsic collector compared to the degenerately doped emitter. Secondly, since most of the collector's length is depleted, the electric field is high (greater than 1×10^7 V/m) therefore, carriers drift at saturation velocities.

For the forward-bias case, the shift to lower values at this point does support the theory of charge accumulation, and the decrease in the current might be a signature of the recombination of the accumulated holes at the collector's barrier. As more holes recombine, the current will decrease, and the concentration of the accumulated holes will also decrease. This leads to the peak shifting back towards its original dark position as the illumination levels increase. The recombination process taking place is most likely of the non-radiative type (Auger recombination), which is typical for high carrier concentrations [119], [129]. We have

attempted to measure any electro-luminescence from these devices, but no emission was detected.

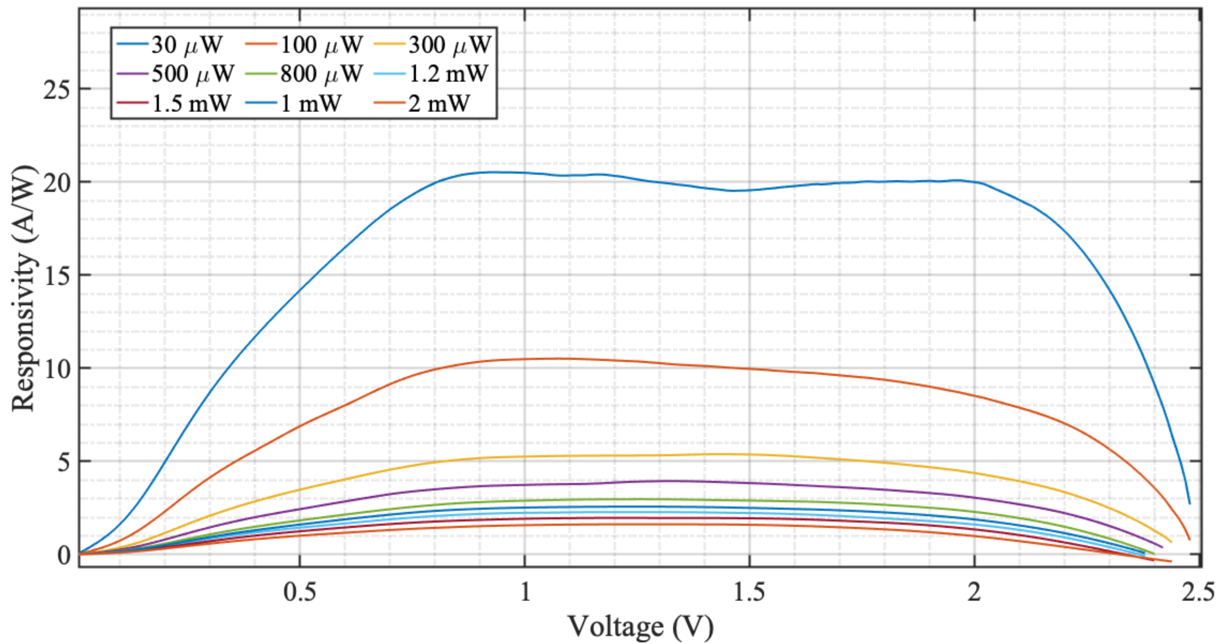

Figure 105: Current responsivity curves under forward bias for sample P-A323.

The responsivity figures in the forward bias case also show an interesting behavior. Mainly the presence of a rather constant response over a certain voltage window. This is due to two reasons; first, the responsivity is driven by the shift in voltage and not a change in current. Second, due to the intrinsic region, there is a large voltage span (between 1 – 2 V) where the shape of the *IVs* is linear. This is an interesting result as it shows responsivity behavior similar to that of a *PIN*-photodiode. However, the responsivity in the reverse bias case is identical to that of the previous wafers.

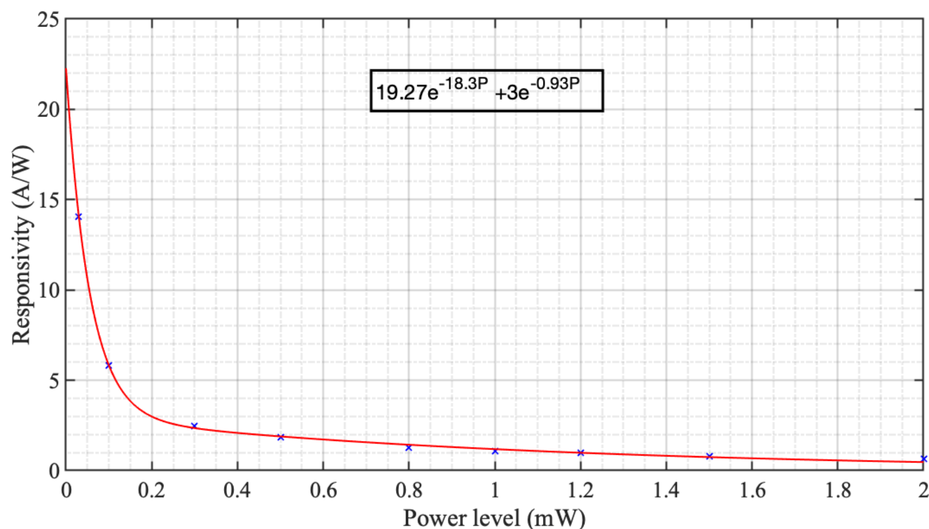

Figure 106: Responsivity versus illumination power under forward bias for sample P-A323.

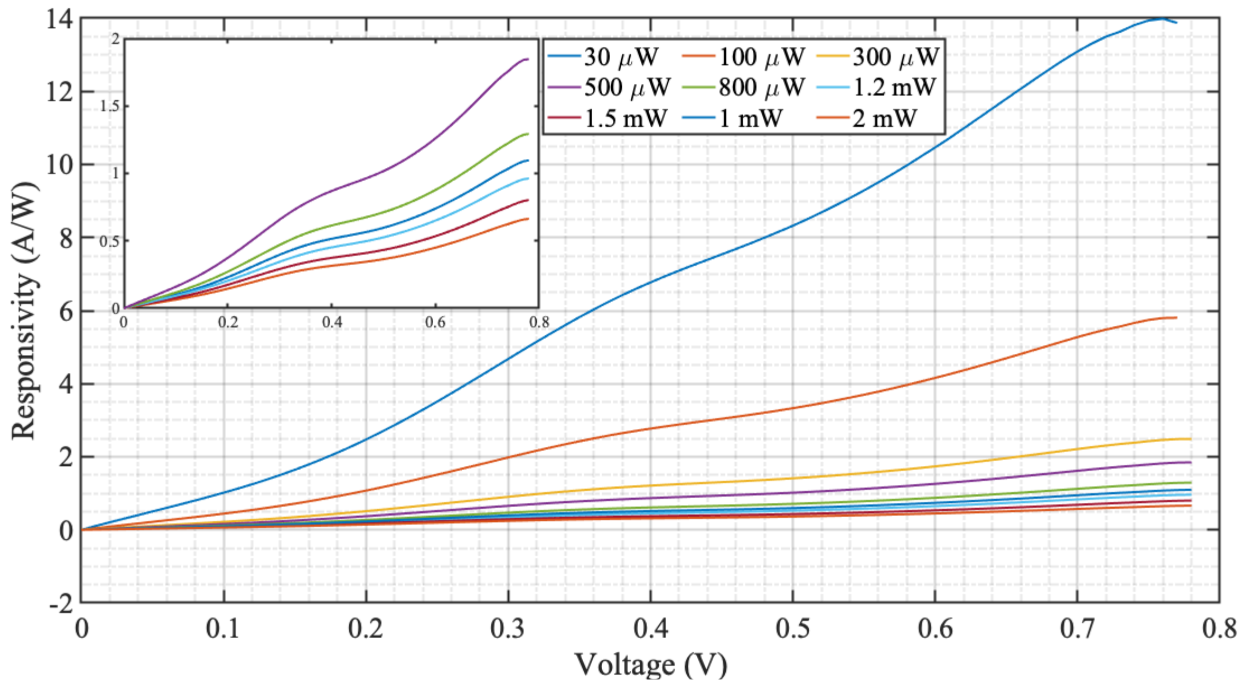

Figure 107: Current responsivity curves under reverse bias for sample P-A323.

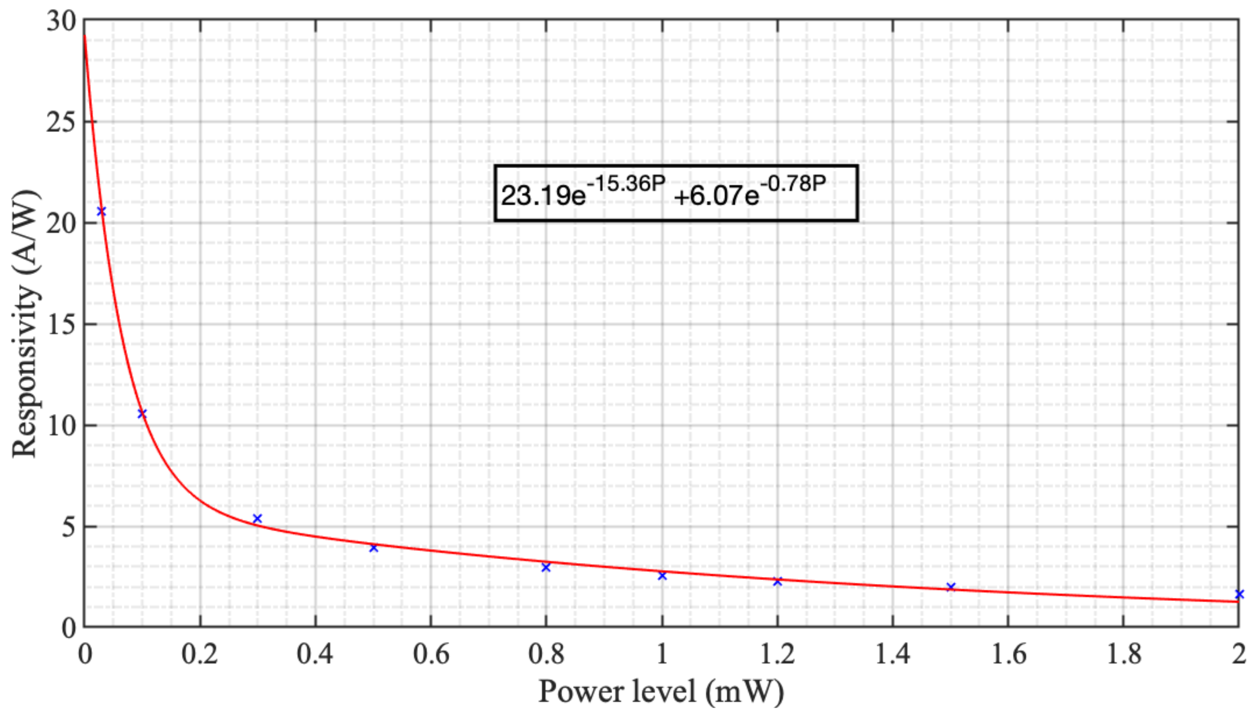

Figure 108: Responsivity versus illumination power under reverse bias for sample P-A323.

5.3.5 Sample P-A325

The epi-design of the first sample is shown in Table 5-5. This epi-layer has a 300 nm absorption region at one end, and a 25 nm region at the other. The doping profile is not symmetric with the longer absorber being intrinsic (unintentionally doped) and the shorter one doped to $1\text{x}10^{17}$ cm^{-3}. Regarding the quantum-well design, this sample has a wide 9.5

nm quantum well between two 1.5 nm *AlAs* barriers. We take the opportunity again to highlight the presence of a thick (200 nm each) bottom contact that is highly doped. Another thing to note about this design is that it is made entirely of $In_{53}Ga_{47}As$ (except for the barriers of course), which means absorption takes place at all locations. The rationale behind designing wider wells was to produce an *NDR* in both bias directions, while maintaining an intrinsic layer at the collector.

Table 5-5: Epi-layer design for sample P-A325.

Layer	Type	Material	Thickness (nm)	Doping level (cm^{-3})
1	N++	$In_{53}Ga_{47}As$	50	3×10^{19}:Si
2	N+	$In_{53}Ga_{47}As$	50	3×10^{18}:Si
3	N-	$In_{53}Ga_{47}As$	300	Undoped
4	I	$In_{53}Ga_{47}As$	5	Undoped
5	I	AlAs	1.5	Undoped
6	I	$In_{53}Ga_{47}As$	9.5	Undoped
7	I	AlAs	1.5	Undoped
8	I	$In_{53}Ga_{47}As$	5	Undoped
9	N-	$In_{53}Ga_{47}As$	25	1×10^{17}:Si
10	N+	$In_{52}Al_{48}As$	200	3×10^{18}:Si
11	N++	$In_{53}Ga_{47}As$	200	3×10^{19}:Si
12	SI	InP	-	

This sample is built on the same concept as P-A323, with an elongated collector of 300 nm. This will allow us to see the effect of the length of the intrinsic absorption region on the overall device responsivity. Again, the quantum well here was widened further to 9.5 nm to have a peak voltage at around the same value as sample P-A323. This would be important for comparison purposes.

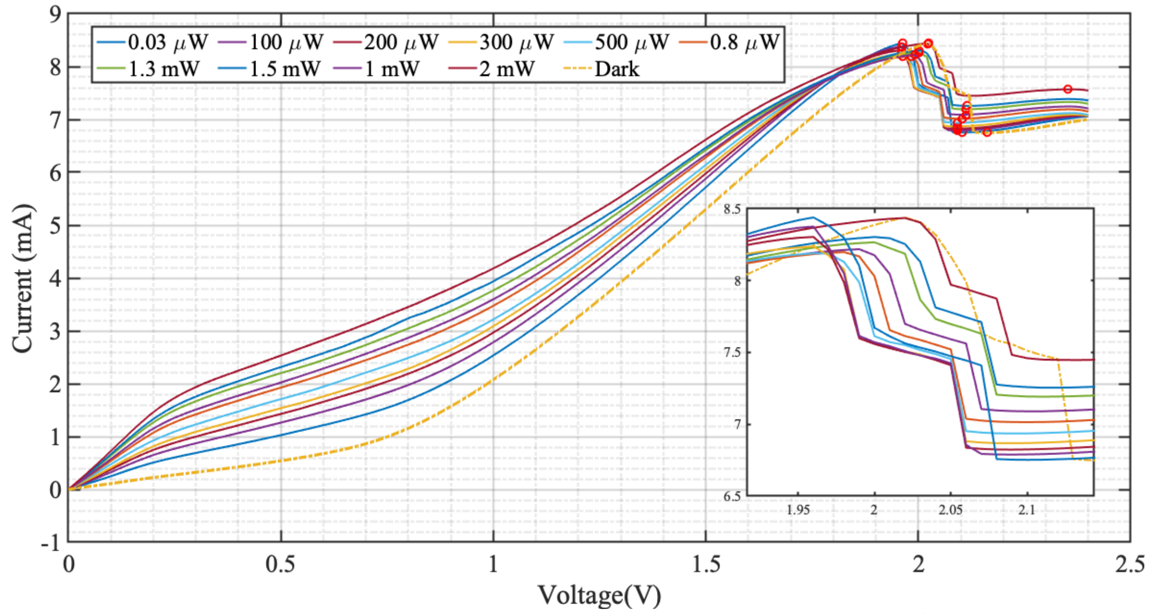

Figure 109: IV curves under forward bias for sample P-A325 (15 μm² diameter).

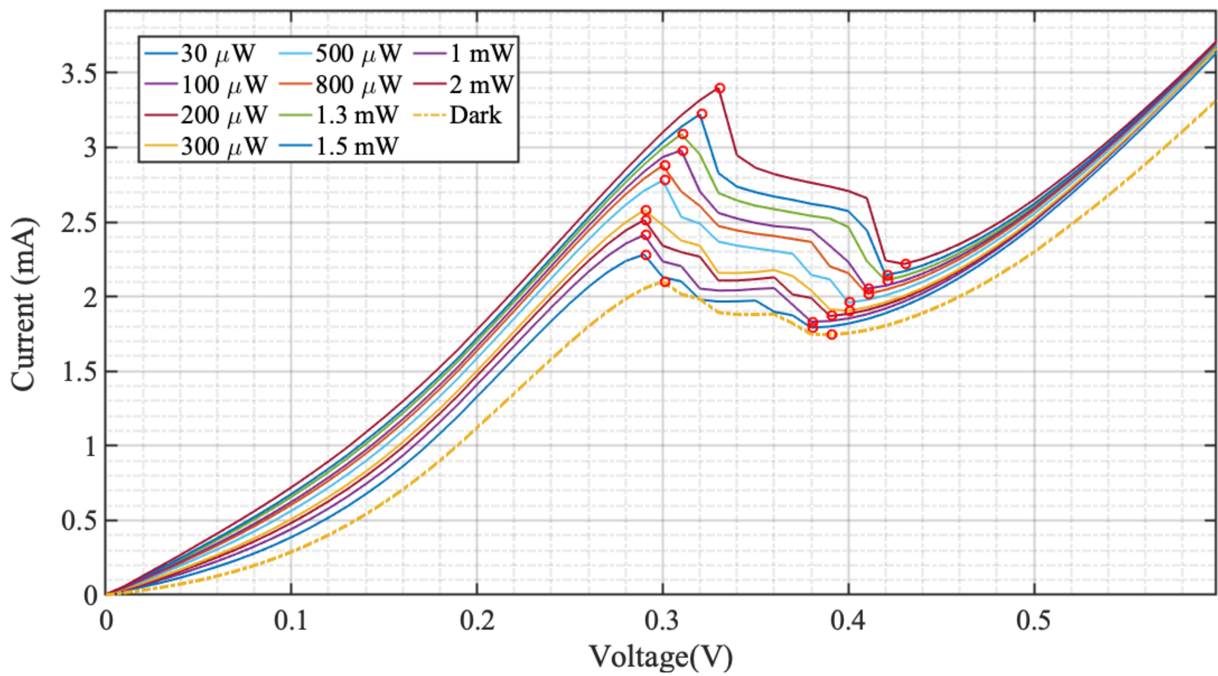

Figure 110: IV curves under reverse bias for sample P-A325 (15 μm² diameter).

Regarding the voltage shift, this sample exhibits the same behavior as P-A323. The discussion made regarding sample P-A323 applies here as well.

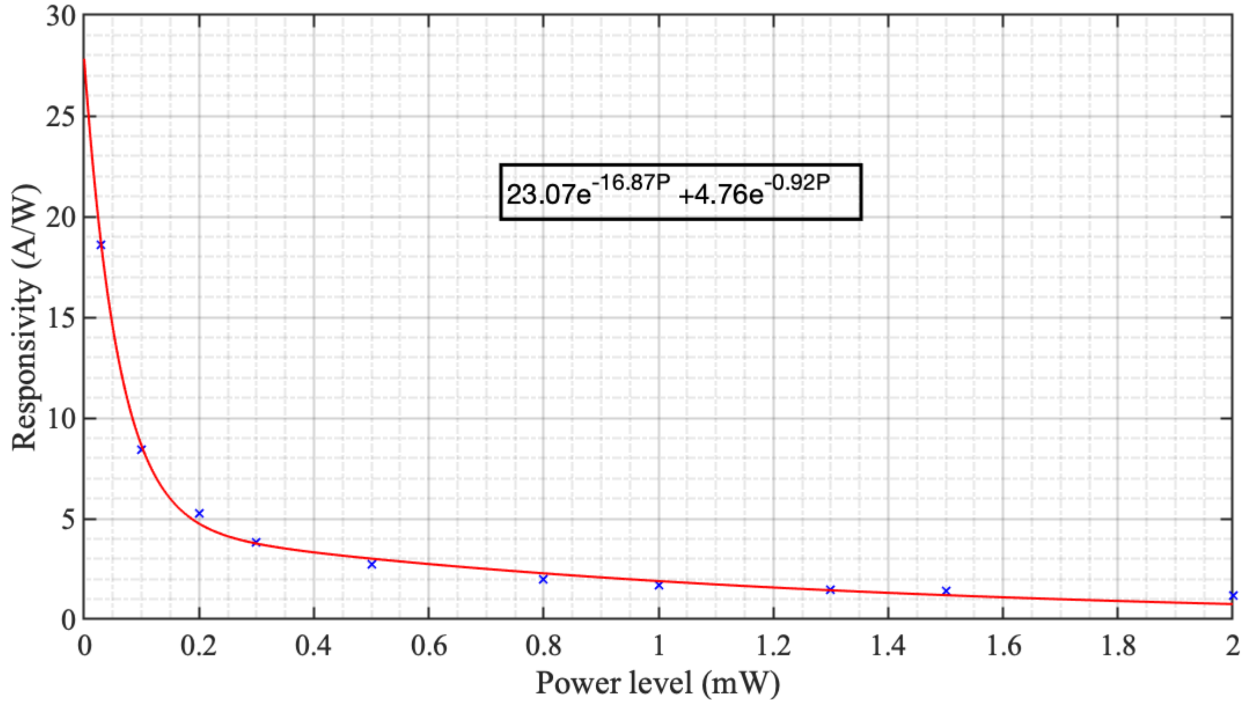

Figure 111: Responsivity versus illumination power under forward bias for sample P-A325.

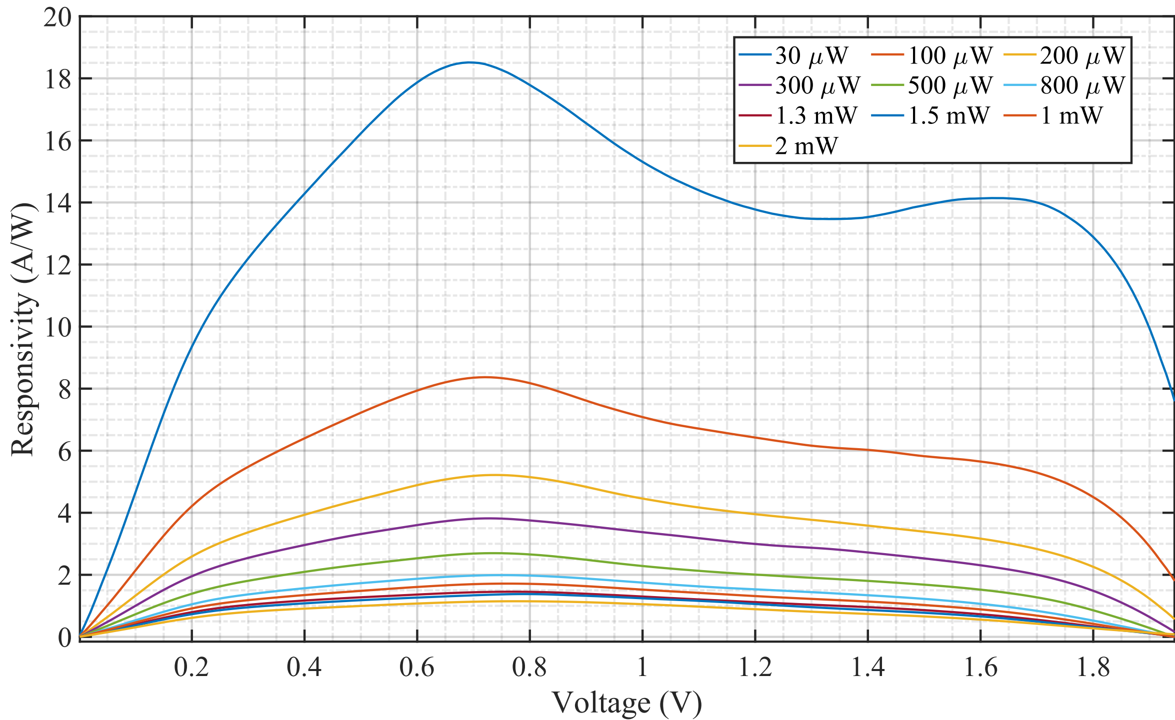

Figure 112: Current responsivity under forward voltage for sample P-A325.

There are a couple of things to note about the responsivity in Figure 112 compared to the responsivity of sample P-A323.

First, the maximum responsivity for sample P-A323 is higher for the same illumination level. For instance, at 30 μW the responsivity for P-A323 is around 20 A/W, while the

maximum responsivity for P-A325 is 18 A/W. Although the results might seem counterintuitive, since the absorption length in P-A325 is longer, this sort of output is logical. Considering that the bottom contact of these samples is at the backside of the substrate, the light will pass through the device at least twice. This is because the beam will reflect from the bottom metallization and get re-absorbed in the device. The point is; that most of the beam's energy is absorbed in both cases because the absorption length is in the micro-meter range. Given the exponential nature of the carrier generation due to light absorption, any increase in the length of the main absorption region (the collector) will not increase the number of generated carriers by much. On the other hand, elongating the collector will reduce the total concentration of the generated carriers, thereby reducing the overall photocurrent. This explains why the responsivity is lower for sample P-A325.

The second observation is the reduction in the voltage span, over which the responsivity is constant. This can be attributed to the lower peak voltage of sample P-A325 at around 2 V compared to 2.5 V for sample P-A323.

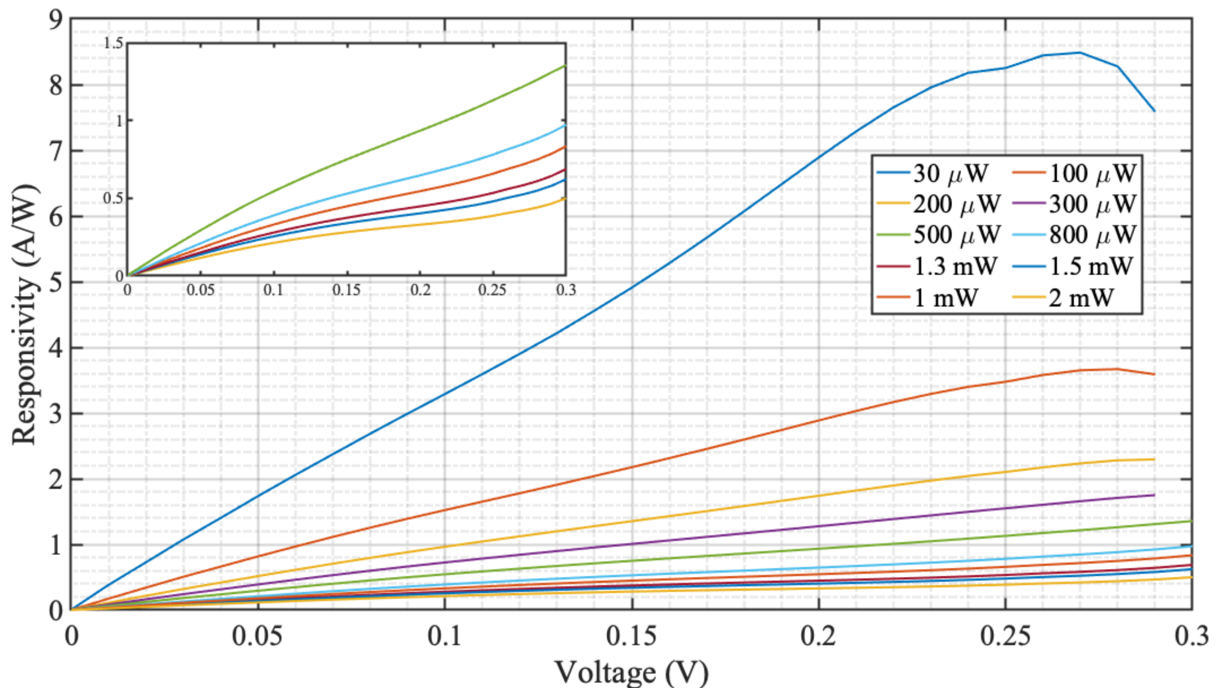

Figure 113: Current responsivity under reverse bias for sample P-A325.

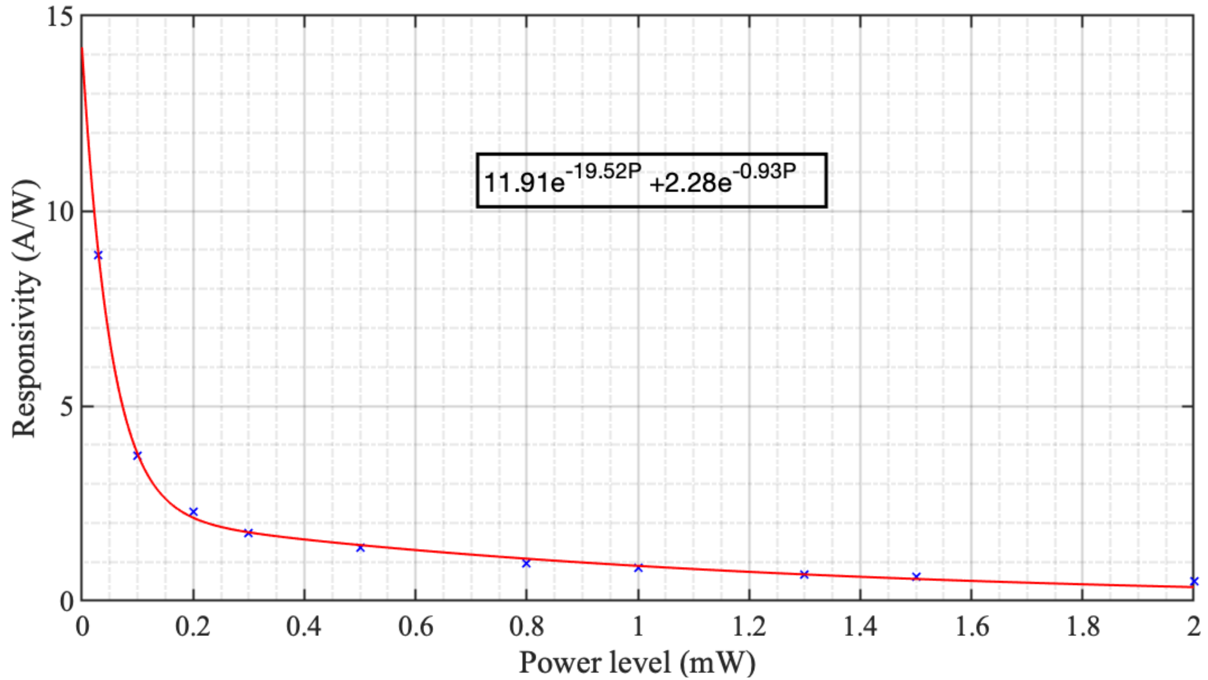

Figure 114: Responsivity versus illumination power under reverse bias for sample P-A325.

At this stage it is appropriate to summaries the main features of the samples. These are shown in Table 5-6.

Table 5-6: Summary of the main samples' characteristics.

Sample name	Responsivity at 1 mW (A/W)	Responsivity at 31 pW (A/W)	Maximum peak voltage shift (mV)	Maximum ΔV (mV)
NC1800	20	-	-90	190
S99	45	1.4×10^{7}	100	150
S98	9	9×10^{6}	100	100
P-A323 (RB)	2.2	-	0	15
P-A325 (RB)	1	-	30	100
P-A323 (FB)	1	-	-100	750
P-A325 (FB)	1.8	-	-65	60

5.3.6 *Wafer A73*

The epi-layer design of this sample is shown in Table 5-7. This wafer has a 500 nm absorption region at both sides of the *DBQW* with a 5.7 nm quantum well between 1.7 nm *AlAs* barriers. The absorption region for this sample has small amounts (around 8%) of aluminum added. This has the effect of increasing the bandgap to around 0.85 - 0.9 eV [130], [131] therefore, its responsivity to 1.55 μm light is not high hence, we only will use this wafer in the impulse response section for speed considerations, and to demonstrate the *RTD-PD*'s amplification capabilities.

Table 5-7: Epi-layer design for sample A73.

Layer	Type	Material	Thickness (nm)	Doping level (cm^{-3})
1	N++	$In_{53}Ga_{47}As$	100	2×10^{19}:Si
2	N+	$In_{52}Al_{48}As$	300	2×10^{18}:Si
3	N-	$In_{53}Al_{0.08}Ga_{46.2}As$	500	5×10^{16}:Si
4	I	$In_{53}Al_{0.08}Ga_{46.2}As$	2	Undoped
5	I	$AlAs$	1.7	Undoped
6	I	$In_{53}Ga_{47}As$	5.7	Undoped
7	I	$AlAs$	1.7	Undoped
8	I	$In_{53}Al_{0.08}Ga_{46.2}As$	2	Undoped
9	N-	$In_{53}Al_{0.08}Ga_{46.2}As$	500	5×10^{16}:Si
10	N+	$In_{52}Al_{48}As$	300	2×10^{18}:Si
11	N++	$In_{53}Ga_{47}As$	500	2×10^{19}:Si
12	SI	InP	20	-

5.3.7 Photoconductive wafer

The epi-layer design of this sample is shown in Table 5-8. This does not have a *DBQW* instead it only has a 1 µm long $In_{53}Ga_{47}As$ absorption region, with n-type doping at a level of 5×10^{16} cm^{-3}. This also has a thick bottom contact layer and layers of $In_{52}Al_{48}As$ at both ends.

Table 5-8: Epi-layer design for sample "Photoconductor".

Layer	Type	Material	Thickness (nm)	Doping level (cm^{-3})
1	N++	$In_{53}Ga_{47}As$	100	2×10^{19}:Si
2	N+	$In_{52}Al_{48}As$	300	2×10^{18}:Si
3	N-	$In_{53}Ga_{47}As$	1000	5×10^{16}:Si
4	N+	$In_{52}Al_{48}As$	300	2×10^{18}:Si
5	N++	$In_{53}Ga_{47}As$	500	2×10^{19}:Si
6	I	InP	20	

One of the main ideas behind this wafer was to study how the double barrier is affecting both the speed and responsivity of a device by testing a similar structure without the inclusion of the *DBQW*.

This epi-layer is interesting on its own and deserves more attention to its principle of operation, as the devices on the wafer resemble a double heterostructure diode (*DHD*).

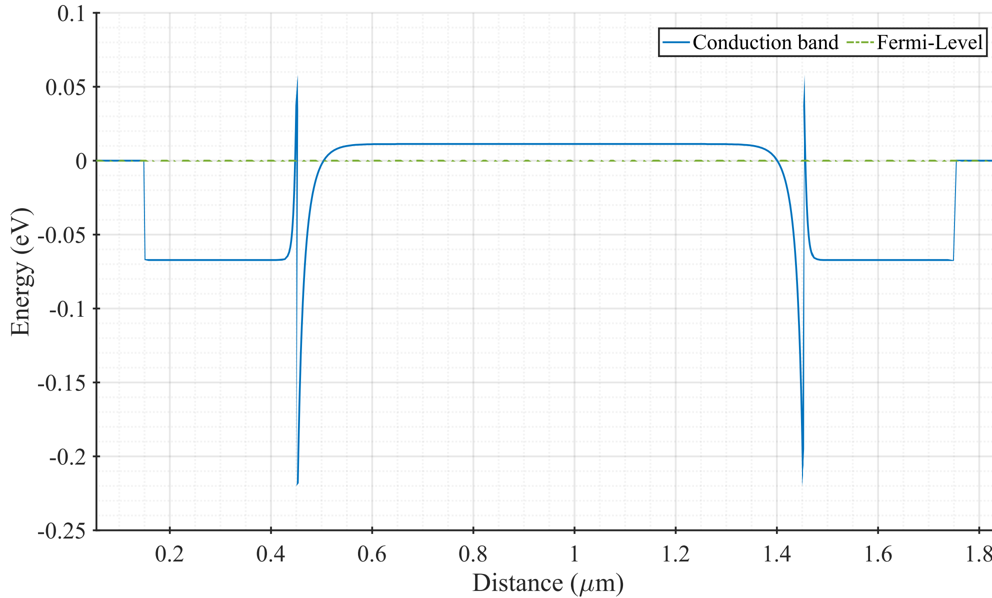

Figure 115: conduction band diagram (flat-band) of DHD (green line is the Fermi-energy).

First of all, the device has two heterointerfaces between the $In_{48}Al_{52}As$ and $In_{53}Ga_{47}As$ layers. The band lineup between these two material systems is of the straddling edge type, which gives an effective barrier height in the conduction band of around 250 meV on each side. As with any heterointerface, this forms an accumulation region at one end and a depletion region at the other. Since there are two heterojunctions, there will always be one forward-biased junction and one reverse-biased junction. The reverse-biased junction will widen as more potential is applied, giving rise to an area of high resistance in the device. Contrary to a normal photoconductor, the potential will mostly drop across the high resistance depletion region, not on the main absorption region of the device. The depletion width at 1 V will be around 200 nm, which leaves about 800 nm of the device with a near-zero electric field. Therefore, the expected device current will be low as the resistance is in the range of kΩs. The expected current for such devices should be in the 10-mA range, depending on the size. We believe that the *NDR* observed in some of these devices is due to a combination of the Gunn effect and tunneling from the heterointerface. Given the doping concentration level, the Fermi level should be about 100 meV below the top of the hetero-barrier. Therefore, the tunneling current will increase until around 0.2 V, after which the transport mechanism will be dominated by the thermionic emission. This is supported by a simulation using Silvaco with different transport models used. The inclusion of the drift-diffusion, tunneling, and Gunn effects yields the results observed in the tested devices.

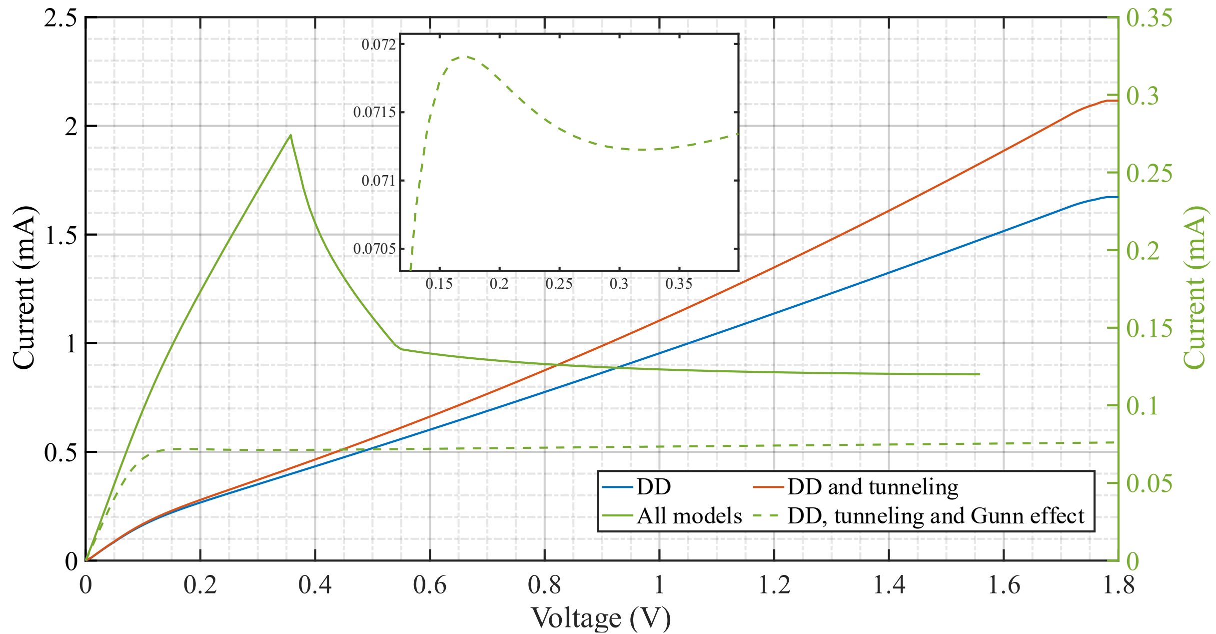

Figure 116: Silvaco simulation of DHD with drift diffusion and Tunneling models. Inset shows the NDR resulting from the Gunn effect between 0.15 V and 0.35 V.

However, due to the Gunn effect, detecting light is highly improbable. That is why most of the devices tested in the first run did not show any response to light, which we attributed to closed optical windows at first. This turned out not to be the case for all of them, although the yield on window opening was not high. To prove so, we applied high voltage to some of the devices, which should break the heterointerface down and make the device-effectively- a photoconductor. By doing so, these devices started showing higher currents and responses to light. It could also be the case, that with high voltage, there is charge accumulation at the heterointerface, which lowers the barriers, paving the way for thermionic emission. This is evident in some devices which show higher currents but tend to revert to their original state when applying a reverse polarity for one run and testing them in their normal polarity again.

Figure 117 shows how a typical device starts off with a nearly linear *IV* then (as per the simulations) we see a drastic decrease in current due to both tunneling and the advent of the Gunn effect, and an *NDR*-like *IV* is observed. When a reverse sweep is done, the current remains low. The device holds its state of low current until a reverse polarity sweep is made which applies a voltage that is at least the same as the peak voltage in the set-cycle. We then observe a sharp increase in current and the return path now has higher current values. Doing another forward sweep afterwards will give rise to the *NDR*-like behavior again. This points

to the potential of using *DHD* as memory devices. One explanation is that charge stored at the heterojunction of $In_{53}Ga_{47}As/In_{52}Al_{48}As$ maintains a high electric field across the device after the *NDR*-like curve occurs. This explains why the current remains very low, the ratio between the current in the forward sweep to that of the reverse sweep also points that mobility has changed drastically. When a reverse polarity is applied, accumulated charged being to escape giving rise to the spike in current observed after which the device shows higher currents again.

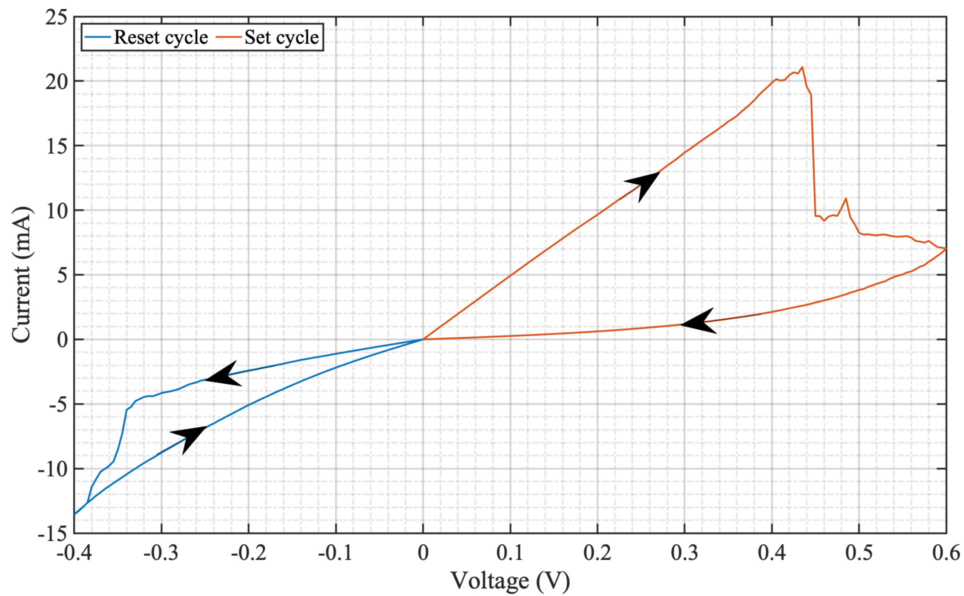

Figure 117: Double-heterostructure diode NDR-like behavior.

Moving forward with their operation as photoconductors, Figure 118 shows typical *IVs* of a photoconductor.

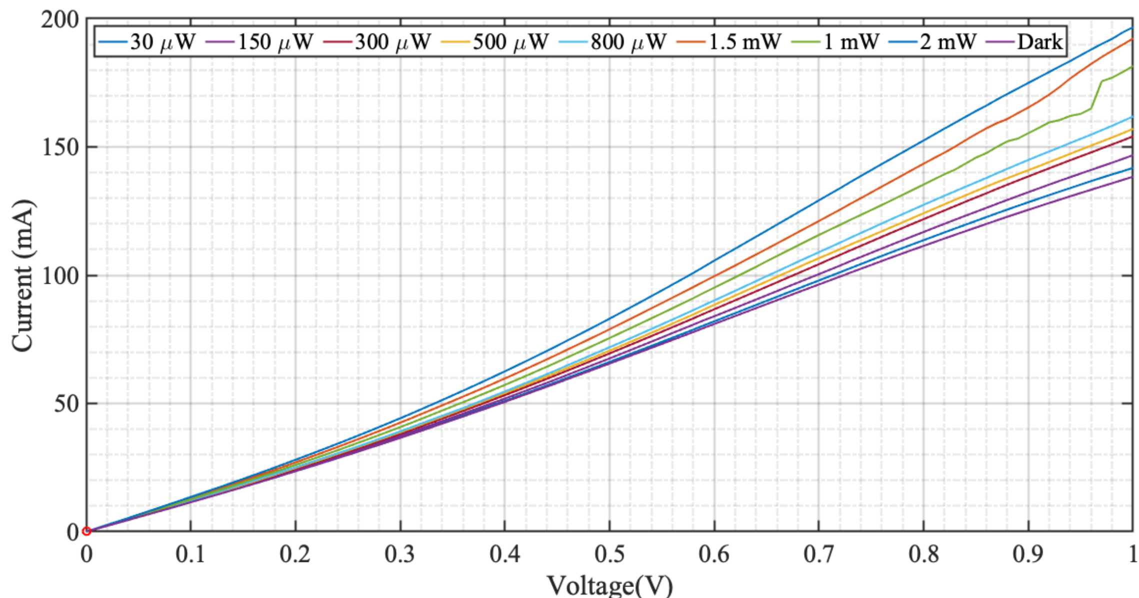

Figure 118: IV curves for double heterostructure diode (10×10 μm²).

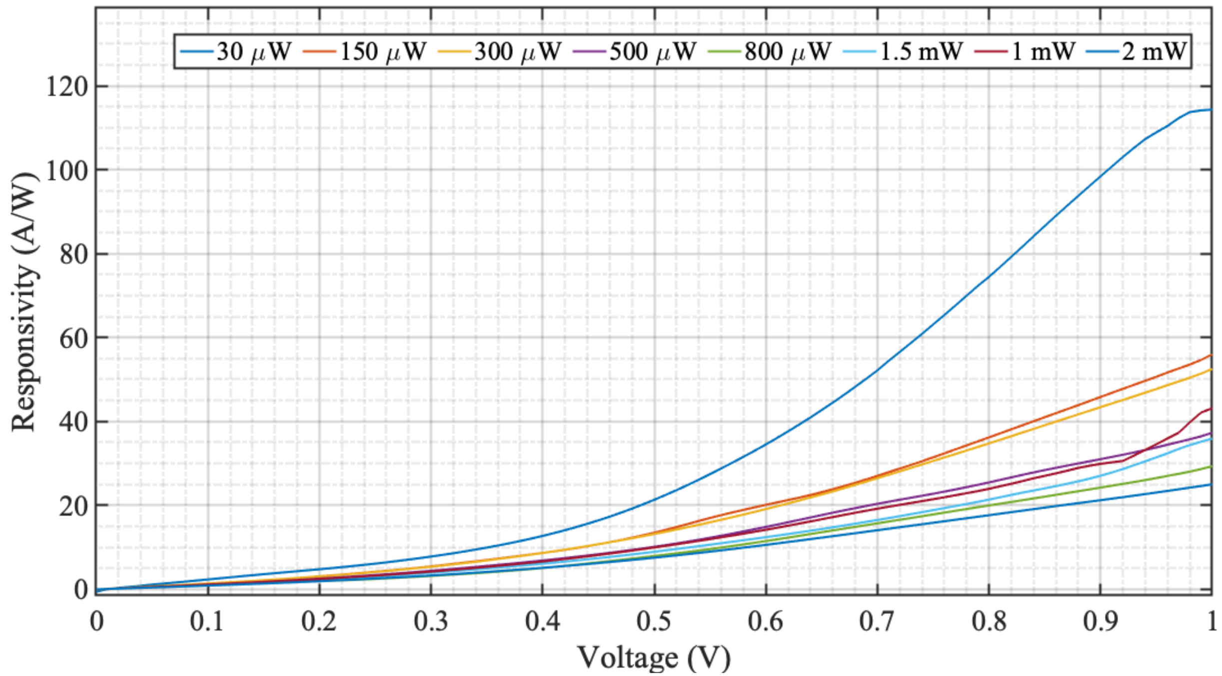

Figure 119: Current responsivity for double heterostructure diode (10×10 μm²).

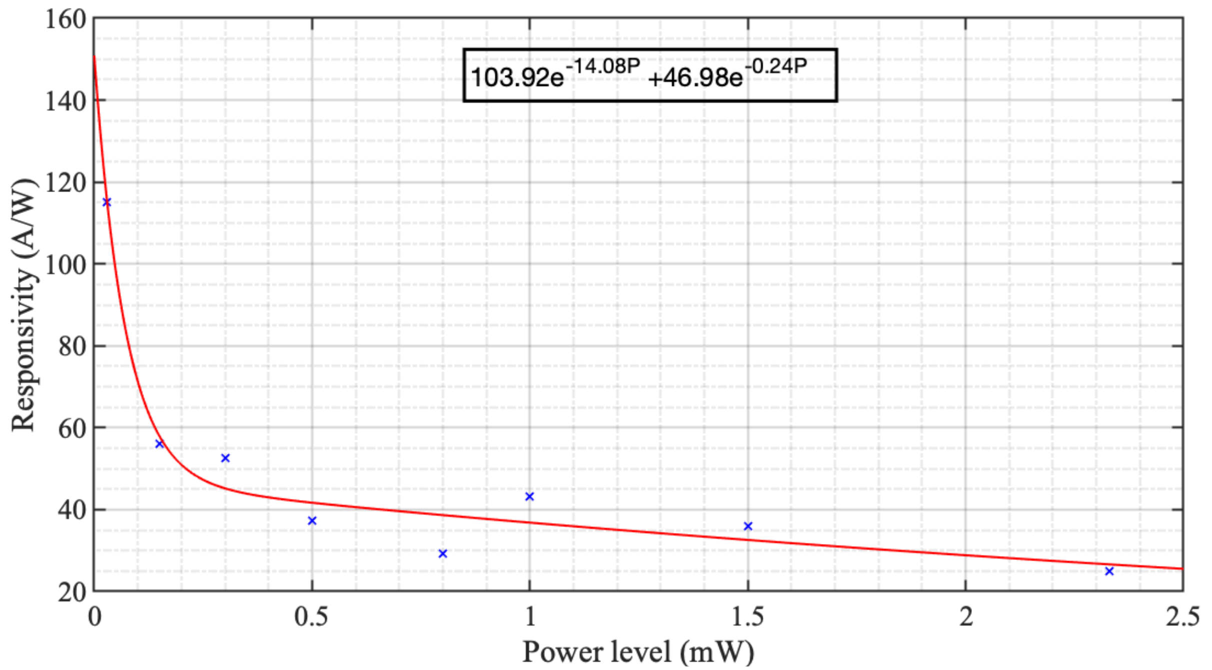

Figure 120: Responsivity as function of the applied illumination level for double heterostructure diode.

5.3.8 Sample PIN-RTD

The epilayer for the *PIN-RTD*, detailed in chapter 4, is shown in Table 5-9. We take this opportunity to stress the idea behind this design, which is to delay the formation of the *2DEG* at the emitter's side, thereby building enough potential drop across the emitter. This approach allows for high electric fields at both the emitter and the collector regions.

Furthermore, the contacts are of a higher bandgap material, which should eliminate charge generation in them, leading to a faster-operating device, as outlined in the next section.

Table 5-9: Epi-layer design for sample PIN-RTD.

Layer	Type	Material	Thickness (nm)	Doping level (cm^{-3})
1	*P++*	InP	*50*	8×10^{18}:Zn
2	*P+*	InP	*100*	1×10^{18}:Zn
3	*P*	$In_{53}Ga_{0.12}As_{0.25}P$	*15*	1×10^{18}:Zn
4	*P*	$In_{53}Ga_{0.19}As_{0.40}P$	*30*	1×10^{18}:Zn
5	*P-*	$In_{53}Ga_{47}As$	*500*	1×10^{15}:Zn
6	*I*	$In_{53}Ga_{47}As$	*10*	Undoped
7	*I*	AlAs	*1.5*	Undoped
8	*I*	$In_{53}Ga_{47}As$	*5.7*	Undoped
9	*I*	AlAs	*1.5*	Undoped
10	*I*	$In_{53}Ga_{47}As$	*10*	Undoped
11	*N-*	$In_{53}Ga_{47}As$	*500*	1×10^{15}:Si
12	*N*	$In_{53}Ga_{0.19}As_{0.40}P$	*30*	1×10^{18}:Si
13	*N*	$In_{53}Ga_{0.12}As_{0.25}P$	*15*	1×10^{18}:Si
14	*N+*	InP	*200*	1×10^{18}:Si
15	*N++*	InP	*50*	8×10^{18}:Si

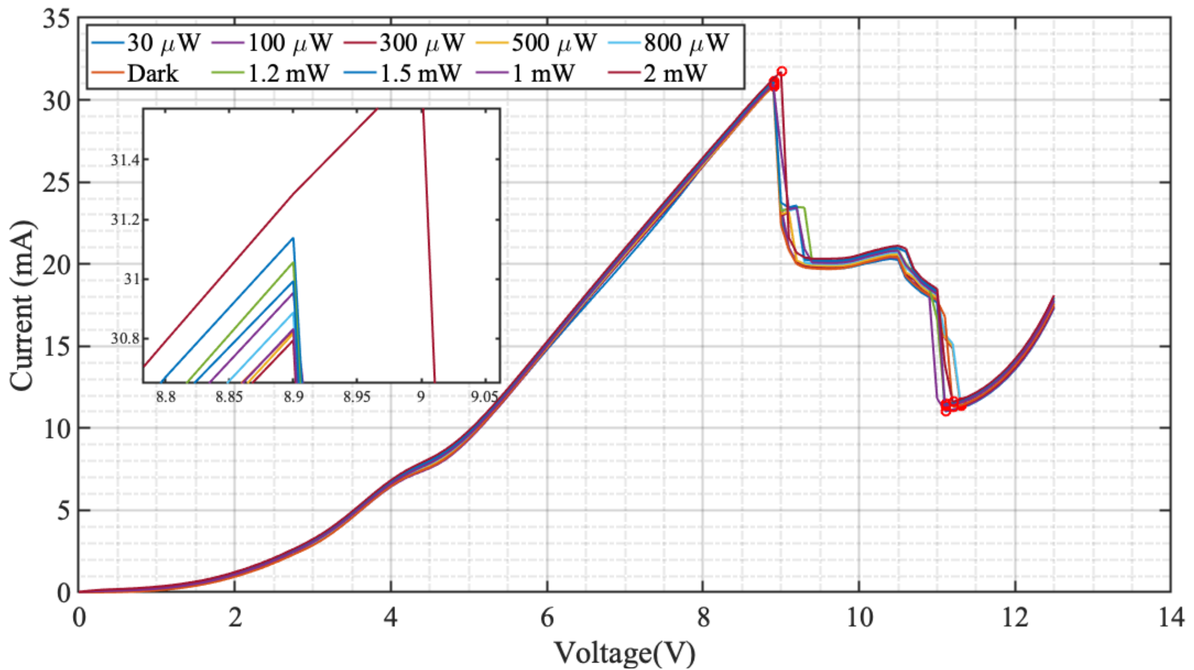

Figure 121: IV curves under reverse bias for sample PIN-RTD (25x25 µm²).

Observing the *IV* curves, it is clear that the design works in principle since the main features of the *RTD* are clear. The devices show a *PVCR* of 3 and a ΔV of nearly 2 volts. According to the predictions and simulations in chapter 3, the peak should occur (ideally) at

1 V. We believe the reason for so is mainly the Ohmic contacts. There was a challenge in getting Ohmic contacts to p-type *InP*, and even with the working devices, the contact resistance was not ideal. Other devices on the same sample show a peak at nearly 12 V while others showed one at around 6 V. Clearly, fabrication has to do with such a variation.

Regarding light detection, we see that there is a slight increase in the peak current when illuminated with light and no significant shift in the peak, except for a slight shift to a higher value for the 2 mW illumination case. We observed this behavior for four other devices on the same wafer, which suggests that this could be a characteristic of the device. This could also be due to a partially closed optical window. As for the current responsivity, we see a similar non-linear behavior as with the previous unipolar *RTD-PD*s, however, its value is negative. A negative responsivity means that the illuminated current is lower than the dark current. This is analogous to the case observed in samples P-A323/5 where there was a reduction of the current under illumination. This signals higher recombination rates that are associated with high levels of generation. The maximum responsivity observed for these devices is around 15 A/W at 30 μW of illumination power, which is much higher than any PIN-based photodiode on the market. The same trend of responsivity dependence on the illumination power is also observed with a responsivity value between 1 and 5 A/W for illumination levels in the 1 – 2 mW ranges, as depicted by Figure 123.

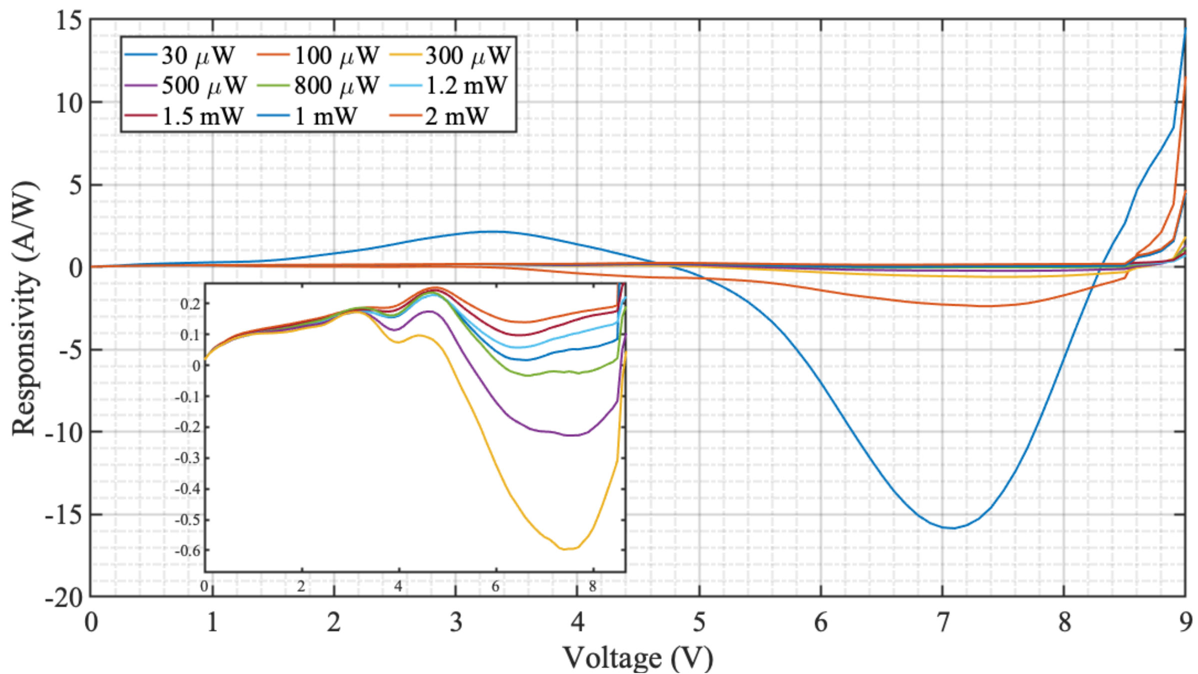

Figure 122: Current responsivity under reverse bias for sample PIN-RTD.

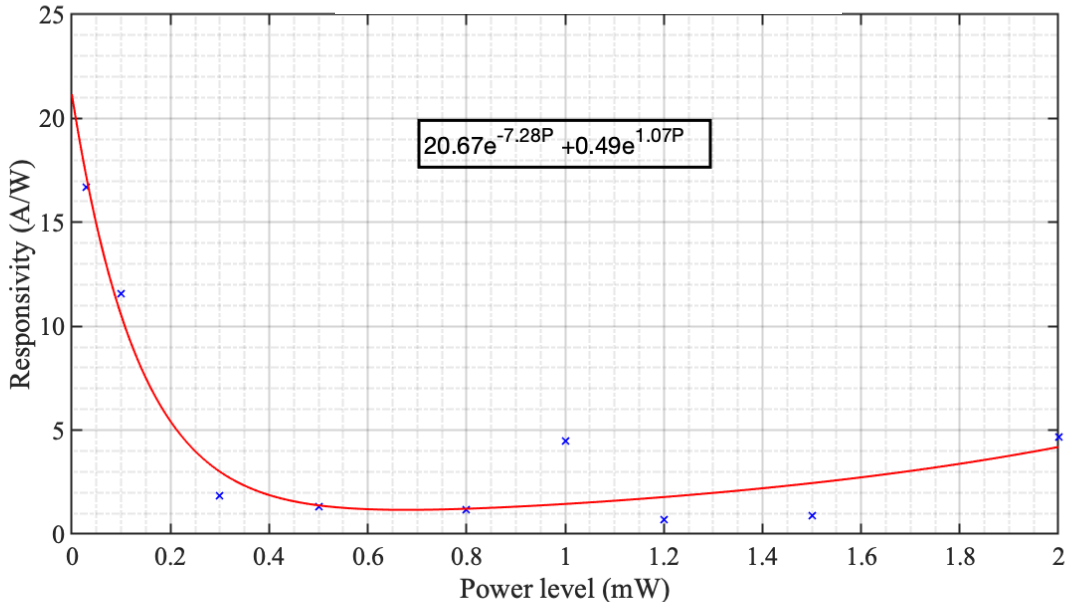

Figure 123: Responsivity versus illumination levels under reverse bias for sample PIN-RTD.

An interesting aspect of this design is that, in forward bias, the device becomes an emitter of 1.55 µm light through electroluminescence. Due to charge accumulation, the quasi-Fermi potentials at both the emitter and the collector sides go well into their respective bands (i.e.: degeneracy conditions). This means that the condition outlined in chapter 4 for light emission is satisfied (E_{FC} - E_{FV} > E_g). Most of the devices did not hold well while being forward-biased due to the high currents, but some did operate at moderate voltages, and the light emitted was measured. The measurement was by aligning the fiber directly above the optical window and measuring the power through a power meter. The results are shown in Figure 124. The values for R^2 and adjusted R^2 are 99.56%.

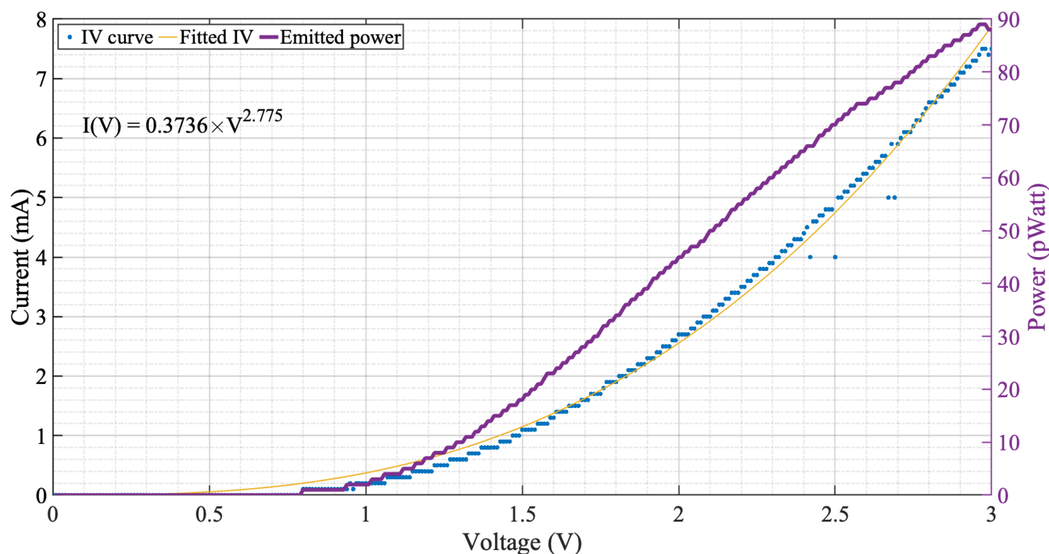

Figure 124: Emission power at 1.55 µm from sample PIN-RTD in forward bias.

5.3.9 Discussion and notes

In this section, we present some notes related to the responsivity and the peak voltage shift on the previous measurements.

We can summarize the responsivity of all previous epi-layers in one place as in Figure 45. The best performance was for sample S99, which had most of its absorption at the emitter's side (contact and 250 nm absorber). This is followed by the photoconductive wafer, which had its absorption mainly in the 300 nm contact layer and the 1 μm long absorber. This is an interesting result as it points out that the *DBQW* is indeed increasing the responsivity. The figure also shows that sample S99 outperforms sample S98 in responsivity. This is mainly due to the longer absorption at the emitter's side.

Looking at the results of samples P-A323/5, the responsivity of sample P-A323 is superior to that of P-A325 in both bias directions. We attributed this to the reduction in the photocurrent for a longer absorber when the entire energy of the light beam is absorbed. Although at reverse bias conditions the emitter's length differs between the two wafers, they share the same highly doped collector of 25 nm. However, the quantum well width is quite different between the two samples. Recall that the quantum well was stretched in sample P-A325 to have an operating voltage near that of sample P-323 in the forward bias case, but this has the effect of lowering the Eigenstates in the reverse bias as well, which shows up now at a voltage around 0.3 V.

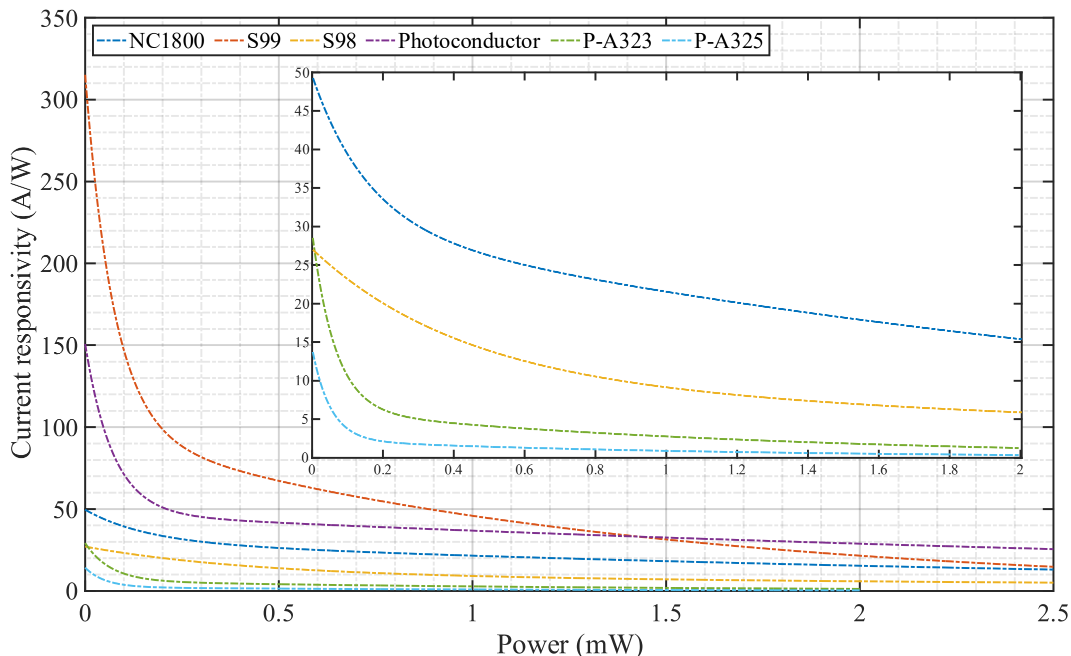

Figure 125: Responsivity versus illumination levels for all wafers in reverse bias mode.

The peak voltage shift has been previously investigated by many in the literature [51], [53], [54], [132]. The widely accepted explanation for such a shift is the accumulation of generated holes near the collector barrier. This charge results in a modification of the electrostatic field around the quantum well, effectively lowering the energy Eigenstates in the well and hence shifting the peak voltage to a lower value. Others have included the effect of conductance enhancement in the absorption region and tried to incorporate that effect into typical *RTD* IV models [133], [134]. However, these efforts did not lead to a concrete model which can resemble the observed shift seen in the above epi-layer designs. One model proposed by [133] is based on two implicit assumptions, first that the absorption only takes place at the collector's side and second all the generated holes are accumulated (none of them tunnels out or recombines). These assumptions are reasonable for the structures portrayed by the authors, nonetheless, do not resemble the entire picture as *RTD-PD*s can be designed with various topologies for the absorption region including those with absorption at the emitter and collector at the same time [135]. Furthermore, the explanation of charge accumulation does not explain the increase in the peak voltage seen in the above devices. Some have claimed that the conductance enhancement at the emitter can explain the observed shift in voltage, however, that is unlikely due to two reasons; first, at bias values near the peak voltage, we have shown that the emitter is mainly screened due to the high accumulation of charge near the barrier, which means that no potential will be dropping across it regardless of the enhancement imposed by the photo-generated charges. Second, assuming what the authors propose is true, a more conductive emitter will allow more potential to drop across the *DBQW* structure and hence lower the energy Eigenstates yielding a shift to a lower voltage, which is contradictory to the observation. In an effort to model such phenomena, we propose an alternative approach based on the results obtained in chapter 3 for the explanation of the peak voltage shift due to the change in built-in potential and the change in the Fermi-energy level. The idea is to calculate the excess generated charge due to photo-absorption in each region, and then use the models obtained in chapter 3 to calculate the shift. Notice, that the approach is oriented about the idea of the change in built-in potential around the *DBQW* due to the excess generation of carriers, therefore, charge accumulation is embedded into this approach as this modified built-in

potential is the potential resulting from such an accumulation of charges. And hence, what is proposed here is a mathematical way of quantifying this shift.

The first step is to be able to calculate the excess carriers generated due to light absorption and link that to the power of the incident beam. The first step is to calculate the photon flux given by (*5-5*)

$$\phi = \frac{P_{incident}}{h\nu} \quad (5\text{-}5)$$

This gives the number of photons incident per unit time. These photons will get absorbed and generate electron-hole pairs according to the internal quantum efficiency (**ζ**), coupling efficiency, and the reflection.

Starting from (*5-6*), the power of the incident beam in a semiconductor is given by

$$I(x) = I_o e^{-\alpha x} \quad (5\text{-}6)$$

Therefore, the power absorbed by the material is given by the derivative:

$$I_{absorbed}(x) = -\alpha I_o e^{-\alpha x} \quad (5\text{-}7)$$

Plugging this into (*5-5*) gives the photon flux as function of distance in a semiconductor:

$$\phi(x) = \frac{-\alpha P_o e^{-\alpha x}}{Area. h\nu} \quad (5\text{-}8)$$

The excess carrier concentration due to light absorption as a function of distance is then given by (*5-9*), while τ is the minority carrier lifetime.

$$n_{carriers}(x) = \phi(x). \zeta. (1 - \Re). \frac{\tau}{L_{absorption}} \quad (5\text{-}9)$$

Therefore, the average carrier concentration in each segment of the *RTD-PD* (the emitter or collector) is given by (*5-10*)

$$\int_{L_{absorption}} n_{carriers}. dx \quad (5\text{-}10)$$

Bearing in mind that (*5-10*) gives the average value and hence assumes uniform and constant distribution of generated carriers. If the integral in (*5-10*) is carrier out, the results will be as in (*5-11*) which tallies well with the results shown by [111].

$$n_{carriers} = \phi(x). \zeta. (1 - \Re). (1 - e^{-\alpha L_{absorption}}). \frac{\tau}{Volume} \quad (5\text{-}11)$$

To test the results of (*5-11*), the equation is used to calculate the photocurrent of a PIN photodiode we have at our labs. The *PIN* photodiode (Agilent light-wave detector) gives

output voltages as shown in Table 5-10 for various light illumination levels. The signal was measured on an oscilloscope with an input impedance of 50 Ω, accordingly the values of the generated current were calculated. Since carriers in a *PIN* photodetector flow at saturation speeds, the drift current that is calculated depending on values of the carrier concentrations predicted by (*5-11*), which are also listed in the same table. Noting that the lifetime used is around 14 ps as stated in the impulse response of the detector's datasheet. The results are in close agreement which indicates that the method produces accurate results. The absorption coefficient was assumed to be 8500 cm^{-1} and the absorption length was assumed to be 1 μm and the drift velocity around 5×10^4 m/s (saturation velocity) [121].

Table 5-10: Photocurrent of the light-wave 32GHz PIN-Photodiode.

Optical power	Detected voltage (mV)	Current (μA)	Calculated current (μA) using (*5-11*)
300 μW	7.8	156	120
500 μW	10	200	200
700 μW	15	300	281
1 mW	21	420	401
2 mW	40	800	802

By observing the shift trends (both to the left and right), one can see that they are quite different in their nature, hinting at the possibility of these two observations being of different physical origins. We can see such a difference by examining the peak voltage as a function of the illumination level curves. The shift to lower values seems linearly dependent on the illumination level and changes at a higher rate than the shift to higher values. This is apparent from the derivative of each section. Furthermore, the shift to higher values seems to follow a non-linear rhythm, with saturation occurring at high illumination levels. This saturation is believed to be due to the band-filling effect and mobility saturation. As more carriers get generated, states at the conduction band begin to fill up at a much higher rate than the recombination, effectively increasing the bandgap. Such a phenomenon induces self-transparency in the material and can saturate the photocurrent and, consequently, the observed shift. Bearing in mind that, the internal quantum efficiency of the material will also go down due to high levels of illumination. The internal quantum efficiency is given by(*5-12*)

$$\zeta = \frac{\tau_{non-radiative}}{\tau_{total}} \tag{5-12}$$

with the total recombination time given by (*5-13*)

$$\frac{1}{\tau_{total}} = \frac{1}{\tau_{radiative}} + \frac{1}{\tau_{non-radiative}} \quad (5\text{-}13)$$

As is well known [136], increasing the carrier concentration in a material promotes Auger recombination leading to a reducing in the total lifetime and hence the internal quantum efficiency as well.

5.4 Impulse response

One of the main objectives of this work is to study the speed limitations of *RTD-PD*s. The methodology employed is to study all the physical time constants that control the devices' photodetection performance including the *RC* time constant, dielectric relaxation time, transit time, and carrier lifetime. In this section, we go through the details of obtaining the time response of each epi-layer to an impulse of light. The idea behind doing so is to determine the response time of each sample and compare that time value with the characteristic times mentioned above, thereby determining the most significant factor limiting the speed and affecting the measured bandwidth.

If we consider a simple photoconductor that is subjected to a very short pulse of light (light is switched off after the pulse is injected), that beam will trigger a current signal through the detector. This current will eventually decay to zero at a rate proportional to the minority carrier's lifetime. This is because the system needs to relax back to its original state through recombination. Ideally, this should be done with no bias applied so that the electric field does not contribute to charge transport.

Assuming a generation rate as in (*5-14*), at thermal equilibrium the generation rate equals that of recombination as in (*5-15*). When light is switched off the continuity equation becomes as in (*5-16*). The decay constant in this expression is the minority carrier lifetime. We can model this mathematically with an optical generation rate function in the form of a rectangular pulse (*G(t)*) with a pulse width of T_{pulse} and some amplitude G_0. This generation rate will equal the recombination rate (*R(t)*) at equilibrium, which depends on the excess photo-generated carriers (δn) and the lifetime.

$$G(t) = G_0 . rect(\frac{t}{T_{pulse}}) \quad (5\text{-}14)$$

$$\mathrm{R(t)} = \frac{\delta n}{\tau_{lifetime}} \tag{5-15}$$

$$\frac{\mathrm{d}}{\mathrm{dt}}(\delta n) = -\frac{\delta \mathrm{n}}{\tau_{\mathrm{lifetime}}} \tag{5-16}$$

$$\mathrm{G_0} = \frac{\delta \mathrm{n_0}}{\tau_{\mathrm{lifetime}}} \tag{5-17}$$

$$\delta n(t) = \delta n_0 e^{-\frac{t}{\tau_{lifetime}}} \tag{5-18}$$

Given the above, there are a couple of things to pay attention to. First, carriers generated should not be "driven" by any sort of voltage source, that is, no electric field should be there to transport the charges and they should be left to diffuse. Furthermore, the length of the semiconductor in question has to be at least one diffusion length long as given by (*5-19*), where *D* is the diffusion coefficient.

$$\mathrm{L_{diffusion}} = \sqrt{D.\tau_{lifetime}} \tag{5-19}$$

If, however, the length is less than the diffusion length, this will yield a lifetime measurement of a lower value as in this case charges will recombine at the contacts (assuming ideal contacts), or the system will be going back to equilibrium when charges leave the semiconductor and sink into the supply. This is analogues to a short-base diode [69].

In order to measure the impulse response and get the lifetime associated with the devices, the setup in Figure 126 was used. The 1.55 μm laser light source was externally modulated using a Mach-Zehnder modulator with a pulse signal having a width of 500 ps and a repetition rate between 1 and 3 MHz. The low frequency assures that the system has enough time to recover, thereby resembling a single pulse that is repeated every 1 μs. Using higher frequencies runs into the risk of getting wrong values if the relaxation time of the system is of the same order as the repetition rate.

What is of interest, is the study of how the systems impulse response is affected with voltage. To do that a MATLAB program was written to control the data acquisition equipment. The bias was started from zero and increased to cover the whole *IV* curve of the device. At each point the light pulse was injected and the generated electrical signal was recorded on the oscilloscope. Then the light beam power was changed covering a range from hundreds of microwatts to the milliwatt range and the same process was repeated again. This approach gave valuable data as how the impulse response changes with both bias and

illumination intensity. Theoretically, high levels of carrier generation (greater than the background doping) should decrease the carrier lifetime, with the main recombination being of the non-radiative type. The average light power for the results presented here is 1 mW.

The lifetime is calculated using the 10%, 90% decay intervals for an average number of pulses in each run. Each wafer was measured between 3 to 5 times with different devices as well. The results here are the average repeatable results acquired.

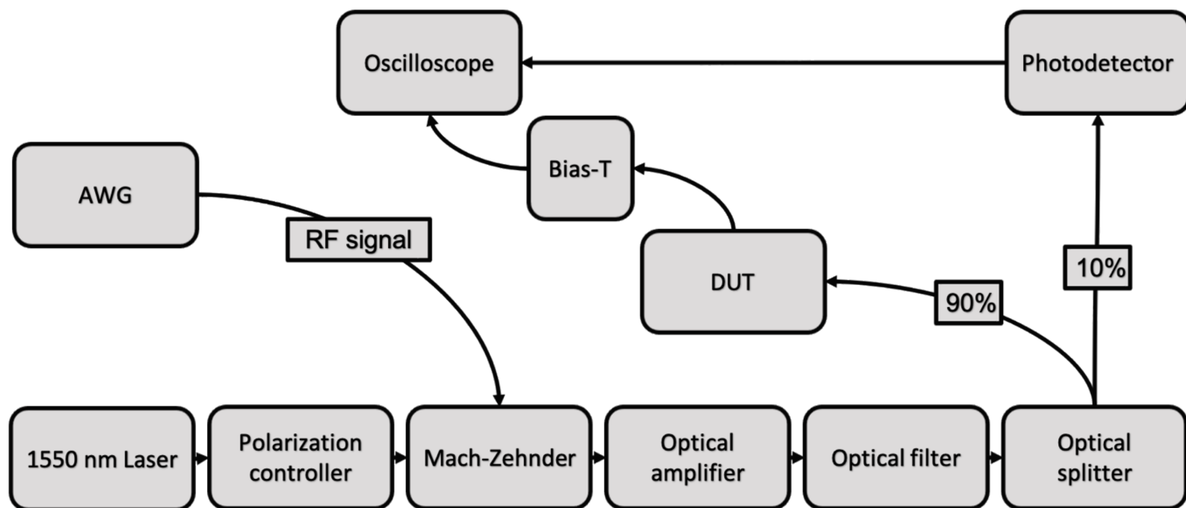

Figure 126: Optical characterization setup used to measure the optical impulse response.

Some epi-layers showed an optical response at zero bias, however, not all of them did. This would resemble the most accurate lifetime measurement. Unfortunately, the ones that did, had very low signal levels, so a small voltage (around 100 mV) had to be applied.

Figure 127 shows how the lifetime evolves with voltage for epi-layers NC1800, S99, S98, 73A, and the photoconductive wafer. All devices chosen here are 10×10 μm^2.

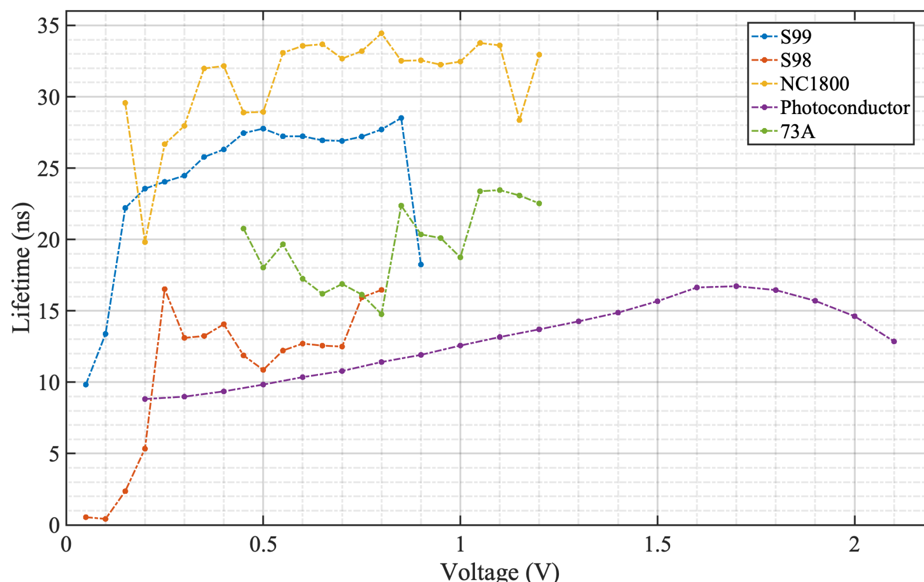

Figure 127: Lifetime as function of voltage for epi-layers grown by IQE.

From the above results it can be seen that the average lifetime for the *RTD-PD* is in the tens of nanoseconds range (at low voltages around 100 – 200 mV), with wafer NC1800 having the highest average of around 33 ns followed by S99 with an average of 27 ns, then by A73 with around 20 ns and finally S98 with 14 ns. It noticeable that the lifetime of the *RTD-PD* is significantly higher than that of the photoconductive wafer which also has an average lifetime of about 13 ns. With that in mind, it is clear that the presence of the *DBQW* has an effect on the overall lifetime of the system, particularly since the photoconductive wafer has the same design as that of wafer *A73* with the *DBQW* removed.

Moving forward, we show in Figure 129 the same results for epi-layers P-A323 and P-A325, which were grown and fabricated at the University of Würzburg using gas-source molecular beam epitaxy. The impulse response of these devices is much faster and ranges between 1 to 2 nanoseconds (again at low voltages around 200 mV). This is partially due to the nearly depleted collector region that transports the photo-generated charges at higher speeds. Other reasons might be due to the presence of impurities during the growth from the *MBE* chamber itself and the thinner bottom contact. This is apparent from the current responsivity figures shown earlier and how these devices show lower responsivities when compared to other wafers with similar absorption regions.

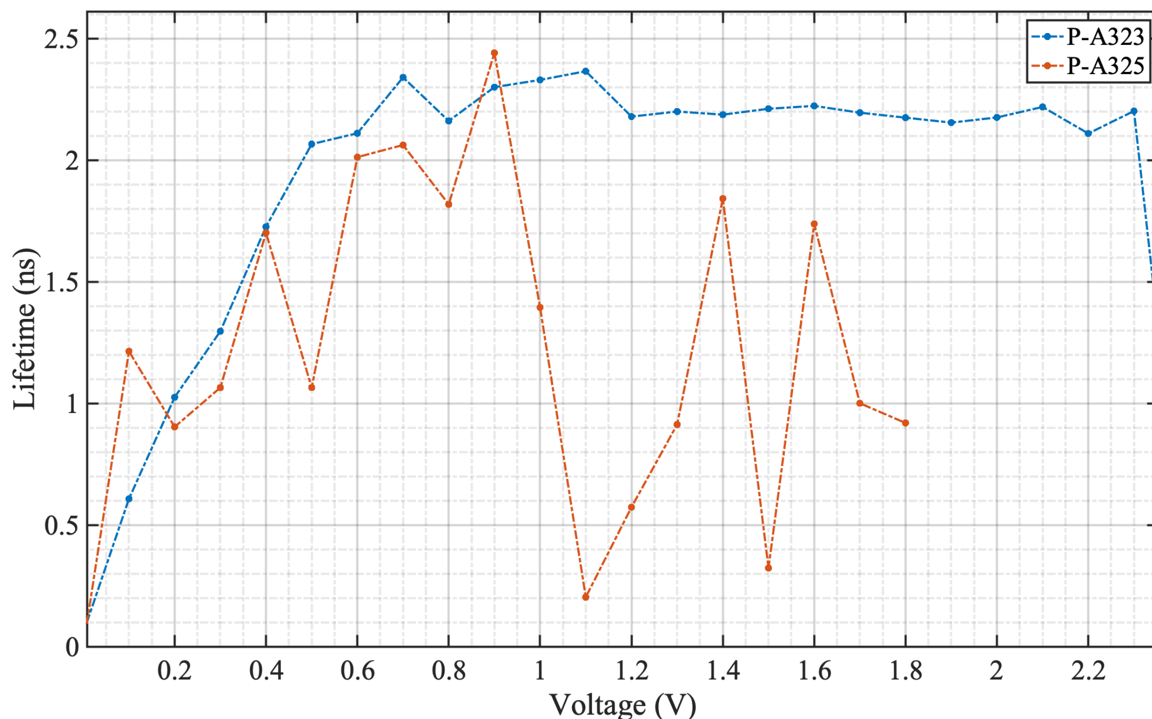

Figure 128: Lifetime as function of voltage for epi-layers grown at the university of Würzburg.

From the results obtained so far, and given typical values of 50 Ω resistance and an *RTD-PD* capacitance in the hundreds of fF range (we calculate and simulate the capacitance in chapter 6), the response time for these *RTDs* should be much faster (below the ns range). The same argument goes for the dielectric relaxation time given by (*5-20*), and the transit time, both of which are in the ps range. Where (*N*) is the carrier concentration.

$$\tau_{\mathrm{relaxation}} = \frac{\epsilon}{\mu \mathrm{Ne}} \tag{5-20}$$

Finally, we present the results for the fastest sample, which is the PIN-*RTD*. The obtained results are not straightforward and require some investigation. Figure 129 shows how the response time changes as a function of voltage for this sample. We note that the response time follows the width of the original pulse until voltages of around 2 V but then starts to increase until it reaches an average value of 1 ns near the peak. Leaving the *NDR* and going into the second *PDR*, the response time goes back to follow the original pulse. This result shows that the response time of the *PIN-RTD* goes up as more charges accumulate near the *DBQW*, pointing out the possibility of the lifetime of the accumulated charges being proportional to the concentration of the accumulated minority carriers. This sample is faster than all other samples (NC1800, S99, S98, 73A, and the photoconductive sample), which showed a lifetime in the tens of nanoseconds range. This means that the speed limiting mechanism for these wafers differs from the *PIN-RTD*. What the other wafers have in common is the presence of a thick $In_{53}Ga_{47}As$ bottom contact layer. This layer, although highly doped, does absorb light. Being highly doped the electric field in this layer is nearly zero, and carriers would have to recombine for them to be eliminated, which imposes a lifetime limit on the bandwidth of these devices. This, however, is not the case with the *PIN-RTD* sample with the high bandgap *InP* contacts. But, the results from P-A323/5 show lifetimes that range from 1 – 2 ns, albeit having $In_{53}Ga_{47}As$ contacts. This is mainly attributed to the much thinner contact layers for both samples. Moreover, we believe that the *MBE* chamber used during growth does have some impurities. Such impurities are known to reduce the carrier lifetime through Shockley-Reed-Hall (*SRH*) recombination at the expense of reduced responsivity.

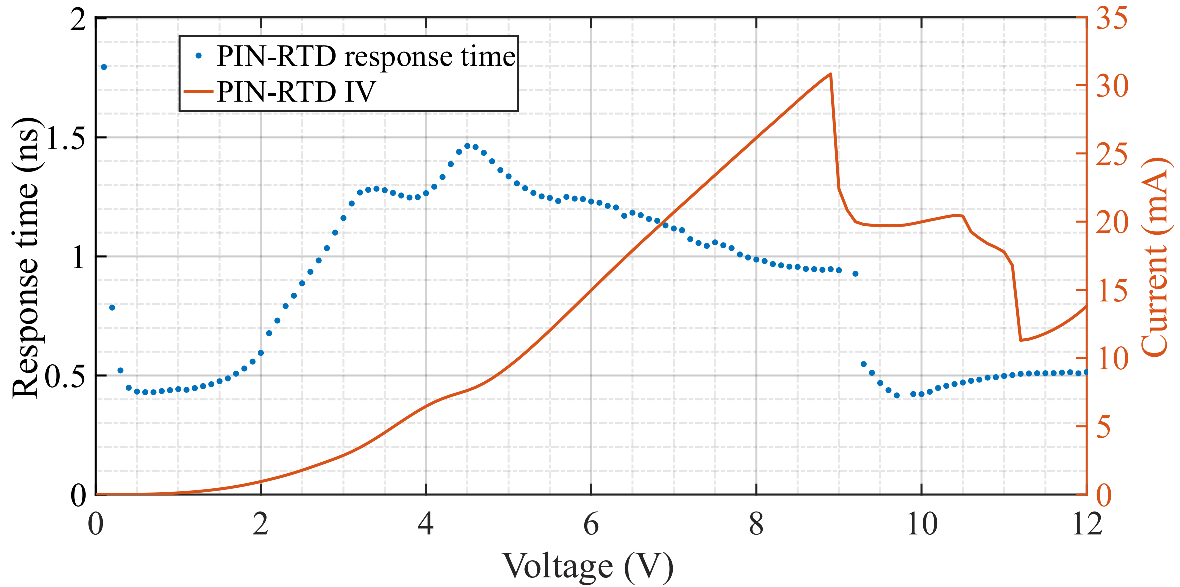

Figure 129: Response progress as function of voltage of PIN-RTD (reverse bias conditions).

Figure 130 shows a summary of the impulse response of all the samples, clearly showing the fastest response for the *PIN-RTD* sample. One thing to note is the response of P-A323/5. There seems to be reflections interfering with the signal. This is thought to be associated with the fact that the fabricated devices did not have any suitable means of coupling the *RF* energy into the probes (i.e.: no waveguide or ground-signal-ground configuration). The mask used is meant only to do *DC* measurements.

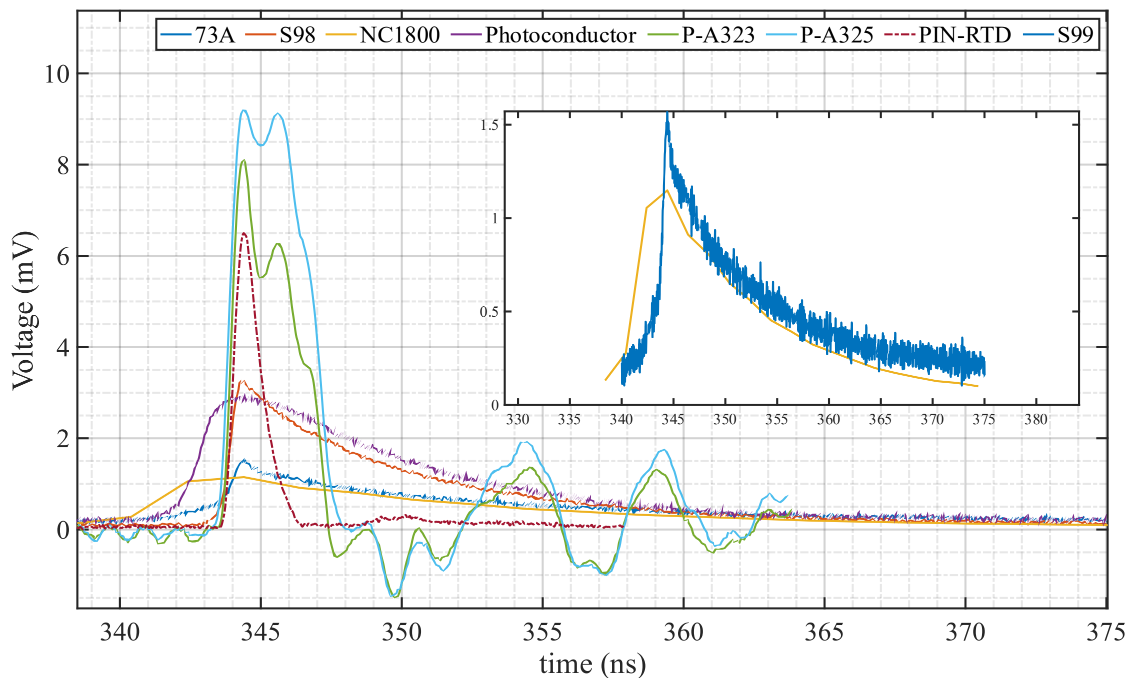

Figure 130: Impulse response for all tested samples.

5.4.1 3dB bandwidth

To measure the bandwidth, we need to measure the *3dB* cutoff frequency for each sample. To do this, we used the same impulse response setup and shined sinusoidally modulated light into the devices. The frequency of the sinewave was gradually increased, and the power of the detected signal was measured. The *3dB* bandwidth is defined as the bandwidth at which the power goes down by *3dB* from the *DC* value (i.e.: the signal's power goes down to half its DC/low-frequency value). This was done using a MATLAB program that controlled the measuring instruments and produced the required Bode plots.

In Figure 131 the Bode plots of all samples are gathered from which the *3dB* bandwidth can be deduced, noting that these Bode plots were taken at voltages where the impulse response was the fastest for each device. These voltages were 0.7 V for sample S98 and 1 V for the rest of the samples.

Here we highlight the difference between the optical bandwidth and the electrical bandwidth. The *3dB* electrical bandwidth has the definition we stated earlier, however, for optical detectors the optical *3dB* bandwidth is equivalent to the *6dB* electrical bandwidth.

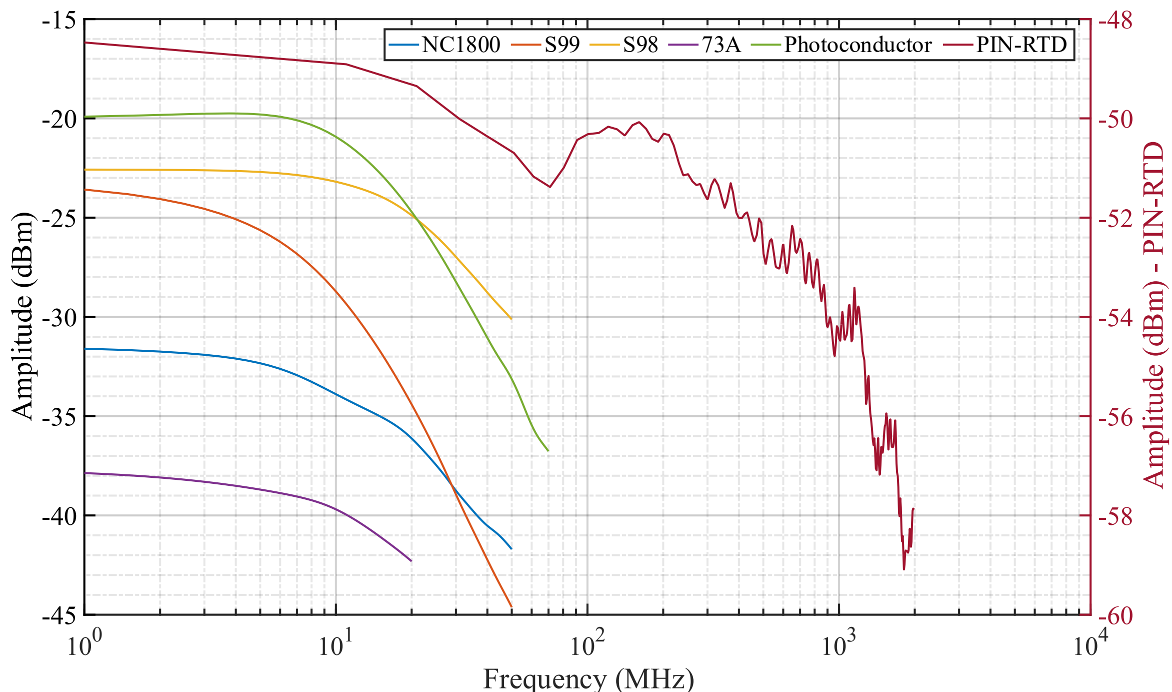

Figure 131: Bode plots showing the 3dB bandwidth of all samples.

It is clear that removing the absorption in the contact regions yields faster devices. Furthermore, if we calculate the 3dB bandwidth using (*5-21*), and take epi-layer S98 as an example then the anticipated bandwidth is around 25.5 MHz using the impulse response

values obtained before. The other wafers show bandwidths in the 10's of MHz range. This further supports the argument that the main speed limiting factor is the lifetime.

$$f_{3dB} = \frac{0.35}{\tau_{falltime}} \tag{5-21}$$

Table 5-11: 3dB bandwidth of all samples.

Sample	3dB bandwidth (MHz)	
	Electrical	Optical
NC1800	12	23
S99	8	12
S98	26	37
A73	15	35
DHD	16	20
PIN-*RTD*	370	1260

The results seem to suggest that the maximum electrical bandwidth achieved by the fastest sample (*PIN-RTD*) is around 380 MHz and around 1.26 GHz optical, which are lower than the anticipated 10 GHz bandwidth.

To better understand what is going on, we examine Figure 132 which shows the *IV* curves of different devices on the same *PIN-RTD* sample.

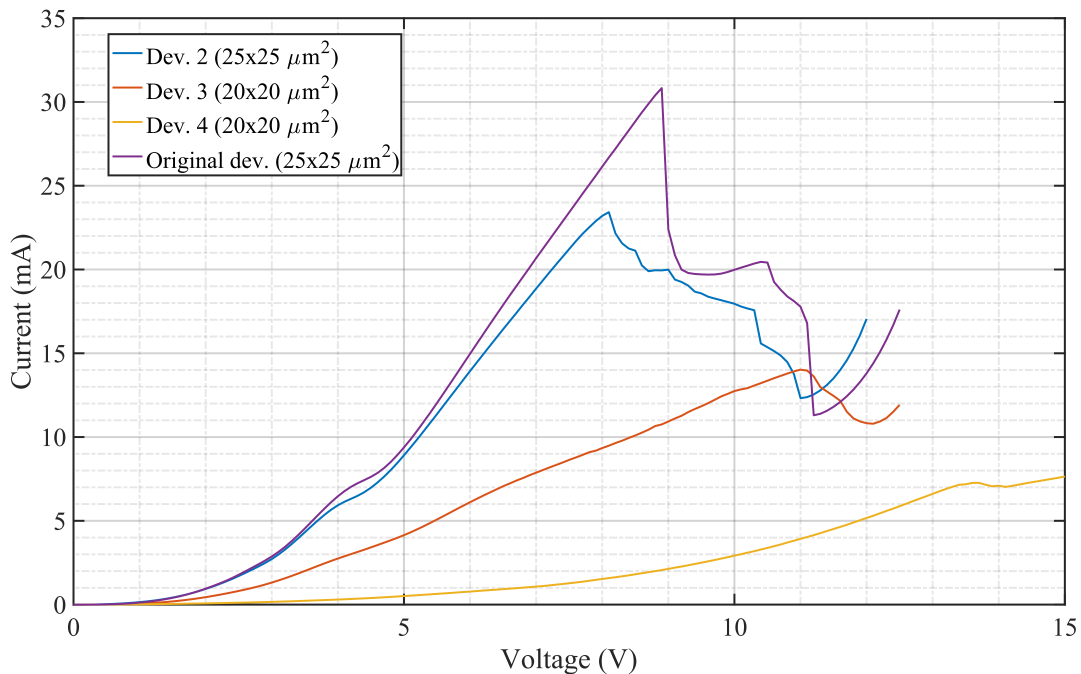

Figure 132: PIN-RTD IVs for various devices.

The main thing to note about these IVs is the varying *RTD* parameters, specifically the *PVCR* and peak current. The 3dB bandwidths of all these devices were also measured at the

bias point with the fastest response and the results were surprising. The device with the mildest *NDR* showed a cut-off frequency of around 1.28 GHz electrical and 1.75 optical, with the others showing lower and lower bandwidths until we reach the 380 MHz electrical / 1.2 obtained from the first device.

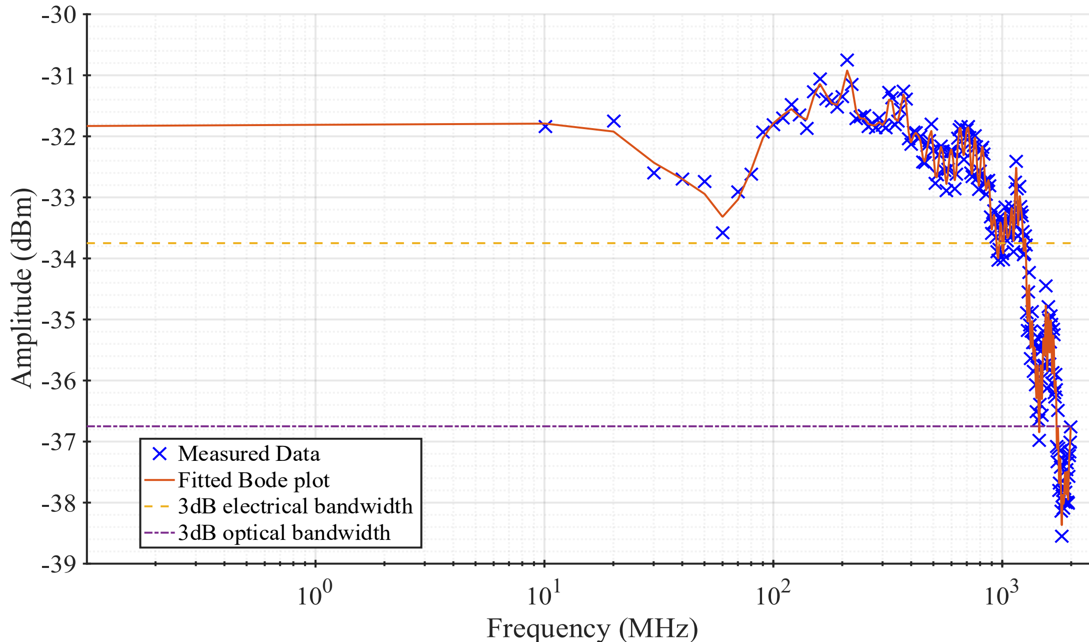

Figure 133: 3dB-Bandwidth of the device with the mildest NDR.

This behavior can be explained by concentration of accumulated charge at the emitter. If we assume that the speed limitation for the *PIN-RTD* is actually the lifetime of the accumulated charge, these results start to make sense. A milder *NDR* designates that the valley current is quite high with regard to the peak current. This means that the carriers being injected are not accumulating as much, and tend to escape thorough thermionic emission, thereby, contributing to higher valley currents. So, we can say that a milder *NDR* points to lower accumulation lifetimes. Furthermore, by looking at the peak current values, it seems that the injection rate at the emitter (source of current) is lower, and since the accumulation rate is the difference between the injection and transmission rates, this means that less charges are accumulating as well leading to a reduced lifetime and a higher bandwidth. We can therefore conclude that the main limitation to the speed of *RTD-PD*s is the lifetime of the accumulated charge near the emitter, which suggests that *RTD-PD*s are intrinsically low speed devices. The reason for such *NDR* shapes is most likely due to fabrication related issues, particularly with the contact resistance, as higher contact resistance leads to lower current injection levels. As a final note, it is interesting to state the conditions when an *NDR* would

not show up in a device with a *DBQW* structure. One is the case with the previous epilayers (NC1800, S99 and S98), where the potential drop across the collector is much greater than what goes into the quantum well region effectively shifting the peak to higher values at which the device would not operate. However, this case does not lead to a change in the speed of response. The second is when the Fermi level increases to be aligned or above the resonant level. The third, which is of interest, is the vanishing of the *NDR* when the peak current equals the valley current. If such condition is satisfied, no *NDR* will show. What this physically means is that if the injection rate is comparable to the rate of thermionic emission the *NDR* will be milder and milder to the point where it no longer is detectable. This means that the device will then act as a normal PIN diode (for the case of the *PIN-RTD*) or as a photoconductor/*DHD* for the other samples.

5.5 AC signal detection and amplification

5.5.1 Operation as an amplifier in the NDR

One of the benefits of having a negative differential resistance region in an electronic device is the device's ability to provide regenerative gain or amplification. *RTDs* are one of the best devices that exhibit such phenomena alongside Gunn diodes, tunnel diodes, and resonant tunneling transistors. The main idea of how *NDR*-based devices provide gain is by dynamically changing the *DC* resistance values while in the *NDR*. Looking at Figure 134 we can see how this takes place.

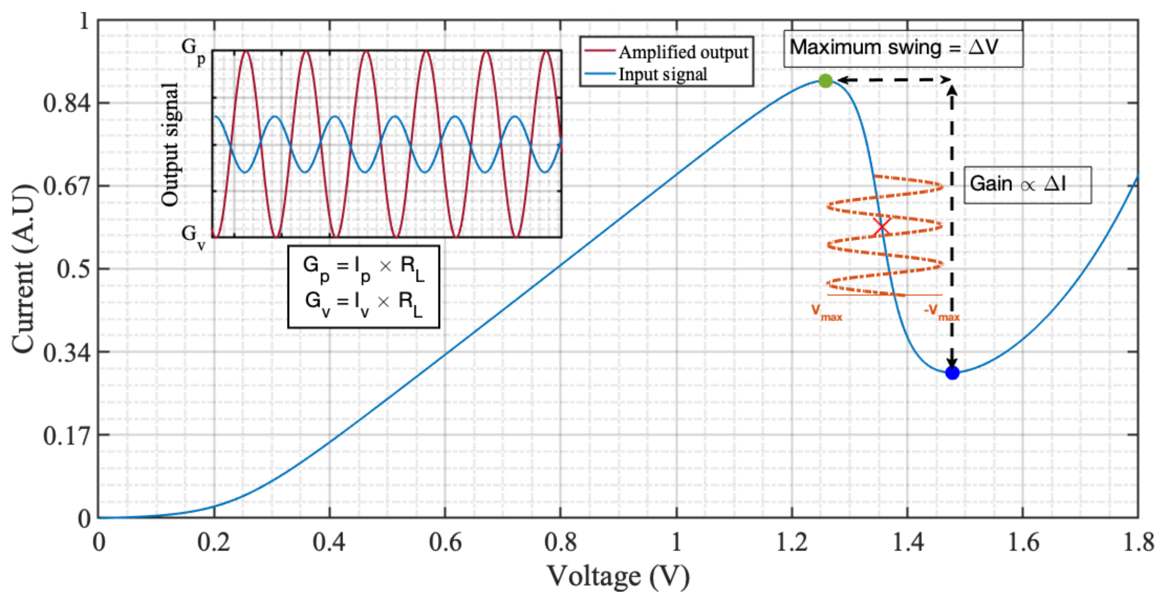

Figure 134: RTD amplification in the NDR, the inset shows the 180 ° phase shift and the amplitude increase.

When the *RTD* is biased in the *NDR* region, the value of the instantaneous *DC* resistance is given by the ratio of the voltage to the current as per Ohm's law. Referring to Figure 134, and considering a *DC* bias point at the middle of the *NDR* (the red cross mark) with an *AC* sinusoidal signal superimposed. During the first half cycle, as the *RTD* voltage is driven towards the peak point, the resistance decreases since the *RTD* voltage point is now lower and the current is more. The opposite argument holds; when the current decreases as the *RTD* voltage is driven towards the valley during the second half cycle. This sort of dynamic *DC* resistance value in the *NDR* can be utilized for amplification. Consider the circuit in Figure 135 where the *RTD* equivalent circuit is used (highlighted in red) with a series connected load resistance. For simplicity, we first consider that the contributions of L and C_{qw} are negligible (low-frequency signals). This reduces the circuit to only R_{ndr} and R_{load}. When the operating point reaches the peak voltage point (green point in Figure 134), the resistance of the *RTD* will be lowest, which increases the output voltage (V_{out}) on the load resistance. The same applies when the voltage point reaches the valley, where the *RTD* resistance is high thereby, decreasing the output voltage on the load resistance.

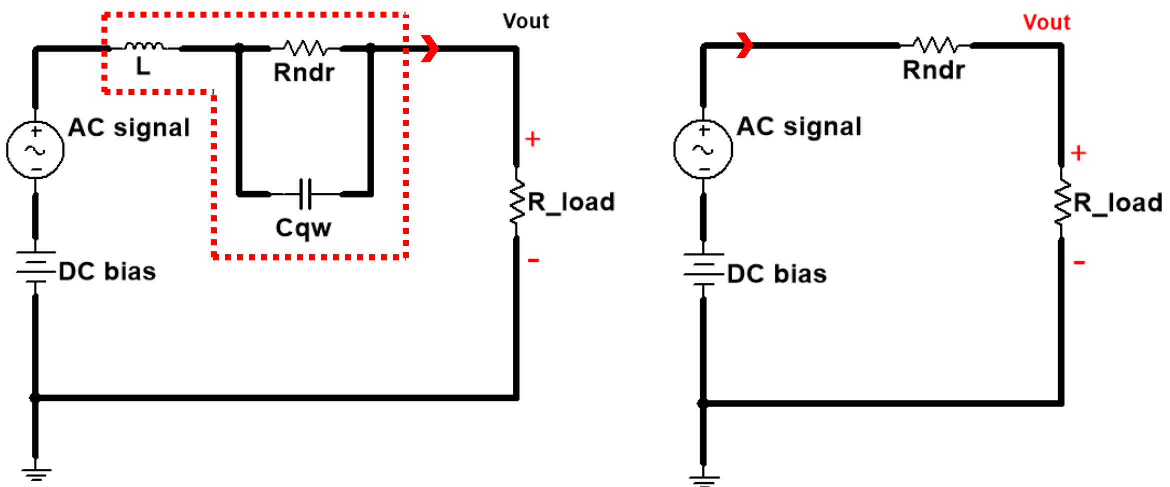

Figure 135: RTD equivalent circuit as an amplifier (left – for high frequency, right – low frequency).

We notice that the maximum voltage swing of the input signal is controlled by the value of ΔV in the *NDR* region, while the amplification is mainly determined by ΔI. The output signal's voltage swing can be determined by the following rationale:

$$V_{outPeak} = I_{peak} R_{Load} \tag{5-22}$$

$$V_{outMin} = I_{valley} R_{Load} \tag{5-23}$$

$$V_{outP-P} = \Delta I \times R_{Load} \tag{5-24}$$

$$\mathrm{V_{out}} = \mathrm{V_s} - \mathrm{iR}_{NDR} \tag{5-25}$$

Assuming that the resistance in the *NDR* is modeled as a negative resistance. Equation (*5-25*) assumes that the value of R_{NDR} to be negative [137]. Also, since the *NDR* has a negative slope, the output signal is expected to be 180° out of phase with the input.

Therefore, to get the value of the gain, we need to find the transfer function which is easily obtained from Figure 135.

$$\mathrm{Gain} = \frac{\mathrm{R_{Load}}}{\mathrm{R_{Load}} + \mathrm{R}_{NDR}} \tag{5-26}$$

Using a similar approach, the gain for a parallel connected load can be deduced to be

$$\mathrm{Gain} = \frac{\mathrm{R}_{NDR}}{\mathrm{R_{Load}} + \mathrm{R}_{NDR}} \tag{5-27}$$

However, for the parallel load case, the output signal will be the current passing through the load resistance not the voltage across it.

For the high frequency case, the contributions of the capacitance and inductance should be considered. This modifies the gain in (*5-26*) to be:

$$\mathrm{Gain} = \frac{\mathrm{R_{Load}}}{\mathrm{R_{Load}} + \mathrm{Z}_{NDR}} \tag{5-28}$$

where Z_{NDR} is given by (*5-29*)

$$\mathrm{Z}_{NDR} = \frac{R_{NDR} + LS + R_{NDR}LC_{qw}S^2}{1 + R_{NDR}SC_{qw}} \tag{5-29}$$

Therefore, in order to harvest the amplification qualities of the *RTD* in the proposed photodetectors, they have to be operated in the *NDR* region. This was tested with some of the epi-layers, mainly the 73A and the *PIN-RTD*. The idea behind the test was to see how this gain can affect the operation of the *RTD-PD*, and how the detected signal compares to a typical *PIN* photodiode. To do so, the optical signal splitter arrangement was changed to 50:50, such that the signal detected by the *RTD-PD* can be compared with that detected by the *PIN*-photodiode. The *RTD-PD* was biased in the *NDR* region, and *AC* modulated light with a frequency of 1 MHz sinewave was injected into the detectors. The results clearly show the amplification effects of the *RTD-PD* over that of a *PIN* detector. The peak-to-peak value of the detected *RTD-PD* signal is nearly 8 times higher. The 180° phase shift is also present as expected.

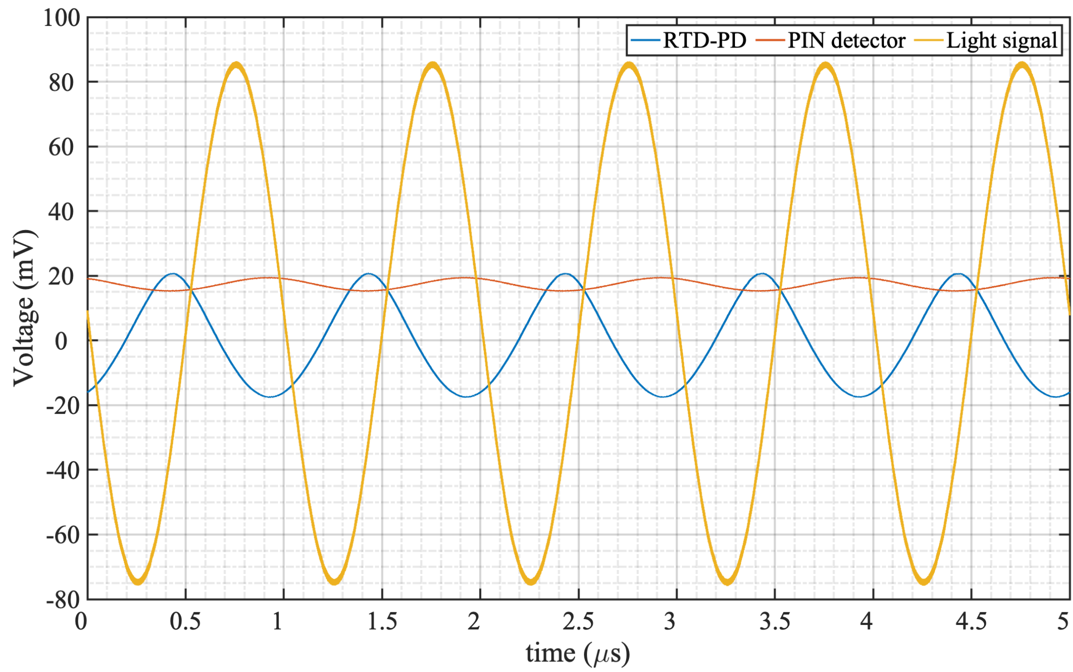

Figure 136: Wafer 73A - RTD-PD and PIN photodiode detected signals with original modulating light signal.

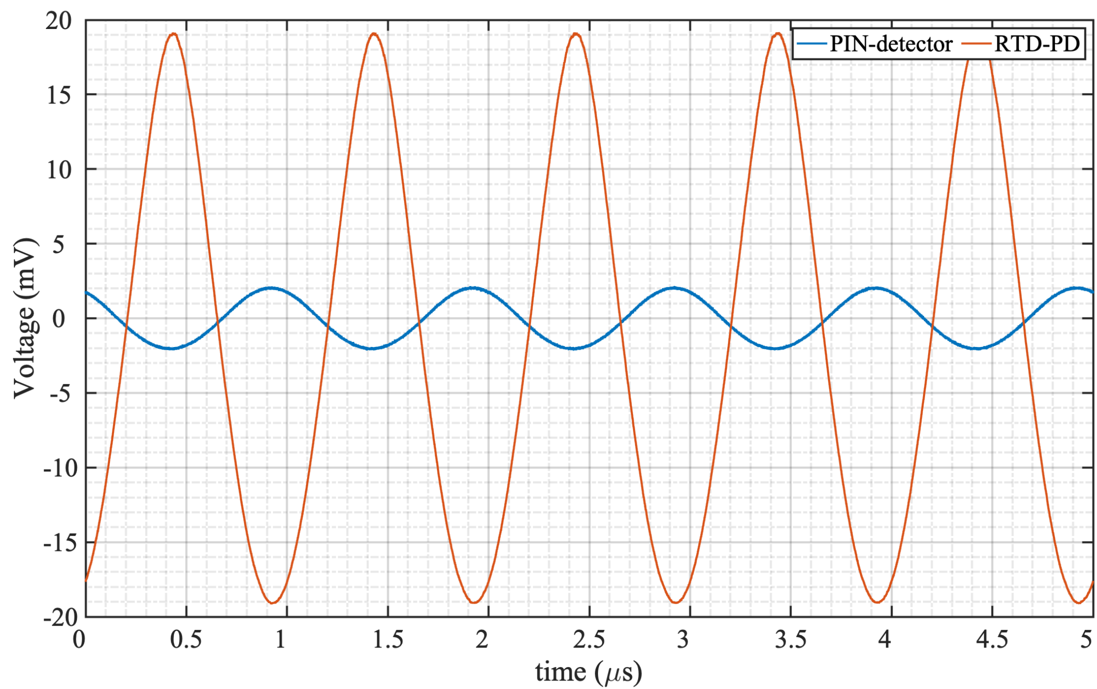

Figure 137: Wafer 73A - RTD-PD and PIN photodiode detected signals (DC offset removed).

5.6 Summary and conclusion

This chapter highlights the main findings of the optical characterization results of multiple epitaxial layer designs for resonant tunnelling diode-based photodetectors (*RTD-PD*). We have studied these epitaxial layers under DC and AC optical excitation and measured their current responsivity under various illumination levels. We have also measured the impulse response and 3dB bandwidths of these devices in order to determine their maximum speed of operation under optically modulated light. We observed that the peak voltage point tends to shift to a lower value when illuminated with low illumination levels without any significant current gain and attributed that to charge accumulation near the collector barrier. We also showed that under higher illumination levels the peak voltage starts to shift in the opposite direction and is accompanied with an increase in the current. That we attributed to more carriers being generated in the emitter side. In terms of responsivity, we have reached values up to 65 A/W for illumination levels in the milliwatt range and around 1×10^7 A/W at the picowatt range. We demonstrated that charge generation in highly doped contact regions is a main source of low optical speed of response and showed that devices that mitigate any charge generation at the contacts have much higher 3dB bandwidths. The work shows that devices based on the *PIN* scheme could go up to 1.75 GHz in optical 3dB bandwidth and we attribute the speed limitation in RTD-PD to the photogenerated carrier's lifetime which accumulate at the barriers.

Chapter 6 : Resonant tunnelling diode – laser diode integration

6.1 Introduction

The chapter aims at studying the integration of laser diodes (*LD*) and resonant tunneling diode photodetectors (*RTD-PD*s). The material system in question for the *RTD-PD*s will be $In_{53}Ga_{47}As/InP$ with target operating wavelengths of 1.55 μm and 1.31 μm. *LD*s and *RTD-PD*s will be investigated analytically and numerically to gain a deeper insight into the *RTD-PD-LD* appropriate configurations and functionalities. The task aims at using circuit models for both *RTD-PD*s and *LD*s to study the outputs of such integrated circuit. The *LD* is connected in series with the *RTD*, such that the *RTD* current is the driving current for the *LD*. The models are programed into MATLAB and various operation modes are simulated depending on the chosen bias point and input signals.

The chapter starts by modeling the *RTD* current-voltage (*IV*) characteristics, for $In_{53}Ga_{47}As/AlAs$ based *RTD* systems. Then moves into the modeling of both the *RTD* and *LD* electrical equivalent circuit. The circuit is then tested under various excitation conditions and the total system is studied under various operating modes. The outputs of these studies are used to develop mathematical models which can predict device behavior and give insight to the design of epitaxial layers. Finally, some practical data is measured in the lab and compared to the results of the simulations.

6.2 Motivation

The study of the integration between *RTDs* and *LD*s is not new, in 1991 Gravè et. al have studied the monolithic integration of an *RTD* with a quantum-well *LD* [138]. This device showed an *NDR* in both electrical and optical domains. The Authors have also exploited the bi-stability properties of the *RTD-LD*, and showed how this device could be used for memory application. Shortly afterwards in 1994, the same system was reported by Sheng et. al [139].

RTDs have shown great potential for high frequency circuit operation. Owing to their highly non-linear *IV* characteristics which are mainly characterized by a negative differential conductance region (*NDC*), *RTDs* have built-in gain properties. By integrating a photo-absorption region within the *RTD* structure, *RTD* photodetectors (*PDs*) can be made. Due to the built-in amplification effects and the non-linearities associated with the electric field around the *DBQW*, *RTD-PD*s serve as new candidates for high frequency and high sensitivity applications. Furthermore, *RTDs* operating in the *NDC* region have shown to operate as electronic oscillators with oscillation frequencies reaching well into the *THz* range with a maximum frequency to date of 1.98 THz [5]. Since the current in the *RTD* can be sufficiently large it can be used to drive a *LD* and drive it in multiple operating regimes. The *RTD* can control the *LD* current by fast switching between the peak and valley current values. Furthermore, utilizing the bi-stability of the *RTD* [140]–[142], it can effectively switch the *LD* on and off. At the same time, *RTDs* operating in the *NDC* region can be used to induce modulated light signals out the *LD*, which paves the way towards opto-electronic oscillators with the integration of *RTD-PD* with *LD*. Such a device has potential in other applications such as frequency division. It has been shown [143], that applying an *AC* signal while the *RTD* is biased in the *NDR* region results in a frequency-division effect that depends on the frequency of the applied AC signal. This points to the use of *RTD-LD* as optical signal generators with adjustable frequencies. Other possible applications include: interfaces for radio-over fiber networks [64], micro-cells to support *5G* and *IoT* applications, and wireless interfaces through the *RTDs* ability to do injection locking. One final application is to build a tunable optical oscillator. This is possible by utilizing the operation of the *RTD* as a voltage-controlled oscillator while biased in the *NDR* region. As there is a certain tuning voltage range, during which the frequency of oscillation changes according to the applied voltage [144].

*RTD-PD*s have shown the tendency of shifting the peak voltage location when illuminated with light [54]. This is clear in Figure 138, which shows the light response of some *RTD-PD* devices we characterized earlier (*NC1800*). The epi-layer for this design is shown in Table 6-1. Such a behavior makes *RTD-PD*s attractive in driving *LD*, as the operating point of the circuit can be changed using light signals from the *NDC* into the *PDC* and vice versa.

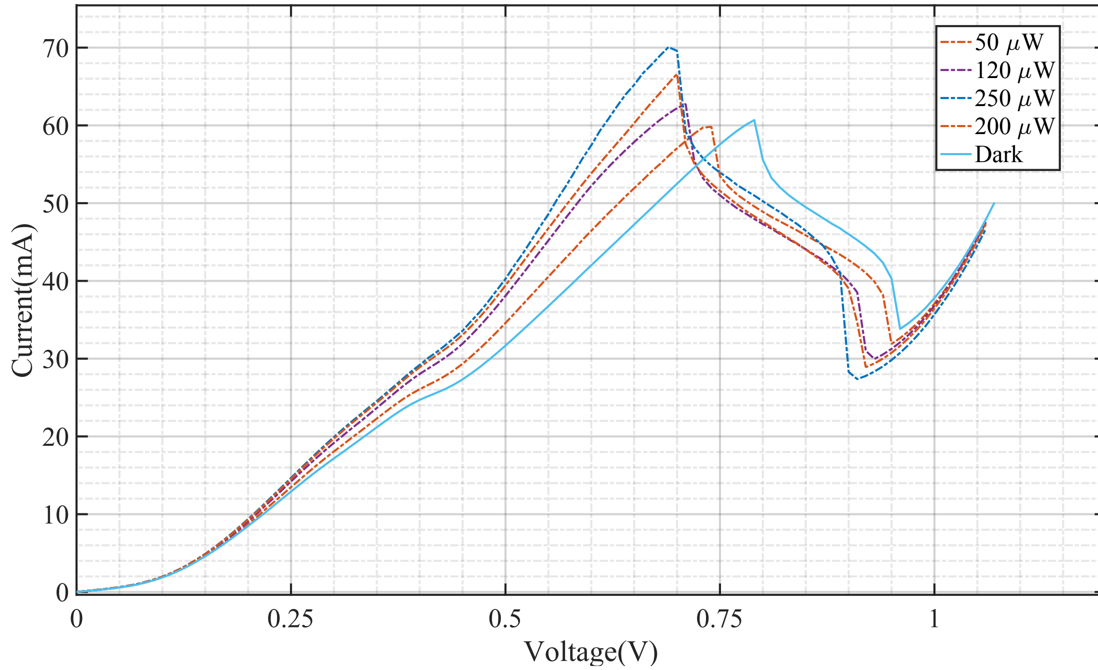

Figure 138: RTD-PD under dark and illumination conditions (10x10 μm²).

Table 6-1: Epitaxial layer design of wafer NC1800.

Layer	Type	Material	Thickness (nm)	Doping level (cm^{-3})
1	N++	$In_{53}Ga_{47}As$	45	3×10^{19}:Si
2	N+	$In_{53}Ga_{47}As$	80	3×10^{18}:Si
3	N-	$In_{53}Ga_{47}As$	500	5×10^{16}:Si
4	I	$In_{53}Ga_{47}As$	2	Undoped
5	I	AlAs	1.7	Undoped
6	I	$In_{53}Ga_{47}As$	4.7	Undoped
7	I	AlAs	1.7	Undoped
8	I	$In_{53}Ga_{47}As$	2	Undoped
9	N-	$In_{53}Ga_{47}As$	20	2×10^{16}:Si
10	N+	$In_{53}Ga_{47}As$	80	3×10^{18}:Si
11	N++	$In_{53}Ga_{47}As$	400	3×10^{19}:Si
12	SI	*InP*	200	-

6.3 Methodology

6.3.1 Modelling of RTD-PD-LD circuits

In order to study the integration of an *RTD* with a *LD*, circuit models for both devices need to be developed. These models are based on the *DC* and *AC* responses obtained from each of these devices. The equivalent circuits can then be combined into a single circuit where the *RTD-PD* is connected in series with the *LD*.

An *RTD* can be modeled using the circuit shown in Figure 139 where R_{line} is a lumped resistance of the bias circuitry and that of the *RTD*, L_{line} represent the inductance of the bias circuitry, C_{RTD} represents the device's capacitance. Finally, the current of the *RTD* is modeled as a voltage dependent current source *I(V)*. As a side note, as the equivalent circuit has *R*, *L* and *C* elements, it is typical to have low frequency oscillations while the device is biased in the *NDR*. The frequency of these oscillations is quite low for typical bias-circuity inductances (μH range) and can be in the hundreds of kHz range.

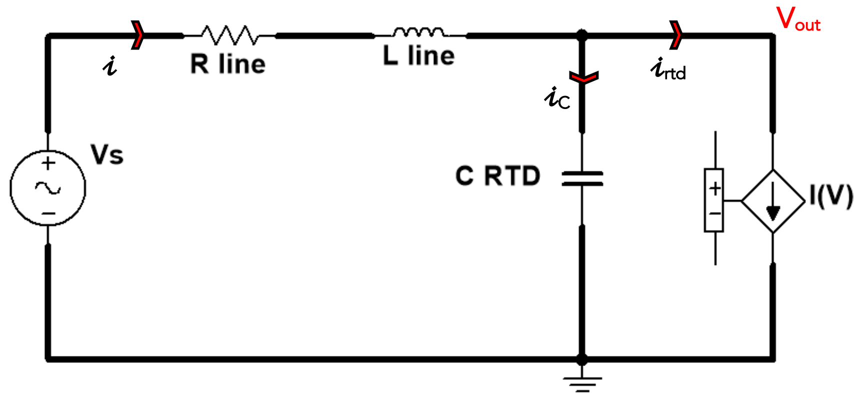

Figure 139: Large signal equivalent circuit of an RTD.

The values for all these circuit elements can be obtained from actual devices in the literature. However, the most important aspect is to get a mathematical expression for the voltage controlled current source which resembles the *RTD IV* relationship.

Various efforts to model the IV characteristics of an *RTD* have been done in literature. The most widespread of which is that of [145]. The Schulman model is used as a curve-fitting method to extract physical data from actual fabricated devices, such as the location of the Fermi-level and quantized Eigenstates. The *J-V* characteristics and accompanying parameters according to this model are given by (6-1) to (6-5).

$$J(V) = A\ln\left(\frac{1+e^{(B-C_s+n_1V)\left(\frac{e}{kT}\right)}}{1+e^{(B-C_s-n_1V)\left(\frac{e}{kT}\right)}}\right)\left(\frac{\pi}{2}+tan^{-1}\left(\frac{C_s-n_1V}{D}\right)\right)+H\left(e^{n_2\frac{V}{kT}}-1\right) \quad (6\text{-}1)$$

$$A = \frac{ekT\Gamma m^*}{4\pi^2\hbar^3} \quad (6\text{-}2)$$

$$B = E_f \quad (6\text{-}3)$$

$$C_s = E_n \quad (6\text{-}4)$$

$$D = \frac{\Gamma}{2} \quad (6\text{-}5)$$

Where E_f and E_n are the Fermi energy and the nth quantized Eigenstate in the quantum well respectively. T is the temperature in kelvin, k the Boltzmann constant, $\hbar$ the reduced Planck constant, m^* the effective mass, e the elementary electron charge, Γ the resonance width in eV and n_1, n_2 and H are fitting parameters. Notice that the second term in (6-1) resembles the diode equation. This part is responsible for the increase in current for the second *PDC* and hence the values of H and n_2 are not of vital importance for our application at the moment.

The main drawback of the Schulman model is that it is not appropriate for designing purposes as one cannot anticipate all the values of the fitting parameters particularly the n_1 parameter in (6-1). Notice that all the other parameters can be calculated theoretically and obtained with a good degree of precision [146]. The parameter n_1 is mainly controlled by the collector's length and it's doping concentration and influences the location of the peak voltage (V_p). The doping in the emitter's side does not influence this parameter much. It is, therefore, important to study the effect of the spacer layer parameters on the location of V_p *[125]*. This has been discussed in chapter 3 where we found that the influence is mainly due to the collector depletion length (L_{CD}), and the actual length of the collector itself (L_c). The depletion length in the collector is dependent on the Debye length, after which the peak voltage stops depending on the length of the collector. The Debye length, in its own, is determined by the doping concentration in the collector as given by (6-6), where ϵ is the dielectric permittivity of the material and $N_{collector}$ is the doping in the collector region. More information will be presented in the results section.

$$L_{Debye} = \sqrt{\frac{\epsilon kT}{N_{collector} e^2}} \tag{6-6}$$

Building on the results of the above study, one can calculate the peak voltage associated with a given $In_{53}Ga_{47}As/AlAs$ structure. The fitting parameter n_1 in the Schulman model can then be calculated by taking the ratio between the peak voltage at the ideal case, (i.e.: when the peak is twice the separation between the Fermi energy and first quantized Eigenstate), and the one calculated from our model as shown in (*6-7*).

$$\mathrm{n_1} = \frac{2(\mathrm{E_n} - \mathrm{E_f})}{\mathrm{V_p}} \tag{6-7}$$

Using this data, a MATLAB program was written to plot the *IV* characteristics of any *RTD* based on the above equations without the need of using numerical simulations which take a long time due to the nature of physical simulators and the use of complex numerical techniques. The program takes as inputs: the simulation voltage range, the doping concentration at both the emitter and the collector, the width of the quantum well, the length of the collector, and the total area of the device. The first step is to calculate the energy Eigenstates inside the quantum well, this is done using a graphical method as detailed in [147]. Next, the Schulman parameter are calculated using the relationships in (6-2) to (6-5), and the *H* parameter according to (6-8) [146]

$$H = e\, n_i^2 \times \left(\left(\frac{D_n}{L_n N_a} \right) + \left(\frac{D_p}{L_p N_d} \right) \right) \quad (6\text{-}8)$$

where D_n, D_p, L_n, L_p, N_a, N_d, and n_i are the electron diffusion constant, hole diffusion constant, electron diffusion length, hole diffusion length, acceptor carrier concentration, donor carrier concentration, and the intrinsic carrier concentration respectively.

The peak voltage is then determined as introduced in chapter 3, through the calculation of the Debye length, and then the value of n_1 can be deduced.

To validate the program one of the devices available at our labs was tested, and the measured *IV* compared with the simulated *IV*. The results of the program show very good resemblance of actual measured devices as in Figure 140. Now we can design any $In_{53}Ga_{47}As/AlAs$ *RTD* device and get the values of the fitting parameters from the MATLAB program, which can then be used to model the voltage dependent current source.

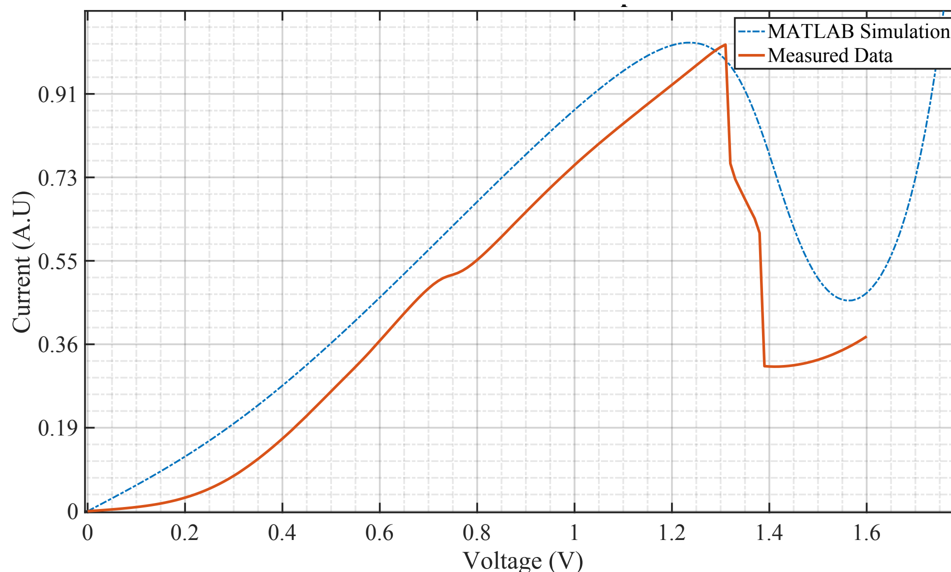

Figure 140: IV curves of measured RTD vs. MATLAB simulation.

We now move to the laser diode. We will start by a brief introduction to the principle of operation of a *LD*. Recall from chapter 4, that the condition for light emission from a semiconductor is that the difference between the quasi-Fermi potentials ($E_{fc} - E_{fv}$) are greater than the bandgap. This requires degeneracy conditions, (the quasi Fermi-level to be above the conduction band edge at the conduction band, and the quasi Fermi-level at the valence band to be below the valence band edge in the valence band), to be present around the active area of the device, where light is to be emitted.

In order to have a coherent source of light, the spontaneous emission coming from the semiconductor is put inside a resonant cavity where the generated light bounces around the cavity and provides feedback to the gain medium (semiconductor). This is analogous to the operation of an oscillator in an electronic system.

Recall that, the light beam intensity though a semiconductor is governed by Beer's law, with γ being the semiconductor gain given by (*6-10*).

$$\mathrm{I(d)} = I_0 e^{\gamma d} \tag{6-9}$$

$$\gamma = \frac{\left(\frac{c}{n}\right)^2 \sqrt{h\nu - E_g} f_g(E)}{8\pi(\mathrm{h}\nu)^2\tau} \tag{6-10}$$

$f_g(E)$ is the probability of emission minus the probability of absorption given in chapter 4. When γ is positive, the semiconductor provides gain through the stimulated emission mechanism with the same rates as those given in chapter 4. To have lasing action, the gain provided by the semiconductor must equal the total losses introduced by the cavity. This is the main equation that governs the working of a laser diode.

A typical semiconductor laser has losses related to the reabsorption of the photons in the material itself, scattering losses, and losses in the resonator. In good semiconductor laser diodes these losses are around 30-50 cm^{-1}. The resonator losses are usually due to the reflections from the semiconductor/air interface and is given by (*6-11*) [68].

$$\alpha_{\mathrm{resonator}} = \frac{1}{2\mathrm{L}} \ln\left(\frac{1}{\mathrm{R_1 R_2}}\right) \tag{6-11}$$

Where L is the length of the cavity, R_1 and R_2 are the reflectivity's of the semiconductor-air interface. Since in a semiconductor laser R_1 and R_2 are equal, (*6-11*) reduces to (*6-12*).

$$\alpha_{\mathrm{resonator}} = \frac{-1}{\mathrm{L}} \ln(\mathrm{R}) \tag{6-12}$$

Usually, semiconductor lasers have a built-in waveguide as part of the layer structure (most *LD* utilize a double-heterostructure design with different refractive indices for the materials), and accordingly not all the generated beam of light is confined inside the gain medium. This is modeled using a confinement factor $\Gamma_{confinement}$. Hence, the main laser equation becomes:

$$\gamma\Gamma_{\mathrm{confinemnt}} = \alpha_{\mathrm{total}} \tag{6-13}$$

There are some important quantities when it comes to the operation of a *LD*, one of which is when the semiconductor medium neither provides gain nor absorbs light. This condition is known as the transparency condition, and the current and carrier concentration at which this occurs are known as the transparency current and carrier concentration respectively. Increasing the gain (current injection) above transparency conditions starts to give rise to spontaneous emission. This commences until the gain equals the loss at which lasing action starts, and the current and carrier densities at which this occurs are known as the threshold current and carrier densities respectively.

The threshold carrier concentration can be calculated using (*6-13*) for a given loss and confinement factor. This results in the calculation of the required quasi-Fermi level separation *(E_{fc} – E_{fv})*, which is used to calculate the threshold carrier concentration using the Joyce-Dixon approximation, or thorough direct integration using (*6-14*) [148].

$$n_c = \frac{m^*\sqrt{2m^*}\int\left(\sqrt{E-E_c}\,dE\right)}{\pi^2\hbar^3} \tag{6-14}$$

When the *LD* operates, the recombination of the electrons and holes produces the light emission. This process affects the carrier concentrations and determines the number of photons emitted (flux). These two quantities are related though the laser rate equations given by (6-15) and (6-16) [149], [150].

$$\frac{dN}{dt} = \frac{I}{eV_{act}} - g_0(N-N_0)\left(1-\epsilon_{comp}S\right)S - \frac{N}{\tau_n} + \frac{N_e}{\tau_n} \tag{6-15}$$

$$\frac{dS}{dt} = \Gamma g_0(N-N_0)\left(1-\epsilon_{comp}S\right)S + \frac{\Gamma\beta\mathrm{N}}{\tau_n} - \frac{S}{\tau_p} \tag{6-16}$$

where τ_n, τ_p, N_o, g_o, ϵ_{comp}, Γ, and V_{act} are the electron lifetime, photon lifetime, the transparency carrier concentration, the gain factor, the gain compression factor, the confinement factor and the volume of the active region respectively. *S* is the photon density; N_e is the equilibrium carrier concentration and β the spontaneous emission factor.

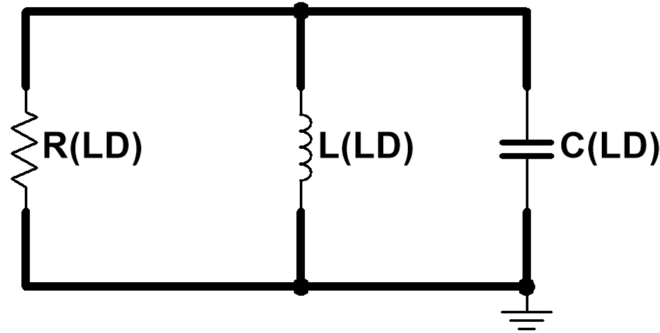

Figure 141: AC electrical equivalent circuit of a laser diode. Without modeling spontaneous emission, self-pulsation.

The same approach is used, the *LD* is modeled as a resistance and a *DC* voltage source, to denote the "on" voltage of the *LD*, in series with a diode. Under *AC* conditions the electrical equivalent circuit of the *LD* is also an *RLC* circuit as shown in Figure 141 [151]. R_{LD}, L_{LD}, and C_{LD} have their origins from the rate equations above, and can be related to their physical parameters [152]. The *RLC* elements to model the *LD* are chosen such that it can operate at around 10 GHz, to that, values of 10.5 Ω, 320 pF and 0.8 pH for *RLC* respectively are chosen. The circuit of Figure 141 is simulated using the SPICE package Multisim to verify that it operates at the desired frequency.

Hence the circuits for modeling the *RTD-PD-LD* for both *AC* and *DC* conditions can be made as is shown in Figure 142. The circuit has two parts one related to the *DC* bias circuitry and another for the *RTD-PD-LD*. The bias circuitry can be decoupled from the *RTD-PD-LD* circuit under high frequency conditions using a decoupling capacitor in the order of the micro farad range. As the impedance of a capacitor is given by (*6-17*)

$$Z_c = \frac{1}{j\omega C} \tag{6-17}$$

To decouple the bias circuit from the resonant circuit capacitance should be sized such that Z_c acts as a short circuit at the required frequencies. This effectively decouples the bias and resonant circuits. It is not unusual to use multiple decoupling capacitors with multiple values. The typical values range from 0.1 µF and can go up to 100 µF [153].

Under high frequency conditions (3 – 10 GHz), a circuit like that in Figure 139 can be used to analyze the response of the circuit. Notice that the *RLC* elements of the *LD* can be lumped into a single impedance when doing *AC* analysis. For simplicity, the *LD* will be modeled by a resistor in series with an ideal diode and a voltage source as in Figure 142. The values of the capacitance and inductance of a typical *LD* are quite small and do not resemble

a very large impedance for frequencies in question. The resistance values are also quite small (a couple of Ohms range), and since the same current goes through the main resistance and the *LD*'s resistance, these can be added together in a single resistance when we do the stability analysis in the coming sections. We will show that with these simplifications the results are still satisfactory.

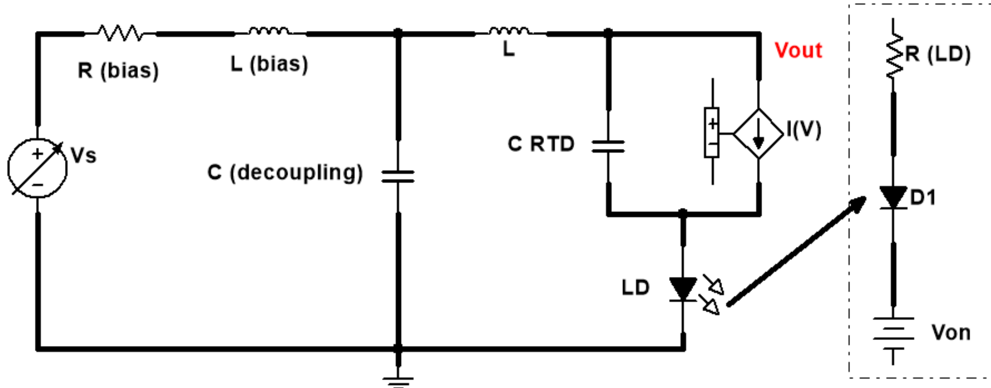

Figure 142: Equivalent circuit of RTD-LD.

The circuit simulations are made using a combination of MATLAB code and Multisim. Multisim is a SPICE-based platform that allows the simulation of various electronic and electric components with the ability to program custom devices such as the *RTD-PD* in our case [154].

As the circuit is built and ready, we now move to investigating the modes of operation of the circuit. To do that, we need to define a certain *RTD-PD* and a *LD* and their associated circuit parameters for simulation. The *RTD-PD* and *LD* model parameters and the values for the *R*, *L* and *C* elements of the equivalent circuit in Figure 142 are listed in Table 6-2 which are based on data from [149], [155] for benchmarking the simulation results. The *LD* has a turn-on voltage of 0.7 V and a threshold current of around 10 mA. The threshold current can be calculated according to (*6-18*) with η_i being the quantum efficiency, where the threshold carrier concentration is deduced as explained earlier.

$$I_{threshold} = \frac{N_{threshold} \times \eta_i \times Volume \times e}{\tau} \tag{6-18}$$

The current-voltage relationship for this laser can be drawn according to the circuit shown in Figure 142 (based on a linearized model), and the anticipated output power versus current can be calculated using (*6-19*) [82], where *n* is the refractive index, and *L* is the cavity length (200 μm assumed).

$$P_o = \frac{hc^2 \tau_p (1-R)}{2en\lambda L}(I - I_{th}) \tag{6-19}$$

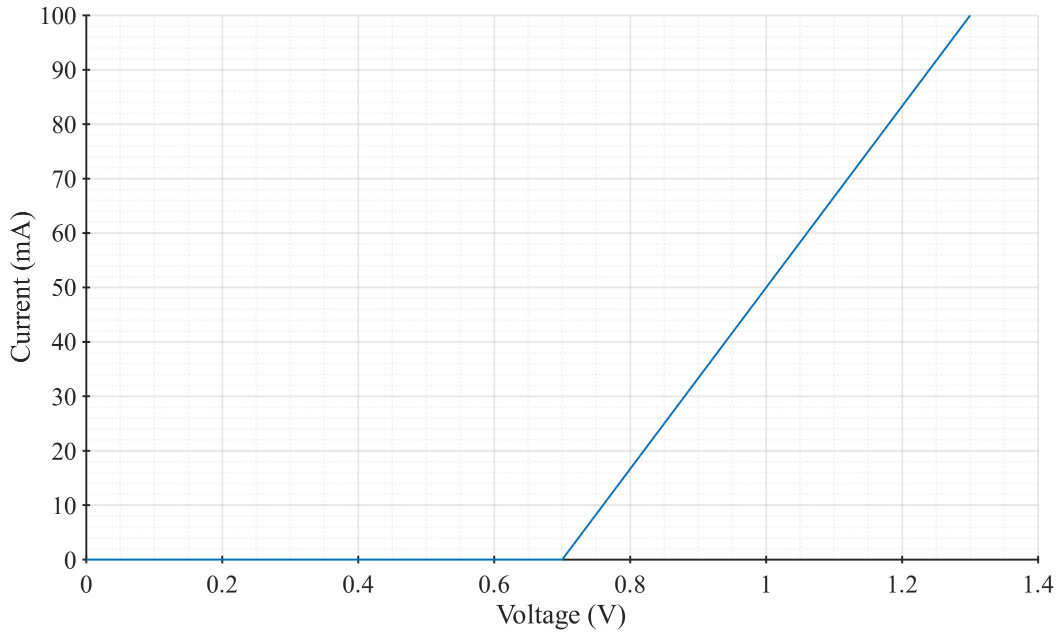

Figure 143: IV curve of LD.

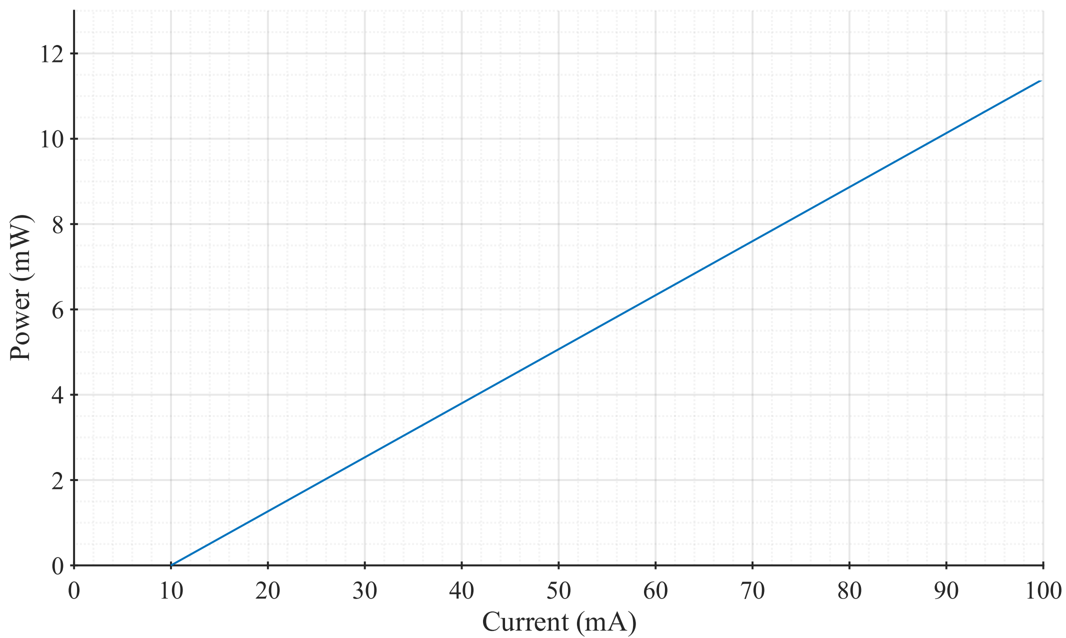

Figure 144: Output optical power of LD.

An important aspect of *LD* operating at high frequencies is the relaxation frequency ($f_{relaxation}$). This aspect imposes a limit on the maximum operating frequency of the *LD* due to the recombination lifetime and is given by (*6-20*) [69], where *I* is the operating current.

$$f_{relaxation} = \frac{1}{2\pi\sqrt{\tau_n \tau_p}} \times \sqrt{\left(\frac{I}{I_{threshold}} - 1\right)} \tag{6-20}$$

Plugging in the numbers in Table 6-2 we get a frequency of around 7 GHz at 55 mA, noting that the *LD* we are considering is a Fabry-Perot laser.

With that in mind and given the *RTD* IV-curve in Figure 145, the *RTD* can be used to turn on and off the *LD* when biased in the *PDC* and the bottom of the *NDC* respectively.

Table 6-2: RTD and LD simulation parameters [141],[142].

Circuit element	Parameter	Value
RTD-Schulman model parameters	A	6.48×10^{-3}
	B	0.0875
	C_s	0.1449
	D	0.005
	H	7.9×10^{-4}
	n_1	0.19
	n_2	0.0284
Bias circuit and equivalent passive components	R	6.2 Ω
	L	8 nH
	C	5 pF
Laser diode	τ_n	2×10^{-9} s
	τ_p	1.1×10^{-12} s
	N_0	1×10^{18} cm^{-3}
	β	3×10^{-2}
	g_0	1×10^{-6} cm^3/s
	ϵ	0.6×10^{-17} cm^3
	Γ	0.44
	V	1×10^{-16}
	V_{on}	0.7 V
	$I_{threshold}$	10 mA

With these parameters the *IV* curve of the *RTD-PD* is shown in Figure 145.

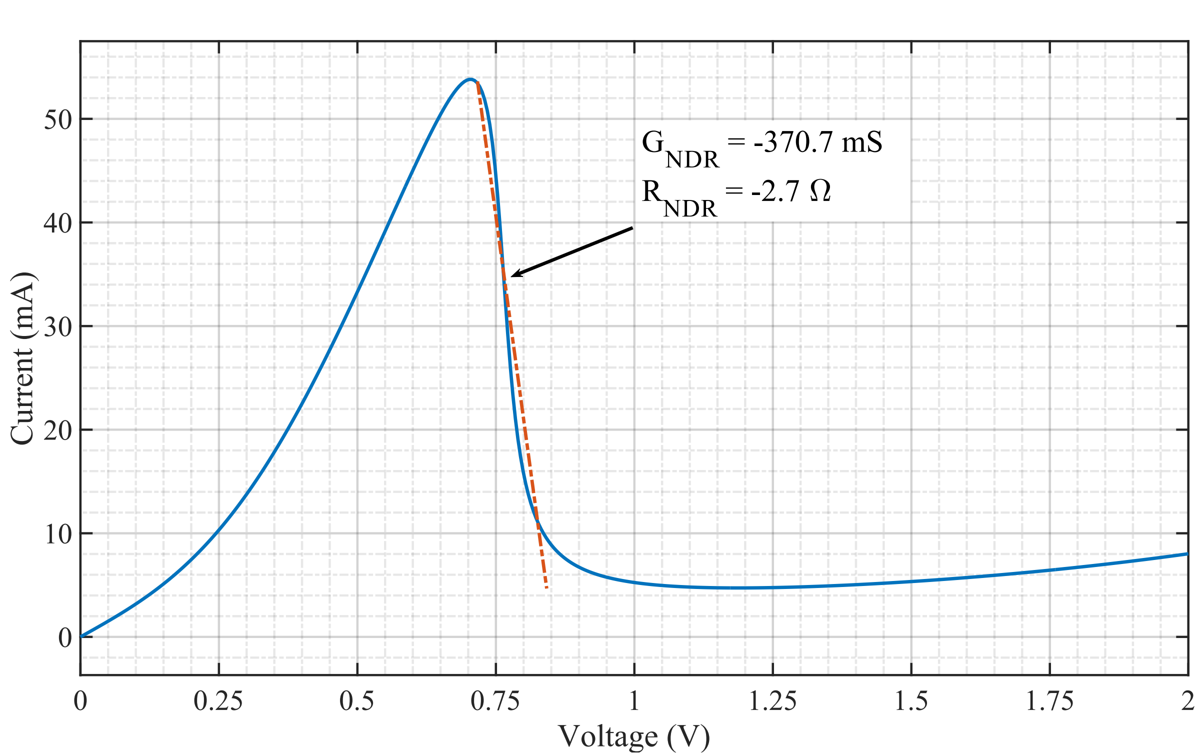

Figure 145: IV curve of the RTD with parameters in Table 6-2. The line shows the linear approximation of the NDC region.

Now, it is important to calculate the value of the conductance at the *NDC* region. Using a linear approximation one can write the *IV* curve in the *NDC* as [146]:

$$I(V) = I_{peak} + (\frac{I_{valley} - I_{peak}}{V_{valley} - V_{peak}})(V - V_{peak}) \tag{6-21}$$

The *NDR* can also be modeled to include voltage dependence, however we will stick to the simplified linear approximation made above. With a suitable load resistance, the *NDR* can be stabilized to have a stable region, over which the slope is voltage independent.

Given the values in Figure 145, the conductance calculated is given by the slope of the linearized *NDC* region, and is equal to –370.7 mS, to which the negative differential resistance value is -2.7 Ω. This approximation will be useful when discussing the stability of the oscillations of *RTD-PD*s as will be discussed shortly.

At high frequency (the bias circuit is effectively decoupled form the *RTD-PD-LD* circuit and the circuit of Figure 142 can be reduced to that shown in Figure 146. The values here represent all the total values including any additional elements (such as capacitors) which might be added to the circuit.

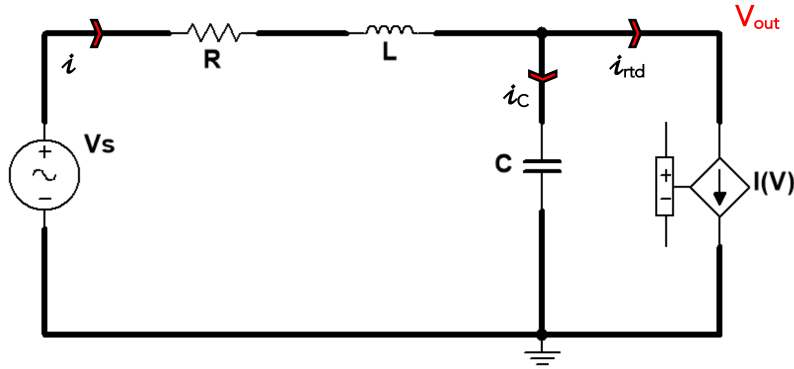

Figure 146: RTD-PD equivalent circuit at high frequency.

The circuit in Figure 146 can be solved by the writing the *KVL* equations and solving for V_{rtd} *(t)*, which is the voltage across the voltage dependent current source (V_{out}). To that, we need to solve for the voltage across the capacitor given by (6-22)

$$\frac{dv_c}{dt} = \frac{i_c}{C} \tag{6-22}$$

where i_c is the current in the capacitor. By applying KCL at the output (V_{out}) node we see that

$$i(t) = i_c + i_{rtd}(v) \tag{6-23}$$

Applying KVL to the larger loop we get:

$$\frac{d^2v_{rtd}(t)}{dt^2} + \frac{R\,dv_{rtd}(t)}{L\,dt} - \frac{v_{rtd}(t)}{LC} - \frac{R}{LC}i_{rtd}(v) - C\frac{di_{rtd(t)}}{dv_{rtd}}\frac{dv_{rtd}}{dt} - \frac{Vs + V_{on}}{LC} = 0 \tag{6-24}$$

Rearranging the terms in (6-24) we get the final equation as shown in (6-25)

$$\frac{d^2v_{rtd}(t)}{dt^2} + \left[\frac{R}{L} + \frac{1}{C}\frac{di_{rtd}(v)}{dv}\right]\frac{dv_{rtd}(t)}{dt} + \frac{R\,i_{rtd}(v)}{LC} - \frac{v_{rtd}(t)}{LC} = \frac{V_s + V_{on}}{LC} \tag{6-25}$$

Equation (6-25) resembles a second order non-linear differential equation known as the Liènard equation. This can be solved by substitution which converts the system to two first order differential equations which have to be solved iteratively, the solutions of which are known as relaxation oscillations. The solution to this equation was conducted using MATLAB.

6.3.2 RTD-PD-LD modes of operation

The circuit will be investigated under various modes of operation determined by the bias point of the *RTD-PD* driving the *LD*. These modes include when the device is biased in the *PDR* and an *AC* signal is applied, when the device is biased in the *NDR* region and the device starts to oscillate, and when the device is switched between the *NDR* and *PDR*.

While the *RTD-PD* is biased in the first *PDC* the device is stable and can supply enough current for the laser diode for light emission. The emission rates and light intensity of the laser are expected to follow the normal current-power curve of the laser. While biased in this

region, if an *AC* signal is superimposed over the *DC* bias the output of the *LD* is expected to follow the input *RF* signal. In our simulations we have chosen a bias point of 0.5 V for the *RTD-PD* with a superimposed sinusoidal wave of frequency 1 *GHz* and amplitude of 100 mV. The *RTD-PD* parameters and the *LD* parameters used are those in Table 6-2.

When the *RTD-PD* is biased in the *NDC*, the device is unstable and oscillates with relaxation oscillations. The frequency and shape of which are dependent on the *RLC* circuit elements that form the bias and measurement networks. In order to operate the previous *RTD-PD-LD* in the *NDC* region, the applied voltage must equal the "on" voltage of the *LD* plus the required bias voltage for the *RTD*. To that a bias voltage of 1.8 V was chosen. Using the values of *R, L* and *C* given in Table 6-2, the undamped natural frequency of the circuit is given by (6-26). Which is around 800 MHz. The results of the simulations will be shown in the results section.

$$f_n = \frac{1}{2\pi\sqrt{LC}} \tag{6-26}$$

We now consider studying the dependence of this relaxation oscillation frequency on the elements comprising it; mainly *R, L* and *C* (in Figure 146). To that the MATLAB simulator will be used to simulate multiple *RLC* values, by changing one variable at a time and monitoring the frequency of the oscillations for a given negative differential resistance value. The study was conducted with resistance values of 2,3,4,5,6 and 7 Ω, the capacitance studies used capacitance values of 0.1, 1,5,10,20, and 30 pF, and finally the inductance values of 1, 8, 20, 40, 60, and 100 nH.

The final region to be investigated, is the result of fast switching operation between the *PDC* and *NDC* regions. This is simulated by a pulse train function which drives the bias point into and out of the *NDC* region at a given frequency. This means that the *RTD-PD* will be oscillating while in the *NDC* and stable while in the *PDC*. If the frequency and amplitude of the signal applied are within a certain range, the circuit shows a spiking output that is characterized by a certain refractory time. This is the time required for the device to go back to equilibrium and be able to be excited again. This sort of behavior is seen in other non-linear systems in biology and chemistry. Where the system does not produce any response to a stimulus that is lower than a certain threshold, while it responds with a large signal (spike) to a stimulus that is above this threshold value. This is also known as the excitability property

of a system [15], [16]. The dynamics of such non-linear systems are described by the non-linear dynamics theory and chaos [17], details about these can be found elsewhere and are outside the scope of this work.

In order to show these oscillations using simulations, the same *RTD-PD* device was used and is biased at 1.72 V (just below the peak voltage), at which the device does not show any oscillations. A positive pulse train of rectangular pulses with a width of 1 ns and frequency of 100 MHz was used to drive the *RTD-PD* into and outside of the *NDC*. The amplitude of the superimposed signal was 100 mV. The output relaxation oscillations are shown in the results section.

At this point, a discussion about the stability criteria for the *RTD-PD-LD* is important. To do that the characteristic equation in the S domain of the circuit in Figure 147 is derived by writing the transfer function *H(S)*.

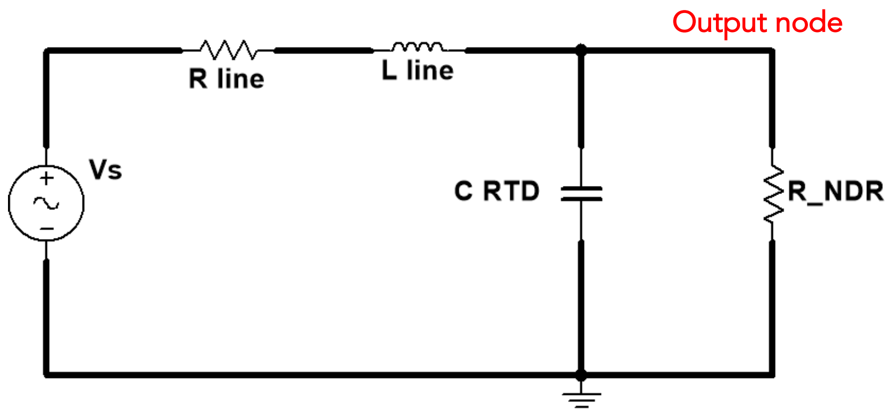

Figure 147: RTD-PD equivalent circuit with linearized NDC region.

$$H(S) = \frac{R_{NDR}}{S^2 + \left(\frac{R}{L} + \frac{1}{CR_{NDR}}\right)S + \frac{R + R_{NDR}}{LCR_{NDR}}} \tag{6-27}$$

The poles of *H(S)* will be used to derive the oscillation conditions and stability criteria, which are given by (6-28). As highlighted earlier, R_{NDR} is more accurately modeled by a voltage dependent resistor.

$$S_{1,2} = \frac{-\left(\frac{R}{L} + \frac{1}{CR_{NDR}}\right) \pm \sqrt{\left(\frac{R}{L} + \frac{1}{CR_{NDR}}\right)^2 - 4\left(\frac{R + R_{NDR}}{LCR_{NDR}}\right)}}{2} \tag{6-28}$$

Here we define the neper frequency α_0 and the undamped natural frequency ω_0 to be equal to

$$\alpha_0 = \frac{1}{2}\left(\frac{R}{L} + \frac{1}{CR_{NDR}}\right) \tag{6-29}$$

$$\omega_0 = \sqrt{\left(\frac{R + R_{NDR}}{LCR_{NDR}}\right)} \tag{6-30}$$

to which (6-28) can be rewritten as in (6-31)

$$S_{1,2} = -\alpha_0 \pm \sqrt{\alpha_0^2 - \omega_0^2} \tag{6-31}$$

In order to get oscillatory response, the system has to have imaginary solutions. This happens when α_0^2 is less than ω_0^2. At the same time the real part of the solution should not be positive, so as not to grow out of bounds. This gives the conditions for oscillations as follows.

$$\alpha_0 < \omega_0 \tag{6-32}$$

$$\alpha_0 \geq 0 \tag{6-33}$$

Applying these conditions, we get the constrains on *R*, R_{NDR}, *L* and *C* for oscillatory behavior.

$$2 + \frac{L}{CR_{NDR}} > R > \frac{L}{CR_{NDR}} - 2 \tag{6-34}$$

Notice that when α_0 is zero, then the system will oscillate with a frequency equal to ω_0, and when α_0 is greater than zero, the system will oscillate with a damped frequency ω_d as given by (6-35).

$$\omega_d = \sqrt{\omega_0^2 - \alpha_0^2} \tag{6-35}$$

From (6-34), we see that the ratio of *L/C* is very important in determining the oscillation conditions for practical systems [156].

Utilizing these conditions, circuits can be designed to have frequencies well into the tens of GHz range. An example circuit with an inductance of 25 pH, capacitance of 2 fF and a resistance of 2 Ω will give a frequency of around 30 GHz. The results section portrays such results. Typical values for the *RTD* capacitance for similar epi-layers of S99 and S98 is in the hundreds of femto-farads for a device area of 100 μm^2 [65]. Therefore, one way to reduce this capacitance is to reduce the overall device size below 1 μm^2.

6.4 Practical experimentation with *RTD-PD*

We then moved to practical experiments at the lab to try and verify some of the results obtained. The epitaxial layer design of the devices used are in Table 6-3 and Table 6-4. Devices with similar epi-structures but with different lengths for the lower doped emitter/collector regions were also tested. These devices have emitter lengths of 250, and

100 nm with a short collector of 20 nm. The first task was to study how the oscillation frequency changes with the applied voltage in the *NDC* region, thereby studying the RTDs as voltage-controlled oscillators (*VCOs*). The devices were biased in the *NDC* region, and the voltage was swept across the entire range of the *NDC* while the frequency of the oscillations was monitored using a high frequency oscilloscope. It was noticed that the frequency of oscillation increased as the voltage was increased with different frequency ranges and voltage tuning ranges for various epitaxial layers. Typical results from the epi-layers we characterized are shown in the results section.

Table 6-3: epitaxial layer design of physical tested RTDs.

Layer	Type	Material	Thickness (nm)	Doping level (cm^{-3})
1	N++	$In_{53}Ga_{47}As$	100	2×10^{19}:Si
2	N+	$In_{52}Al_{48}As$	300	2×10^{18}:Si
3	N-	$In_{53}Al_{0.08}Ga_{46.2}As$	500	5×10^{16}:Si
4	I	$In_{53}Al_{0.08}Ga_{46.2}As$	2	Undoped
5	I	$AlAs$	1.7	Undoped
6	I	$In_{53}Ga_{47}As$	5.7	Undoped
7	I	$AlAs$	1.7	Undoped
8	I	$In_{53}Al_{0.08}Ga_{46.2}As$	2	Undoped
9	N-	$In_{53}Al_{0.08}Ga_{46.2}As$	500	5×10^{16}:Si
10	N+	$In_{52}Al_{48}As$	300	2×10^{18}:Si
11	N++	$In_{53}Ga_{47}As$	500	2×10^{19}:Si
12	SI	InP	20	-

Table 6-4: other epi-layers with varying collector/emitter lengths.

Layer	Type	Material	Thickness (nm)	Doping level (cm^{-3})
1	N++	$In_{53}Ga_{47}As$	100	2×10^{19}:Si
2	N+	$In_{52}Al_{48}As$	100	2×10^{18}:Si
3	N-	$In_{53}Ga_{47}As$	100/250	2×10^{16}:Si
4	I	$In_{53}Ga_{47}As$	2	Undoped
5	I	AlAs	1.7	Undoped
6	I	$In_{53}Ga_{47}As$	5.7	Undoped
7	I	AlAs	1.7	Undoped
8	I	$In_{53}Ga_{47}As$	2	Undoped
9	N-	$In_{53}Ga_{47}As$	20	2×10^{16}:Si
10	N+	$In_{52}Al_{48}As$	100	2×10^{18}:Si
11	N++	$In_{53}Ga_{47}As$	500	2×10^{19}:Si
12	I	$In_{52}Al_{48}As$	100	-
13	SI	InP	20	-

6.4.1 RTD-PDs as excitable systems

Next, we tried to impose the spiking behavior using light excitation as explained earlier. Under light excitation the *RTD-PD* devices show a peak voltage shift to a higher value as shown in Figure 148.

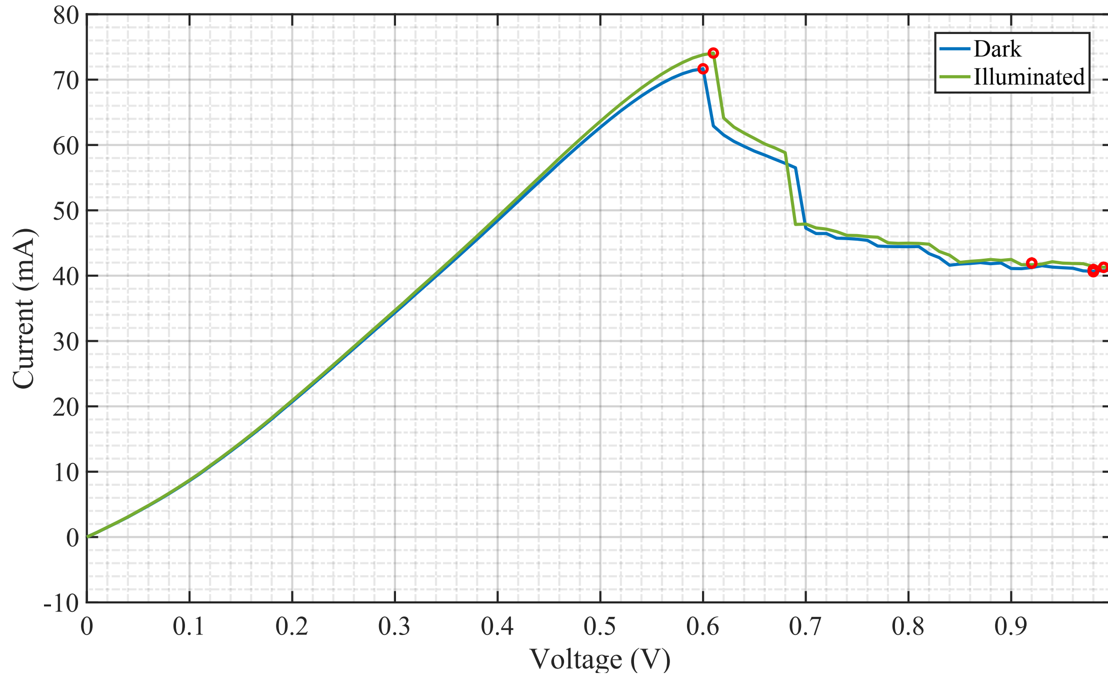

Figure 148: IV curves of actual devices under dark and illumination conditions. Device size 10x10 μm^2.

Therefore, the devices were biased slightly into the *NDC* region and light pulses with a given frequency were shined to impose such a shift. One of the applications of the spiking behavior of *RTD-PD* is for single photon detection. It is noticed that *RTD-PD* tends to shift their peak voltage point either to higher or lower voltages when illuminated with light. This shift can be used to drive the *RTD-PD* in and out of the *NDC* region using appropriate illumination conditions. Since *RTD-PDs* are highly sensitive; owing to their built-in amplification effects, illumination levels required are small. There are mainly two concepts which are currently being investigated for *RTD-PD* as single photon detectors. The first one is the one we just mentioned and is the one investigated in this work. The idea relies on building a sensitive *RTD-PD* such that energy from a single photon can trigger a shift between the peak and the valley, thereby giving a larger signal on the output. The other concept is to incorporate a quantum dot at the collector terminal, near the collector's barrier. This method has been demonstrated first by [60]. The inclusion of a quantum dot (usually an *InAs* quantum dot for *GaAs* and $In_{53}Ga_{47}As$) will trap a single hole. This trapping would result in current

amplification (which can be explained by the Shockley-Ramo theorem) that is proportional to the lifetime of the trapped hole. These detectors have also been demonstrated to operate as single photon counters as well [62], [157], [158].

Experiments utilizing this excitability feature for single photon detection at room temperature were also made using the devices with the previous epi-layers. The devices used were those with the epi-layer shown before with a total capacitance of around 160 pF. The RTD was biased at 0.71 V which is just into the NDC and a 1.31 μm laser was modulated with a pseudo random binary signal (PRBS) with an amplitude of 300 mV_{pp}. The illumination power when spikes started to appear were around 140 nW (emitted by the source), and it was noticed that the frequency of the spikes increased as the illumination power increased. At around 2 μW illumination the spiking frequency was 100 kHz and kept going up until it reached a maximum of 288 kHz at an illumination power of around 350 μW. Increasing the power further made the spikes disappear. During this range of illumination powers, the laser was modulated with frequencies ranging from 50 – 150 MHz. It was also noticed that any change in this frequency range (mainly about 150 MHz) caused the spikes to disappear. It was noticed that the spikes required a certain amount of energy to be induced which was noticed by their dependence on the product of light power and the frequency of modulated light. Figure 149 shows the resulting output. Devices with epi-layer stack as those in Table 6-4, showed spiking behavior at illumination levels as low as 30 nW at room temperature.

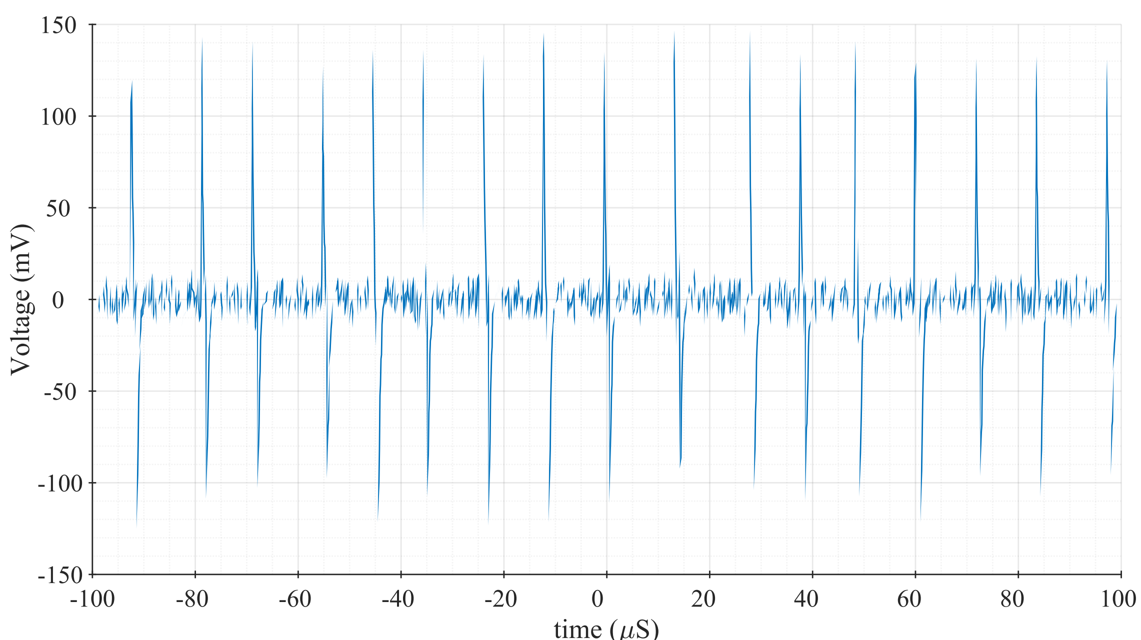

Figure 149: optical spike generation using actual devices.

6.5 Results

6.5.1 Multisim integration of LD and RTD-PD

Next, we show case the results of the Multisim simulations of the *LD*, *RTD* and *RTD-LD* circuits under DC conditions. The results are shown in Figure 151 and Figure 152. Kindly note that the laser used in these simulations has different parameters that those in Table 6-2 with a turn-on voltage of 1.7 V.

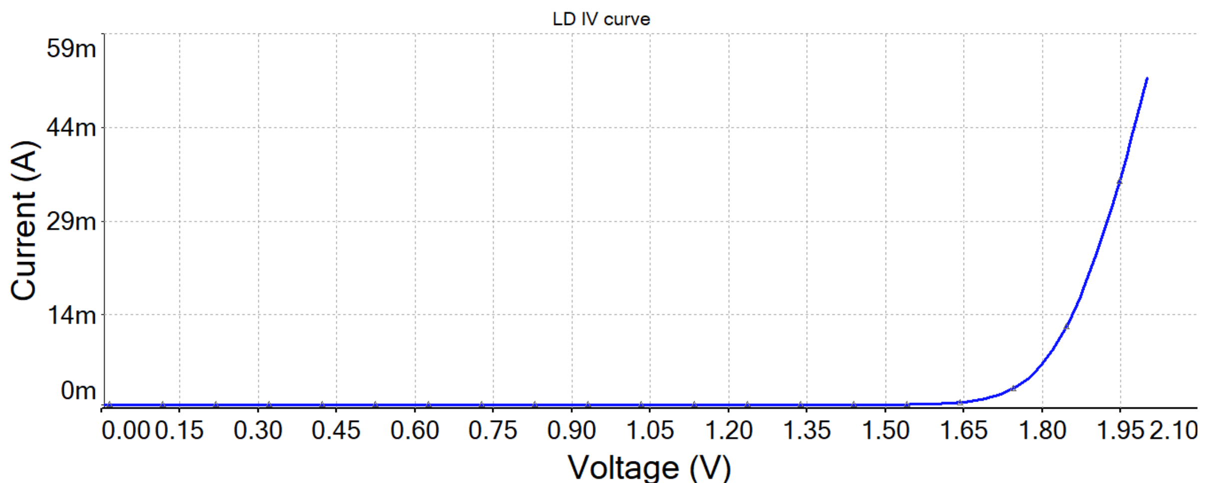

Figure 150: IV curve of a LD run on Multisim (on voltage approx. 1.7V).

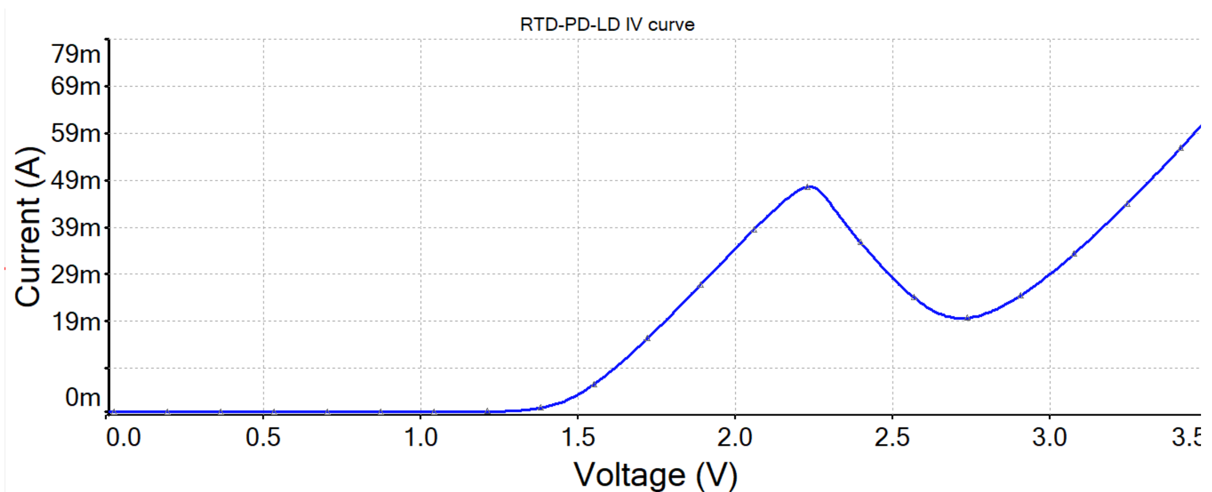

Figure 151: IV curve of RTD-LD circuit run on Multisim.

Under DC conditions, the electrical output of the *RTD-PD-LD* circuit is as shown in Figure 151. We notice that the *IV* curve of the combination is a shifted-version of the *IV* curve of the *RTD-PD*. The shift amount equals the "on" voltage of the *LD*. Such a results is intuitive as the *LD* current is zero before the on voltage, and hence the resulting *IV* gets shifted. Furthermore, Figure 152 shows the relaxation oscillations of the *LD* with the *R, L* and *C*

parameters reported earlier. It can be seen that the *LD* can be modulated up to around 10 GHz.

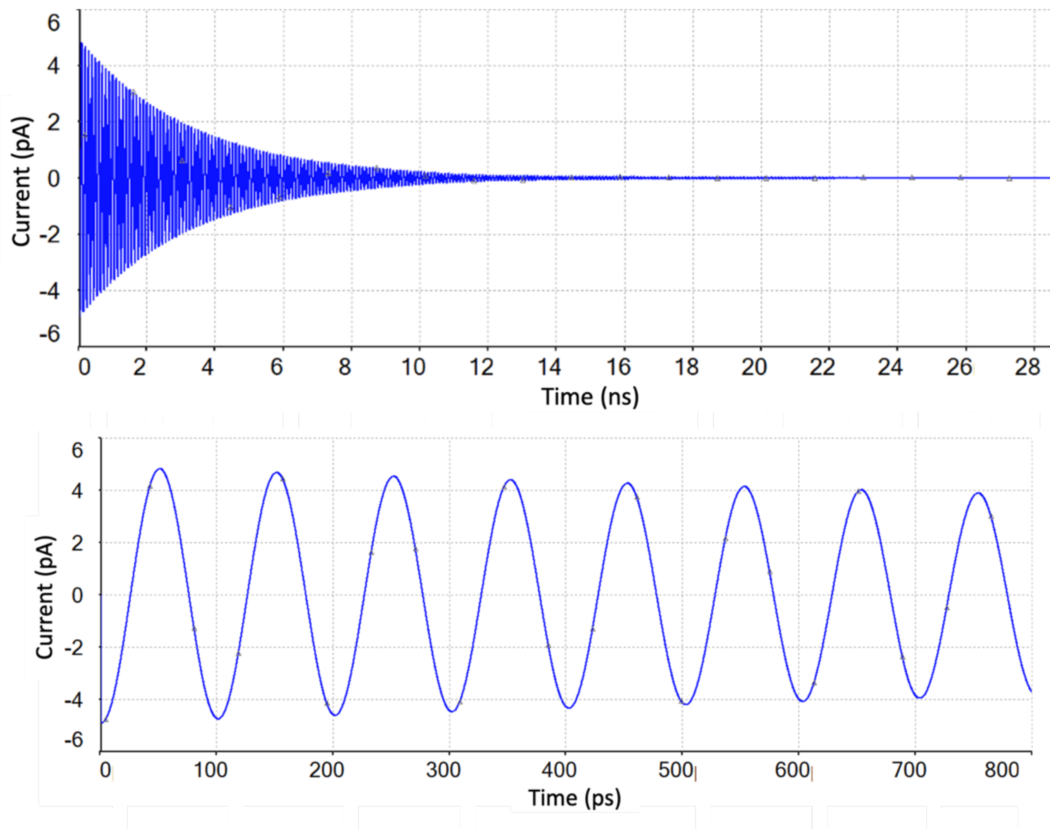

Figure 152: LD relaxation oscillations.

6.6 MATLAB simulation results of *RTD-PD-LD*

6.6.1 Operation in the PDC region

We now move on to the results of MATLAB simulation for the integration of the *RTD-PD-LD* circuit and investigate the various modes of operation stated earlier. The *LD* used in these simulations is the one with the parameters shown in Table 6-2. Typical values for junction capacitance, resistance and inductance for the *LD* are 320 pF, 10 Ω, and 0.8 pH respectively. This gives a relaxation frequency of around 10 GHz as per (*6-36*) without considering R_{NDR}.

$$f_{relaxation} = \frac{1}{2\pi\sqrt{LC}} \tag{6-36}$$

The threshold current is 10 mA as stated earlier. Starting with biasing the *RTD-PD* in the *PDC* region. The results are shown in Figure 153. The current from the simulations tallies well with the value obtained from the *IV* curve in Figure 145.

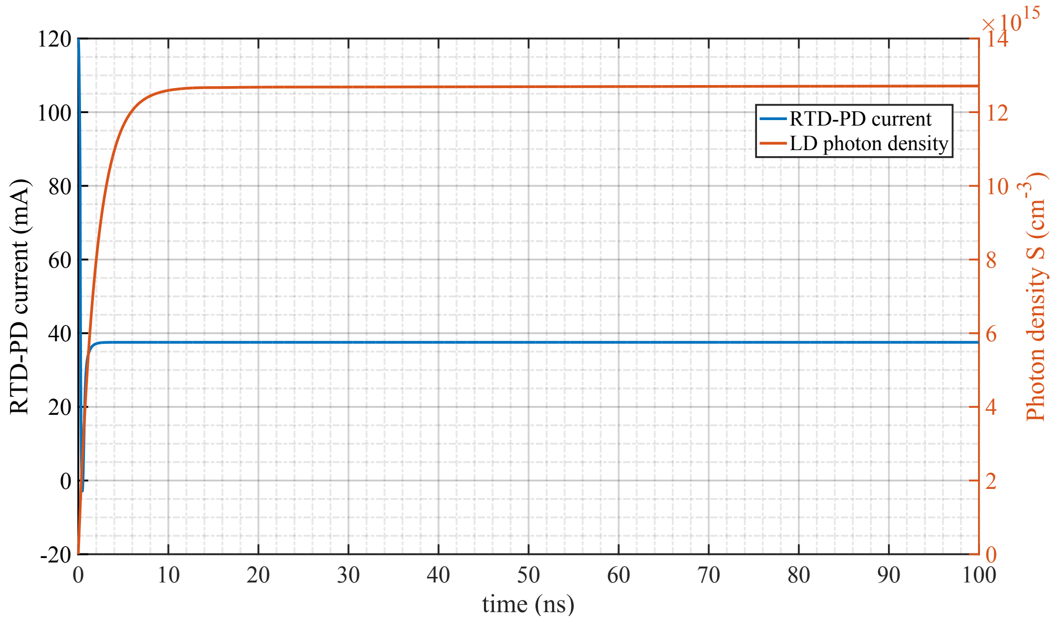

Figure 153: Output current of the RTD-PD when biased at 0.5 V and associated LD photon density.

6.6.2 Operation in the PDC region with RF input

If we now superimpose an *AC* signal on top of the bias voltage the output of the *RTD-PD* will oscillate and hence the *LD* optical output will follow as shown in Figure 154. The chosen signal was a sinusoidal wave with a frequency of 1 GHz and amplitude of 100 mV.

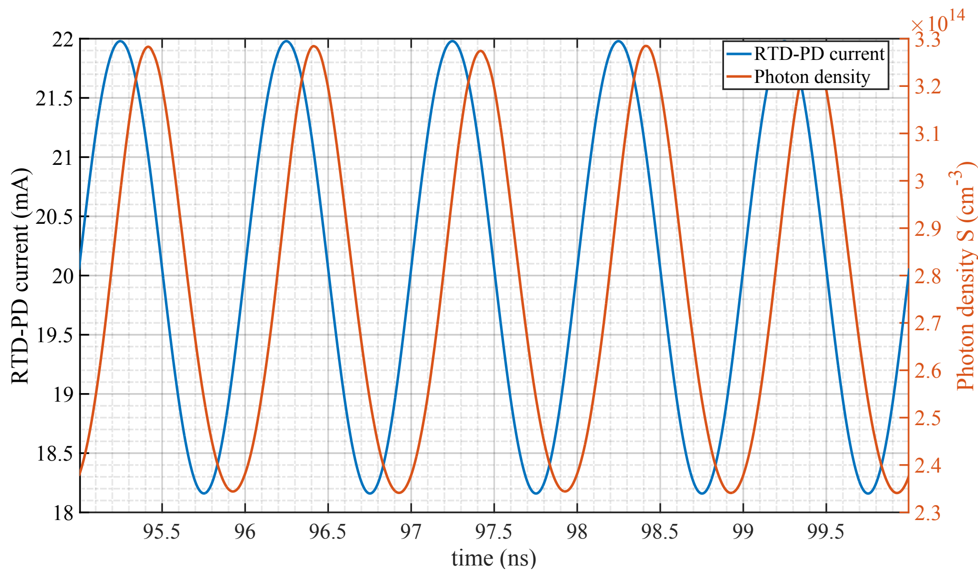

Figure 154: RTD-PD current and LD photon density when biased in the PDC (0.5 V) with 1 GHz RF signal.

The modulation depth of the output photon density given by (6-37) at this operating point is around 0.25.

$$S_{\text{Mod depth}} = \frac{S_{max} - S_{min}}{S_{max}} \tag{6-37}$$

In order to see how the modulation depth changes with the injected current, multiple current injection values with the same superimposed *AC* signal were simulated. The simulator takes in a series of voltage values representing the *DC* bias points and calculates the corresponding *RTD* current according to the *IV*. At each operating current the photon density is calculated, which is then used to calculate the modulation depth. The voltage points in this simulation were (0.25, 0.27, 0.3, 0.35, 0.38, 0.42, 0.44, 0.47, 0.5, 0.53, 0.55, 0.58, 0.61, 0.64 and 0.67), which covered the whole of the *PDR* region. The results are shown in Figure 155. The same was done to measure the modulation index in the current signal given by (6-38), the results are shown in Figure 156. The modulation depth and modulation index are important metrics as they show how much of the output signal is being modulated with respect to a reference level, usually the mean value [159]. As the modulation depth increases so will the signal to noise ratio (*SNR*).

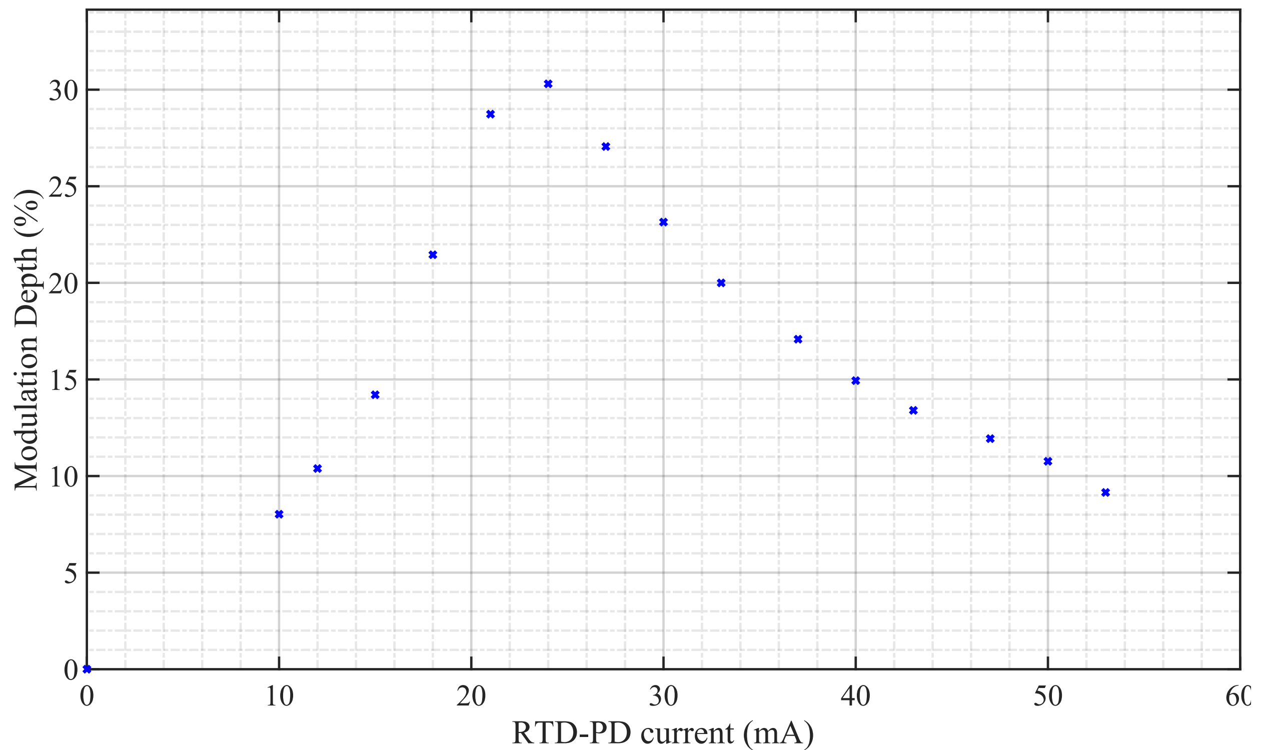

Figure 155: S modulation depth of LD.

$$I_{\text{Mod index}} = \frac{I_{max} - I_{min}}{I_{DC}} \tag{6-38}$$

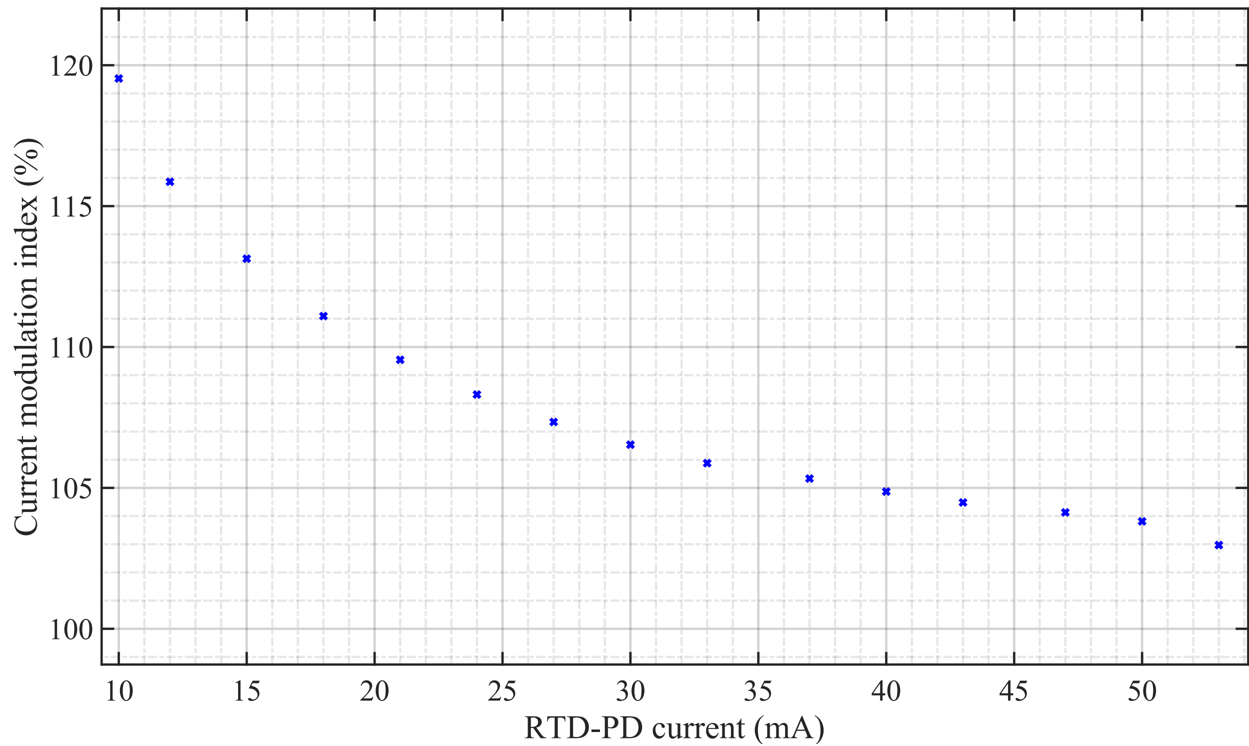

Figure 156: RTD-PD current modulation index.

6.6.3 Operation in the NDC region

Next, we showcase the results obtained for when the device operates in the *NDC* region. The operating bias point was chosen to put the *RTD-PD* in the *NDC* and see if the output results in any relaxation oscillations.

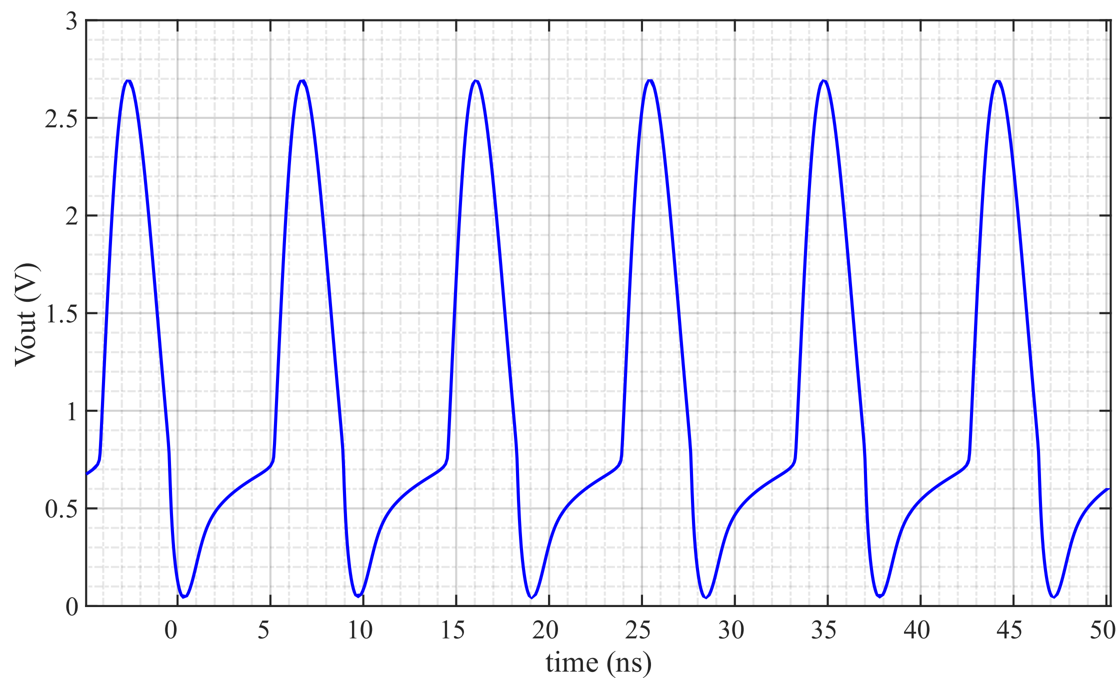

Figure 157: RTD-PD relaxation oscillations.

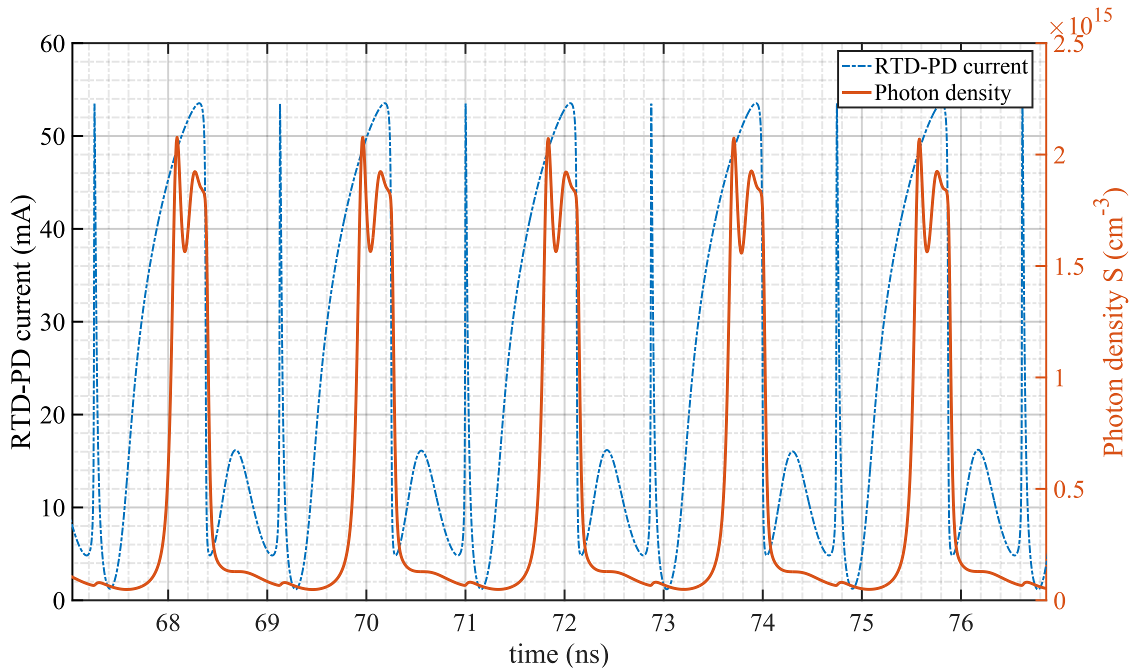

Figure 158: RTD-PD current and LD photon density when biased in the NDC.

We notice that the solution predicts relaxation oscillations the period of which is 1.88 ns, which corresponds to a frequency of around 533 MHz. These values are taken with *R*, *L* and *C* values equation to 6.2 Ω, 8 nH, and 5 pF. The current resulting from this signal will now act to drive the *LD*. It can be seen that the frequency of the output of the *LD* follows that of the driving current. We notice that there is a sort of "spike" in the current signal to which there seems to be no response from the *LD* for. This spike is shown in Figure 159.

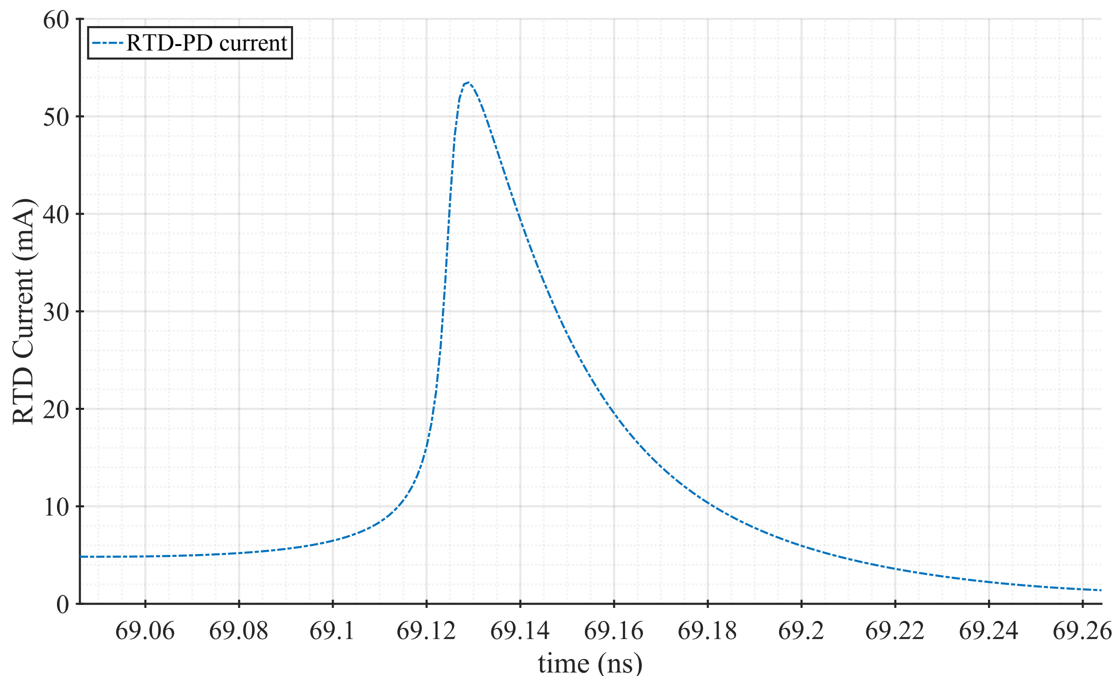

Figure 159: RTD output current spike.

Since the speed of the *LD* is limited by both capacitance and the relaxation frequency, such lack of response might be because the *LD* is too slow to respond. The FWHM time of the above pulse is around 25 ps, which requires a much faster device to respond to. If, hypothetically, the lifetime of the electron was reduced to 2 ps from 2 ns, the relaxation frequency would increase, and the device would respond to the spike as in Figure 160: RTD-PD current and LD photon flux using 2 ps lifetime.

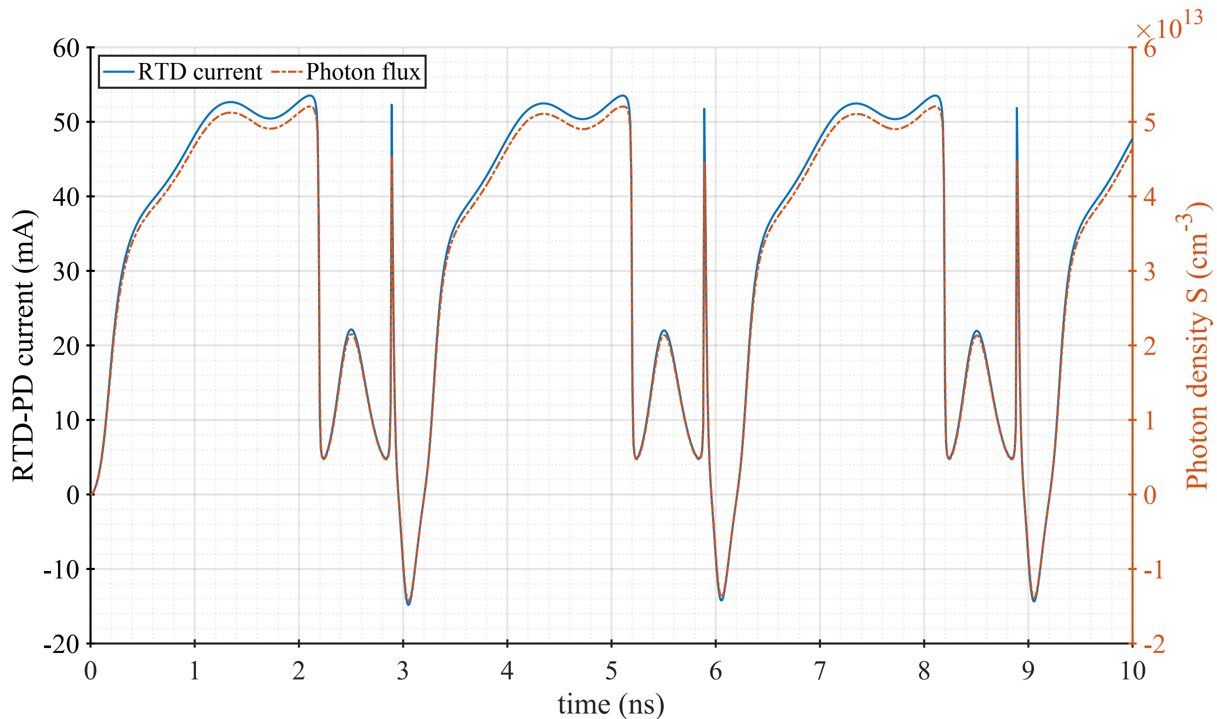

Figure 160: RTD-PD current and LD photon flux using 2 ps lifetime.

To get more insight into the relaxation oscillations frequency, we move to show the results for the studies made on the *R*, *L* and *C* values. The values chosen are the ones highlighted in the text earlier. For each variable study, the other two variables remained constant and only the variable under study was changed. The default values for each element were 6 Ω for the resistance, 5 pF for the capacitance, and 8 nH for the inductance. The outcomes show that the frequency of oscillation is inversely proportional to all *R*, *L*, and *C* elements, with the inductance having the most prominent effect. The mathematical models for each case are listed below. The confidence bounds for all the results are based on 95 % and the adjusted R^2 for the fitted models is about 98%.

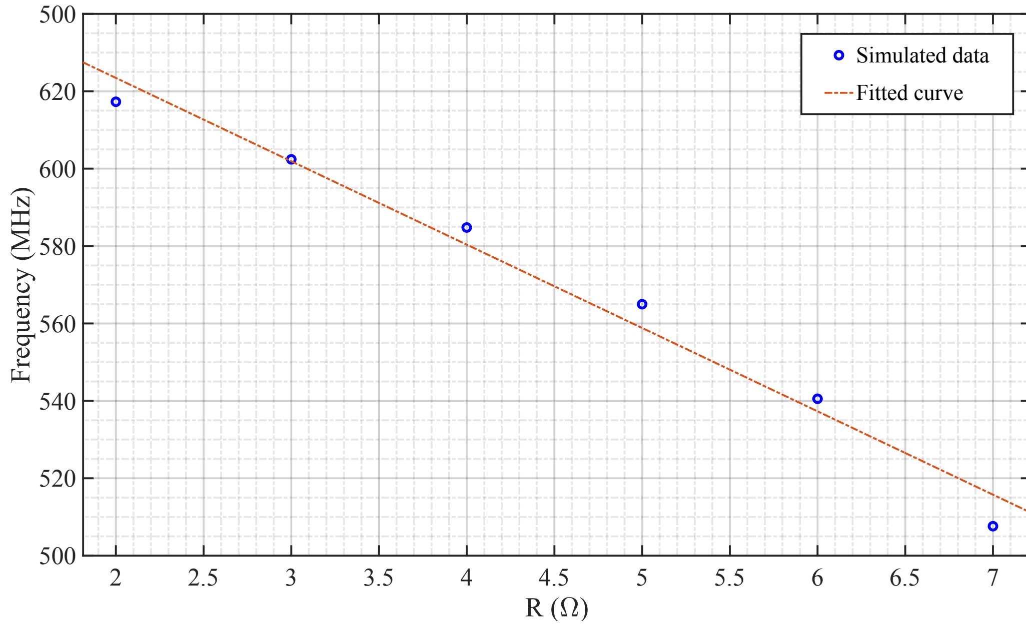

Figure 161: Relaxation frequency dependence on resistance.

$$f(R) = a_1 R + a_2 \quad (6\text{-}39)$$

Where a1 = -2.154e+07 (-2.589e+07, -1.718e+07) and a2 = 6.665e+08 (6.455e+08, 6.875e+08)

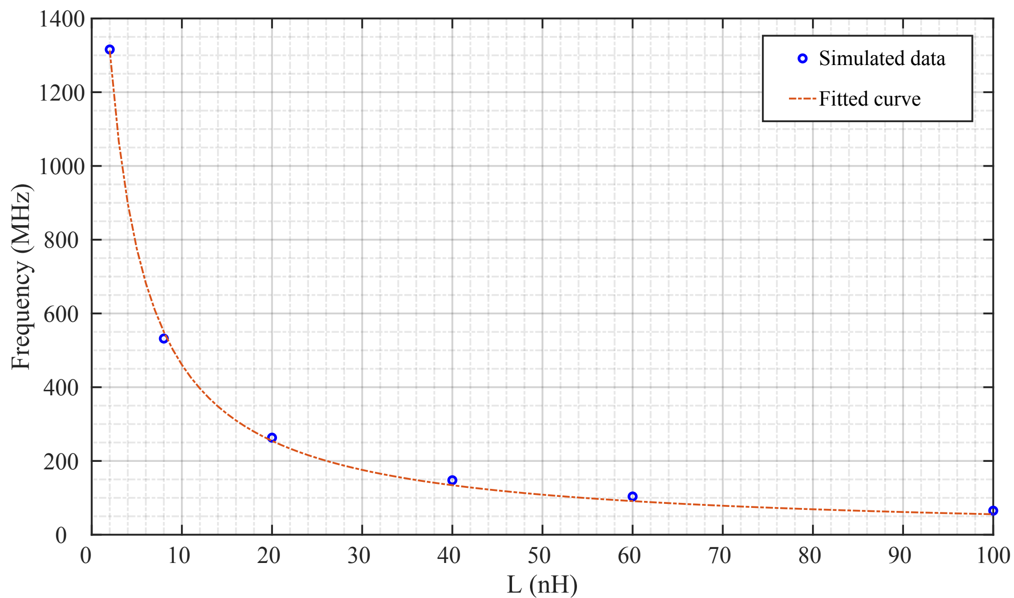

Figure 162: Relaxation frequency dependence on inductance.

$$f(L) = \frac{a_2}{L + b_2} \quad (6\text{-}40)$$

where a2 = 5.681 (4.926, 6.435) and b2 = 2.326e-09 (1.699e-09, 2.953e-09)

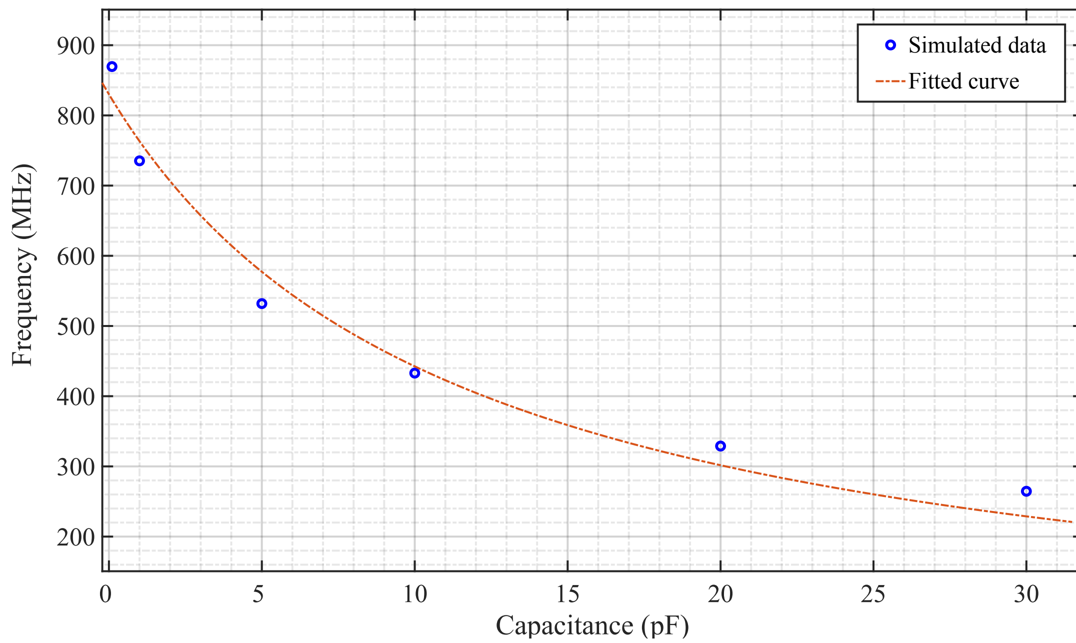

Figure 163: Relaxation frequency dependence on capacitance.

$$f(C) = \frac{a_3}{C + b_3} \tag{6-41}$$

a3 = 0.009477 (0.005674, 0.01328) and b3 = 1.142e-11 (6.017e-12, 1.682e-11)

Finally, the values of R, L and C (2 Ω, 25 pH, and 2 fF for R, L and C), for a given *NDC* value (-2.7 S in this case) can be chosen to make oscillations in the GHz range as stated before. Figure 164 shows the results.

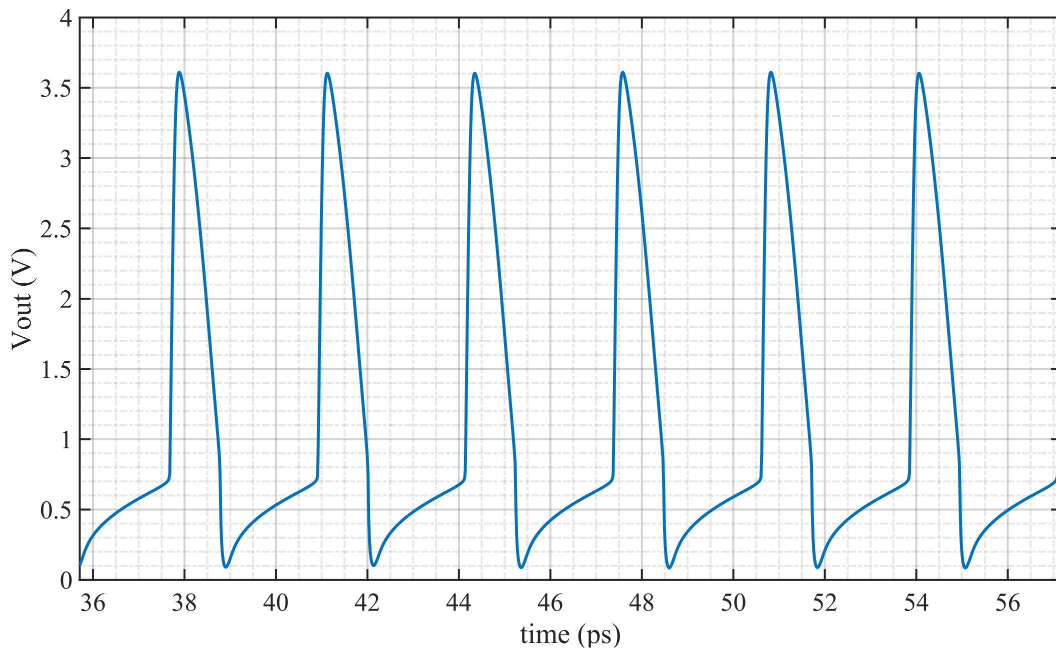

Figure 164: Relaxation oscillations in the tens of GHz range while biased in the NDR (0.8 V).

6.6.4 Operation between PDC and NDC regions

Next, the results for the operation in the spiking behavior are shown below.

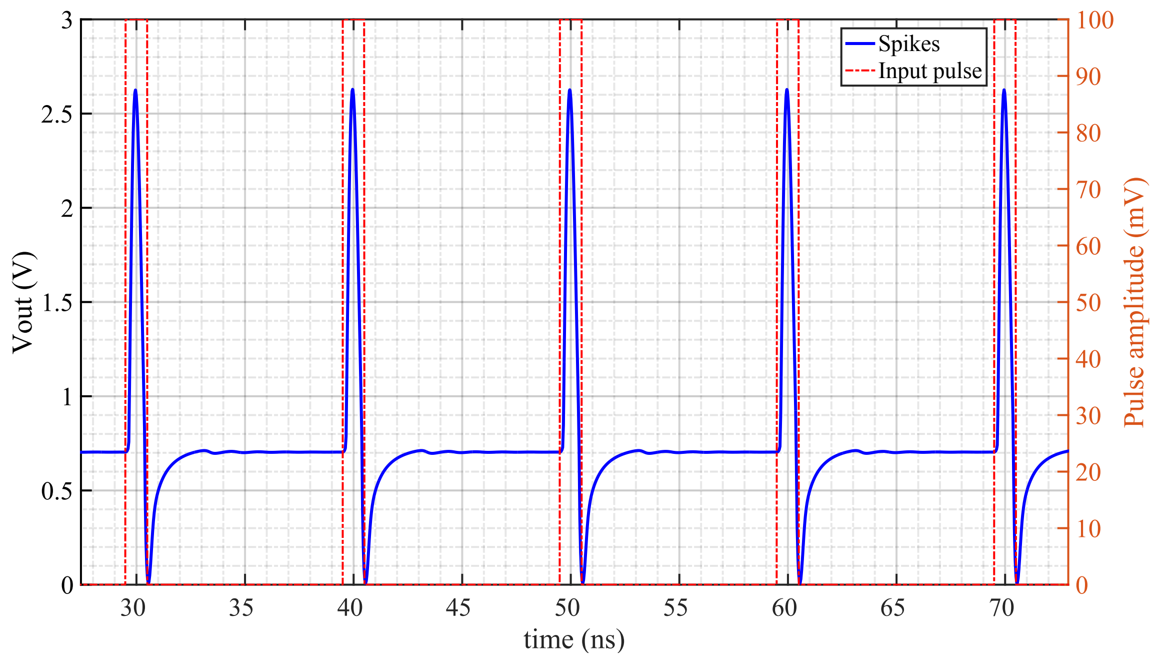

Figure 165: RTD voltage spikes and input pulses.

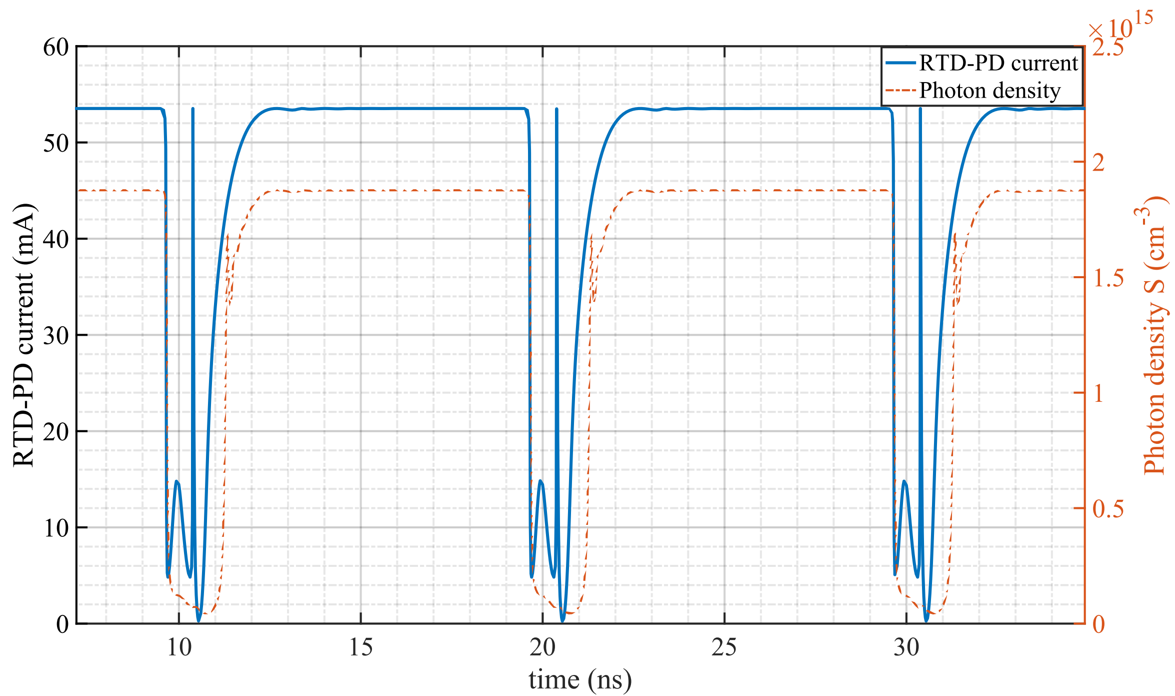

Figure 166: RTD-PD current and LD output photon density.

6.6.5 RTD-PD operation as a VCO

Moving on to practical results, the figures below show the relaxation frequency dependence on the applied voltage, giving data on the operation of the *RTD-PD* as a *VCO*.

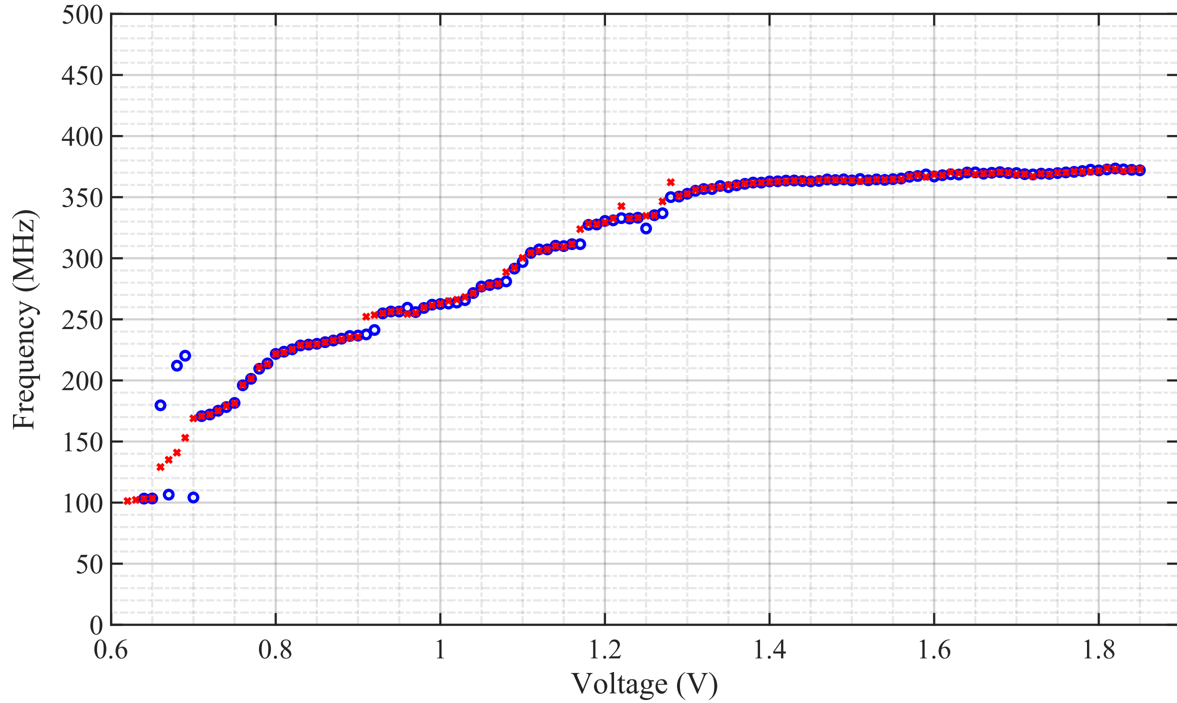

Figure 167: relaxation oscillation frequency as function of voltage in the NDC region (forward and backward sweeps).

The frequency dependence of the *RTD* oscillations on the applied voltage can be modeled using equation (6-42).

$$\mathrm{f}(V) = \frac{p_1 V + p_2}{V^2 + q_1 V + q_2} \tag{6-42}$$

p1 = 1.055e+05 (8.88e+04, 1.221e+05), p2 = -1.076e+05 (-1.279e+05, -8.735e+04), q1 = -2.067(-2.336, -1.798), q2 = 2.055 (1.756, 2.355), p3 = -1.68e+05 (-1.73e+05, -1.631e+05)

The increase in frequency with voltage signals that the capacitance of the *RTD* is changing while it is in the *NDC*. Particularly that the inductance and resistance values are held constant, this points to the fact that the capacitance of the device is decreasing with the oscillation frequency being inversely proportional to both inductance and capacitance.

Since the inductance is constant, this frequency increase should be a result of changes in the capacitance and the resistance in the *NDR*. To see what happens to the capacitance we simulated a *DBQW* structure with a 5.7 nm $In_{53}Ga_{47}As$ quantum well and a 1.7 nm *AlAs*

barriers using ATLAS. As discussed in chapter 2, the *NEGF* equations calculate the wavefunctions at each point and calculate the number of electrons using the trace of the G^n matrix. One approach is to measure the charge at the quantum well as function of voltage. The capacitance can then be calculated by taking the derivative of the charge with respect to voltage. The charge inside the quantum well builds up as the device is biased in the first *PDC*, and starts to leak out when the device goes into the *NDC* [160], [161]. The capacitance [160], [162] seems to peak in the *NDR*, which supports the observations and conclusions of [161], [163]. However, this is in contrast to the findings we observe with the frequency increase. As discussed in chapter (2), the capacitance of the *RTD* can be viewed as that of a parallel plate capacitor formed by the accumulation region at the emitter until the depletion region at the collector as per (6-43). However, a better approach is to calculate the change of charge versus voltage in the collector / emitter charge accumulation regions, which mainly affect the overall capacitance. The simulator was programmed to do that, and as can be seen in Figure 168, the capacitance reaches a value of around 300 fF. To verify this number, the distance in (6-43) can be taken as the sum of the accumulation region at the emitter, the *QW*, and the depletion region of the collector. For an $In_{53}Ga_{47}As$ quantum well, the *DBQW* is around 10 nm, and the majority of the accumulated charge at the collector decays after 3 Debye lengths. Using typical values for $In_{53}Ga_{47}As$, the capacitance for a 100 μm^2 device will be 307 fF. This seems to tally well with the simulations. Since the device is oscillating in the *NDR*, an AC signal will be generated. This leads to lower the relative electric permittivity (ϵ_r) from an original 13.8 at DC for $In_{53}Ga_{47}As$ to 11.8. Such a decrease will lower the capacitance also. Another factor affecting the capacitance, is the increase in the depletion length in the *NDR* region. These two factors contribute to the reduction in capacitance and hence, increase the oscillation frequency.

$$C = \frac{\epsilon A}{d} \tag{6-43}$$

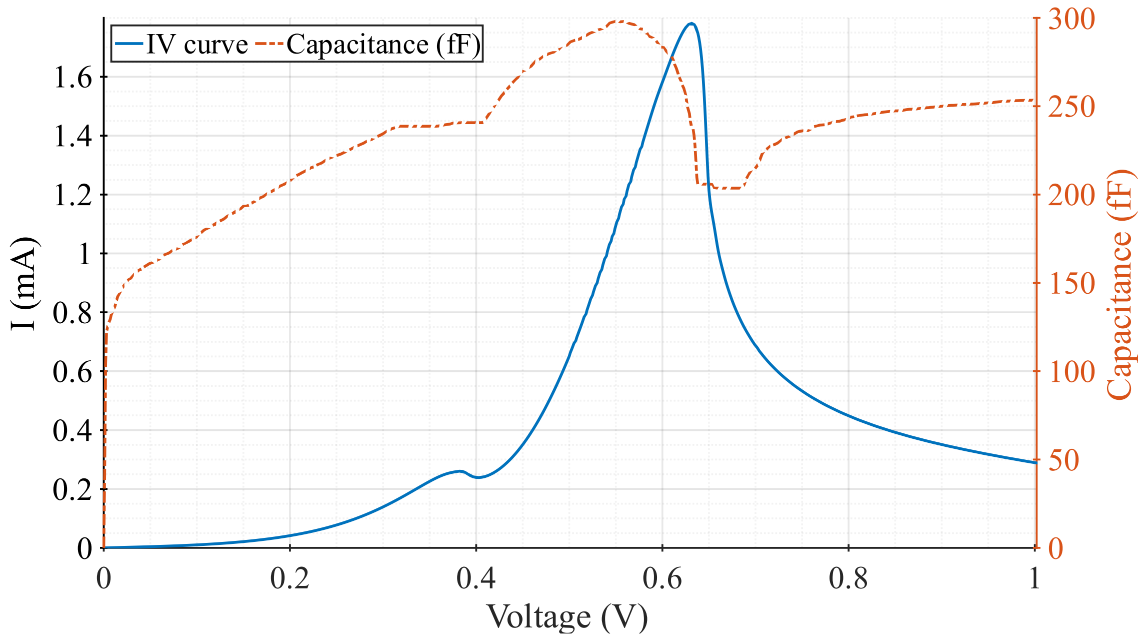

Figure 168: IV curve and capacitance of $In_{53}Ga_{47}As$ *RTD.*

6.7 Summary and conclusion

In this chapter we have studied and simulated the integration of a resonant tunneling diode (*RTD*) with a laser diode (*LD*). To do so, we first designed a tool on MATLAB that allows the prediction of the IV characteristics of $In_{53}Ga_{47}As/AlAs$ *RTD-PD*s without the need for numerical simulations. This was achieved by a multi-factorial study which was made using Silvaco ATLAS to model the peak voltage of the *RTD*. The results were then used with the Schulman model to calculate the location of the peak voltage by calculating the n_1 parameter.

The *RTD* was then modeled using a voltage dependent current source that resembles the IV and the various RLC elements associated with the quantum well and bias circuitry, the *LD* was modeled with a resistance and a voltage source. The equivalent circuits were connected in series such that the *RTD* current now feeds *LD* and the circuit was analyzed under *AC* conditions to calculate the output voltage as function of time. and due to the non-linear nature of the *RTD* current the resulting equations resembled the well-known Liènard equation. The solutions of which are known as relaxation oscillations.

The circuit was studied in multiple regions, beginning with the positive differential conductance region (*PDC*) and then in the negative differential conductance region (*NDC*). When biased in the *PDC*, the *RTD* supplies constant current to the *LD* and the output is a constant power. When biased in the *NDC* region, the *RTD* oscillates with relaxation

frequencies resulting from the solution of the Liénard equation. It was found that the resistance, inductance and capacitances associated with this circuit determine the frequency and shape of these oscillations and that dependence was mathematically modeled. Additionally, the voltage-dependent *NDR* region will also have an effect. Since the current in this mode is oscillatory, the output power of the driven *LD* is expected to oscillate at the same frequency, which was predicted by the circuit simulations made.

Since relaxation oscillations are the main driver for this mode of operation for the *RTD*, multiple *RTD* devices with various epitaxial layers were studied to see the change in oscillation frequency as the voltage increases through the *NDR*. The results show an increase in oscillation frequency with voltage which can be related to the charge release out of the quantum well while the device is biased in the *NDC*. This was also verified by simulations using SILVACO ATLAS, where the charge accumulated inside the quantum well was simulated as function of voltage.

Finally, one last mode of operation was studied. This mode is when the *RTD* is driven into and out of the *NDC* region at a given frequency. This was simulated using Multisim by applying a pulsed voltage to the *RTD* while biased near the peak voltage. The results are spikes of the output voltage, this spiking behavior shows promise for many applications such as single photon detection. Kindly note that his is not an on-off keying scheme as the voltage of these spikes is much higher than the stimulating signal. The same was verified using the light induced voltage shift with physical devices and the conditions for producing such spikes were outlined. The lowest illumination power at room temperate which the *RTD* showed spiking response to was around 30 nW.

Chapter 7 : Conclusion and future work

7.1 Conclusion

In this work we have investigated the possibilities of using $In_{53}Ga_{47}As$/InP double barrier quantum well resonant tunneling diodes (*RTD*) as photodetectors (*PD*). This is done by incorporating light sensitive material into this structure forming what is known as an *RTD-PD*. *RTDs* are great candidates for high speed and high sensitivity photodetection applications. Owing to their non-linear *IV* characteristics various applications can be realized such as optical control of high frequency electronic circuits incorporating *RTD*s.

Since *RTDs* exhibit the phenomena of negative differential conductance (*NDC*), they have the advantage of providing internal electrical gain to the system and hence have built-in amplification effects making them attractive as photodetectors as the need for additional circuitry is eliminated.

We began by introducing what an *RTD* is and its main principle of operation. We then discussed how light interacts with matter (particularly semiconductors) paving the way towards studying *RTDs* with built-in absorption regions using the $In_{53}Ga_{47}As$/InP material system. The choice of this material system was to use these devices in telecommunication applications utilizing the low-loss fiber windows at 1.55 μm and 1.31 μm.

We then discussed the *RTD* output characteristics (peak voltage, peak to valley current ratio, and peak-to-valley voltage span ΔV) dependencies on the structural parameters of an *RTD* using simulations based on the non-equilibrium Greens' functions (*NEGF*) formalism. We first studied the effects of doping concentration in both the emitter and collector regions of the device on the location of its peak voltage. A model that describes the shift happening for both forward bias and reverse bias cases was deduced.

Then the effect of the lengths of both emitter and collector regions on the peak voltage was presented. It was shown that the peak voltage shifts to higher values as the length of both of these regions increases until it eventually becomes independent of the length. The length value at which this occurs depends on the characteristic length in each region, mainly the Thomas-Fermi screening length in the emitter side due to the presence of

the *2DEG*, and the Debye length in the collector region. Both of these cases were also mathematically modeled. Finally, the effects of the previous parameters along with the dimensions of the quantum well on the peak to valley current ratio, ΔV and ΔI were studied separately. It was found that for maximum $\Delta V \Delta I$ a barrier width of 1.3 nm is required when the quantum well is 5.7 nm wide. These studies were single factorial in nature, and a multifactorial study will result in a better understanding of the system. The structure studied was *GaAs/AlAs*.

We have characterized and discussed the optical characterization results of various epitaxial-layer samples which covered a wide range of lengths, doping concentrations, quantum well designs, and contact material. The *RTDs* epitaxial layers consisted mainly of highly doped $In_{53}Ga_{47}As$ contact regions which were rather thick. Particularly at the bottom contact, with thicknesses reaching 500 nm. Such regions form areas of near-zero electric field and were found to be a source of speed limitation for these devices. The results showed a bandwidth for such devices in the 10's of MHz range.

While discussing the designs we have studied all possible factors that might hinder the speed of operation of the device, to that we have studied the *RC* time constant, dielectric relaxation time, carrier drift time, lifetime of accumulated carriers at the emitter, and the carrier lifetime in low electric field regions. We have found that the carrier lifetime was a major speed impeder particularly in highly doped contact areas where the electric field is nearly zero.

The proposed new designs changed both contact regions to be from higher bandgap material (*InP*) instead of $In_{53}Ga_{47}As$, thereby eliminating such limitation. The doping profiles were also made properly using the results we obtained from the Silvaco simulations to ensure sufficient electric field values necessary for high transport speeds of carriers.

Next, we studied the various topologies possible for *RTD-PD* and proposed two main designs based on an *n-i-n* scheme and another on a *p-i-n* scheme. These designs were made such that the resulting devices operate at high speeds reaching up to 10 GHz.

The results of the *PIN-RTD* device indeed show a significant enhancement (from 10's of MHz to the hundreds of MHz range) on the speed of operation as this design solves the issues of charge generation in the contacts and eliminates electric field dead-zones though proper doping. However, the results showed that the electrical cut-off frequency was much

lower than the anticipated 10 GHz down to around 380 MHz. This means that the speed was limited now by the accumulated charge lifetime near the emitter barrier, leading to the conclusion that *RTD-PD* are highly affected by the accumulated charges lifetime, and any high-speed operation will mainly depend on lowering it. We have also showed that devices with mild *NDR* regions tend to operate at higher speeds (1.26 GHz for the highest speed *PIN-RTD* device). The reason for such, is that the accumulation rate is lower with devices with non-ideal *NDRs* and hence the lifetime gets shorter. In the limiting case where the *NDR* is "screened" by having the peak current equal to the valley current, the accumulation rate will negligible and the device will act as a normal *PIN*-detector or a photoconductor.

In order to harvest the advantages of the *RTD* built-in amplification, we have showed that the devices need to operate at the *NDR* region with certain conditions satisfied and compared the detection capabilities of and *RTD-PD* with a commercial PIN-photodiode. *RTD-PD* showed superior amplitudes for the detected signal up to 6 times higher than the commercial PIN-photodetector. This shows that *RTD-PD* are great candidates for low-intensity applications that do not require GHz speeds.

Finally, we have studied and simulated the integration of a resonant tunneling diode (*RTD*) with a laser diode (*LD*). To do so, we first designed a tool on MATLAB that allows the prediction of the IV characteristics of $In_{53}Ga_{47}As/AlAs$ *RTD-PD*s without the need for numerical simulations. This was achieved by a multi-factorial study which was made using Silvaco ATLAS to model the peak voltage of the *RTD*. The results were then used in conjunction with the Schulman model, to produce the *IVs* without needing physical simulations. The *RTD* was then modeled using a voltage dependent current source that resembles the *IV* and the various *RLC* elements associated with the quantum well and bias circuitry, the *LD* was modeled with a resistance and a voltage source.

The equivalent circuits were connected in series such that the *RTD* current now feeds *LD* and the circuit was analyzed under *AC* conditions to calculate the *RTD* voltage as function of time. This voltage is then fed into the IV equation of the *RTD*, to calculate the current that drives the *LD*. Since the *RTD* was modeled as a current dependent voltage source, and given the non-linear nature of the *IV* curve, the resulting *KCL* equations for the *RTD-PD-LD* resembled the well-known Liènard equation. The solutions of which are known as relaxation oscillations. The circuit was studied in multiple regions, beginning with the positive

differential conductance region (*PDC*) and then in the negative differential conductance region (*NDC*). When biased in the *PDC,* the *RTD* supplies constant current to the *LD* and the output is a constant power.

When biased in the *NDC* region, the *RTD* oscillates with self-oscillating frequencies resulting from the solution of the Liénard equation. It was found that the resistance, inductance and capacitances associated with this circuit determine the frequency and shape of these oscillations and that dependence was mathematically modeled. Since the current in this mode is oscillatory, the output power of the driven *LD* is expected to oscillate at the same frequency, which was predicted by the circuit simulations made.

Since relaxation oscillations are the main driver for this mode of operation for the *RTD*, multiple *RTD* devices with various epitaxial layers were studied to see the change in oscillation frequency as the voltage increases through the *NDC*. The results show an increase in oscillation frequency with voltage which can be related to the change in capacitance of the quantum well while the device is biased in the *NDC.* This was also verified by simulations using SILVACO ATALS, where the charge accumulated inside the quantum well was simulated as function of voltage.

One last mode of operation was studied when the *RTD* is driven into and out of the *NDC* region at a given frequency. This was simulated by applying a pulsed voltage to the *RTD* while biased near the peak voltage. The results are spike-like behavior of the output voltage, this spiking behavior shows promise for many applications such as single photon detection. The same was verified using the light induced shift with physical devices and the conditions for producing such spikes were outlined. The lowest illumination power at room temperate which the *RTD* showed spiking response to was around 30 nW. This was the power supplied by the laser.

7.2 Future work

Further work on the subject includes Investigation into the exact amount of energy required to induce optically-controlled spiking behavior of the *RTD-PD* devices and gain a better understanding of the nature of relaxation oscillations in the *NDR* region. It also opens up a vast number of circuit applications where the *RTD-PD* can be used to turn on-off a *LD.*

The results of this work can be further developed study circuits using *RTD-PD*s. The various parts of the *IV* curve make them suitable for operation as optoelectronic mixers as well in the *PDR* regions. Where an optical signal is induced and is mixed with an electronic signal at the input. The concept of mixing is explained next.

7.2.1 Mixing in resonant tunnelling diodes

A mixer is a device that takes two signals of different frequencies and produces signals at frequencies which are a linear combination of the input frequencies. A mixer is usually used to mix a radio frequency signal (*RF*) with that of local oscillator (*LO*) to produce other intermediate frequencies (*IF*). Mixer circuits achieve this functionality by two main ways, either by using elements with non-linear behavior (like diodes and transistors), or by switching the desired signals.

The operation of a mixer in an *RTD-PD* can be understood by looking at Figure 169, and Figure 170, which shows the *IV* characteristics of an *RTD-PD* in the first *PDR*.

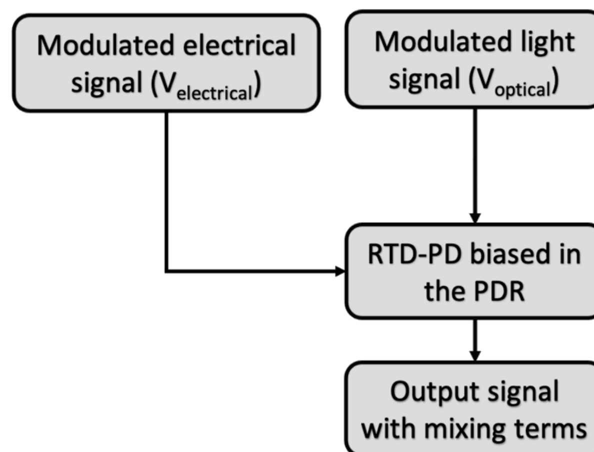

Figure 169: RTD-PD mixer concept.

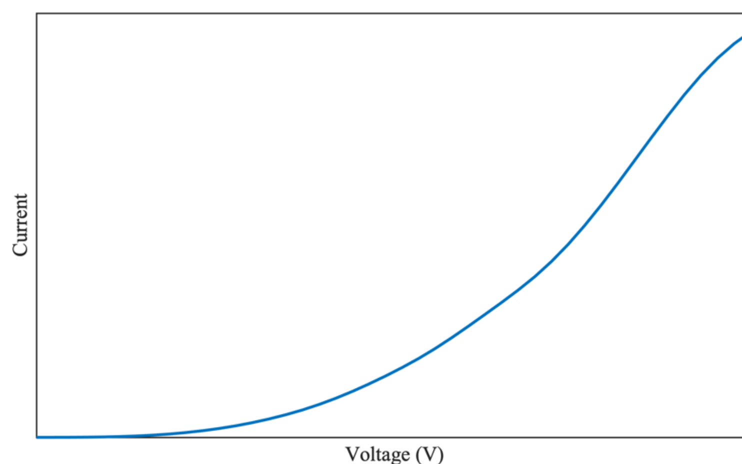

Figure 170: IV characteristics of an RTD-PD.

Since the *IV* curve is non-linear it can be approximated by a Taylor series expansion of the form given below

$$I(V) = a_0 + a_1 V + a_2 V^2 + a_3 V^3 + \cdots .. a_n V^n \tag{7-1}$$

for practical purposes, terms up to the second order (and sometimes the third order) are sufficient to characterize the non-linear response. In such system, when the input signal is made from two frequencies $V_{electrical}$ and $V_{optical}$ the current response will be as follows:

$$V_{electrical} = Acos(\omega_1 t) \tag{7-2}$$

$$V_{optical} = Bcos(\omega_2 t) \tag{7-3}$$

$$I(V) = a_0 + a_1\left(V_{electrical} + V_{optical}\right) + a_2\left(V_{electrical} + V_{optical}\right)^2 \tag{7-4}$$

Expanding these terms yields

$$a_0 + a_1 Acos(\omega_1 t) + a_1 Bcos(\omega_2 t) + \frac{a_2 A^2}{2}(\cos(2\omega_1 t) + \sin(2\omega_2 t)) + \frac{a_2 B^2}{2}(\cos(2\omega_2 t) + \sin(2\omega_1 t)) + a_2 AB(\cos(\omega_1 + \omega_2)\, t) + \sin(\omega_1 + \omega_2)\, t) \tag{7-5}$$

From the above expansion, we see that the output will have a *DC* component, components at the $V_{electrical}$ and $V_{optical}$ frequencies, and two more components, one resembling the harmonics of each, and another is a mixing component (also known as intermodulation) which is a linear combination of both [164].

There are two basic ways in which the *RTD* can be used as a mixer, either by exploiting the non-linear region or by using it as a switch in the *NDR* region. The first way relays on the fact that the IV characteristics on the *RTD* in the non-linear and non-linearity produces intermodulation terms between two signals, effectively producing the sum and difference frequencies. The main advantage of *RTDs* is in terms of lower capacitance, and hence higher frequency.

The other option is to design the *RTD* to have a very steep *NDR* region with high peak to valley ratio. This type of mixer is based on switching, by biasing the *RTD* in the *NDR* region and applying sufficient voltage swing, the device can be switched between high (peak current) and low (valley current) in a very fast way, effectively working as a switching mixer [85] [165].

Appendix : Sample Silvaco code

```
Loop steps=10
go atlas
Assign name = collectorDoping N.VALUE = (1e12, 5e12, 1e13, 5e13, 1e14, 5e14, 1e15, 5e15,
5e16, 1e17) DELTA=1
#Define filename
set fileName = "Test"
#------------------------Voltage control--------------------#
set startVoltage = 0
set endVoltage = 2
set stepSize = 0.1
set simulationType="RB"
set currentVoltage = $startVoltage
set numOfIterations = ($endVoltage - $startVoltage) / $stepSize
#------------------------Voltage control--------------------#
#----------------------RTD geometry--------------------------#
set well=0.0045
set barrier=0.0025
set emitter=0.1
set collector=0.1
#----------------------RTD geometry--------------------------#
#-------------------Control parameters-----------------------#
set devStart=0
set nyf=0.001
set devWidth=1
#-------------------Control parameters-----------------------#
#----------------------Define layers-------------------------#
set layer1=$emitter
set layer2=$layer1+$barrier
set layer3=$layer2+$well
set layer4=$layer3+$barrier
set layer5=$layer4+$collector
set devDepth=$layer5
#----------------------Define layers-------------------------#
#----------------------Define doping-------------------------#
set emitter_doping=5e15
#----------------------Define doping-------------------------#
```

```
#-----------------------Define mesh--------------------------#
mesh diag.flip
x.mesh loc=0.00                     spac=$devWidth
x.mesh loc=$devWidth                spac=$devWidth
y.mesh loc=$devStart                spac=0.01
y.mesh loc=$layer1                  spac=0.0001
y.mesh loc=$layer2                  spac=0.0001
y.mesh loc=$layer3                  spac=0.0001
y.mesh loc=$layer4                  spac=0.0001
y.mesh loc=$layer5                  spac=0.01
#-----------------------Define mesh--------------------------#

#---------------------Define regions-------------------------#
region num=1 material=InGaAs y.max=$layer1                equil.negf
region num=2 material=AlAs   y.min=$layer1 y.max=$layer2
region num=3 material=InGaAs y.min=$layer2 y.max=$layer3
region num=4 material=AlAs   y.min=$layer3 y.max=$layer4
region num=5 material=InGaAs y.min=$layer4                equil.negf
#---------------------Define regions-------------------------#

#--------------------Define Eelctrods------------------------#
if cond =($simulationType="FB")
       elec num=1 name="emitter"    top
       elec num=2 name="collector"  bottom
else
       elec num=1 name="emitter"    bottom
       elec num=2 name="collector"  top
if.end
#--------------------Define Eelctrods------------------------#

#---------------------Define doping--------------------------#
doping reg=1 uniform n.type conc=$emitter_doping
doping reg=5 uniform n.type conc=$collectorDoping
#---------------------Define doping--------------------------#

#---------------Define material parameters-------------------#
material material=InGaAs      EG300=0.75 NC300=2.1e17 NV300=7.7e18 MC=0.043 \
                              PERMITTIVITY=13.9 NI.min=6.3e11 MUN=12000 MUP=300
material material=AlAs        EG300=2.8 NC300=1.5e19 NV300=1.7e19 MC=0.06 \
                              PERMITTIVITY=10.06 NI.min=9.5 MUN=200 MUP=140 Align=0.49
#---------------Define material parameters-------------------#
```

```
#------------------Simulation conditions--------------------#
models n.negf_pl eta.negf=0.0150 esize.negf=4010 eig.ymin=$layer1 eig.ymax=$layer4
method carr=0
output  con.band val.band eigen=3
#------------------Simulation conditions--------------------#

#--------------------Probing station-----------------------#
probe transmission                   filename="collectorDopingTrans "
probe name="Well DOS"                dosvse x=0 y=$layer2+0.5*$well
probe name="Emitter DOS"             dosvse x=0 y=$layer1-$nyf
probe name="Collector DOS"           dosvse x=0 y=$layer4+$nyf
probe name="Well charge - int " integrate charge x=0 y.min=$layer2+$nyf y.max=$layer3-$nyf
probe name="Well charge "            charge x=0 y.min=$layer2+$nyf y.max=$layer3-$nyf
probe name="Emitter charge int"      integrate charge x=0 y.min=$layer1-$nyf y.max=$layer1
probe name="Emitter charge"          charge x=0 y.min=$layer1-$nyf y.max=$layer1
probe name="Collector charge int"    integrate charge x=0 y.min=$layer4 y.max=$layer4+$nyf
probe name="Collector charge"        charge x=0 y.min=$layer4 y.max=$layer4+$nyf
probe name="First bound state"       nbnd.ener state=1 x=0 y=$layer2+$well/2
probe name="Second bound state"      nbnd.ener state=2 x=0 y=$layer2+$well/2
probe name="Current density"         j.total y=$layer4+$nyf
probe name="Well conductivity"       conductivity x=0 y.min=$layer2+$well/2
probe name="Collector conductivity"  conductivity x=0 y=$layer5-$nyf
#--------------------Probing station-----------------------#

#-----------------------Simulation-------------------------#
log outf=Log_$fileName$collectorDoping$simulationType
solve init
save outf=init_$fileName$collectorDoping$simulationType   negf.log negf.eig

LOOP steps = $numOfIterations
solve vcollector=$currentVoltage name=collector vstep=0.01 \
vfinal = $currentVoltage + $stepSize negf.eig
set currentVoltage = $currentVoltage + $stepSize
save outf=str_$fileName$currentVoltage$collectorDoping$simulationType negf.log negf.eig
L.END

log off
L.END
quit
#----------------------Simulation-------------------------#
```

References

[1] J. F. Martins-Filho *et al.*, "Ultra-broad-band photodetection in a resonant tunneling device," in *Proceedings of the 2001 SBMO/IEEE MTT-S International Microwave and Optoelectronics Conference. (Cat. No.01TH8568)*, Belem, Brazil, 2001, vol. 1, pp. 325–328. doi: 10.1109/SBMOMO.2001.1008776.

[2] J. F. Martins-Filho, R. E. de Araujo, A. S. L. Gomes, J. M. L. Figueiredo, C. R. Stanley, and C. N. Ironside, "High photodetection gain in a resonant tunneling diode waveguide modulator/detector," in *LEOS 2000. 2000 IEEE Annual Meeting Conference Proceedings. 13th Annual Meeting. IEEE Lasers and Electro-Optics Society 2000 Annual Meeting (Cat. No.00CH37080)*, Rio Grande, Puerto Rico, 2000, vol. 1, pp. 15–16. doi: 10.1109/LEOS.2000.890650.

[3] W. Zhang *et al.*, "Optical direct intensity modulation of a 79GHz resonant tunneling diode-photodetector oscillator," *Opt. Express*, vol. 27, no. 12, p. 16791, Jun. 2019, doi: 10.1364/OE.27.016791.

[4] S. Watson *et al.*, "Resonant tunneling diode photodetectors for optical communications," *Microw. Opt. Technol. Lett.*, vol. 61, no. 4, pp. 1121–1125, Apr. 2019, doi: 10.1002/mop.31689.

[5] R. Izumi, S. Suzuki, and M. Asada, "1.98 THz resonant-tunneling-diode oscillator with reduced conduction loss by thick antenna electrode," in *2017 42nd International Conference on Infrared, Millimeter, and Terahertz Waves (IRMMW-THz)*, Cancun, Mexico, Aug. 2017, pp. 1–2. doi: 10.1109/IRMMW-THz.2017.8066877.

[6] Hamamatsu, "Room temperature THz QCL sources." [Online]. Available: https://www.hamamatsu.com/jp/en/our-company/business-domain/central-research-laboratory/optical-materials/qcl.html

[7] V. Doychinov, H. Steenson, and Patel, *Resonant-Tunneling Diode Based Reflection Amplifier. 22nd European Workshop on Heterostructure Technology (HETECH)At: Glasgow, UK. September 2013.* 2013.

[8] M. Feiginov, "Frequency Limitations of Resonant-Tunnelling Diodes in Sub-THz and THz Oscillators and Detectors," *J. Infrared Millim. Terahertz Waves*, vol. 40, no. 4, pp. 365–394, Apr. 2019, doi: 10.1007/s10762-019-00573-5.

[9] G. Iannaccone, G. Lombardi, M. Macucci, and B. Pellegrini, "Enhanced Shot Noise in Resonant Tunneling: Theory and Experiment," *Phys. Rev. Lett.*, vol. 80, no. 5, pp. 1054–1057, Feb. 1998, doi: 10.1103/PhysRevLett.80.1054.

[10] L. Reggiani, V. Y. Aleshkin, and A. Reklaitis, "Shot noise enhancement and suppression in single- and multiple- barrier diodes," presented at the SPIE's First International Symposium on Fluctuations and Noise, Santa Fe, NM, May 2003, p. 116. doi: 10.1117/12.496962.

[11] V. Ya. Aleshkin *et al.*, "Coherent approach to transport and noise in double-barrier resonant diodes," *Phys. Rev. B*, vol. 70, no. 11, p. 115321, Sep. 2004, doi: 10.1103/PhysRevB.70.115321.

[12] V. S. Syzranov *et al.*, "Single-well resonant-tunneling diode heterostructures based on In0.53Ga0.47As/AlAs/InP with the peak-to-valley current ratio of 22:1 at room temperature," *Bull. Lebedev Phys. Inst.*, vol. 40, no. 8, pp. 240–243, Aug. 2013, doi: 10.3103/S106833561308006X.

[13] J. H. Smet, T. P. E. Broekaert, and C. G. Fonstad, "Peak-to-valley current ratios as high as 50:1 at room temperature in pseudomorphic In $_{0.53}$ Ga $_{0.47}$ As/AlAs/InAs resonant tunneling diodes," *J. Appl. Phys.*, vol. 71, no. 5, pp. 2475–2477, Mar. 1992, doi: 10.1063/1.351085.

[14] H. H. Tsai, Y. K. Su, H. H. Lin, R. L. Wang, and T. L. Lee, "P-N double quantum well resonant interband tunneling diode with peak-to-valley current ratio of 144 at room temperature," *IEEE Electron Device Lett.*, vol. 15, no. 9, pp. 357–359, Sep. 1994, doi: 10.1109/55.311133.

[15] J. Rinzel and G. Huguet, "Nonlinear Dynamics of Neuronal Excitability, Oscillations, and Coincidence Detection," *Commun. Pure Appl. Math.*, vol. 66, no. 9, pp. 1464–1494, Sep. 2013, doi: 10.1002/cpa.21469.

[16] W. Zhang, A. Al-Khalidi, J. Figueiredo, Q. R. A. Al-Taai, E. Wasige, and R. H. Hadfield, "Analysis of Excitability in Resonant Tunneling Diode-Photodetectors," *Nanomaterials*, vol. 11, no. 6, p. 1590, Jun. 2021, doi: 10.3390/nano11061590.

[17] S. H. Strogatz, *Nonlinear dynamics and chaos: with applications to physics, biology, chemistry, and engineering*, Second edition. Boulder, CO: Westview Press, a member of the Perseus Books Group, 2015.

[18] T. J. Slight and C. N. Ironside, "Investigation Into the Integration of a Resonant Tunnelling Diode and an Optical Communications Laser: Model and Experiment," *IEEE J. Quantum Electron.*, vol. 43, no. 7, pp. 580–587, Jul. 2007, doi: 10.1109/JQE.2007.898847.

[19] D. H. Auston, K. P. Cheung, and P. R. Smith, "Picosecond photoconducting Hertzian dipoles," *Appl. Phys. Lett.*, vol. 45, no. 3, pp. 284–286, Aug. 1984, doi: 10.1063/1.95174.

[20] C. H. Lee, Ed., *Picosecond optoelectronic devices*. Orlando: Academic Press, 1984.

[21] S. Y. Chou, Y. Liu, W. Khalil, T. Y. Hsiang, and S. Alexandrou, "Ultrafast nanoscale metal-semiconductor-metal photodetectors on bulk and low-temperature grown GaAs," *Appl. Phys. Lett.*, vol. 61, no. 7, pp. 819–821, Aug. 1992, doi: 10.1063/1.107755.

[22] A. Krotkus, S. Marcinkevtilus, K. Grigoras, V. Pasiskevicius, and J. A. Tellefsen, "Ultrafast carrier relaxation in low-temperature grown In/sub x/Ga/sub 1-x/As layers," in *Conference on Lasers and Electro-Optics Europe*, Amsterdam Netherlands, 1994, pp. 365–366. doi: 10.1109/CLEOE.1994.636646.

[23] Y. Chen, S. S. Prabhu, S. E. Ralph, and D. T. McInturff, "Trapping and recombination dynamics of low-temperature-grown InGaAs/InAlAs multiple quantum wells," *Appl. Phys. Lett.*, vol. 72, no. 4, pp. 439–441, Jan. 1998, doi: 10.1063/1.120766.

[24] J. Mangeney, L. Joulaud, P. Crozat, J.-M. Lourtioz, and J. Decobert, "Ultrafast response (~2.2 ps) of ion-irradiated InGaAs photoconductive switch at 1.55 μm," *Appl. Phys. Lett.*, vol. 83, no. 26, pp. 5551–5553, Dec. 2003, doi: 10.1063/1.1633030.

[25] S. J. Jo, S.-G. Ihn, J.-I. Song, K.-J. Yee, and D.-H. Lee, "Carrier dynamics of low-temperature-grown In0.53Ga0.47As on GaAs using an InGaAlAs metamorphic buffer," *Appl. Phys. Lett.*, vol. 86, no. 11, p. 111903, Mar. 2005, doi: 10.1063/1.1872207.

[26] H.-J. Song *et al.*, "Microwave Photonic Mixer Utilizing an InGaAs Photoconductor for Radio over Fiber Applications," *IEICE Trans. Electron.*, vol. E90-C, no. 2, pp. 457–464, Feb. 2007, doi: 10.1093/ietele/e90-c.2.457.

[27] R. Horvath, J.-F. Roux, J.-L. Coutaz, and J. Poëtte, "Characterization of ultrafast InGaAs photoconductors and their application to signal processing in radio-over-fibre telecommunications," *Lith. J. Phys.*, vol. 58, no. 1, Mar. 2018, doi: 10.3952/physics.v58i1.3654.

[28] C. Graham, R. Gwilliam, and A. Seeds, "Nitrogen ion implanted InP based photo-switch," *Opt. Express*, vol. 20, no. 24, p. 26696, Nov. 2012, doi: 10.1364/OE.20.026696.

[29] B. P. Figueroa, R. M. S. Kawabata, A. D. B. Maia, M. P. Pires, and P. L. Souza, "Effect of doping on the figures of merit for quantum-well infrared photodetectors based on InGaAs/InAlAs," in *28th Symposium on Microelectronics Technology and Devices (SBMicro 2013)*, Curitiba, Brazil, Sep. 2013, pp. 1–4. doi: 10.1109/SBMicro.2013.6676123.

[30] B. Globisch, R. J. B. Dietz, S. Nellen, T. Göbel, and M. Schell, "Terahertz detectors from Be-doped low-temperature grown InGaAs/InAlAs: Interplay of annealing and terahertz performance," *AIP Adv.*, vol. 6, no. 12, p. 125011, Dec. 2016, doi: 10.1063/1.4971843.

[31] H. C. Liu, Ed., *Intersubband transitions in quantum wells: physics and device applications. 1: ...* San Diego, Calif.: Acad. Press, 2000.

[32] Leo Esaki, George A. Sei Halasz, Leroy L. Chang, "Infrared optical devices of layered structures," US4205331A, 1978 [Online]. Available: https://patents.google.com/patent/US4205331A/en

[33] J. S. Smith, "A new infrared detector using electron emission from multiple quantum wells," *J. Vac. Sci. Technol. B Microelectron. Nanometer Struct.*, vol. 1, no. 2, p. 376, 1983, doi: 10.1116/1.582560.

[34] B. F. Levine, K. K. Choi, C. G. Bethea, J. Walker, and R. J. Malik, "New 10 μm infrared detector using intersubband absorption in resonant tunneling GaAlAs superlattices," *Appl. Phys. Lett.*, vol. 50, no. 16, pp. 1092–1094, Apr. 1987, doi: 10.1063/1.97928.

[35] K. M. S. V. Bandara, B. F. Levine, and M. T. Asom, "Tunneling emitter undoped quantum-well infrared photodetector," *J. Appl. Phys.*, vol. 74, no. 1, pp. 346–350, Jul. 1993, doi: 10.1063/1.354115.

[36] P. D. Grant, R. Dudek, M. Buchanan, and H. C. Liu, "Room-Temperature Heterodyne Detection up to 110 GHz With a Quantum-Well Infrared Photodetector," *IEEE Photonics Technol. Lett.*, vol. 18, no. 21, pp. 2218–2220, Nov. 2006, doi: 10.1109/LPT.2006.884267.

[37] H. C. Liu, H. Luo, C. Song, Z. R. Wasilewski, A. J. SpringThorpe, and J. C. Cao, "Terahertz Quantum Well Photodetectors," *IEEE J. Sel. Top. Quantum Electron.*, vol. 14, no. 2, pp. 374–377, 2008, doi: 10.1109/JSTQE.2007.910710.

[38] L. Sun, B. Su, L. Lu, J. Xue, and D. H. Zhang, "Avalanche multiplication process in InGaAsP/InP quantum well infrared photodetectors," in *2011 International Conference on Electronics, Communications and Control (ICECC)*, Ningbo, China, Sep. 2011, pp. 1913–1916. doi: 10.1109/ICECC.2011.6067929.

[39] J.-H. Lu *et al.*, "A Superlattice Infrared Photodetector Integrated With Multiple Quantum Wells to Improve the Performance," *IEEE J. Quantum Electron.*, vol. 43, no. 1, pp. 72–77, Jan. 2007, doi: 10.1109/JQE.2006.884584.

[40] J. Aberl, M. Brehm, T. Fromherz, J. Schuster, J. Frigerio, and P. Rauter, "SiGe quantum well infrared photodetectors on strained-silicon-on-insulator," *Opt. Express*, vol. 27, no. 22, p. 32009, Oct. 2019, doi: 10.1364/OE.27.032009.

[41] M. Hakl *et al.*, "Ultra-fast quantum-well infared photodetectors operating at 10µm with flat response up to 70GHz at room temperature," 2020, doi: 10.48550/ARXIV.2007.00299.

[42] H. Kumar and A. K. Pandey, "GeSn-Based Multiple-Quantum-Well Photodetectors for Mid-Infrared Sensing Applications," *IEEE Trans. NanoBioscience*, vol. 21, no. 2, pp. 175–183, Apr. 2022, doi: 10.1109/TNB.2021.3136571.

[43] L. C. Chiu, J. S. Smith, S. Margalit, A. Yariv, and A. Y. Cho, "Application of internal photoemission from quantum-well and heterojunction superlattices to infrared photodetectors," *Infrared Phys.*, vol. 23, no. 2, pp. 93–97, Mar. 1983, doi: 10.1016/0020-0891(83)90018-0.

[44] D. D. Coon and R. P. G. Karunasiri, "New mode of IR detection using quantum wells," *Appl. Phys. Lett.*, vol. 45, no. 6, pp. 649–651, Sep. 1984, doi: 10.1063/1.95343.

[45] L. C. West and S. J. Eglash, "First observation of an extremely large-dipole infrared transition within the conduction band of a GaAs quantum well," *Appl. Phys. Lett.*, vol. 46, no. 12, pp. 1156–1158, Jun. 1985, doi: 10.1063/1.95742.

[46] D. D. Coon, R. P. G. Karunasiri, and L. Z. Liu, "Narrow band infrared detection in multiquantum well structures," *Appl. Phys. Lett.*, vol. 47, no. 3, pp. 289–291, Aug. 1985, doi: 10.1063/1.96195.

[47] D. D. Coon, R. P. G. Karunasiri, and H. C. Liu, "Fast response quantum well photodetectors," *J. Appl. Phys.*, vol. 60, no. 7, pp. 2636–2638, Oct. 1986, doi: 10.1063/1.337085.

[48] A. Harwit and J. S. Harris, "Observation of Stark shifts in quantum well intersubband transitions," *Appl. Phys. Lett.*, vol. 50, no. 11, pp. 685–687, Mar. 1987, doi: 10.1063/1.98066.

[49] B. F. Levine, "Quantum-well infrared photodetectors," *J. Appl. Phys.*, vol. 74, no. 8, pp. R1–R81, Oct. 1993, doi: 10.1063/1.354252.

[50] K. K. Choi, "Reduction of photoconductive gain in quantum well infrared photodetectors," *J. Appl. Phys.*, vol. 80, no. 2, pp. 1257–1259, Jul. 1996, doi: 10.1063/1.362868.

[51] S. C. Kan, S. Wu, S. Sanders, G. Griffel, and A. Yariv, "Optically controlled resonant tunneling in a double-barrier diode," *J. Appl. Phys.*, vol. 69, no. 5, pp. 3384–3386, Mar. 1991, doi: 10.1063/1.348515.

[52] H. S. Li, "Photocontrolled double-barrier resonant-tunneling diode," *J. Vac. Sci. Technol. B Microelectron. Nanometer Struct.*, vol. 12, no. 2, p. 1269, Mar. 1994, doi: 10.1116/1.587019.

[53] P. W. Park, H. Y. Chu, S. G. Han, Y. W. Choi, G. Kim, and E. Lee, "Optical switching mechanism based on charge accumulation effects in resonant tunneling diodes," *Appl. Phys. Lett.*, vol. 67, no. 9, pp. 1241–1243, Aug. 1995, doi: 10.1063/1.114384.

[54] T. S. Moise, Y. -C. Kao, L. D. Garrett, and J. C. Campbell, "Optically switched resonant tunneling diodes," *Appl. Phys. Lett.*, vol. 66, no. 9, pp. 1104–1106, Feb. 1995, doi: 10.1063/1.113826.

[55] T. S. Moise, Y.-C. Kao, C. L. Goldsmith, C. L. Schow, and J. C. Campbell, "High-speed resonant-tunneling photodetectors with low-switching energy," *IEEE Photonics Technol. Lett.*, vol. 9, no. 6, pp. 803–805, Jun. 1997, doi: 10.1109/68.584996.

[56] J. M. L. Figueired, C. N. Ironside, and C. R. Stanley, "The electric field switching in resonant tunneling diode electroabsorption modulator," in *Optical Fiber Communication Conference and International Conference on Quantum Information*, Anaheim, California, 2001, p. WDD62. doi: 10.1364/OFC.2001.WDD62.

[57] B. Romeira, L. Pessoa, H. Salgado, C. Ironside, and J. Figueiredo, "Photo-Detectors Integrated with Resonant Tunneling Diodes," *Sensors*, vol. 13, no. 7, pp. 9464–9482, Jul. 2013, doi: 10.3390/s130709464.

[58] Y. Dong *et al.*, "Resonant tunnelling diode photodetector operating at near-infrared wavelengths with high responsivity," *Electron. Lett.*, vol. 51, no. 17, pp. 1355–1357, Aug. 2015, doi: 10.1049/el.2015.1041.

[59] A. Pfenning, F. Hartmann, F. Langer, M. Kamp, S. Höfling, and L. Worschech, "Cavity-enhanced AlGaAs/GaAs resonant tunneling photodetectors for telecommunication wavelength light detection at 1.3 µm," presented at the SPIE Optical Engineering + Applications, San Diego, California, United States, Sep. 2015, p. 960810. doi: 10.1117/12.2188614.

[60] J. C. Blakesley *et al.*, "Efficient Single Photon Detection by Quantum Dot Resonant Tunneling Diodes," *Phys. Rev. Lett.*, vol. 94, no. 6, p. 067401, Feb. 2005, doi: 10.1103/PhysRevLett.94.067401.

[61] D. M. Zhou *et al.*, "The photocurrent of resonant tunneling diode controlled by the charging effects of quantum dots," *Opt. Quantum Electron.*, vol. 45, no. 7, pp. 687–692, Jul. 2013, doi: 10.1007/s11082-013-9672-6.

[62] A. Pfenning, J. Jurkat, A. Naranjo, D. Köck, F. Hartmann, and S. Höfling, "Resonant tunneling diode photon number resolving single-photon detectors," in *Infrared Remote Sensing and Instrumentation XXVII*, San Diego, United States, Sep. 2019, p. 10. doi: 10.1117/12.2529929.

[63] B. Romeira, K. Seunarine, C. N. Ironside, A. E. Kelly, and J. M. L. Figueiredo, "A Self-Synchronized Optoelectronic Oscillator Based on an RTD Photodetector and a Laser Diode," *IEEE Photonics Technol. Lett.*, vol. 23, no. 16, pp. 1148–1150, Aug. 2011, doi: 10.1109/LPT.2011.2154320.

[64] H. I. Cantu, B. Romeira, A. E. Kelly, C. N. Ironside, and J. M. L. Figueiredo, "Resonant Tunneling Diode Optoelectronic Circuits Applications in Radio-Over-Fiber Networks," *IEEE Trans. Microw. Theory Tech.*, vol. 60, no. 9, pp. 2903–2912, Sep. 2012, doi: 10.1109/TMTT.2012.2206606.

[65] A. Al-Khalidi *et al.*, "Resonant Tunneling Diode Terahertz Sources With up to 1 mW Output Power in the *J* -Band," *IEEE Trans. Terahertz Sci. Technol.*, vol. 10, no. 2, pp. 150–157, Mar. 2020, doi: 10.1109/TTHZ.2019.2959210.

[66] J. Webber, N. Nishigami, J.-Y. Kim, M. Fujita, and T. Nagatsuma, "Terahertz Wireless CDMA Communication Using Resonant Tunneling Diodes," in *2019 IEEE Globecom Workshops (GC Wkshps)*, Waikoloa, HI, USA, Dec. 2019, pp. 1–6. doi: 10.1109/GCWkshps45667.2019.9024595.

[67] J. Park, J. Lee, and K. Yang, "A 24-GHz Low-Power RTD-Based ON–OFF Keying Oscillator With an RTD Pair Configuration," *IEEE Microw. Wirel. Compon. Lett.*, vol. 28, no. 6, pp. 521–523, Jun. 2018, doi: 10.1109/LMWC.2018.2831201.

[68] Y. Nishida, N. Nishigami, S. Diebold, J. Kim, M. Fujita, and T. Nagatsuma, “Terahertz coherent receiver using a single resonant tunnelling diode,” *Sci. Rep.*, vol. 9, no. 1, p. 18125, Dec. 2019, doi: 10.1038/s41598-019-54627-8.

[69] J.-P. Colinge and C. A. Colinge, *Physics of semiconductor devices*, 1. softcover ed. New York, NY: Springer, 2006.

[70] D. A. Neamen, *Semiconductor physics and devices: basic principles*, 4th ed. New York, NY: McGraw-Hill, 2012.

[71] G. Parker, *Introductory semiconductor device physics*. Bristol ; Philadelphia: Institute of Physics Pub, 2004.

[72] R. F. Pierret, *Semiconductor device fundamentals*. Reading, Mass: Addison-Wesley, 1996.

[73] P. Harrison, *Quantum wells, wires and dots: theoretical and computational physics*, 3rd ed. West Sussex, England ; Hoboken, NJ: Wiley, 2009.

[74] M. E. Levinshtein, S. L. Rumyantsev, and M. Shur, *Handbook series on semiconductor parameters*. Singapore; New Jersey: World Scientific, 1996.

[75] S. M. Sze and K. K. Ng, *Physics of semiconductor devices*, 3rd ed. Hoboken, N.J: Wiley-Interscience, 2007.

[76] D. J. Griffiths and D. F. Schroeter, *Introduction to quantum mechanics*, Third edition. Cambridge ; New York, NY: Cambridge University Press, 2018.

[77] J. H. Davies, *The physics of low-dimensional semiconductors: an introduction*. Cambridge, U.K. ; New York, NY, USA: Cambridge University Press, 1998.

[78] H. Mizuta and T. Tanoue, *The physics and applications of resonant tunnelling diodes*, Digitally printed 1. paperback version. Cambridge: Cambridge Univ. Press, 2006.

[79] L. Esaki, “New Phenomenon in Narrow Germanium p − n Junctions,” *Phys. Rev.*, vol. 109, no. 2, pp. 603–604, Jan. 1958, doi: 10.1103/PhysRev.109.603.

[80] MIT, “Quantum physics I,” *Ocw.mit.edu*, 2022. https://ocw.mit.edu/courses/physics/8-04-quantum-physics-i-spring-2013

[81] B. E. A. Saleh and M. C. Teich, *Fundamentals of photonics*, 2nd ed. Hoboken, N.J: Wiley Interscience, 2007.

[82] S. O. Kasap, *Optoelectronics and photonics: principles and practices*, 2nd ed. Boston: Pearson, 2013.

[83] A. Alqurashi, “A New Approximation of Fermi-Dirac Integrals of Order 1/2 by Prony’s Method and Its Applications in Semiconductor Devices,” PhD Thesis, 2017.

[84] T. C. L. G. Sollner, W. D. Goodhue, P. E. Tannenwald, C. D. Parker, and D. D. Peck, “Resonant tunneling through quantum wells at frequencies up to 2.5 THz,” *Appl. Phys. Lett.*, vol. 43, no. 6, pp. 588–590, Sep. 1983, doi: 10.1063/1.94434.

[85] K. Chang, *Encyclopedia of RF and microwave engineering*. 2005. Accessed: Apr. 11, 2022. [Online]. Available: http://app.knovel.com/hotlink/toc/id:kpERFMEV04/encyclopedia-of-rf

[86] J. M. Gering, D. A. Crim, D. G. Morgan, P. D. Coleman, W. Kopp, and H. Morkoç, “A small-signal equivalent-circuit model for GaAs-Al $_{x}$ Ga $_{1-x}$ As resonant tunneling heterostructures at microwave frequencies,” *J. Appl. Phys.*, vol. 61, no. 1, pp. 271–276, Jan. 1987, doi: 10.1063/1.338872.

[87] Silvaco Inc., “Atlas user’s manual: Device simulation software.” Silvaco Inc., 2016.

[88] G. Green, *An Essay on the Application of Mathematical Analysis to the Theories of Electricity and Magnetism*. author, 1828. [Online]. Available: https://books.google.jo/books?id=GwYXAAAAYAAJ

[89] L. V. Keldysh, "Diagram technique for nonequilibrium processes," *Zh Eksp Teor Fiz*, vol. 47, pp. 1515–1527, 1964.

[90] S. Datta, *Electronic Transport in Mesoscopic Systems*, 1st ed. Cambridge University Press, 1995. doi: 10.1017/CBO9780511805776.

[91] S. Datta, "The non-equilibrium Green's function (NEGF) formalism: An elementary introduction," in *Digest. International Electron Devices Meeting,* San Francisco, CA, USA, 2002, pp. 703–706. doi: 10.1109/IEDM.2002.1175935.

[92] C. Kim and A. Brandli, "High-Frequency High-Power Operation of Tunnel Diodes," *IRE Trans. Circuit Theory*, vol. 8, no. 4, pp. 416–425, 1961, doi: 10.1109/TCT.1961.1086849.

[93] S.-J. Wei, H. C. Lin, R. C. Potter, and D. Shupe, "A self-latching A/D converter using resonant tunneling diodes," *IEEE J. Solid-State Circuits*, vol. 28, no. 6, pp. 697–700, Jun. 1993, doi: 10.1109/4.217986.

[94] R. Masoudian and N. Hatefi Kargan, "The Effect of Structural Parameters on the Electronic States and Oscillator Strength of a Resonant Tunneling Quantum Well Infrared Photodetector," *Int. J. Opt. Photonics*, 2015.

[95] P. Mounaix, O. Vanbesien, and D. Lippens, "Effect of cathode spacer layer on the current-voltage characteristics of resonant tunneling diodes," *Appl. Phys. Lett.*, vol. 57, no. 15, pp. 1517–1519, Oct. 1990, doi: 10.1063/1.103381.

[96] D. Banasree, P. Manas, and M. Saikat, "Effects on I-V characteristics of RTD due to different parametric variations," in *2017 Devices for Integrated Circuit (DevIC)*, Kalyani, India, Mar. 2017, pp. 257–261. doi: 10.1109/DEVIC.2017.8073947.

[97] K. S. Grishakov and V. F. Elesin, "Emitter Spacer Layers Influence on the Dynamic Characteristics of Resonant-Tunneling Diode," *IEEE Trans. Electron Devices*, vol. 64, no. 7, pp. 2963–2969, Jul. 2017, doi: 10.1109/TED.2017.2699693.

[98] S. G. Muttlak, O. S. Abdulwahid, J. Sexton, M. J. Kelly, and M. Missous, "InGaAs/AlAs Resonant Tunneling Diodes for THz Applications: An Experimental Investigation," *IEEE J. Electron Devices Soc.*, vol. 6, pp. 254–262, 2018, doi: 10.1109/JEDS.2018.2797951.

[99] H. Yoo, "Effect of structural parameters on resonant tunneling diode performance," Oregon state University, 1990.

[100] M. Charmi and M. H. Yousefi, "Design Considerations of Structural Parameters in Resonant Tunneling Diode by None-Equilibrium Green Function Method," *J. Nano-Electron. Phys.*, vol. 7, 2015.

[101] S. Ipsita, P. K. Mahapatra, and P. Panchadhyayee, "Optimum device parameters to attain the highest peak to valley current ratio (PVCR) in resonant tunneling diodes (RTD)," *Phys. B Condens. Matter*, vol. 611, p. 412788, Jun. 2021, doi: 10.1016/j.physb.2020.412788.

[102] I. Vurgaftman, J. R. Meyer, and L. R. Ram-Mohan, "Band parameters for III–V compound semiconductors and their alloys," *J. Appl. Phys.*, vol. 89, no. 11, pp. 5815–5875, Jun. 2001, doi: 10.1063/1.1368156.

[103] K. B. Lipkowitz and ed, *Reviews in computacional chemistry IV*. New York: Wiley-VCH, 1993.

[104] A. Ghatak and S. Lokanathan, *Quantum Mechanics: Theory and Applications*. Dordrecht: Springer Netherlands, 2004. doi: 10.1007/978-1-4020-2130-5.
[105] D. Vasileska, S. M. Goodnick, and G. Klimeck, *Computational electronics: semiclassical and quantum device modeling and simulation*. Boca Raton: Boca Raton, 2010.
[106] M. A. Md Zawawi and M. Missous, "Design and fabrication of low power GaAs/AlAs resonant tunneling diodes," *Solid-State Electron.*, vol. 138, pp. 30–34, Dec. 2017, doi: 10.1016/j.sse.2017.09.004.
[107] M. K. Jackson, M. B. Johnson, D. H. Chow, T. C. McGill, and C. W. Nieh, "Electron tunneling time measured by photoluminescence excitation correlation spectroscopy," *Appl. Phys. Lett.*, vol. 54, no. 6, pp. 552–554, Feb. 1989, doi: 10.1063/1.100928.
[108] J. I. Pankove, *Optical processes in semiconductors*, Unabridged republ. with slight corr. New York: Dover, 1975.
[109] J. G. Webster, Ed., *Wiley encyclopedia of electrical and electronics engineering*. New York: John Wiley, 1999.
[110] U. I. Sensors, "Sensors Unlimited." [Online]. Available: http://www.sensorsinc.com/
[111] S. L. Chuang, *Physics of photonic devices*, 2nd ed. Hoboken, N.J: John Wiley & Sons, 2009.
[112] S. Ramo, "Currents Induced by Electron Motion," *Proc. IRE*, vol. 27, no. 9, pp. 584–585, Sep. 1939, doi: 10.1109/JRPROC.1939.228757.
[113] W. Shockley, "Currents to Conductors Induced by a Moving Point Charge," *J. Appl. Phys.*, vol. 9, no. 10, pp. 635–636, Oct. 1938, doi: 10.1063/1.1710367.
[114] X. Sun *et al.*, "High spectral response of self-driven GaN-based detectors by controlling the contact barrier height," *Sci. Rep.*, vol. 5, no. 1, p. 16819, Dec. 2015, doi: 10.1038/srep16819.
[115] F. Ren and J. C. Zolper, Eds., *Wide energy bandgap electronic devices*. New Jersey: World Scientific, 2003.
[116] M. A. Kinch, S. R. Borrello, B. H. Breazeale, and A. Simmons, "Geometrical enhancement of HgCdTe photoconductive detectors," *Infrared Phys.*, vol. 17, no. 2, pp. 137–145, Mar. 1977, doi: 10.1016/0020-0891(77)90106-3.
[117] Y. Dan, X. Zhao, K. Chen, and A. Mesli, "A Photoconductor Intrinsically Has No Gain," *ACS Photonics*, vol. 5, no. 10, pp. 4111–4116, Oct. 2018, doi: 10.1021/acsphotonics.8b00805.
[118] S. Paul, J. B. Roy, and P. K. Basu, "Empirical expressions for the alloy composition and temperature dependence of the band gap and intrinsic carrier density in $Ga_x In_{1-x} As$," *J. Appl. Phys.*, vol. 69, no. 2, pp. 827–829, Jan. 1991, doi: 10.1063/1.348919.
[119] T. P. Pearsall, Ed., *GaInAsP alloy semiconductors*. Chichester [West Sussex] ; New York: Wiley, 1982.
[120] D. Chattopadhyay, S. K. Sutradhar, and B. R. Nag, "Electron transport in direct-gap III-V ternary alloys," *J. Phys. C Solid State Phys.*, vol. 14, no. 6, pp. 891–908, Feb. 1981, doi: 10.1088/0022-3719/14/6/014.
[121] J. Manuel Torres Pereira, "Modeling the frequency response of p^+ InP/n^- InGaAs/n^+ InP photodiodes with an arbitrary electric field profile," *COMPEL - Int. J. Comput. Math. Electr. Electron. Eng.*, vol. 26, no. 4, pp. 1114–1122, Aug. 2007, doi: 10.1108/03321640710756438.

[122] C. H. Henry, R. A. Logan, F. R. Merritt, and C. G. Bethea, "Radiative and nonradiative lifetimes in n-type and p-type 1.6 μm InGaAs," *Electron. Lett.*, vol. 20, no. 9, p. 358, 1984, doi: 10.1049/el:19840245.

[123] A. Brillant, *Digital and analog fiber optic communications for CATV and FTTx applications*. Hoboken, N. J: Wiley-Interscience, 2008.

[124] electronics notes, "Photodiode structures." [Online]. Available: https://www.electronics-notes.com/articles/electronic_components/diode/photodiode-detector-structures-fabrication-materials.php

[125] S. Alomari and J. Figueiredo, "Simulation and Modelling of Resonant Tunneling Diode Peak Voltage Dependence on Spacer Layers," in *2021 35th Symposium on Microelectronics Technology and Devices (SBMicro)*, Campinas, Brazil, Aug. 2021, pp. 1–4. doi: 10.1109/SBMicro50945.2021.9585751.

[126] S. Adachi, *Physical properties of III-V semiconductor compounds: InP, InAs, GaAs, GaP, InGaAs, and InGaAsP*. New York: Wiley, 1992.

[127] E. Zielinski, H. Schweizer, K. Streubel, H. Eisele, and G. Weimann, "Excitonic transitions and exciton damping processes in InGaAs/InP," *J. Appl. Phys.*, vol. 59, no. 6, pp. 2196–2204, Mar. 1986, doi: 10.1063/1.336358.

[128] Awan, Iram Taj, "Optical and transport properties of PIN GaAs/AlAs resonant tunneling diodes," Universidade Federal de São Carlos, Brasil, 2014.

[129] T. Kozakai, "HOLE ACCUMULATION EFFECT OF InGaAs HIGH-ELECTRON-MOBILITY TRANSISTORS WITH A 1550-nm WAVELENGTH FEMTOSECOND PULSE LASER," *Int. J. GEOMATE*, vol. 17, no. 61, Sep. 2019, doi: 10.21660/2019.61.4576.

[130] Y. S. Yong, H. Y. Wong, H. K. Yow, and M. Sorel, "A convenient band-gap interpolation technique and an improved band line-up model for InGaAlAs on InP," *Appl. Phys. B*, vol. 99, no. 3, pp. 477–486, May 2010, doi: 10.1007/s00340-010-4000-3.

[131] J. P. Praseuth, M. C. Joncour, J. M. Gérard, P. Hénoc, and M. Quillec, "Growth and characterization of AlGaInAs lattice matched to InP grown by molecular-beam epitaxy," *J. Appl. Phys.*, vol. 63, no. 2, pp. 400–403, Jan. 1988, doi: 10.1063/1.340252.

[132] P. England, J. E. Golub, L. T. Florez, and J. P. Harbison, "Optical switching in a resonant tunneling structure," *Appl. Phys. Lett.*, vol. 58, no. 9, pp. 887–889, Mar. 1991, doi: 10.1063/1.104467.

[133] A. Pfenning *et al.*, "Photocurrent-voltage relation of resonant tunneling diode photodetectors," *Appl. Phys. Lett.*, vol. 107, no. 8, p. 081104, Aug. 2015, doi: 10.1063/1.4929424.

[134] I. J. S. Coêlho, J. F. Martins-Filho, J. M. L. Figueiredo, and C. N. Ironside, "Modeling of light-sensitive resonant-tunneling-diode devices," *J. Appl. Phys.*, vol. 95, no. 12, pp. 8258–8263, Jun. 2004, doi: 10.1063/1.1728290.

[135] S. Alomari and J. Figueiredo, "Resonant Tunneling Diode Based Photodetectors Design Rules for Telecom Applications," in *2021 IEEE International Conference on Telecommunications and Photonics (ICTP)*, Dhaka, Bangladesh, Dec. 2021, pp. 1–5. doi: 10.1109/ICTP53732.2021.9744181.

[136] R. K. Ahrenkiel, R. Ellingson, S. Johnston, and M. Wanlass, "Recombination lifetime of In0.53Ga0.47As as a function of doping density," *Appl. Phys. Lett.*, vol. 72, no. 26, pp. 3470–3472, Jun. 1998, doi: 10.1063/1.121669.

[137] S. P. Gentile, *Basic Theory and Application of Tunnel Diodes*. Van Nostrand, 1962. [Online]. Available: https://books.google.pt/books?id=M7u_AAAAIAAJ
[138] I. Gravé, S. C. Kan, G. Griffel, S. W. Wu, A. Sa'ar, and A. Yariv, "Monolithic integration of a resonant tunneling diode and a quantum well semiconductor laser," *Appl. Phys. Lett.*, vol. 58, no. 2, pp. 110–112, Jan. 1991, doi: 10.1063/1.104970.
[139] H. Sheng and S.-J. Chun, "Properties of monolithic integration of a resonant tunneling diode and a quantum well laser," *Superlattices Microstruct.*, vol. 16, no. 2, p. 157, Sep. 1994, doi: 10.1006/spmi.1994.1130.
[140] E. S. Alves *et al.*, "Observation of intrinsic bistability in resonant tunnelling devices," *Electron. Lett.*, vol. 24, no. 18, p. 1190, 1988, doi: 10.1049/el:19880809.
[141] F. W. Sheard and G. A. Toombs, "Space-charge buildup and bistability in resonant-tunneling double-barrier structures," *Appl. Phys. Lett.*, vol. 52, no. 15, pp. 1228–1230, Apr. 1988, doi: 10.1063/1.99165.
[142] T. C. L. G. Sollner, "Comment on '"Observation of intrinsic bistability in resonant-tunneling structures,"'" *Phys. Rev. Lett.*, vol. 59, no. 14, pp. 1622–1622, Oct. 1987, doi: 10.1103/PhysRevLett.59.1622.
[143] B. Romeira *et al.*, "Synchronisation and chaos in a laser diode driven by a resonant tunnelling diode," *IET Optoelectron.*, vol. 2, no. 6, pp. 211–215, Dec. 2008, doi: 10.1049/iet-opt:20080024.
[144] C. N. Ironside, J. M. L. Figueiredo, B. Romeira, T. J. Slight, L. Wang, and E. Wasige, "Resonant tunneling diode-laser diode optoelectronic integrated circuit operating as a voltage controlled oscillator," presented at the SPIE Europe Microtechnologies for the New Millennium, Dresden, Germany, May 2009, p. 736614. doi: 10.1117/12.822570.
[145] J. N. Schulman, H. J. De Los Santos, and D. H. Chow, "Physics-based RTD current-voltage equation," *IEEE Electron Device Lett.*, vol. 17, no. 5, pp. 220–222, May 1996, doi: 10.1109/55.491835.
[146] M. H. R. Faria, R. V. T. da Nobrega, and U. R. Duarte, "10-Steps Method to Extract the I-V Curve of Resonant Tunneling Diode Based on Experimental Data Preserving Physical Parameters," in *Proceedings of the 4th Brazilian Technology Symposium (BTSym'18)*, vol. 140, Y. Iano, R. Arthur, O. Saotome, V. Vieira Estrela, and H. J. Loschi, Eds. Cham: Springer International Publishing, 2019, pp. 303–312. doi: 10.1007/978-3-030-16053-1_29.
[147] J. H. Davies, *The Physics of Low-dimensional Semiconductors: An Introduction*, 1st ed. Cambridge University Press, 1997. doi: 10.1017/CBO9780511819070.
[148] J. Singh, *Semiconductor optoelectronics: physics and technology*. New York: McGraw-Hill, 1995.
[149] P. V. Mena, Sung-Mo Kang, and T. A. DeTemple, "Rate-equation-based laser models with a single solution regime," *J. Light. Technol.*, vol. 15, no. 4, pp. 717–730, Apr. 1997, doi: 10.1109/50.566695.
[150] S. A. Javro and S. M. Kang, "Transforming Tucker's linearization laser rate equations to a form that has a single solution regime," *J. Light. Technol.*, vol. 13, no. 9, pp. 1899–1904, Sep. 1995, doi: 10.1109/50.464741.
[151] J. Katz, S. Margalit, C. Harder, D. Wilt, and A. Yariv, "The intrinsic electrical equivalent circuit of a laser diode," *IEEE J. Quantum Electron.*, vol. 17, no. 1, pp. 4–7, Jan. 1981, doi: 10.1109/JQE.1981.1070628.

[152] M. Morishita, T. Ohmi, and J. Nishizawa, "Impedance characteristics of double-hetero structure laser diodes," *Solid-State Electron.*, vol. 22, no. 11, pp. 951–962, Nov. 1979, doi: 10.1016/0038-1101(79)90068-6.

[153] NI, "Decoupling techniques." [Online]. Available: https://www.analog.com/media/en/training-seminars/tutorials/MT-101.pdf

[154] "Multisim." National Instruments. [Online]. Available: https://www.ni.com/en-gb/shop/electronic-test-instrumentation/application-software-for-electronic-test-and-instrumentation-category/what-is-multisim.html

[155] T. J. Slight, B. Romeira, L. Wang, J. M. L. Figueiredo, E. Wasige, and C. N. Ironside, "A LiÉnard Oscillator Resonant Tunnelling Diode-Laser Diode Hybrid Integrated Circuit: Model and Experiment," *IEEE J. Quantum Electron.*, vol. 44, no. 12, pp. 1158–1163, Dec. 2008, doi: 10.1109/JQE.2008.2000924.

[156] Herbert J. Reich, *Functional Circuits and Oscillators*, Repirnt edition. Boston Technical Publishers, 1965.

[157] H. W. Li *et al.*, "Quantum dot resonant tunneling diode for telecommunication wavelength single photon detection," *Appl. Phys. Lett.*, vol. 91, no. 7, p. 073516, Aug. 2007, doi: 10.1063/1.2768884.

[158] S. S. Hees, B. E. Kardynal, P. See, A. J. Shields, I. Farrer, and D. A. Ritchie, "Effect of InAs dots on noise of quantum dot resonant tunneling single-photon detectors," *Appl. Phys. Lett.*, vol. 89, no. 15, p. 153510, Oct. 2006, doi: 10.1063/1.2362997.

[159] Dr. Rüdiger Paschotta, "Modulation depth." RP Photonics.com. [Online]. Available: https://www.rp-photonics.com/modulation_depth.html

[160] K. Fobelets, C. Van Hoof, J. Genoe, J. Stake, L. Lundgren, and G. Borghs, "High-frequency capacitance of bipolar resonant tunneling diodes," *J. Appl. Phys.*, vol. 79, no. 2, p. 905, 1996, doi: 10.1063/1.360870.

[161] T. Wei and S. Stapleton, "Capacitance of resonant tunneling diodes with spacer layers," *Solid-State Electron.*, vol. 38, no. 2, pp. 465–469, Feb. 1995, doi: 10.1016/0038-1101(94)00119-Z.

[162] J. Genoe *et al.*, "Capacitances in double-barrier tunneling structures," *IEEE Trans. Electron Devices*, vol. 38, no. 9, pp. 2006–2012, Sep. 1991, doi: 10.1109/16.83722.

[163] T. Wei and S. Stapleton, "Effect of spacer layers on capacitance of resonant tunneling diodes," *J. Appl. Phys.*, vol. 76, no. 2, pp. 1287–1290, Jul. 1994, doi: 10.1063/1.357788.

[164] W. F. Egan, *Practical RF system design*. New York; Hoboken, N.J: IEEE, 2010.

[165] H. Zumbahlenas and Analog Devices, inc, Eds., *Linear circuit design handbook*. Amsterdam ; Boston: Elsevier/Newnes Press, 2008.